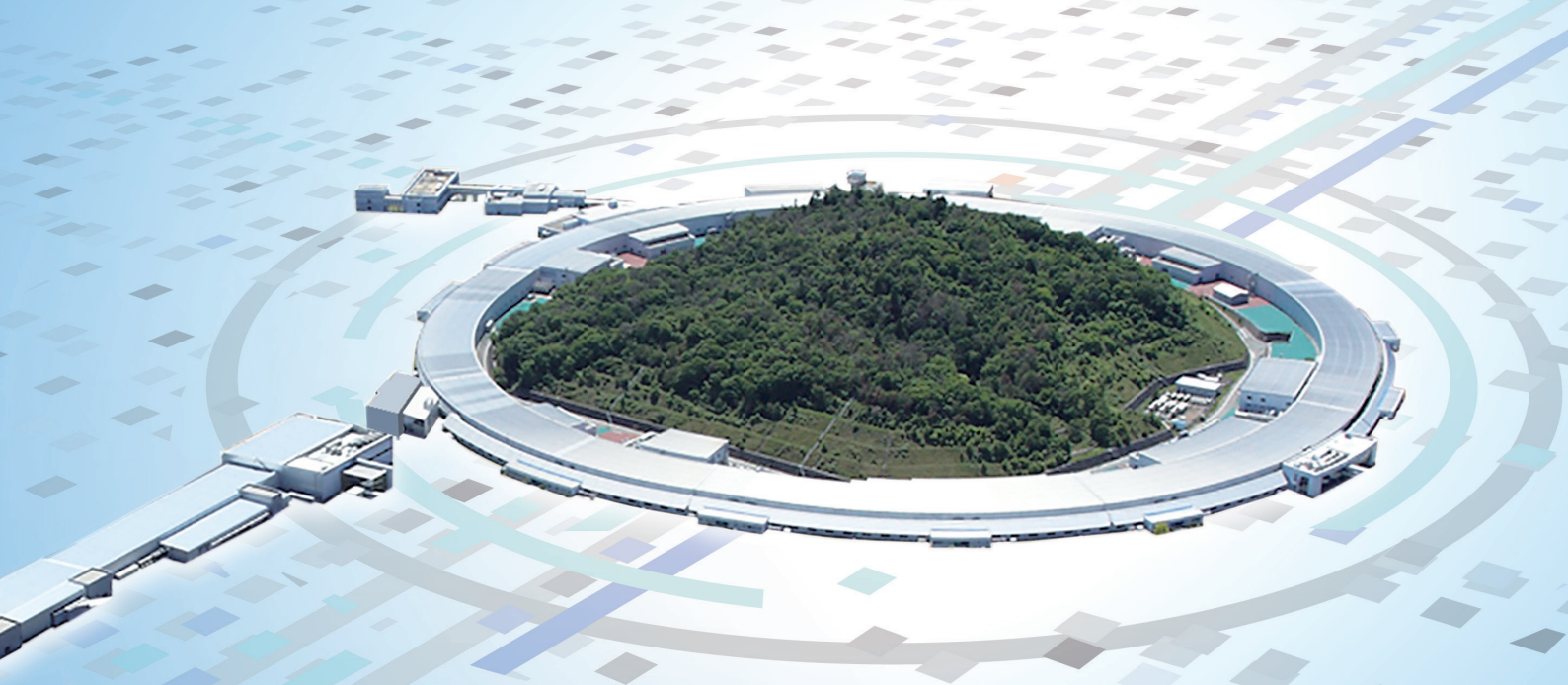

SPring-8 Research Frontiers 2013

ISSN 1349-0087
SPring-8 Document D2014-010

SPring-8
Research Frontiers 2013

CONTENTS

Note: The principal publication(s) concerning each article is indicated with all author's names in italics in the list of references.

Preface

Since beginning operations in 1997, SPring-8 has welcomed over 160,000 users. In 2013, we had 7,800 users conduct 1,240 experiments at the 26 public beamlines and 5,600 users conduct 560 experiments at the 19 contract beamlines. The operation time of the storage ring in 2013 was approximately 4,300 h, 80% of which (3,400 h) was available to users. This is about 1,000 h less than a typical year due to large-scale renovations of the aging cooling water and air-conditioning system. In the past 15 years, research conducted at SPring-8 has resulted in 8,000 published papers, and the average number of citations per paper is as high as 16. In 2013, about 800 papers were published.

User operations of the SACLA X-ray free electron laser (XFEL) facility began in March 2012. In 2013, two beamlines (BL3 for XFEL and BL1 for broadband spontaneous light) were available to users, but all experiments were conducted at BL3. The total operation time in 2013 was about 7,000 h, and the user time was about 3,500 h. We had 680 users conduct 54 experiments in 2013. In 2012 and 2013, SACLA experiments resulted in 7 and 20 published papers, respectively. Thus, the SPring-8 campus provides a unique environment where the SPring-8 and SACLA facilities operate synergistically.

In 2013, users of the SPring-8 and SACLA facilities reported their research in high-impact journals such as *Nature* and *Science*. Fields of study included structural biology, medical biology, materials science, chemical science, earth science, planetary science, environmental science, nuclear physics, industrial applications, and facility methodology. In this 2013 volume, we will report the highlights of scientific achievements from the SPring-8 and SACLA users.

I am very grateful to the many authors and experts who contributed their papers to this volume. Special thanks are due to Dr. Naoto Yagi and the members of the editorial board for their constant efforts.

土肥義治

Yoshiharu Doi
President
SPring-8/JASRI

Editor's Note

SPring-8 Research Frontiers 2013 covers advances made mainly in the second half of 2012 (2012B) and the first half of 2013 (2013A). Remarkable scientific achievements at SPring-8 and SACLA in diverse scientific fields, including industrial applications, are described. The development of accelerators, beamlines, and experimental apparatus, and the present status of the SPring-8 and SACLA facilities are also presented. In addition, the activities using NewSUBARU, which forms an integral part of the research complex, are introduced.

Although this report is called SPring-8 Research Frontiers, it is meant to include all activities at the SPring-8 site. This is a historic year for SACLA because this is the first time scientific reports from experiments conducted at SACLA are included. The two reports in Chemical Science are on the photoionization processes caused by a very short, intense X-ray pulse. Such experiments are only possible with the laser pulse of SACLA. Additional information about SACLA's operational status and ongoing technical developments are described in the Facility Status and Accelerator & Beamline Frontiers, respectively.

The scientific contributions from SPring-8 are, as usual, high quality and diverse, demonstrating that SPring-8 is an essential research tool in a variety of scientific and industrial fields. A new beamline for quark-nuclear physics, LEPS2 (BL31LEP), is now operational. The new beamline and the upgrade of the pre-existing LEPS beamline are described in the Nuclear Physics section.

Dr. Hideo Ohno who served as an editor in chief since 2011, has left the editorial board. We would like to thank him for his efforts and patience in this role. Dr. Ichiro Hirosawa has also left the editorial board, and the new editor in chief would like to express his sincere gratitude for his long-lasting contribution to the industrial applications in Research Frontiers publications. Dr. Norimichi Sano has joined the editorial board in Dr. Hirosawa's place.

In the layout of Research Frontiers, photographs of flowers grown at the SPring-8 campus and the Harima Science Garden City have been inserted. The photographs taken by Mr. S. Tsujimoto and Mr. M. Sugiura are greatly appreciated.

Copies of SPring-8 Research Frontiers will be mailed upon request. The full text is also available on the SPring-8 website (http://www.spring8.or.jp/). For a list of publications produced by SPring-8 users and staff, please visit the publication database at https://user.spring8.or.jp/uisearch/publication2/.

We extend our appreciation to those who have recommended excellent research results suitable for publication in SPring-8 Research Frontiers. We would also like to express our sincere gratitude to the users and staff of SPring-8 for contributing to this issue.

Editorial Board

SCIENTIFIC FRONTIERS

Life Science :


"Rupinasu" - *Lupinus*

To resolve three-dimensional structures of biomacromolecules, macromolecular crystallography (MX) is an essential and powerful method, which provides static but precise structures of molecules. As synchrotron beamlines advances, crystals structures can be analyzed from diverse aspects. Last year we reported the first results from micro-focus beamline BL32XU in which its microbeam, which reaches 1 μm, was effectively applied to microcrystals and ill-diffracting crystals. This year BL41XU has been upgraded by installing new optical components that produce a high-flux beam with various beam dimensions of 3 to 50 μm and a new pixel array X-ray detector for ultrafast data collection up to 100 Hz. These improvements will promptly contribute to high-throughput and high-precision data collection. Moreover, we have established a simultaneous measurement technique using ultraviolet and visible absorption spectroscopies, and a post-crystallization treatment using humid air. With the X-ray free electron laser facility, SACLA, serial femtosecond crystallography has been established for vast number of tiny crystals, and diverse macromolecular crystals are analyzed in the SPring-8 campus. Due to these cutting-edge resources, many outstanding results have been reported in 2013. Here we summarize into three subjects in structural biology: rational drug design, molecular recognition, and dynamic structure analysis.

Rational drug design is a key technology to tackle diseases. Cycles of biological assays and computational estimations improve drugs. MX provides detailed images of the drug binding environment on the molecular surface of proteins, including strong and specific interactions between small molecules and proteins. Often efforts to treat serious endemics such as neglected tropical diseases are limited because drug development is expensive. For example, the pathogen that causes African sleeping sickness is a trypanosoma protozoa transmitted by an insect, the tsetse fly. Shiba *et al.* resolved the structure of a protozoan drug target, TAO in a complex with a drug candidate. Their finds will accelerate fine-tuning of the drug. Additionally in cancer research, one of the *termini ad quem* is the establishment of molecularly targeted therapy. Although the Ras protein is a very promising target for the therapy, a pharmacophore (a possible drug binding pocket) has yet to be been identified. Kataoka *et al.* are the first to find a pharmacophore in the crystal structure and biochemical assay and are currently developing novel anti-cancer drugs.

Structural Biology

Molecular recognition among molecules larger than drugs is essential to achieve more complicated biological mechanisms. Selenium is a micronutrient incorporated as an unusual amino acid, selenocysteine, which has a strong redox activity that is useful for various catalyses. Itoh *et al.* determined the structures of the homododecameric SelA protein that produces the amino acid. Cooperation of the ring-like oligomeric assembly is essential to recognize the substrate and to convert catalysis of sulfur to selenium. Peroxisomes are organelles, which contribute to cell development, are involved in catabolism of fatty acids, etc. In the organelle assembly, matrix proteins are recognized with those signal peptides and translated into the organelle by the protein receptors, peroxins. Pan *et al.* have determined the structure of peroxins; in this case molecular recognition by peroxins helps tag the matrix for organelle assembly. Toll-like receptors, a key player in an innate immune system, recognize ligand molecules derived from pathogenic organisms. Upon ligand recognition and biding, Tanji *et al.* found that the double-ring structure of the dimeric receptor is rearranged and activated.

Molecular motion expands the functional ability of elastic protein molecules. Dynamical structural changes of proteins affect the affinity toward other molecules via molecular recognition, produce mechanical or chemical forces, etc. Although the MX technique only resolves a static photograph, a series of snapshots for different states can be used to construct a molecular movie. Na^+,K^+-ATPase generates a concentration gradient of sodium and potassium ions across a cell membrane. This potential energy and voltage are essential to drive molecular devices and transduce signals. Toyoshima *et al.* determined that its structure in the ADP-binding E1 state shows three sodium ions, and suggested that this high affinity state is an induced sequential structural transition by an allosteric effect initiated by the first sodium binding. V-ATPase also shows a rotatory movement as an ion pump transporting protons across the membrane due to the energy of ATP hydrolysis. Suzuki *et al.* determined the structure of V-ATPase in three different states and finely depicted the machinery of the molecular motor. Because multi-drug transporters allow drug resistance to pathogens and cancer cells, it is a considerable target for drug development. Through two structural snapshots, Tanaka *et al.* showed the dynamical open/close movement of the transporter. Nyirenda *et al.* determined the mobile region in the C-terminal domain of oligosaccharyltransferases, which are key enzymes in protein glycosylation, by MX and investigated the dynamical properties in detail by a further NMR study. They revealed that this mobility is essentially efficient scanning and recognition of the glycosylated signal peptide.

Takashi Kumasaka

Crystal structure of the trypanosome cyanide-insensitive alternative oxidase

Alternative oxidase (AOX) is a non-protonmotive ubiquinol oxidase catalyzing the four-electron reduction of dioxygen to water and belongs to the membrane-bound diiron carboxylate protein family [1]. This protein has been found in many organisms from prokaryotes to eukaryotes, such as higher plants, algae, yeast, slime molds, free-living amoebae, eubacteria, nematodes, and parasites including *Trypanosoma brucei* [2]. *T. brucei* causes human African sleeping sickness and nagana in livestock, which are called neglected tropical diseases (NTDs[§]). These are endemic in low-income populations in developing countries of Africa. Since current treatments are poorly targeted and show serious side effects and poor efficacy, the development of chemotherapy and the continued search for new unique therapeutic targets for African trypanosomiasis are urgently required. *T. brucei* has two different stages within its life cycle; the procyclic form in the tsetse fly and the bloodstream form in the mammalian host. Once the parasites invade the mammalian host in the bloodstream, both the cytochrome respiratory pathway and oxidative phosphorylation disappear and are replaced by the trypanosome alternative oxidase (TAO), which functions as the sole terminal oxidase to re-oxidize NADH accumulated during glycolysis [2]. Since NADH re-oxidation is essential for parasite survival and mammalian hosts do not possess this protein, TAO is considered to be a unique target for anti-trypanosomal drugs. Indeed, we have previously reported that the antibiotic ascofuranone, isolated from pathogenic fungus *Ascochyta viciae*, specifically inhibits the quinol oxidase activity of TAO at sub-nanomolar concentrations (IC_{50} = 0.13 nM) and rapidly kills the parasites. Furthermore, we have confirmed the chemotherapeutic efficacy of ascofuranone *in vivo* [3,4]. To develop a rational design of further potent and safer anti-trypanosomal drugs, we have determined the structures of TAO in the presence or absence of an ascofuranone derivative, AF2779OH, which also strongly inhibits TAO (IC_{50} = 0.48 nM) and dissolves in water more easily than ascofuranone.

TAO was expressed in *Escherichia coli*, purified and crystallized using *n*-octyl β-D-glucopyranoside (OG) and tetraethylene glycol monooctylether (C8E4) as detergents. Since TAO includes a diiron carboxylate center, phase angles were obtained by SAD using anomalous scattering effects of iron atoms. All X-ray diffraction experiments were performed at beamlines **BL41XU** and **BL44XU** of SPring-8 and BL-17A of Photon Factory.

The crystal structure of the inhibitor-free TAO determined at 2.85 Å resolution reveals that there are two homodimers in an asymmetric unit [5]. As shown in Fig. 1, each monomer consists of a long N-terminal arm, six long α-helices (α1-α6) and four short helices (S1-S4). The α2, α3, α5, and α6 helices are arranged in an antiparallel fashion and form a four-helix bundle that accommodates a diiron center, as widely observed in other diiron carboxylate proteins [5]. A large hydrophobic region that is formed by α1, α4, the C-terminal region of α2, and the N-terminal region of α5 from both monomers (Fig. 2(a)) spreads out on one side of the dimer surface, but the opposite side of the dimer surface is relatively hydrophilic, suggesting that the dimer is bound to the mitochondrial inner membrane via this hydrophobic region in an interfacial fashion. In addition, basic residues (Arg106, Arg143, Arg180, Arg203, and Arg207) are distributed along a boundary between the hydrophobic and hydrophilic regions of the dimer surface (Fig. 2(b)). They are conserved across all amino acid sequences of the membrane bound AOXs and their locations make these residues ideal candidates to interact with the negatively charged phospholipid head groups of membranes [5]. The structure of the diiron active site was refined as an oxidized Fe(III)-Fe(III) form with a single hydroxo-bridge, as previously predicted

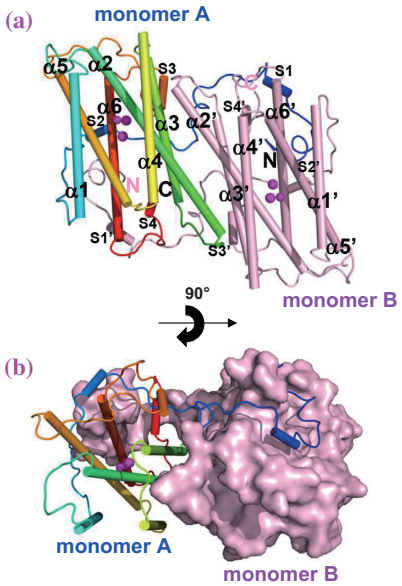

Fig. 1. Overall structure of TAO. **(a)** Schematic drawing of TAO dimer. Helices are shown as cylinders. Monomer A is rainbow-colored from blue (N-terminus) to red (C-terminus), and monomer B is pink. **(b)** The N-terminal arm of monomer A extends into monomer B, suggesting that the arm is important in dimerization. Monomer B is shown in a surface representation.

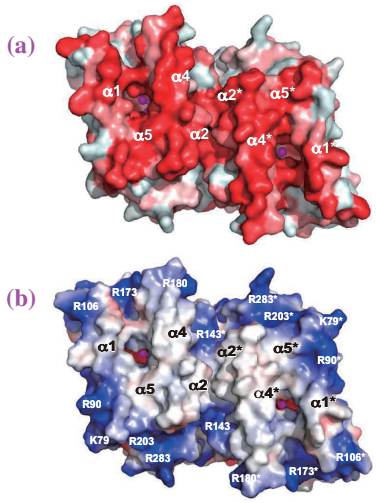

Fig. 2. Membrane bound region of TAO. Surface representation of the TAO membrane-bound region. Colors follow **(a)** the hydrophobicity scale: red, high hydrophobicity; white, low hydrophobicity, and **(b)** the electrostatic surface potential: blue, positive; red, negative. Diiron atoms are shown as magenta spheres.

from spectroscopic studies. The active site, which is located in a hydrophobic environment deep inside the TAO molecule, comprise the diiron center, conserved glutamate (Glu123, Glu162, Glu213, Glu266) and histidine (His165, His269) residues. In addition, the conserved hydrophobic residues (Lue122, Ala126, Leu212, Ala216, Tyr220, Ile262) are within 6 Å of the diiron center. The most striking feature of the diiron active site in the oxidized state is that, as predicted from earlier FTIR studies, His165 and His269 are too distant from both Fe1 and Fe2 to coordinate to the diiron center. Accordingly, TAO is the first detailed structure of an oxidized diiron active site that contains only carboxylate but no histidine ligands [5].

The structure of TAO in a complex with AF2779OH determined at 2.6 Å resolution reveals how the inhibitor, as well as ascofuranone, is recognized by TAO (Figs. 3(a), 3(b) and 3(c)); [5]). The binding cavity of AF2779OH is located near the membrane surface between helices α1 and α4 and is lined by 16 residues (Val92, Arg96, Phe99, Arg118, Cys119, Phe121, Leu122, Glu123, Val125, Met190, Leu212, Glu213, Glu215, Ala216, Thr219, and Tyr220) plus Cys95 (Figs. 3(c) and 3(d)), which are highly conserved among the membrane-bound AOXs. It is also apparent that the aromatic head of AF2779OH is located close to the diiron active site and C2-OH forms hydrogen bonds with Arg118 and Thr219 (Fig. 3(d)). In the AF2779OH-TAO complex, the distance between His165 and Fe1 is shorter than that observed in the inhibitor-free structure, and hence, His165 can now coordinate with Fe1, unlike His269 [5].

In conclusion, we believe that the structures determined in this study will contribute to the more complete understanding of the structure-function relationship of all AOXs. In addition, the structure of the AF2779OH-TAO complex indicates that the interactions between substituents of the AF2779OH aromatic head and TAO play an important role in the inhibition of TAO. This information would help the development of ascofuranone derivatives with better properties as a drug, and will not only be beneficial for the control of trypanosomiasis and other human diseases, such as cryptosporidiosis and candidiasis, but also for the control of plant diseases caused by phytopathogenic fungi.

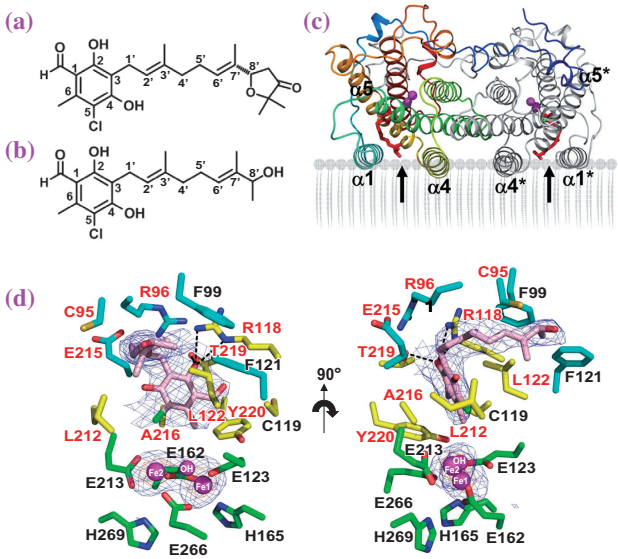

Fig. 3. Structure of the TAO-AF2779OH complex. **(a)** The chemical structure of ascofuranone. **(b)** The chemical structure of AF2779OH. **(c)** Overall structure of the TAO-AF2779OH complex. AF2779OH is shown as red sticks. Monomers A and B are shown as rainbow colored and grey, respectively. The AF2779OH-binding cavities are shown by arrows. **(d)** The AF2779OH binding region of monomer A. The residues interacting with the ring and tail of AF2779OH (pink stick) are shown as yellow and cyan sticks, respectively. Hydrogen bonds are depicted as dotted lines. The electron density map is also shown.

Tomoo Shiba[a], Kiyoshi Kita[b] and Shigeharu Harada[a,*]

[a] Dept. of Applied Biology, Kyoto Institute of Technology
[b] Dept. of Biomedical Chemistry, The University of Tokyo

*E-mail: harada@kit.ac.jp

References

§ http://www.who.int/neglected_diseases/en/
[1] A.L. Moore and M.A. Albury: Biochem. Soc. Trans. **36** (2008) 1022.
[2] M. Chaudhuri *et al.*: Trends Parasitol. **22** (2006) 484.
[3] Y. Yabu *et al.*: Parasitol. Int. **52** (2003) 155.
[4] Y. Yabu *et al.*: Parasitol. Int. **55** (2006) 39.
[5] *T. Shiba, Y. Kido, K. Sakamoto, D.K. Inaoka, C. Tsuge, R. Tatsumi, G. Takahashi, E.O. Balogun, T. Nara, T. Aoki, T. Honma, A. Tanaka, M. Inoue, S. Matsuoka, H. Saimoto, A.L. Moore, S. Harada and K. Kita: Proc. Natl. Acad. Sci. USA* ***110*** *(2013) 4580.*

Structure-based drug design of small-molecule Ras inhibitors having anti-tumor activity

Small GTPases H-Ras, K-Ras and N-Ras (collectively called Ras) are the products of the *ras* proto-oncogenes and function as a molecular switch by cycling between GTP-bound active and GDP-bound inactive forms (Ras·GTP and Ras·GDP, respectively) in a variety of intracellular signaling pathways controlling cell growth, differentiation and apoptosis. Ras·GTP binds directly and activates downstream effectors such as Raf kinases, phosphoinositide 3-kinases (PI3Ks), RalGEFs and phospholipase Cε. Conversion of Ras·GDP to Ras·GTP is catalyzed by guanine nucleotide exchange factors (GEFs) such as Son-of-sevenless (Sos) and induces allosteric conformational changes in two flexible regions, termed switch I (residues 32-38) and switch II (residues 60-75), both of which constitute a principal interface for effector recognition. Ras are presumed to be one of the most promising targets for anti-cancer drug development because they are frequently activated by point mutations in human cancers. Nonetheless, there is no effective molecular targeted therapy for Ras at present now that farnesyl transferase inhibitors, which block posttranslational farnesylation of Ras necessary for membrane targeting, have been unsuccessful. Although recent success in drug discovery using structure-based drug design (SBDD) for AIDS and influenza has boosted hopes for its application to anti-cancer drug development, Ras have been presumed refractory to this approach because they lack apparently "druggable" pockets on their surface. Recently, by X-ray crystallography we solved novel crystal structures of the GTP-bound forms of M-Ras, a close homologue of Ras, and its mutant, which corresponded to a novel conformation called state 1, a GTP-bound inactive form, possessing surface pockets suitable for drug binding [1,2] (Fig. 1). This led us to apply SBDD to target Ras·GTP by utilizing the structural information on the surface pockets and obtain small-molecule Ras inhibitors [3].

The screening method used is summarized in Fig. 2. First, we applied the Molecular Mechanics Poisson-Boltzman surface area (MMPB-SA) method with an AMBER96 force field to carry out a computer docking screen of a virtual library containing 40,882 compounds based on the high-resolution (1.35 Å) crystal structure of M-Ras^{P40D}, carrying an H-Ras-type amino acid substitution at residue 40, in complex with a non-hydrolyzable GTP analogue guanosine 5'-(β,γ-imido)triphosphate (GppNHp), which had been determined using beamlines **BL38B1** and **BL41XU**

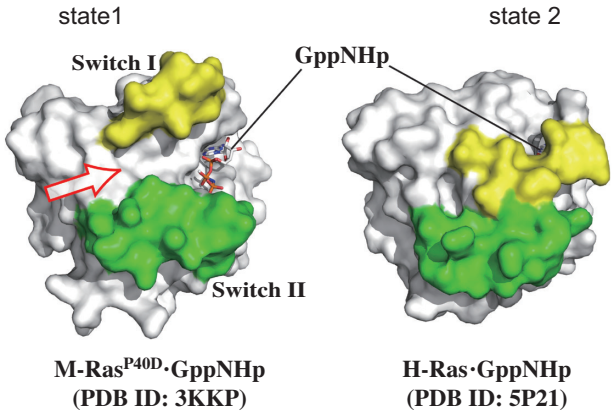

Fig. 1. Novel crystal structure solved with M-Ras^{P40D}·GppNHp in state 1 possessing a drug-accessible surface pocket (arrow) surrounded by the guanine nucleotide and the two switch regions (Switch I, yellow; Switch II, green). By contrast, the previously determined crystal structure of H-Ras·GppNHp in state 2 did not have such a pocket.

[2]. The selected compound Kobe0065, N-(3-chloro-4-methylphenyl)-2-{2,6-dinitro-4-(trifluoromethyl) phenyl}hydrazinecarbothioamide, and its analogue Kobe2602 (Fig. 2), identified by a computer-assisted similarity search, efficiently inhibited binding of H-Ras·GTP to Raf kinases both *in vitro* and at the cellular level. The compounds effectively inhibited both anchorage-dependent and -independent growth and induce apoptosis of mouse fibroblast NIH3T3 cells transformed by the mutationally activated H-*ras*^{G12V} gene, which was accompanied by downregulation of downstream molecules such as MEK/ERK downstream of Raf kinases, Akt downstream of PI3Ks and RalA downstream of RalGEFs. Moreover, they inhibited the upstream regulator Sos by interfering with Ras·GTP-binding to its allosteric regulatory site. The IC_{50} values of Kobe0065 and Kobe2602 for the inhibition of anchorage-independent growth of H-*ras*^{G12V}-transformed NIH3T3 were approximately 0.5 and 1.4 μM, respectively. The compounds were capable of inhibiting the anchorage-independent growth of human cancer cell lines carrying various activating mutations of the H-*ras*, K-*ras* and N-*ras* genes but not those carrying the mutationally activated *raf* or *PI3K* gene, indicating their specific inhibitory action on all the three Ras isoforms irrespective of the nature of the activating mutations. Furthermore, the compounds exhibited a potent anti-tumor activity, which was comparable to that of the approved anti-cancer drug sorafenib, on a xenograft of human colon

carcinoma SW480 cells carrying the mutationally activated *K-ras*^{G12V} gene by oral administration. The NMR structure of a complex of a Kobe0065-analogue Kobe2601 with H-Ras^{T35S}·GppNHp, exclusively adopting the state 1 conformation [4], confirmed its insertion into one of the surface pockets and provided a molecular basis for binding inhibition toward multiple Ras·GTP-interacting molecules [3] (Fig. 3). The fluorobenzene ring of Kobe2601 was located in close proximity to the side chains of Lys5, Leu56, Met67, Gln70 and Tyr74 of H-Ras. These six residues formed a hydrophobic surface pocket in the neighborhood of switch I, indicating that the fluorobenzene ring was inserted into the pocket through hydrophobic interaction. This study proved the effectiveness of our novel strategy for SBDD to target Ras·GTP and the resulting Kobe0065-family compounds may serve as a novel scaffold for the development of Ras inhibitors with higher potency and specificity.

Since the middle '90s, ^{31}P-NMR spectroscopic studies on Ras by Dr. Kalbitzer's group have unveiled their novel structural feature, i.e. conformational dynamics of their GTP-bound forms exhibiting equilibrium between two distinct states, state 1 and state 2, representing "inactive" and "active" conformations, respectively. Recently, we have determined a number of crystal structures of M-Ras·GppNHp, H-Ras·GppNHp and their mutants representing state 1, state 2 and their intermediates to show that hydrogen-bonding interactions of Thr35 (in switch I) and Gly60 (in switch II) with the γ-phosphate of GTP are abolished in state 1, which results in formation of a surface pocket (1, 2, 5). The pocket structure of M-Ras^{P40D}·GppNHp was successfully used for the discovery of the Kobe0065-family compounds as described above. Moreover, we clarified the molecular basis for the conformational dynamics of Ras·GTP by X-ray crystallography and NMR spectroscopy (2, 4, 5). This information could be utilized not only for the structural optimization of the Kobe0065-family compounds but also for the discovery by SBDD of a novel class of small-molecule Ras inhibitors.

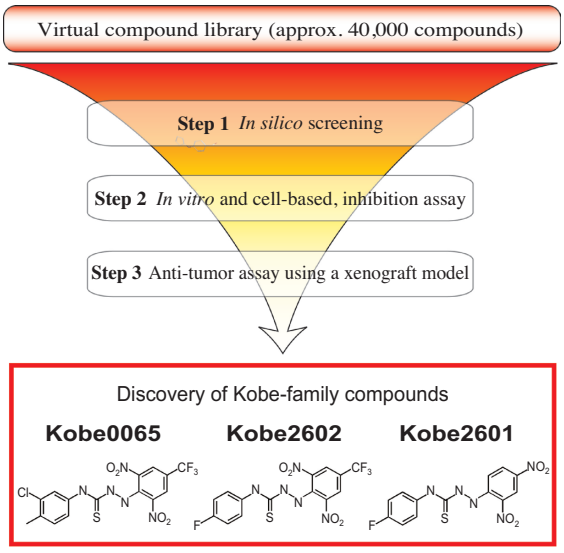

Fig. 2. Strategy for the development of Ras inhibitors used in the present study. Step1: screening for candidate compounds by computer-docking simulation targeting the surface pocket found in M-Ras^{P40D}·GppNHp. Step2: assays for inhibitory activities of the compounds on *in vitro* Ras/Raf-binding and proliferation of cancer cell lines carrying the activated *ras* oncogenes. Step3: assays for anti-tumor activity of the compounds on a xenograft of human colon cancer cells carrying the activated K-*ras* gene (K-*ras*^{G12V}).

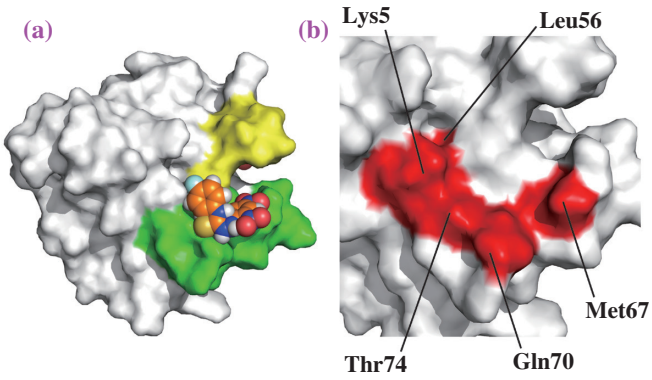

Fig. 3. Molecular basis for the interaction of the Kobe0065-family compounds with H-Ras. **(a)** The lowest energy solution structure of the complex between H-Ras^{T35S}·GppNHp and a Kobe0065-analogue Kobe2601 is shown by a surface model (Switch I, yellow; Switch II, green) while Kobe2601 is shown by a space filling model (C, orange; O, red; N, blue; H, gray; S, gold; F, light blue). **(b)** A close-up view of the compound-binding pocket in the complex (right), where the residues showing the intramolecular Nuclear Overhauser Effects are highlighted in red.

Shima Fumi and Tohru Kataoka*

Department of Biochemistry and Molecular Biology,
Kobe University Graduate School of Medicine

*E-mail: kataoka@people.kobe-u.ac.jp

References

[1] M. Ye *et al.*: J. Biol. Chem. **280** (2005) 31267.
[2] F. Shima *et al.*: J. Biol. Chem. **285** (2010) 22696.
[3] *F. Shima, Y. Yoshikawa, M. Ye, M. Araki, S. Matsumoto, J. Liao, L. Hu, T. Sugimoto, Y. Ijiri, A. Takeda, Y. Nishiyama, C. Sato, S. Muraoka, A. Tamura, T. Osoda, K. Tsuda, T. Miyakawa, H. Fukunishi, J. Shimada, T. Kumasaka, M. Yamamoto and T. Kataoka: Proc. Natl. Acad. Sci. USA* ***110*** *(2013) 8182.*
[4] M. Araki *et al.*: J. Biol. Chem. **286** (2011) 39644.
[5] K. Matsumoto *et al.*: J. Biol. Chem. **286** (2011) 15403.

Crystal structure of bacterial selenocysteine synthase SelA in complex with tRNA^{Sec} reveals the selenocysteine formation mechanism in bacteria

Selenium is an essential human micronutrient. It is present in proteins in the form of the special amino acid selenocysteine (Sec). Sec is structurally similar to cysteine and serine, and the selenium replaces the sulfur and oxygen atoms of cysteine and serine, respectively. Among the 25 human Sec-containing proteins (selenoproteins), most are redox proteins. Since the selenol group of Sec is easily deprotonated as compared to the cysteine thiol group (pKa 5.2 *vs* 8.3), selenoproteins have stronger redox activities than their cysteine-containing counterparts.

Sec is the 21st amino acid that is incorporated into proteins translationally. It is encoded by the UGA codon, and the Sec-specific transfer RNA (tRNA^{Sec}) has the UCA anticodon (Fig. 1), which is complementary to UGA in mRNA. The UGA codon is a stop codon, and it usually encodes a translation termination signal. Depending on the special mRNA sequence downstream of UGA, the UGA is recoded as a Sec codon.

In the usual translation system, the canonical 20 amino acids are ligated to their tRNAs by their cognate aminoacyl-tRNA synthetases (aaRSs); e.g., seryl-tRNA synthetase (SerRS) ligates serine to serine tRNA (tRNA^{Ser}) (Fig. 1). In contrast, Sec lacks its own aaRS, and is synthesized by the tRNA-dependent conversion of serine (Fig. 1). The first step in Sec synthesis is the ligation of serine to tRNA^{Sec} to form seryl-tRNA^{Sec} (Ser-tRNA^{Sec}) by SerRS, which is also responsible for ligating serine to tRNA^{Ser} (Fig. 1). In Eukaryotes (including human) and Archaea, *O*-phosphoseryl-tRNA^{Sec} kinase (PSTK) phosphorylates the Ser moiety of Ser-tRNA^{Sec}, and then the phosphoserine is converted to Sec by Sep-tRNA^{Sec}:Sec-tRNA^{Sec} synthase (SepSecS) (Fig. 1). Archaea are prokaryotic organisms, but they are evolutionally closer to Eukaryotes than Bacteria. In contrast, in Bacteria, the Sec synthase SelA directly converts Ser to Sec without phosphorylation (Fig. 1). The crystal structures of PSTK [1] and SepSecS [2] in complex with tRNA^{Sec} have clarified the mechanisms of substrate recognition and catalysis. In contrast, the crystal structure of SelA has not been determined due to its huge molecular mass, as described below.

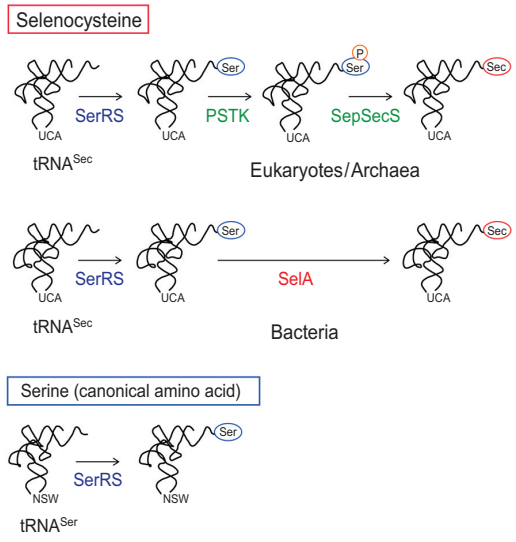

Fig. 1. Sec synthesis system. The schemes of the tRNA^{Sec}-dependent Ser-to-Sec conversions in Eukaryotes/Archaea and Bacteria. Phosphorylation is required in the eukaryotic/archaeal system. SerRS is responsible for serine ligation to both tRNA^{Sec} and tRNA^{Ser}.

We crystallized SelA from the bacterium *Aquifex aeolicus*, and determined the crystal structures of the full-length and an N-terminally truncated mutant of SelA at 3.2 and 3.9 Å resolutions, respectively [3]. The diffraction data were collected at beamline **BL41XU**. SelA is a homodecameric enzyme composed of a pentamer of intimate dimers, and the 10 subunits form a star-shaped ring structure (Fig. 2(a)). The

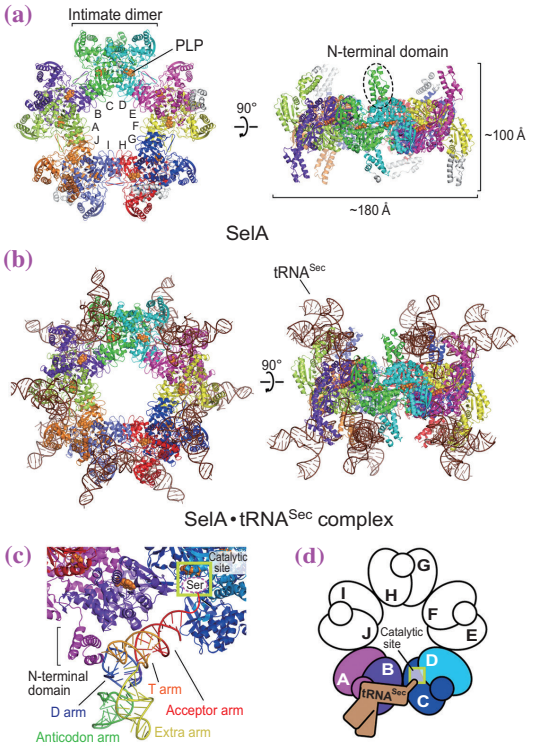

Fig. 2. Crystal structures of SelA. **(a,b)** Overall structures of SelA (without tRNA^{Sec}) and the Sel•tRNA^{Sec} complex. **(c,d)** Close-up view and scheme of the interaction between the SelA subunits and tRNA^{Sec}.

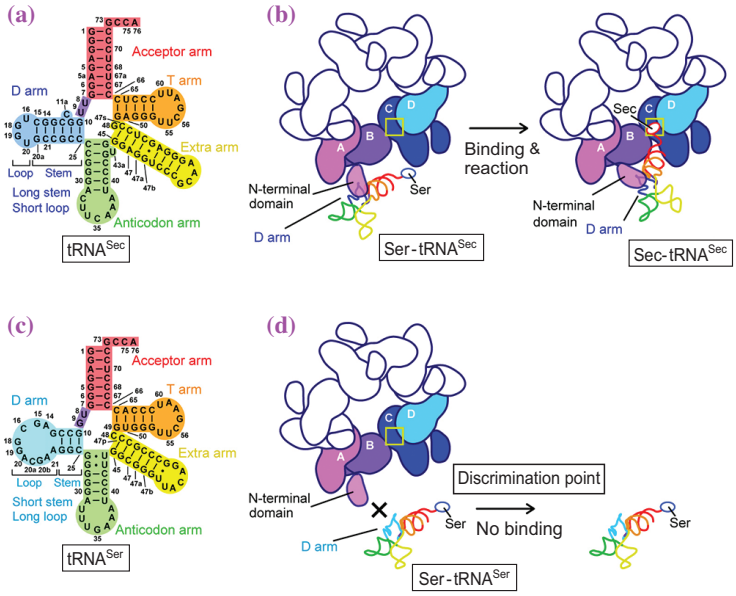

Fig. 3. tRNA discrimination mechanism. **(a,c)** Secondary structures of $tRNA^{Sec}$ and $tRNA^{Ser}$. **(b,d)** SelA discriminates $tRNA^{Sec}$ from $tRNA^{Ser}$ by interacting with the D arm of $tRNA^{Sec}$.

total molecular mass exceeds 500 kDa. The SelA decamer has regular pentagonal symmetry, since the 10 subunits are identical to each other. Each subunit consists of the N-terminal, core, and C-terminal domains, and the N-terminal domains are flexible and protrude from the pentagon (Fig. 2(a)). There are 10 catalytic sites located in the subunit interfaces within the intimate dimers. The cofactor pyridoxal phosphate (PLP) is bound to each catalytic site. PLP is the active form of vitamin B_6, and is a cofactor for many enzymes that function in amino acid metabolism.

We also crystallized SelA in the complex with $tRNA^{Sec}$, and determined its structure at 7.5 Å resolution (Fig. 2(b)). The decameric SelA binds 10 $tRNA^{Sec}$s, and the total molecular mass is about 800 kDa, which is comparable to the smaller particle of the bacterial ribosome (30S, 900 kDa). Each $tRNA^{Sec}$ interacts with four SelA subunits; i.e., subunits A–D (Fig. 2(a,d)). The N-terminal domain of subunit A interacts with the D arm of $tRNA^{Sec}$, subunit B interacts with the acceptor stem, and subunit C interacts with the acceptor arm end. The 3′-terminus of $tRNA^{Sec}$, which carries the ligated Ser, is likely to be able to reach the active site located on the subunit C-D interface, although the $tRNA^{Sec}$ used for crystallization lacked the ligated Ser.

The mutant SelA that lacked the N-terminal domain did not bind $tRNA^{Sec}$, while the dimeric mutant retained the $tRNA^{Sec}$ binding ability [3], indicating that the N-terminal domain is responsible for $tRNA^{Sec}$ binding. However, both of the mutants lacked activity, and thus not only $tRNA^{Sec}$ binding but also the decameric quaternary structure is essential for SelA catalysis.

The Ser-to-Sec conversion requires strict specificity. If SelA interacted with serine tRNA ($tRNA^{Ser}$), then it would convert the Ser-ligated $tRNA^{Ser}$ (Ser-$tRNA^{Ser}$) to Sec-$tRNA^{Ser}$, and Sec would be mis-incorporated into Ser codons. Since serine is a canonical amino acid, the amount of $tRNA^{Ser}$ in cells is much larger than that of $tRNA^{Sec}$, suggesting that it is essential for SelA to discriminate $tRNA^{Sec}$ from $tRNA^{Ser}$. $tRNA^{Sec}$ is the largest tRNA, and it has unique secondary and tertiary structures [4,5]. The D arm of $tRNA^{Sec}$ has longer stem and shorter loop regions, as compared to the canonical tRNAs (Fig. 3(a,c)). The SelA·$tRNA^{Sec}$ complex structure shows that the N-terminal domain of SelA recognizes the unique structure of the $tRNA^{Sec}$ D arm, and thus discriminates $tRNA^{Sec}$ from $tRNA^{Ser}$ (Fig. 3(b,d)).

Most PLP-dependent enzymes function as dimers or tetramers. In contrast, SelA is a decamer, and its four subunits work together with one Ser-$tRNA^{Sec}$. In the conversion reaction, subunit A recognizes Ser-$tRNA^{Sec}$ (i), subunits A and B bind Ser-$tRNA^{Sec}$ (ii), subunit C interacts with the acceptor-arm end of $tRNA^{Sec}$ (iii), and subunits C and D convert the ligated Ser to Sec (iv) (Fig. 3(b)). Since SelA is a ring structure, subunits C–F work on the adjacent Ser-$tRNA^{Sec}$, where subunit C plays the roles of (i) and (ii). Each subunit can perform the four roles. The proper arrangement of the five intimate dimers is important for catalysis and discrimination, and the decameric ring structure stabilizes this arrangement.

Yuzuru Itoh[a,b,c,†] and Shigeyuki Yokoyama[a,c,d,*]

[a] Department of Biophysics and Biochemistry, The University of Tokyo
[b] Institute of Molecular and Cellular Biosciences, The University of Tokyo
[c] RIKEN Systems and Structural Biology Center/Yokohama
[d] RIKEN Structural Biology Laboratory/Yokohama

[†]Present address: Institut de Génétique et de Biologie Moléculaire et Cellulaire, France

*E-mail: yokoyama@riken.jp

References

[1] S. Chiba *et al.*: Mol. Cell **39** (2010) 410.
[2] S. Palioura *et al.*: Science **325** (2009) 321.
[3] *Y. Itoh, M.J. Bröcker, S. Sekine, G. Hammond, D. Söll, S. Yokoyama: Science **340** (2013) 75.*
[4] Y. Itoh *et al.*: Nucleic Acids Res. **37** (2009) 6259.
[5] Y. Itoh *et al.*: Nucleic Acids Res. **41** (2013) 6729.

Molecular recognition mechanism of peroxisomal targeting signal–2, PTS2

In eukaryotic cells, peroxisomes are responsible for many important metabolic functions, such as catabolism of fatty acids. Dysfunctions of peroxisomes cause fatal developmental problems in humans and hinder proliferation of yeast cells. More than 20 conserved proteins are necessary to assemble functional peroxisomes and they are named peroxins (Pex) [1]. Peroxins target peroxisomal matrix proteins synthesized in cytosol to peroxisome and translocate them into the matrix. Those matrix proteins usually possess either of two types of peroxisomal targeting signals (PTS1 or PTS2) for appropriate targeting. While the structural basis of PTS1 recognition by peroxin 5 (Pex5p) has been revealed by the crystal structures, that of PTS2 remains to be determined [2]. We studied the recognition mechanism of PTS2 from *Saccharomyces cerevisiae* to reveal the general mechanism of PTS2 recognition [3].

PTS2 is a conserved nonapeptide motif (R-[L/V/I/Q]-XX-[L/V/I/H]-[L/S/G/A]-X-[H/Q]-[L/A]) at the N-terminal end of cargo proteins. In this motif, the residues at positions 1 and 8 showed strict limitations to only a few types of hydrophilic residues, whereas the residues at positions 2, 5 and 9 are limited to mainly hydrophobic residues [4]. Receptor peroxin Pex7p recognizes PTS2 only in the presence of a co-receptor peroxin [5]. In *S. cerevisiae*, either Pex18p or Pex21p functions as the co-receptor instead of Pex5pL, the longer isoform of Pex5p in mammals. By determining the crystal structure of a PTS2-recognition complex (Pex7p-Pex21p-PTS2), we endeavored to answer the following questions: why are the key residues of PTS2 limited to specific positions and specific types of residues, how does Pex7p form the binding site for PTS2, and how do the co-receptor peroxins support Pex7p for PTS2 recognition?

Well-diffracted crystals were obtained when we used individually purified Pex7p Δ257–265, the C-terminal 99 residues of Pex21p (Pex21pC), and Fox3pN-MBP to reconstitute the PTS2-recongnition complex (Fig. 1). Fox3pN-MBP is a fusion protein of the N-terminal 15 residues of *S. cerevisiae* Fox3p and the maltose binding protein from *Escherichia coli*. The best diffraction dataset was collected at beamline **BL41XU**. The crystal structure was determined by the molecular replacement method with the crystal structures of a WD40 protein and MBP as search models and refined to the resolution of 1.8 Å.

The crystal structure clearly defined a cooperative mechanism in which both Pex7p and Pex21pC are necessary for PTS2 recognition (Fig. 1). Pex7p forms a β-propeller structure that is similar to those of other WD40 proteins. Pex21pC has an extended shape with an α-helical region, a small β-sheet, and an extended C-terminal loop. Both the top surface of Pex7p and the helical region of Pex21pC share the rule to form a

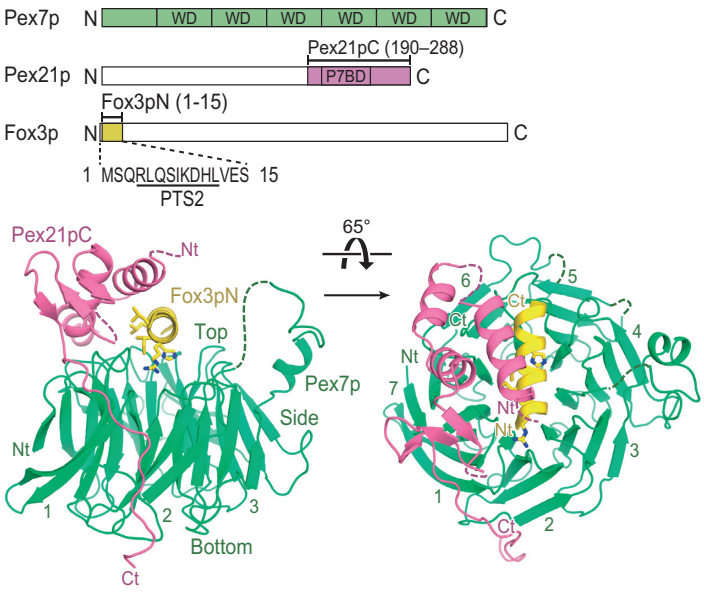

Fig. 1. Overall structure of the PTS2-recognition complex and sequence diagram of its components. Numbers in the lower panel indicate the number of blades of the β-propeller structure. The side chains of key residues of PTS2 in Fox3pN are shown as stick models. WD, WD40 motif; P7BD, Pex7p binding domain.

binding pocket for PTS2. These regions of Pex7p and Pex21pC are composed of well-conserved residues. Mammalian Pex5pL also contains a homologous region corresponding to the helical region of Pex21pC. This manner of pocket formation has not been reported in other targeting signal systems (e.g., PTS1, mitochondrial targeting signal, nuclear localization signal), in which binding pockets for targeting signals are formed by single receptor proteins.

Our crystal structure revealed the precise interactions between the key residues of PTS2 and its receptor proteins. The 15 residues of Fox3pN, including the sequence of the PTS2, fold into an α-helix and fit tightly into the binding pocket (Fig. 2). The buried surface area of Fox3pN is large and accounts for 70% of its total surface area. By forming an α-helix, the key residues are separated into two groups: hydrophilic key residues (Fox3p Arg4 and His11) and hydrophobic key residues (Fox3p Leu5, Ile8, and Leu12). These two groups of key residues fit into the complementary grooves in the binding pocket of PTS2. The hydrophilic key residues form salt bridges and hydrogen bonds with the residues of the hydrophilic groove on the top surface of Pex7p (Pex7p Asp61, Glu106, Thr178, Glu222, and Glu304). The hydrophobic key residues are inserted into the hydrophobic groove between Pex7p and Pex21pC. Consequently, the hydrophobic residues from all three proteins form a hydrophobic core around the residue Pex21p Phe236 (Fig. 2).

The structure implies that this hydrophobic core is important in ternary complex formation. Therefore, we performed pull-down assays with purified proteins and *in vivo* PTS2-EGFP transport assays with *Δpex7* or *Δpex18Δpex21 S. cerevisiae* strains to analyze the effects of mutations (Pex7p L34D and Pex21p F236D) that were expected to destabilize the complex formation [3]. The results of pull-down assays clearly showed that wild-type Pex7p and Pex21pC were able to form stoichiometric ternary complexes, but Pex7p L34D and Pex21p F236D mutants could not. The expression of wild-type Pex7p in the *Δpex7* strain or wild-type Pex21pC in the *Δpex18Δpex21* strain was able to restore the PTS2-EGFP transport to peroxisomes, but the expression of Pex7p L34D and Pex21p F236D mutants could not. Thus, we confirmed that the cooperative hydrophobic core formation is necessary for strong binding of PTS2.

In summary, we reported, for the first time, the crystal structure of a PTS2-recognition complex and our findings revealed a cooperative mechanism for PTS2 recognition. That is, Pex7p and the co-receptor peroxin cooperatively form the binding pocket of PTS2. Residues of Pex7p and Pex21p forming the binding pocket of PTS2 are well conserved from yeast to humans, which suggests that it is likely the manner of PTS2 recognition in yeast is also used in higher eukaryotes. The specific assignment of the key residues in the PTS2 motif is to ensure that two types of key residues can be lined up in two directions upon forming the α-helix and can be recognized by two complementary grooves in the PTS2 binding pocket.

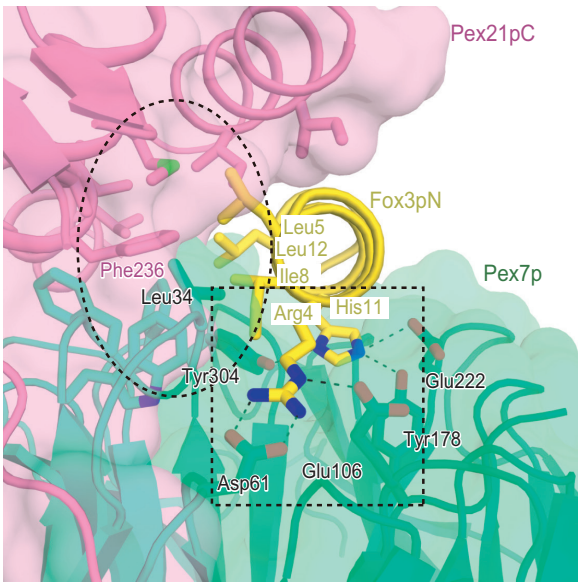

Fig. 2. Close-up view of the PTS2 binding pocket. The side chains of key residues of PTS2 and the residues of Pex7p and Pex21p that interact with PTS2 key residues are shown as stick models. Dashed ellipse indicates the position of hydrophobic core and dashed box indicates the hydrophilic groove.

Dongqing Pan* and Hiroaki Kato

Dept. of Structural Biology, Kyoto University

*E-mail: pan.dongqing@pharm.kyoto-u.ac.jp

References

[1] H.W. Platta and R. Erdmann: Trends Cell Biol. **17** (2007) 474.
[2] W.A. Stanley *et al.*: FEBS Lett. **581** (2007) 4795.
[3] *D. Pan, T. Nakatsu, H. Kato: Nat. Struct. Mol. Biol. **20** (2013) 987.*
[4] P.B. Lazarow: Biochim. Biophys. Acta **1763** (2006) 1599.
[5] W. Schliebs and W.H. Kunau: Biochim. Biophys. Acta **1763** (2006) 1605.

Crystal structures of innate immune RNA receptor human TLR8

The Toll-like receptors (TLRs) are a family of pattern-recognition receptors that recognize pathogen-associated molecular patterns and activate innate immune system [1]. The TLR consists of the extracellular leucine-rich repeat (LRR) domain, transmembrane domain, and intracellular TIR domain. In general, unliganded forms of TLRs are believed to exist as monomers that transform into the activated dimer upon ligand binding. TLR7 and TLR8 are expressed in the endosome and recognize single-stranded (ss) RNA from viruses [2]. Moreover, TLR7 and TLR8 are known to be activated by synthetic imidazoquinoline compounds, some of which are applied in medical treatments [3], but unavailability of the structural information of TLR8 hampers the further development of drugs targeting TLR8. We determined the crystal structures of unliganded and liganded forms of TLR8 to clarify the ligand recognition and activation mechanisms of TLR8 [4].

The extracellular domain of human TLR8 was expressed in *Drosophila* S2 cells and purified to homogeneity. TLR7, TLR8, and TLR9 conserve a long inserted loop (Z-loop) between LRR14 and LRR15 (Fig. 1(a)). TLR7 and TLR9 were reported to require the Z-loop cleavage to become functional [5]. Expressed TLR8 was already cleaved at the Z-loop; hence it was assumed to be functional, and the resultant N- and C-terminal fragments were associated with each other in the purification steps. Both unliganded and liganded forms of TLR8 were eluted as dimers in gel-filtration chromatography, which suggests that TLR8 creates preformed dimers. We sought to determine the crystal structures of the unliganded form of TLR8 and liganded forms of TLR8 with chemical ligands, namely, CL097, CL075, and R848. The TLR8/R848 complex structure was initially determined using Pt and Cs derivatives, and the other structures were determined by the molecular replacement method using the refined TLR8/R848 structure. The unliganded form was determined at 2.3 Å, and the liganded forms were determined at 2.0-2.7 Å (TLR8/CL097, TLR8/CL075, TLR8/R848 form1-3). The diffraction datasets of the unliganded form of TLR8 and TLR8/R848 form 2 were collected at beamline **BL41XU**.

The TLR8 monomer had a ring-shaped structure in which N- and C-terminal fragments interacted directly (Fig. 1(b)). LRR14 and LRR15 interacted to form a parallel β-sheet structure, similar to other LRRs, which resulted in concave face of the ring structure of TLR8. The Z-loop was stabilized by hydrophobic interactions with LRR3-LRR8 in the concave face. TLR7, TLR8, and TLR9 have inserted loops in LRR2, LRR5, LRR8, LRR11, LRR18, and LRR20. These loops protruded into the dimerization interface, and contributed to the ligand recognition and dimerization in the TLR8 structure as described below.

Consistent with the results of gel filtration chromatography, TLR8 formed m-shaped dimers in which two C-termini converged in the middle in both the unliganded and liganded forms (Figs. 1(c), 1(d)).

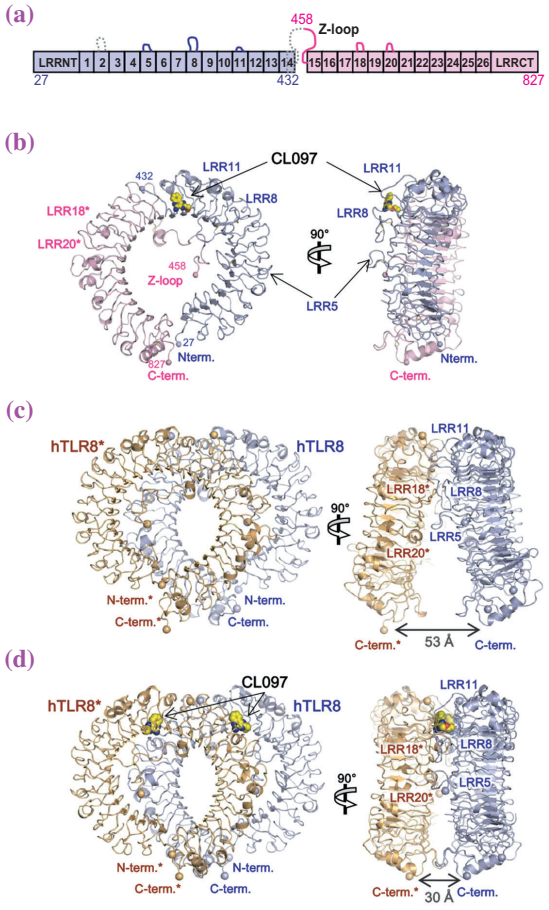

Fig 1. Structures of human TLR8. **(a)** Schematic representation of the domain organization of human TLR8. LRRs are indicated by numbered boxes. The N- and C-terminal halves of hTLR8 are shown in light blue and pink, respectively. **(b)** Monomer structure of hTLR8/CL097 complex showing the lateral face (left) and the convex face from the N-terminal side (right). The bound CL097 is shown in spheres. The C, O, and N atoms of CL097 are shown in yellow, red, and blue, respectively. Front (left) and side (right) views of the unliganded hTLR8 dimer **(c)** and hTLR8/CL097 dimer **(d)**. TLR8 and its dimerization partner TLR8* are shown in light blue and light orange, respectively.

Throughout this report, we indicate the second TLR8 and its residues in the dimeric TLR8 with asterisks. The C-termini of the two TLR8 protomers were separated by 53 Å in the unliganded form, whereas the C-termini were brought into close proximity (~30 Å) in the liganded forms.

Two clear electron densities corresponding to the ligand were observed in the dimerization interface, indicating that these ligands acted as glue for two protomers (Fig. 2). These two ligand binding sites were related by the two-fold axis. The mode of interactions between ligands and TLR8 were similar among three chemical ligands (Fig. 2); the benzene rings of the ligands underwent stacking interaction with the F405 side chain, and the amidine group of the quinolone moieties of the ligands formed hydrogen bonds with the D543* side chain. The N atoms of imidazole (R848, CL097) or thiazole (CL075) moieties formed hydrogen bonds with the T574* main chain. The hydrophobic moieties of the ligands protruded into a hydrophobic pocket consisting of Y348, V378, I403, F405, and V573*. To examine whether these residues are effective for ligand recognition on the cellular level, we conducted NF-κB reporter assay. Alanine mutations of these residues weakened or diminished activity when stimulated by both small chemical ligands and ssRNA. This result demonstrated that these residues are involved in the recognition of both chemical ligands and ssRNA.

The structures of the unliganded and liganded forms of TLR8 revealed the activation mechanisms of TLR8. In the unliganded form, the interactions between LRR8 and LRR18*, as well as LRR11-13 and LRR14*-15*, are the major contributors to the dimerization. Upon ligand binding, the dimerization interface is rearranged; LRR8 interacts with LRR18*-20*, and LRR11-13 with LRR17*-18*. In addition, LRR5 and LRR20* undergo new interactions after the rearrangement. Accordingly, the dimerization interface increases from 1290 Å^2 to 2150 Å^2, and two protomers come into closer proximity from 53 Å to 30 Å (Figs. 1(c), 1(d)), which enables the subsequent dimerization of the TIR domains and downstream signaling (Fig. 3).

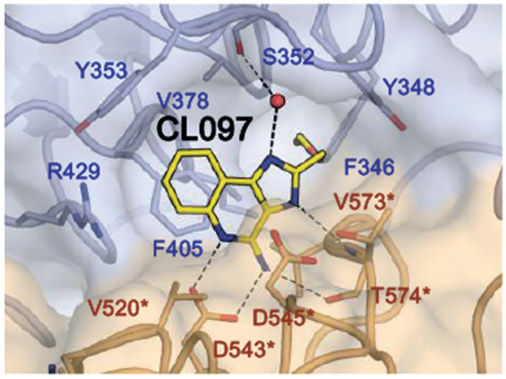

Fig 2. Ligand recognition sites of TLR8. Detailed view of the interactions between TLR8 and CL097.

In this research, we presented a ligand-induced structural rearrangement mechanism of TLR8 activation, offering a new aspect of regulation mechanism of TLRs and a possibility modulating the TLR activation by perturbing the rearrangement. In addition, we also elucidated the details of the ligand recognition mechanism of TLR8, which will enable the rational design of drugs targeting TLR8.

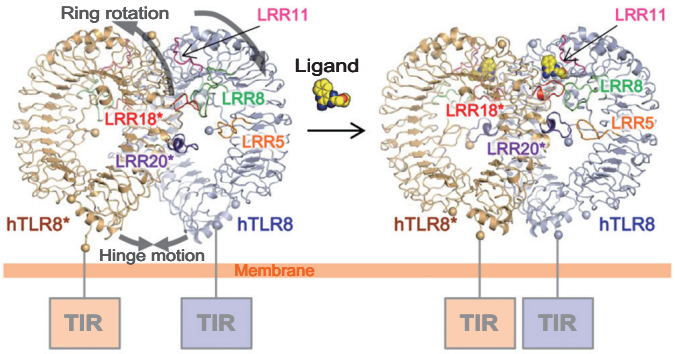

Fig 3. Reorganization of TLR8 dimer upon ligand binding. Structural reorganization of TLR8 dimer induced by ligand binding. Unliganded TLR8 (left) and liganded TLR8 (right) are shown schematically.

Hiromi Tanji*, Umeharu Ohto and Toshiyuki Shimizu

Graduate School of Pharmaceutical Sciences,
The University of Tokyo

*E-mail: 5820302753@mail.ecc.u-tokyo.ac.jp

References

[1] T. Kawai, S. Akira: Nat. Immunol. **11** (2010) 373.
[2] F. Heil *et al.*: Science **303** (2004) 1526.
[3] M. Jurk *et al.*: Nat. Immunol. **3** (2002) 499.
[4] *H. Tanji, U. Ohto, S. Takuma, K. Miyake, T. Shimizu: Science* ***339*** *(2013) 1426.*
[5] S.E. Ewald *et al.*: Nature **456** (2008) 658.

Crystal structure of Na^+,K^+-ATPase with bound sodium ion

Na^+,K^+-ATPase is one of the representative members of P-type ATPase family that includes sarcoplasmic reticulum Ca^{2+}-ATPase (SERCA) and gastric H^+,K^+-ATPase. Na^+,K^+-ATPase transports three sodium ions (Na^+) out and two potassium ions (K^+) into the cell per molecule of ATP hydrolyzed (Fig. 1). It is expressed in all animal cells and is implicated in many fundamental processes in life, notably excitation of nerve cells and contractions of heart muscle. In the reaction cycle, there are two major states, E1 and E2 [1,2]. E1 is a state with a high affinity for Na^+ and E2 has a low affinity for Na^+ but a high affinity for K^+. It has been an interesting question how Na^+,K^+-ATPase selectively and efficiently transports ions into or out the cells. In 2009, our group determined a crystal structure of Na^+,K^+-ATPase in $E2{\cdot}P_i$ with two bound K^+ ions at 2.4 Å resolution and showed how this enzyme selectively binds K^+ [3]. Furthermore, we recently succeeded in determining the crystal structures of this ATPase in E1~P·ADP with three bound Na^+ at 2.8 Å resolution using **BL41XU** [4].

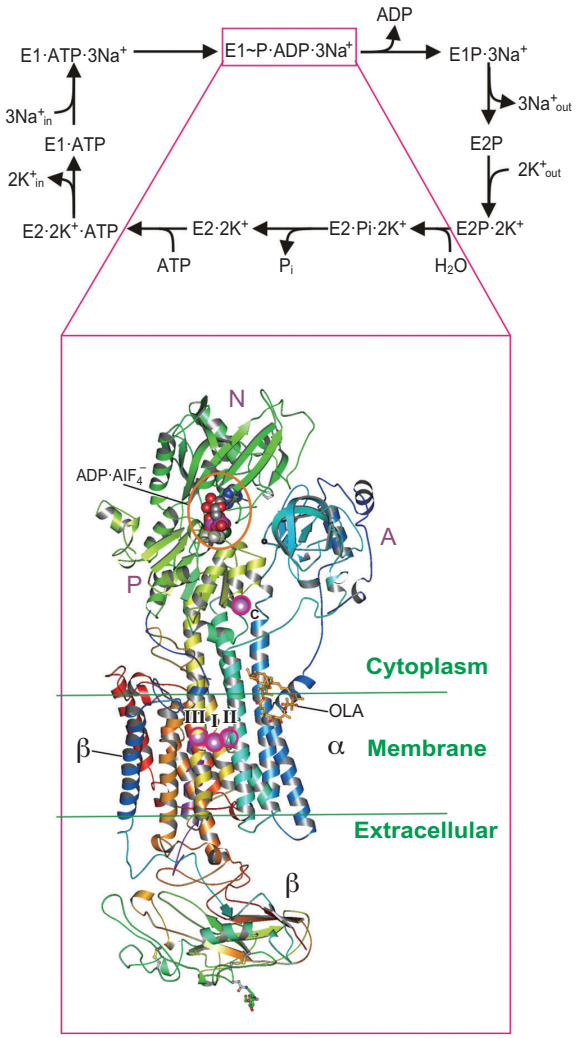

Fig. 1. The reaction cycle and a crystal structure of Na^+,K^+-ATPase in $E1{\sim}P{\cdot}ADP{\cdot}3Na^+$. Top panel shows a simplified reaction cycle. Bottom panel shows the whole complex. Na^+,K^+-ATPase consists of α and β subunits and an auxiliary FXYD protein. The α-subunit is the catalytic subunit, consisting of three cytoplasmic domains and 10 transmembrane helices. Violet spheres represent bound Na^+ (I-III and C)and OLA is oligomycin.

Na^+,K^+-ATPase consists of three components: α-subunit (the catalytic unit), a heavily glycosylated β-subunit, and a tissue-specific auxiliary regulatory polypeptide known as FXYD proteins (Fig. 1). α-subunit has four distinct domains: cytoplasmic actuator (A), phosphorylation (P) and nucleotide binding (N) domains and a transmembrane domain. The crystal structures show three Na^+ ions bound in the transmembrane (M) domain and provide two major conclusions for selective transport of ions by Na^+,K^+-ATPase. One is that this enzyme binds three Na^+ ions sequentially and cooperatively. Na^+ binding to the first site (site III), the unique site to Na^+,K^+-ATPase, leads to a formation of the second binding site (site I). Then, Na^+ binding to site I creates the third binding site (site II) by repositioning of the extracellular half of the transmembrane helix of M4 (M4E). Such sequentially and cooperatively formed Na^+ binding sites, especially site III, are highly constrained to fit only Na^+ (ionic radius = 0.95 Å) and not K^+ (1.33 Å) (Fig. 2). In addition, the short distance (3.4 Å) between Na^+ ions bound at sites I and II indicates that larger K^+ or divalent cations (e.g. Ca^{2+}) cannot bind because of the physical size and/or electrostatic repulsion.

Another major conclusion is that only the binding of the right-sized ion (i.e. Na^+) to site III allows productive phosphoryl transfer from ATP. Site III is located in the hinge between the two halves of the M5 helix (M5C and M5E) and controls the position of the P-domain, as M5C is integrated into the P-domain. For phosphoryl transfer to take place, a proper arrangement of the three cytoplasmic domains is necessary. Such an arrangement is realized only by the binding of the right-sized ion to site III.

The crystal structure also shows how oligomycin, an antibiotic, blocks the activity of Na^+,K^+-ATPase. Oligomycin is known to bind to Na^+,K^+-ATPase in E1P but not in E2P, unlike cardiotonic glycosides such as ouabain and digitoxin. In the structure complexed

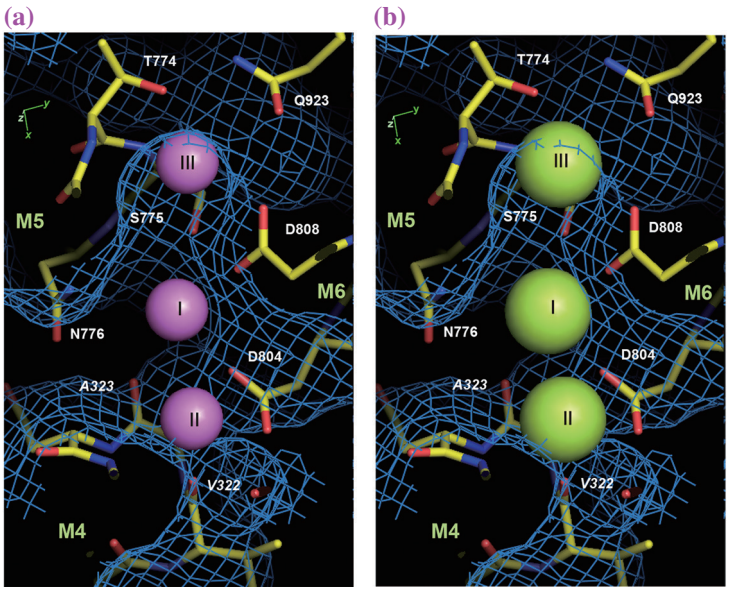

Fig. 2. Continuous cavity connecting three Na^+-binding sites. Na^+ accessible surface (blue net) with three Na^+ (**a,** violet spheres) and K^+ (**b,** green spheres) placed in the Na^+ binding sites. In **(b)** it is evident that the cavity is too small for K^+.

with oligomycin, it is located at the junction of M1 and M1' and sterically blocks the transition into the E2P state (Fig. 3).

Na^+,K^+-ATPase is the target of digitalis, a cardiotonic glycoside prescribed for more than two centuries, and is implicated in many diseases, such as high blood pressure, neurological disorders and cancers. The crystal structure described here provides a solid basis for developing drugs that regulate the activity of Na^+,K^+-ATPase.

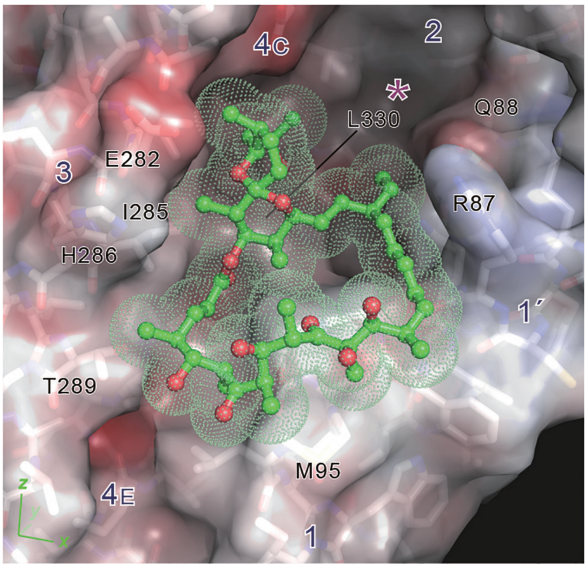

Fig. 3. Binding cavity for oligomycin; surface representation, colored according to the surface potential (blue, positive; red, negative). Green dotted spheres show van der Waals surface of oligomycin.

Chikashi Toyoshima*, Haruo Ogawa and Ryuta Kanai

Institute of Molecular and Cellular Biosciences,
The University of Tokyo

*E-mail: ct@iam.u-tokyo.ac.jp

References

[1] R.W. Albers: Annu. Rev. Biochem. **36** (1967) 727.
[2] R.L. Post *et al.*: J. Biol. Chem. **247** (1972) 6530.
[3] T. Shinoda *et al.*: Nature **459** (2009) 446.
[4] *R. Kanai, H. Ogawa, B. Vilsen, F. Cornelius and C. Toyoshima: Nature* ***502*** *(2013) 201.*

Rotation mechanism of V_1-ATPase

Vacuolar ATPases (V-ATPases) function as proton pumps, which are involved in many processes such as bone resorption and cancer metastasis, and these membrane proteins represent attractive drug targets for osteoporosis and cancer. Their structures resemble those of F-ATPases, which function as ATP synthase in mitochondria, chloroplasts and bacteria. These ATPases consist of a hydrophilic portion (F_1 and V_1) and a membrane-embedded ion-transporting portion (F_o and V_o), and have a similar reaction mechanism that occurs through rotation. F_1-ATPase has been investigated in detail, and the molecular mechanism has been proposed on the basis of crystal structures of the complex [1], and extensive single-molecule observation of the rotation [2]. Similar V_1-ATPase experiments have been conducted using the *Thermus thermophiles* enzyme, which functions physiologically as an ATP synthase. The crystal structures of the A_3B_3DF (V_1) complex at low resolution suggest differences in its structure and interactions compared with F_1-ATPases [3]. Single-molecule analyses of V_1-ATPase also suggest differences in torque generation and the coupling scheme of the rotation mechanism compared with F_1 [4]. *Enterococcus hirae* V-ATPase acts as a primary ion pump similar to eukaryotic V-ATPase, which transports Na^+ or Li^+, instead of H^+ ions. Recently, we have succeeded in obtaining the crystal structures of A_3B_3 and V_1-ATPase complexes at high resolution, which enabled the generation of a model of the rotational mechanism.

We determined the crystal structures of the nucleotide-free (2.8 Å) A_3B_3 (denoted as eA_3B_3) and the AMP-PNP-bound (3.4 Å) A_3B_3 (denoted as bA_3B_3) using beamline **BL41XU** (Fig. 1(a,c)) [5]. In eA_3B_3, one of the three A subunits adopts a closed conformation (denoted as A_C), which shifts the structure into the center of the A_3B_3 ring, whereas the other two A subunits adopt similar open conformations (denoted as A_O and $A_{O'}$) (Fig. 1(b)). Similarly, one of the three B subunits shows a closed conformation (denoted as B_C) compared with the others (denoted as B_O and $B_{O'}$). The conserved nucleotide-binding sites are located between the three different combinations: A_OB_C, $A_{O'}B_O$, and $A_CB_{O'}$ pairs. On the other hand, in bA_3B_3, AMP-PNP:Mg molecules bind at two $A_CB_{O'}$ each, and not at the other A_OB_C (Fig. 1(d)).

We designated these A_OB_C pairs as the 'empty' form on the basis of their apparent very low affinity for AMP-PNP:Mg, and these $A_CB_{O'}$ pairs as the 'bound' form take the ATP-bound form. The $A_{O'}B_O$ in eA_3B_3 seems to change to $A_CB_{O'}$ upon binding with AMPPNP:Mg. We designated this unique $A_{O'}B_O$ pair of eA_3B_3 as the 'bindable' form. These asymmetries suggest that the formation of the A_3B_3 hexamer ring imposes a restriction on the AB pair and induces conformational changes that cooperatively generate one empty (ATP-unbound form), one bindable (ATP-accessible form), and one bound (ATP-bound form) conformation, which in turn determine the order of nucleotide binding in the ring in the right-handed rotational orientation viewed from the top of the V_1 complex.

Next, we crystallized and solved the crystal structure of the nucleotide-free (2.2 Å) V_1-ATPase (denoted as eV_1) (Fig. 2(a)) and the AMP-PNP-bound (2.7 Å) V_1-ATPase (denoted as bV_1). A and B subunits assembled asymmetrically and a central axis composed of D and F subunits penetrated into the cavity of the A_3B_3 hexamer.

The structures of eA_3B_3 and eV_1, which should have been induced by interaction with the DF complex, are compared. The eV_1 has an empty form (A_OB_C) and a bound form ($A_CB_{O'}$), but the bound form of eV_1 is positioned as the site of the bindable form of eA_3B_3 when both empty forms are superimposed. Therefore, the DF binding seems to induce a change from the bindable eA_3B_3 to the bound form, similar to the conformational changes of the eA_3B_3 induced by AMP-PNP binding. The remaining AB pair of eV_1 represents a more tightly packed structure composed of closer A and B subunit conformations approaching the center of the A_3B_3 ring. This is not observed in the structure of the A_3B_3 complex (Fig. 2(b)). We designated the

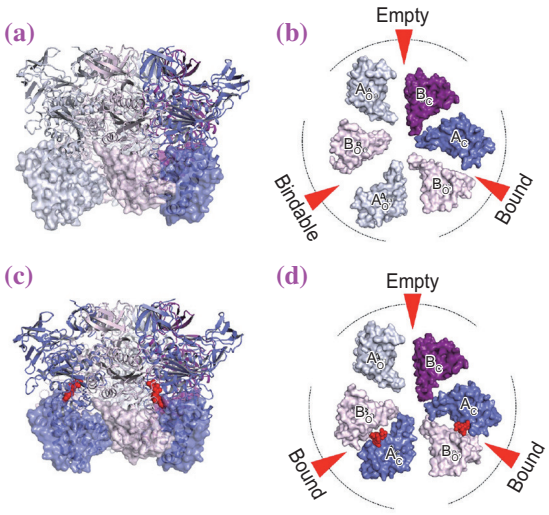

Fig. 1. Structure of the A_3B_3 complex. **(a)** Side view of the nucleotide-free A_3B_3 structure (eA_3B_3). **(b)** Top view of the C-terminal domain (shown in (a) as a transparent surface) of eA_3B_3 from the N-terminal β-barrel side. Red triangles indicate the nucleotide-binding sites. **(c)**-**(d)** Structures of the AMP-PNP-bound A_3B_3 complex (bA_3B_3).

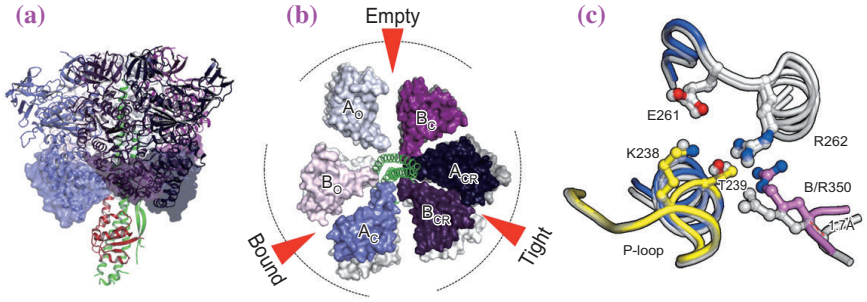

Fig. 2. Structure of the A_3B_3DF complex. **(a)** Side view of the nucleotide-free A_3B_3DF structure (eV_1). **(b)** Top view of the C-terminal domain of eV_1, as in Fig. 1(b), superimposed at the empty form onto that of transparent eA_3B_3 (gray). **(c)** Nucleotide-binding sites. Tight form in eV_1 (color) and bound form in eA_3B_3 (gray).

new conformations as the 'tight' form ($A_{CR}B_{CR}$), and DF complex binding seems to change the bound form of eA_3B_3 to the tight form. In bV_1, the overall structure of bV_1 was similar to that of eV_1, although the binding sites of bound and tight forms were occupied with AMP-PNP:Mg.

In the tight form, the position of the conserved Arg-finger (Arg350 of B_{CR}), which helps ATP hydrolysis, was closer to the nucleotide-binding site than that in the bound form (Fig. 2(c)). Thus, the ATP hydrolysis is stimulated by this approach triggered by the movement of the Arg-finger, which is induced by binding between the DF complex and A_3B_3.

On the basis of these asymmetric structures, a rotation model of V_1 was proposed (Fig. 3). The V_1-ATPase is bound to two ATP:Mg molecules in the bound and tight forms (Fig. 3(a)). Bound ATP in the tight form is awaiting ATP hydrolysis. When ATP is hydroid in the tight form, V_1-ATPase starts the rotary reaction. The conformation of the A_3B_3 part in V_1-ATPase may return to eA_3B_3 in a cooperative manner (Fig. 3(b)). Thus, while the tight form changes to the empty form with the release of ADP and phosphate, the empty form changes to the bindable form. However, the interaction between the DF and the tight form might prevent these structural changes, and an intermediate state may exist instead of the state of eA_3B_3. After that, the new ATP molecule binds to the bindable form, and the conformation changes to the bound form. Thus, the state may be similar to that of bA_3B_3 (Fig. 3(c)). Then, the DF rotates, and the bound form from the beginning changes to the next tight form vie interaction with the DF complex. In brief, the V_1-ATPase returns to the initial state (Fig. 3(d)).

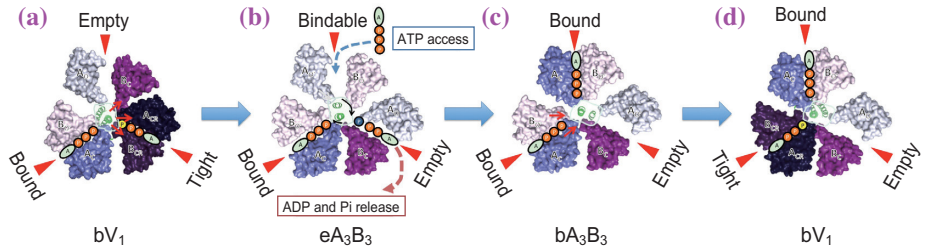

Fig. 3. Rotation model of V_1-ATPase. Top view of the C-terminal domain viewed as in Figs. 1(b, d) and Fig. 2(b). ATP with yellow "P" in (a) and (d) represents an ATP molecule that is committed to hydrolysis. The blue "P" in (b) represents a phosphate molecule after ATP hydrolysis. **(a)** The AMP-PNP-bound V_1: first two ATPs are bound in the bound and tight forms. The reaction is triggered by the ATP hydrolysis in the tight form. **(b)** The nucleotide-free A_3B_3: by the conversion to ADP and phosphate, the conformation of the A_3B_3 part in V_1-ATPase may return to eA_3B_3 (ground structure of A_3B_3complex) in a cooperative manner. The tight form changes to the empty form with the release of ADP and phosphate and the empty form changes to the bindable form. **(c)** The AMP-PNP-bound A_3B_3: by new ATP binding to the bindable form, the conformation changes to bA_3B_3, which has two bound forms with two ATP, and then the DF rotates. **(d)** The bound form from the beginning changes to the next tight form, induced by DF binding, and the V_1-ATPase returns to the initial state with 120° rotation.

Kano Suzuki[a,*] and Takeshi Murata[a,b]

[a] Department of Chemistry, Chiba University
[b] JST/PRESTO

*E-mail: r2sd3103@chiba-u.jp

References

[1] J. P. Abrahams *et al.*: Nature **370** (1994) 621.
[2] H. Noji *et al.*: Nature **386** (1997) 299.
[3] N. Numoto *et al.*: EMBO Rep. **10** (2009) 1228.
[4] H. Imamura *et al.*: Proc. Natl. Acad. Sci. USA **102** (2005) 17929.
[5] *S. Arai, S. Saijo, K. Suzuki, K. Mizutani, Y. Kakinuma, Y. Ishizuka-Katsura, N. Ohsawa, T. Terada, M. Shirouzu, S. Yokoyama, S. Iwata, I. Yamato and T. Murata: Nature* ***493*** *(2013) 703.*

Crystal structure of multidrug transporter MATE

Toxic compounds essentially must be exported from the cell to maintain life. MATE (multidrug and toxic compound extrusion) transporters function in the efflux of endogenous cationic and lipophilic substances using an electrochemical gradient of H^+ or Na^+ across the membrane [1], and are ubiquitously distributed in archaea, bacteria, and eukaryotes. Bacterial MATE transporters confer multidrug resistance (MDR) to pathogens, such as multi-antibiotic-resistant *Staphylococcus aureus*, which has received much attention as a hospital-acquired infection. In cancer cells, MATE transporters export structurally diverse anti-cancer drugs, causing fatal reductions in the therapeutic efficacies of anti-cancer drugs. Thus, the demand for the discovery of inhibitory molecules of MATE transporters is high because of their clinical importance.

PfMATE was crystallized using the lipidic cubic phase (LCP) method. The tiny crystals (20~30 μm) grown in LCP diffracted X-rays to 2.2 Å resolution at maximum on beamline **BL32XU**. Diffraction data sets were collected by the helical data collection method using a microbeam with a 1 μm width and a 5 μm height [2]. Co-crystallization with the cyclic peptides (generated by the RaPID system [3]) improved the quality of the SeMet-derivatized crystals, which facilitated the phase determination by the single-wavelength anomalous diffraction (SAD) method. The peptides may restrict the rocker-switch motion of the lobes and lead to improved quality. Additionally, the cyclic peptides have the ability to inhibit the extrusion function of PfMATE. Finally, we determined the outward-open structures in two different conformations ("straight" and "bent" conformations at 2.4 and 2.5 Å resolutions, respectively) (Fig. 1).

The structure of PfMATE consists of 12 transmembrane-helices (TMs) forming two pseudo-symmetrical lobes, an N-lobe (TM1-TM6) and a C-lobe (TM7-TM12), which are related by a pseudo-two-fold symmetry axis. Therefore, the rocker-switch mechanism similar to that employed by the major facilitator superfamily (MFS) transporters was proposed [4]. The PfMATE structure adopts a V-shaped conformation, with the central cleft open toward the extracellular side, representing an outward-open state. A large hydrophobic central cleft can be divided into two cavities, the N- and C-lobe cavities. The N-lobe cavity is larger than the C-lobe cavity. In the outward-open state, we found that it adopts two distinct conformations, the "bent" and "straight" conformations, in terms of the structure of the TM1 helix in the N-lobe (Fig. 1). In the straight conformation, TM1 forms a single and straight helix, whereas in the bent conformation, it is unstrained and kinked at Pro26 and Gly30 and bent toward the TM2 side. As a result, the N-lobe cavity, which is mainly formed between TM1 and TM2, is collapsed in the bent conformation. To investigate the importance of Pro26, we mutated Pro26 to Ala and Ile, which markedly reduced the transport activities, although the membrane expression of all of the mutants was confirmed. TM1 is kinked at Pro26 in the bent conformation, which is essential to drug export activity.

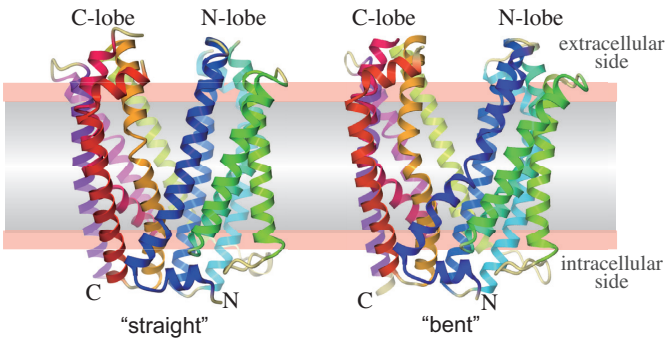

Fig. 1. Overall structures of PfMATE. Schematic representations of the two conformations of PfMATE, viewed from the membrane. The molecules are shown as ribbons with each helix colored as a rainbow, from the N terminus (blue) to the C terminus (purple).

A significant rearrangement of the side chain interactions was also observed between the straight and bent conformations, notably at the apex of the N-lobe cavity (Fig. 2(a)). Some acidic residues are clustered in this site. In the straight conformation, Asp184 is within hydrogen bonding distance with Asp41 (2.8 Å), suggesting that the carboxylate group of either Asp41 or Asp184 is protonated. In view of the fact that Asp184 is buried in the protein core while Asp41 is exposed to the bulk solvent, it is likely that Asp184 is protonated and Asp41 is deprotonated. In contrast, in the bent conformation, Asp41 is closer to TM2. Asp184 also forms a direct hydrogen bond with Asp41. This interaction network is further surrounded by the hydrophobic environment, and sequestered from the solvent region of the extracellular half channel. Therefore, in the bent conformation, the Asp41 and Asp184 side chains are probably both protonated, since a charged group in such a low-dielectric environment inside the protein is energetically unfavorable. This is consistent with the fact that the bent-form crystals appeared under acidic conditions. To investigate the importance of these acidic residues in the N-lobe cavity, we performed complementation assays of Asp41 and Asp184 mutants. These mutations abolished both the drug

and H^+ transport activities, indicating the importance of these acidic residues in the antiport mechanism. The change in the protonation state of the Asp41 side chain may trigger the rearrangement, thereby inducing the structural conversion from the straight conformation to the bent conformation.

To investigate the drug recognition mechanism, we determined the 2.9-Å-resolution crystal structure of PfMATE in the presence of a norfloxacin derivative compound (Br-NRF). In this complex structure, an electron density that resembles the shape of the Br-NRF molecule was observed in the N-lobe cavity (Fig. 2(b)). The Br-NRF molecule is mainly recognized by shape complementarity. To further explore the roles of these residues in substrate recognition, we performed complementation assays of their mutants. The Ala mutants of Met173, Asn180, and Met206 abolished the function, indicating the importance of these residues in the recognition of the substrates.

We further determined the macrocyclic peptide complex structure in two distinctive binding modes. The MaL6 peptide consists of a 17-aa macrocyclic structure. In the complex structure with MaL6, PfMATE adopts the straight conformation, and the cyclic peptide binds between the N- and C-lobes by forming a β-hairpin structure. The peptide mainly interacts with the extracellular side of TMs 2, 7, and 8, but does not interact with the N-lobe cavity. Therefore, the interaction is limited to the extracellular entrance of PfMATE. In contrast, the MaD5, which has a lariat like structure containing a 7-aa macrocycle, deeply bind within the central cleft. Thus, these peptides may provide new scaffolds for the development of potent inhibitors against MATE transporter families from bacteria and eukaryotes.

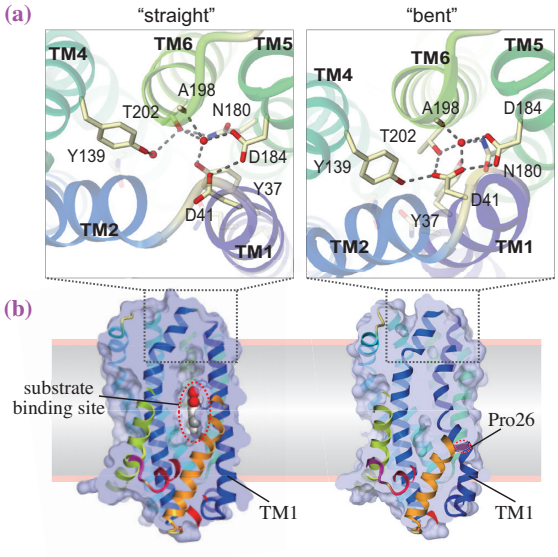

Fig. 2. Differences between two conformations. **(a)** Close-up views of the interaction networks in the two forms at the apex of the N-lobe cavity. Black dashed lines indicate hydrogen bonds. **(b)** Surface models viewed from the central cleft, highlighting the N-lobe cavity. The Br-NRF molecule is depicted by a space-filling model in the N-lobe cavity of the straight conformation.

In this study [5], we proposed the last step of the H^+-driven drug extrusion mechanism by MATE, on the basis of the present structural and functional analyses (Fig. 3). After the structural conversion from the inward-open state to the outward-open state, PfMATE is deprotonated, and the drug substrate resides in the cavity (corresponding to the present Br-NRF complex straight form structure). The protonation of Asp41 induces the bending of TM1 at Pro26, which collapses the N-lobe cavity and extrudes the bound substrate into the extracellular space (corresponding to the present bent form structure). Finally, the protonated transporter undergoes further structural conversion to the inward-open state. The complete understanding of the H^+/drug antiport cycle of MATE awaits the elucidation of the structures capturing the occluded and inward-open states.

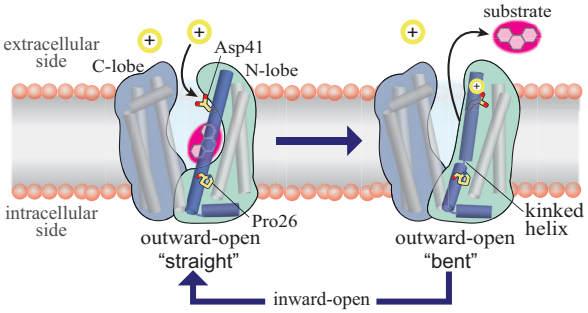

Fig. 3. Drug extrusion mechanism by MATE. In the drug-binding, "straight" outward-open conformation, a cation (yellow) binds to the conserved acidic cluster. Cation binding to D41 induces TM1 (blue) bending and changes the conformation to the "bent" form, which extrudes substrate drugs (magenta). Through the inward-open state, the substrate binding induces structural changes back to the outward-open state.

Yoshiki Tanaka, Ryuichiro Ishitani and Osamu Nureki*

Department of Biophysics and Biochemistry,
The University of Tokyo

*E-mail: nureki@biochem.s.u-tokyo.ac.jp

References

[1] M.H. Brown *et al.*: Mol. Microbiol. **31** (1999) 394.
[2] K. Hirata *et al.*: AIP Conf. Proc. **1234** (2010) 901.
[3] C.J. Hipolito and H. Suga: Curr. Opin. Chem. Biol. **16** (2012) 196.
[4] Y. Yin *et al.*: Science **312** (2006) 741.
[5] *Y. Tanaka, C.J. Hipolito, A.D. Maturana, K. Ito, T. Kuroda, T. Higuchi, T. Katoh, H.E. Kato, M. Hattori, K. Kumazaki, T. Tsukazaki, R. Ishitani, H. Suga and O. Nureki: Nature* ***496*** *(2013) 247.*

Crystallographic and NMR evidence for flexibility in oligosaccharyltransferases and its catalytic significance

Asparagine-linked glycosylation (N-glycosylation) of proteins is widespread not only in eukaryotes, but also in archaea and some eubacteria. The entire process of protein N-glycosylation is divided into three steps: oligosaccharide donor synthesis, oligosaccharyl transfer reaction, and oligosaccharide processing (Fig. 1). The first step is the production of the oligosaccharide donor, the lipid-linked oligosaccharide (LLO). An oligosaccharide chain is assembled on a lipid-phospho carrier. In principle, the carrier is dolichol diphosphate in eukaryotes and archaea, and undecaprenol diphosphate in eubacteria, with the exceptions of halophilic and methanogenic archaea, which use dolichol monophosphate. The second step is the transfer of the oligosaccharide chain, preassembled on the lipid-phospho carrier, onto proteins. A membrane-bound enzyme, oligosaccharyltransferase (OST), catalyzes the formation of a covalent bond between the sugar residue of the reducing end of the oligosaccharide chain and the side-chain amide groups of the asparagine residues in proteins. The catalytic subunit of the OST enzyme is a polypeptide chain referred to as "STT3" (staurosporine and temperature sensitivity 3) in eukaryotes, "AglB" (archaeal glycosylation B) in archaea, and "PglB" (protein glycosylation B) in eubacteria, although they originated from a common ancestor. The eukaryotic OST is a multisubunit protein complex containing STT3, but the lower eukaryotic protozoan OST, and the archaeal and eubacterial OSTs, are single subunit enzymes consisting only of the STT3/AglB/PglB protein. In principle, the acceptor asparagine resides in the N-glycosylation sequon (Asn-X-Ser/Thr; X ≠ Pro), but glycosylation also occurs in atypical sequences, such as Asn-X-Cys, Asn-Gly-X, and Asn-X-Val (X ≠ Pro), albeit at very low frequencies. Eubacteria use an extended and thus more restrictive version of the sequon (Asp/Glu-X-Asn-Y-Ser/Thr; X, Y ≠ Pro) .

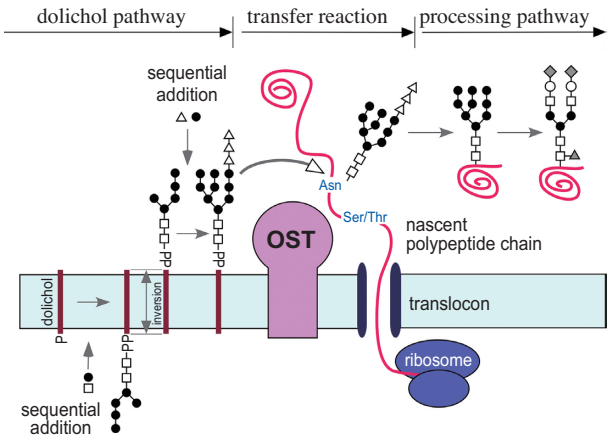

Fig. 1. Schematic representation of the N-glycosylation reaction. Oligosaccharyltransferase is the central enzyme of N-linked protein glycosylation.

The STT3/AglB/PglB proteins consist of an N-terminal multispan transmembrane region and a C-terminal globular domain. Multiple STT3/AglB/PglB proteins may be encoded in a single genome. As exemplified by the AglBs referred to in this study, *Archaeoglobus fulgidus* contains three paralogs. We discriminate among these archaeal paralogs with a letter plus an optional number, such as L (long) or S1 (short, number 1).

We previously determined the crystal structures of the C-terminal globular domains of *Pyrococcus furiosus* AglB-L [1], *Archaeoglobus fulgidus* AgB-S1 [2], and *Campylobacter jejuni* PglB [3]. The comparison of the three crystal structures unexpectedly revealed significant local variations in the conformations of about 25-residue segments in the C-terminal globular domains [2].

In this study, we have determined two crystal structures of the C-terminal globular domains of *P. horikoshii* AglB-L and *A. fulgidus* AglB-S2 [4]. The one-to-one structural comparison of the five crystal structures confirmed that the C-terminal globular domains of the AglB/PglB proteins contained the special plastic segment, and identified the resting state conformation of the plastic segment, free of crystal contact effects (Fig. 2).

We characterized the dynamic properties of the plastic segment in solution by ^{15}N NMR relaxation analyses. We selected the C-terminal domain of *A. fulgidus* AglB-S2 because it is the smallest among the three domains of life. Intriguingly, the mobile region contains the binding pocket for the recognition of the +2 Ser/Thr residue in the consensus sequence (Fig. 2). In agreement, the flexibility restriction forced by an engineered disulfide crosslink abolished the enzymatic activity, and its cleavage fully restored the activity (Fig. 3). These results suggest the necessity of multiple conformational states in the reaction. The dynamic nature of the Ser/Thr pocket could facilitate the efficient scanning of N-glycosylation sequons along nascent polypeptide chains.

We demonstrated that comparative structural biology is an effective approach for analyzing the

structural and dynamic relationships of proteins. The structural comparison of the closely and distantly related AglB and PglB proteins led to the unexpected discovery of the mobile region in the C-terminal globular domain (Fig. 2). The comparative structural approach is also useful for the selection of the most suitable protein for certain purposes; the smallest AglB was selected for the NMR relaxation study, and the thermostable AglB was suitable for the custom-designed mutagenesis study, which required high protein stability to tolerate the boldly designed mutations (Fig. 3).

The isolated C-terminal domains are catalytically inactive, and thus we must know the three-dimensional structures of the full-length STT3/AglB/PglB proteins to elucidate the catalytic mechanism of OST. We determined the crystal structure of the full-length *A. fulgidus* AglB-L in two crystal forms at 2.5 Å (space group *C*2 in the presence of *n*-octyl-β-D-glucopyranoside) and 3.4 Å ($P4_32_12$ in lauryldimethylamine-oxide) resolutions [5]. X-ray diffraction data were collected at beamlines **BL44XU** and **BL32XU**. This is the second solved OST structure, after the eubacterial *C. lari* PglB determined by another group. The structural comparison of the two full-length OST proteins confirmed and extended the dynamic view of the N-glycosylation catalytic cycle, involving the plastic EL5 loop in the transmembrane region (Fig. 3), and the dynamic Ser/Thr binding pocket in the CC unit [5].

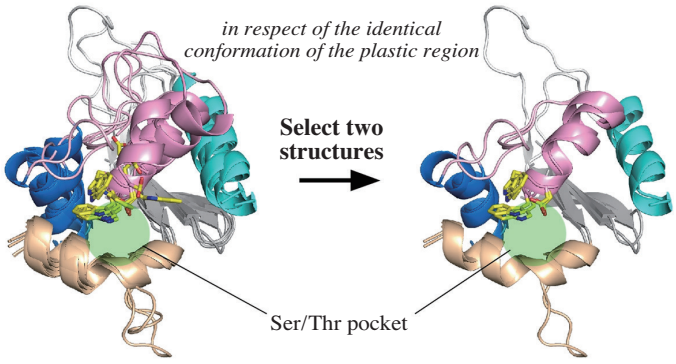

Fig. 2. Superposition of the CC structural unit in the five crystal structures of the C-terminal globular domains of the AglB/PglB proteins. The region that exhibits large plasticity includes the WWDYG motif (yellow side chains) and the following α-helical and loop regions (pink backbones). The right panel shows the two selected structures that share the identical conformation of the plastic region. This conformation is assumed to be the resting state conformation. The shaded circles indicate the position of the +2 Ser/Thr pocket.

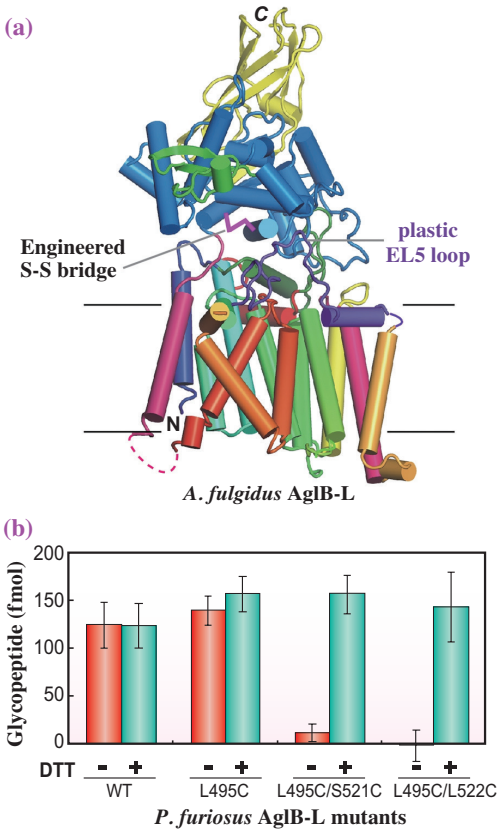

Fig. 3. Effects of the flexibility restriction in the C-terminal domain of *P. furiosus* AglB-L on OST activity. **(a)** The position of the engineered disulfide bond is shown by magenta sticks on the structure of the full-length *A. fulgidus* AglB-L protein. **(b)** Two double cysteine mutants (L495C/S521C and L495C/L522C) of the full-length *P. furiosus* AglB-L protein were constructed. As a negative control, a single cysteine mutant (L495C) was also generated. The *P. furiosus* AglB-L mutants bearing the engineered disulfide bond (red bars) had virtually no activity, whereas the same mutants without the disulfide crosslink after DTT treatment (blue bars) had completely restored activity.

James Nyirenda, Shunsuke Matsumoto
and Daisuke Kohda*

Medical Institute of Bioregulation, Kyushu University

*E-mail: kohda@bioreg.kyushu-u.ac.jp

References

[1] M. Igura *et al.*: EMBO J **27** (2008) 234.
[2] S. Matsumoto *et al.*: Biochemistry **51** (2012) 4157.
[3] N. Maita *et al.*: J. Biol. Chem. **285** (2010) 4941.
[4] *J. Nyirenda, S. Matsumoto, T. Saitoh, N. Maita, N.N. Noda, F. Inagaki and D. Kohda: Structure **21** (2013) 32.*
[5] S. Matsumoto *et al.*: Proc. Natl. Acad. Sci. USA **110** (2013) 17868.

Life Science :

It is interesting to see how eager biologists are to make use of new experimental techniques. Some even develop novel techniques for a particular experiment. In addition to benefiting their own research, these efforts promote significant advances in biological sciences. The biological problems tackled by these scientists are often long-standing fundamental ones, and SPring-8 has been benefited by the efforts of these innovative biologists. The four reports in this section are good examples.

Iwamoto and Yagi of SPring-8/JASRI used an ultra-high speed CMOS camera to record the diffraction from muscle proteins in a bumblebee during a wing beat. Although the strong X-ray from a SPring-8 undulator beamline has been available for some years, an X-ray detector fast enough to capture a wing beat has not. The new CMOS camera is capable of recording 5,000 frames per second. When it is coupled to an X-ray image intensifier with a short-decay phosphor, it works as an ultra-high speed X-ray detector. They also used the same camera to observe the motion of wings to find a correlation with the time-resolved X-ray diffraction data, which is related to the molecular structural changes in the muscle cells. The motion of one wing triggers the motion of the other wing in an alternating fashion. The triggering mechanism seems to be similar to that in other types of muscles, including human muscles.

Medical Biology

In eukaryotic nuclei, the long genetic DNA is folded into compact chromosomes. The organization of DNA in chromosomes has been a matter of debate for many years. It is generally assumed that a long strand of DNA must be folded regularly to make a compact packing. However, although there have been reports on regular repeats in chromosomes, the precise structure has never been revealed. Maeshima *et al.* used X-ray scattering techniques to investigate this long-standing question. Using an ultra-low angle scattering technique, they demonstrated that such a regular structure does not exist in human mitotic chromosomes. This surprising finding suggests that irregular folding is actually important for the dynamic function of cells.

Nango and his colleagues are interested in the high-resolution structure of bone. There is a tubular structure in bone called the canaliculi with a diameter of about 0.25 μm. They used two types of X-ray microscopes with a zone plate to study bone at this structural level. One type utilizes a defocused condition, which causes edge-enhancement in the image that helps visualize the fine structure of the canaliculi. The other is Talbot interferometry, which uses a pair of gratings to obtain a phase-contrast image, allowing the high-density resolution necessary to estimate bone matrix mineralization. Combining these two techniques for CT (Computed Tomography) provides three-dimensional structural information, and changes in the mineralization of the regions surrounding the osteocyte canalicular network were elucidated.

NRVS (Nuclear Resonance Vibrational Spectroscopy), which is specific for the displacement of Fe atoms, is a novel method to study the chemical states of metal atoms, especially Fe, in proteins. The technique, which was developed by Prof. S. Cramer's group (University of California, Davis), has been demonstrated in various metalloproteins. A group led by Prof. Solomon of Stanford University has applied this technique to mononuclear non-heme iron (NHFe) enzymes, which play important roles in human cells. Analysis of the NRVS spectra of these proteins and theoretical computations led to the elucidation of an intermediate state of a quadrivalent iron atom bound with oxygen. This novel approach to evaluate protein function will be applied to many metalloproteins in the future.

Naoto Yagi

Wing-beat mechanism of insect revealed by ultrafast X-ray movies

For aerodynamic reasons, small insects must beat their wings at high frequencies in order to fly. For example, the wing-beat frequencies of mosquitoes are around 500 Hz. It is very difficult to produce such fast oscillations by repeating ordinary contraction-relaxation cycles, each of which is elicited by a command from the motor nerve. Instead, these small insects have developed a special kind of flight muscles to drive their wings. These muscles are called "asynchronous flight muscles." These muscles are kept constantly activated during flight, and they undergo self-sustained oscillations. They are called asynchronous because their high-frequency oscillations are maintained by low-frequency nerve commands just to keep the muscles activated.

Although cross-striated as vertebrate skeletal muscles are, asynchronous flight muscles work with different principles. They do not move wings directly. They deform the thoracic exoskeleton that houses them, and the wings move up and down as a result of this deformation. There are left-right pairs of two antagonistic flight muscles, called dorsal longitudinal muscle (DLM) and dorso-ventral muscle (DVM). These pairs are arranged in a manner so that when one shortens, the other is stretched. Asynchronous flight muscles are equipped with a mechanism of stretch activation, a mechanism in which the muscle generates a large delayed force when stretched externally. When one of the antagonistic muscles shortens, it stretches the other. Then the stretched one generates a large force, and stretches back the other muscle. By repeating this process, the flight muscles can maintain self-sustained oscillations.

Thus, stretch activation is essential for the asynchronous action of flight muscles, but its molecular mechanism is still unclear despite decades of researches. Traditionally, isolated and demembranated flight muscle cells (skinned muscle fibers) have been used to study the molecular mechanism of stretch activation. Skinned fibers can be made to contract and relax by exchanging solutions, and generate stretch-activated force when stretched externally. They also give rise to high-quality diffraction patterns when irradiated with X-rays, and from these patterns we have extracted some clues to the behavior of constituent protein molecules when the fibers are stretch-activated. However, it remains unclear how accurately the observations made on skinned fibers reproduce the events undergoing in the flight muscles of live insects.

Here we have recorded ultrafast 2-dimensional X-ray diffraction movies from live bumblebees during wing-beat at an unprecedented rate of 5,000 frames/s, by using the high-flux **BL40XU** beamline [1]. The diffraction patterns were taken during "ethered flight," i.e., the bee was allowed to beat its wings while its body was fixed at a position by gluing its thorax to an aluminum tube. Bumblebees beat their wings at ~120 Hz (single wing-beat cycle, ~8 ms), i.e., ~40 frames/wing-beat, allowing detailed analysis. Two fast CMOS video cameras were used for data collection: One recorded the diffraction patterns, and the other recorded the wing-beat of the bee. The two cameras were synchronized by connecting them in a master-slave fashion, so that the X-ray frames were accurately correlated to the phase of wing-beat. The X-rays were irradiated at the point at which the two antagonistic flight muscles cross, so that their diffraction patterns were recorded at the same time.

Figure 1 shows one of the X-ray movie frames, created by summing data from 9 bees. A number of spot-like reflections are observed, and they originate from the near-crystalline arrangement of contractile proteins within muscle fibers. The reflections can be indexed by using Miller indices (*hkl*) as for other crystals. Patterns from both DLM and DVM are recorded on the same frame, and the reflections from these muscles can be distinguished because the axes of the two muscles make an angle of ~60°. In

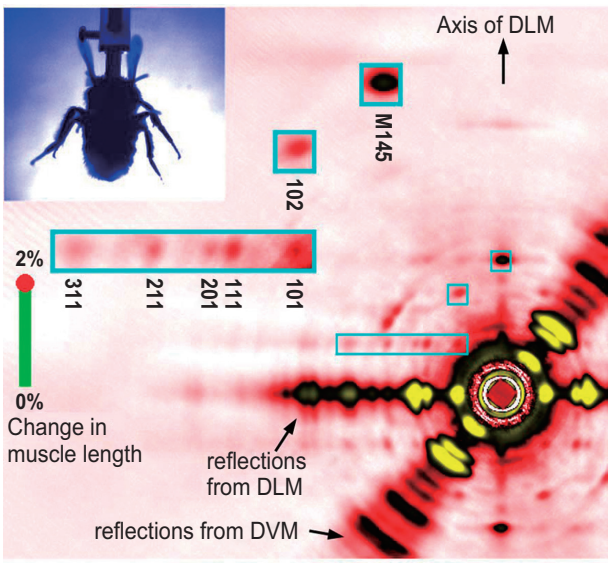

Fig. 1. One of the frames of X-ray diffraction movies. The pattern is re-oriented so that the fiber axis of DLM is vertical. [1]

the figure, the regions of reflections of interest are magnified in cyan boxes.

In the movie (provided as a supplemental material for the original paper), these reflections strengthen and weaken with the phase of wing-beat. By analyzing these reflections, the length change and force of muscle fibers can be estimated as well as the movement and structural change of constituent protein molecules. Figure 2 shows a part of the results of analyses. The top row for each muscle shows the estimate of change of muscle fiber length. The middle row shows the intensity changes of reflections reporting the strong attachment of myosin and actin, the two major contractile proteins in muscle. Their attachment and a subsequent structural change in myosin are believed to cause force generation. The bottom row is related to the most crucial finding in this study, and shows the intensities of two reflections, 111 and 201. A strengthening of 111 and a concomitant weakening of 201 occur in the stretch phase, a timing at which stretch activation occurs. Therefore these intensity changes may be related to a structural change that triggers stretch activation.

Figure 3 shows possible structural changes that account for the intensity changes of 111 and 201 reflections. Their reciprocal intensity changes can be caused by a mass movement from the blue area to the red area in the unit cell, and it is most readily explained by an azimuthal rotation of the tail region of myosin head (the blue object in Fig. 3. The part of myosin molecule that generates force). Then the mechanism of stretch activation may be explained as follows: The externally applied stretch causes distortion of myosin heads already attached to the actin filaments in the weak binding form. The distortion (azimuthal rotation) converts the myosin head from the weak binding form to the strong binding form, inducing force generation and enhancements of signals indicated in the middle row of Fig. 2.

A mechanism of distortion-induced enhancement of force has already been reported for vertebrate skeletal muscle [2], and therefore this may be a mechanism common to myosin in various types of muscles. If so, it can be said that insects have developed the mechanism of stretch activation by refining a pre-existing mechanism of myosin in ancestors common to both insects and vertebrates.

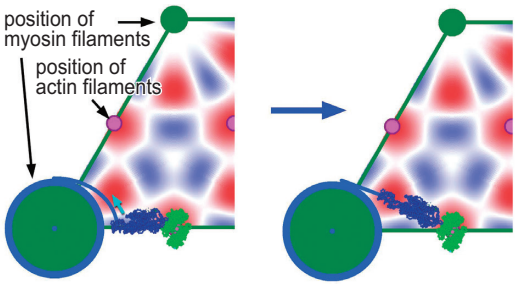

Fig. 3. Structural change within a unit cell that explains the observed intensity changes of 111 and 201 reflections. The 111 reflection is more intense than 201 in red areas, and vice versa in blue areas. [1]

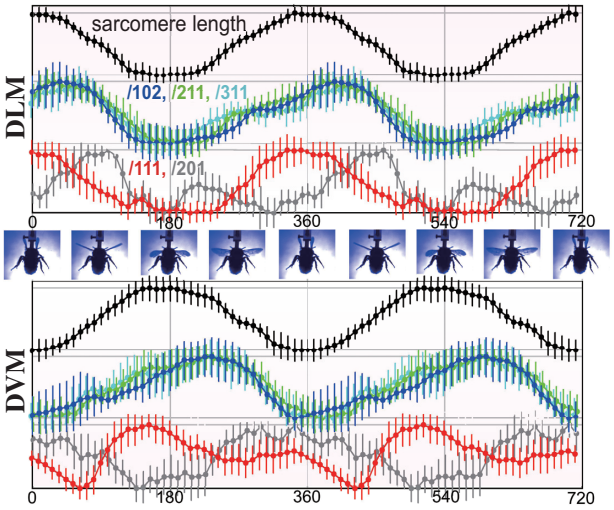

Fig. 2. Results of analyses of X-ray diffraction movies. Top rows, estimated changes of fiber lengths; middle rows, intensity changes of reflections that report myosin binding to actin; bottom rows, intensity changes of reflections considered to report the triggering events of stretch activation. The plots are made for 2 wing-beat cycles. [1]

Hiroyuki Iwamoto* and Naoto Yagi

SPring-8/JASRI

*E-mail: iwamoto@spring8.or.jp

References

[1] *H. Iwamoto and N. Yagi: Science* ***341*** *(2013) 1243.*
[2] H. Iwamoto: Biophys. J. **68** (1995) 243.

Irregular organization in the human chromosomes revealed by X-ray scattering

How is a long strand of DNA organized in the cell? In molecular biology textbooks, we often find a typical figure (Fig. 1(a)). To begin with, DNA is wrapped around histones and forms a "nucleosome" (10-nm fiber) structure. This nucleosome has been assumed to be folded into the regular "30-nm chromatin fiber." In one of the famous models, the "hierarchical helical folding model," it is assumed that the 30-nm chromatin fiber is folded progressively into larger fibers such as ~100-nm and then ~200-nm fibers, to form the final mitotic chromosomes (Fig. 1(b)) or large chromatin fiber (chromonema fiber) in interphase cell nuclei.

What do mitotic chromosomes actually look like in cells? To see chromosomes as intact as possible, we performed cryo-electron microscopy (cryo-EM) [1]. Surprisingly, cryo-EM and subsequent computational image processing did not reveal any 30-nm chromatin fibers in the mitotic chromosomes, but merely a uniform disordered structure, which strongly argues against the "established view" (Figs. 1(a) and 1(b)).

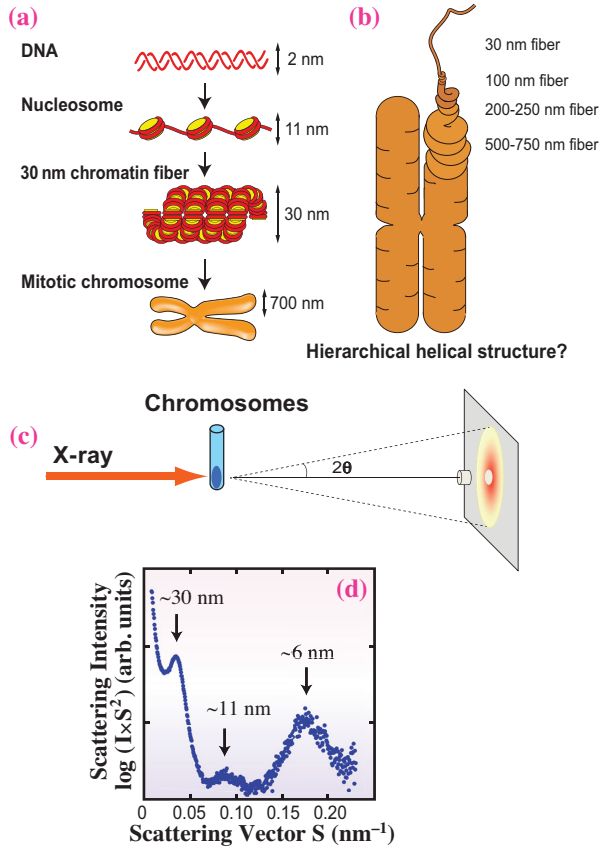

Fig. 1. **(a)** Textbook image of chromatin, **(b)** hierarchical helical folding model, **(c)** experimental setting of small-angle X-ray scattering, and **(d)** a typical scattering pattern of human mitotic chromosomes.

On the other hand, cryo-EM observation can examine only a limited portion of a chromosome, not the whole, because the section thickness is only around 50 nm. It was thus difficult to observe possible hierarchical regular structures in the chromosomes, if any.

To investigate the bulk structure of the mitotic chromosomes in solution, we performed small-angle X-ray scattering (SAXS) [2,3]. Generally, when X-rays are irradiated onto non-crystal materials, scattering at small angles can generally reveal periodic structures within samples (Fig. 1(c)). At beamline **BL45XU**, the synchrotron X-ray beam was irradiated onto isolated human chromosomes at the bottom of a glass capillary, and scattering patterns were recoded (Fig. 1(c)). A typical scattering pattern of mitotic chromosomes showed three peaks: 30-nm, weak 11-nm, and 6-nm peaks (Figs. 1(d) and 2(a)). This result is completely consistent with those of experiments conducted by Langmore & Paulson [4]. While the 11 nm and 6 nm peaks are believed to originate from the spatial arrangement of nucleosomes, but the 30-nm peak was assumed to represent the side-by-side packing of the 30-nm chromatin fibers, and has long been regarded as strong evidence for the existence of these fibers in chromosomes. However, why could we not observe such a 30-nm structure in the mitotic chromosomes by cryo-EM?

To elucidate the nature of the 30-nm peak observed by SAXS, the isolated chromosomes were examined by cryo-EM. Again, no 30-nm chromatin structures were observed inside chromosomes. However, the cryo-EM images unexpectedly showed that the chromosome surface was coated with electron-dense granules of the similar size as ribosomes (Fig. 2(a), bottom). Biochemical analyses confirmed that they are ribosomes contaminating the chromosome surface. The ribosomes were regularly stacked with a ~30 nm spacing. We removed the ribosomes from the chromosome surface by washing with an isotonic buffer, with maintaining the size and shape of chromosomes (Fig. 2(b), bottom). Strikingly, in the chromosomes, no 30-nm peaks were detected by SAXS (Fig. 2(b), top). However, other peaks originating from the internal structure of nucleosomes remained (Figs. 2(a) and 2(b)). We then concluded that regularly folded 30-nm chromatin fibers are essentially not present in human mitotic chromosomes.

Next, we investigated an entire region of mitotic chromosomes at beamline **BL29XUL** using a newly developed apparatus for ultra-small-angle X-ray

scattering (USAXS) (Fig. 2(c)) [2,5]. Again, we found no regular periodic structures, including the 100–150 or 200–250 nm structure, between ~50 and 1000 nm in mitotic chromosomes (Fig. 2(d)), contradicting the hierarchical helical folding model (Fig. 1(b)). The cryo-EM, SAXS, and USAXS data collectively indicate that the irregularly folded nucleosome fibers make up the bulk structure of human mitotic chromosomes.

How is the nucleosome fiber organized into a mitotic chromosome? Since condensin and topoisomerase IIα, which are essential for chromosome condensation, form an axis in the chromosome, we assume that they globally hold the nucleosome fibers around the chromosomal center (Fig. 3(a)) [2]. Locally, nucleosome fiber is folded in an irregular manner toward the chromosome center (Fig. 3(a)). Furthermore, SAXS and USAXS also revealed that there are no periodic structures in the chromatin in the interphase cells [3], suggesting that the bulk interphase chromatin also consists of irregularly folded nucleosome fibers (Fig. 3(b)).

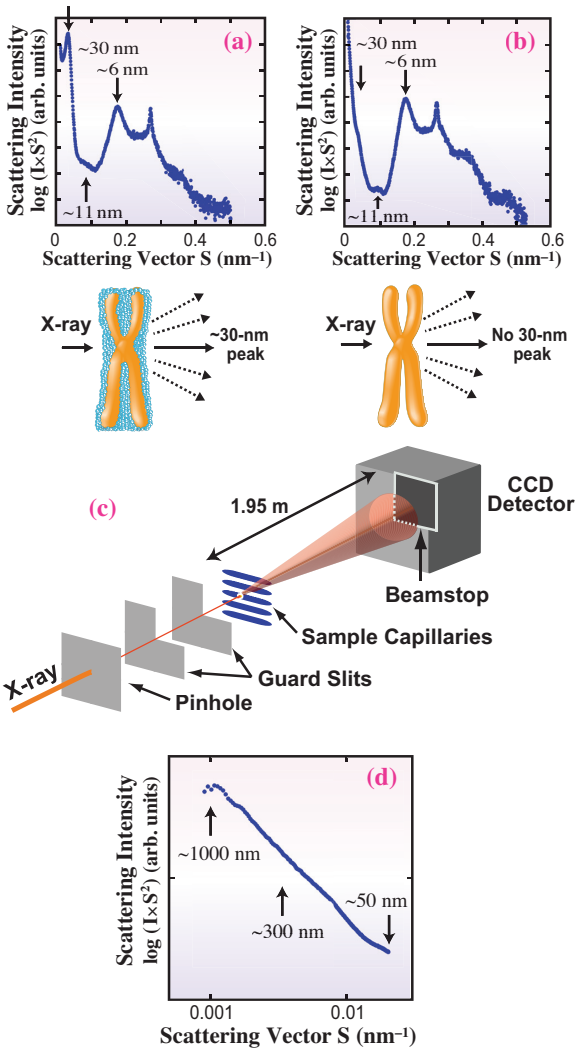

Fig. 2. **(a)** SAXS profile of mitotic chromosome fraction with ribosomes (top) and scheme (bottom), **(b)** SAXS profile without ribosomes (top) and scheme (bottom), **(c)** experimental setting for USAXS [5], and **(d)** USAXS profile of human mitotic chromosomes.

In conclusion, X-ray scattering analysis revealed that interphase chromatin and mitotic chromosomes have similar local organizations: compact, irregular folding of nucleosome fibers without the 30-nm chromatin fiber (Figs. 3(a) and 3(b)). Although the term "irregular" or "disordered" might give the impression that the organizations are likely functionally irrelevant, the irregular folding implies little physical constraint and a highly dynamic property, leading to a high degree of DNA accessibility. The irregular organization may thus have several advantages in template-directed biological processes in interphase nuclei, including RNA transcription and DNA replication and repair/recombination.

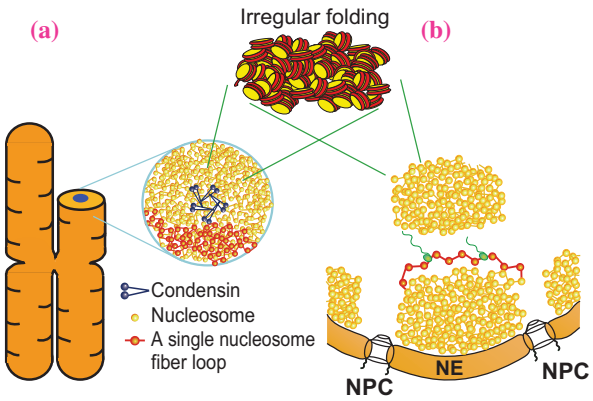

Fig. 3. **(a)** Model structure of mitotic chromosomes and **(b)** interphase chromatin. NE, nuclear envelop; NPC, nuclear pore complex.

Kazuhiro Maeshima[a,b,*], Yoshinori Nishino[b,c] and Yasumasa Joti[d]

[a] Structural Biology Center, National Institute of Genetics
[b] SPring-8/RIKEN
[c] Research Institute for Electronic Science, Hokkaido University
[d] SPring-8/JASRI

*E-mail: kmaeshim@nig.ac.jp

References

[1] M. Eltsov *et al.*: Proc. Natl. Acad. Sci. USA **105** (2008) 19732.
[2] *Y. Nishino, M. Eltsov, Y. Joti, K. Ito, H. Takata, Y. Takahashi, S. Hihara, A.S. Frangakis, N. Imamoto, T. Ishikawa, K. Maeshima: Embo J. **31** (2012) 1644.*
[3] Y. Joti *et al.*: Nucleus **3** (2012) 404.
[4] J.P. Langmore and J.R. Paulson: J. Cell Biol. **96** (1983) 1120.
[5] Y. Nishino *et al.*: Phys. Rev. Lett. **102** (2009) 18101.

Talbot-defocus multiscan tomography to study the lacuno-canalicular network in mouse bone

Osteocytes may possibly be direct involved in bone remodeling [1]. However, definite evidence has not yet been reported. The cells involved in bone remodeling consist of osteocytes for detecting mechanical stress, osteoblasts for bone formation, and osteoclasts for bone resorption. Osteocytes extend their dendrites inside the canaliculi, which run in every direction, with a diameter of approximately 0.25 μm. A dendrite of one osteocyte comes into contact with a dendrite of another osteocyte through the gap junction. The canaliculi are also opened for bone marrow, vessels, and bone surfaces. Inside the bone, three dimensionally, the osteocytes are separeted from each other by a few tens of micrometers. Osteoblasts produce the collagen fiber, osteoid, at the surface of the bone. In the resting stage, osteoblasts degenerate into thin and flat forms distributed across the bone surface. Osteoclasts are over a few tens to hundred of micrometers in size and have a bone resorption ability. The osteoclasts resorb both collagen and mineral crystals at the bone surface, digest them and transport them to the opposite side and release the degraded products outside of the cell. When a fracture occurs, bone remodeling is initiated and the bone is repaired. Conventionally, the mechanism is believed to be as follows. Osteocytes detect the fracture using canaliculi. Through the osteocyte canalicular network, a signal is transmited to the osteoblasts on the surface of the bone.

When the osteoblast receives the signal, it induces the differentiation of osteoclasts. The induced osteoclasts initiate resorption of the bone and burrow into the damaged area. On the surface of the resorbed edge, the osteoblasts align. They simultaneously form lamellar bone of approximately ≥10 μm thickness. During bone formation, a part of the osteoblast is embedded in the lamellar structure. The mechanism behind this remains unclear. The embedded osteoblasts extend dendrites to osteocytes, which exist inside the bone, and also extend to the bone surface. The embedded osteoblasts differentiate into osteocytes. The lamellar bones are stacked layer by layer, and the fractured bone is replaced by new bone. However, a recent study has reported the possibility that osteocytes are directly involved in bone remodeling [2].

To clarify this possibility, the following technical requirements are needed: (1) extract canaliculi three dimensionally. (2) detect the change of mineralization based on mineral metabolism surrounding the canaliculi, and (3) obtain a view that covers the complete osteocyte canalicular network.

The conventional methods have limitations. In most analyses, the bone specimens are decalcified using acids, the field of view is narrow, and the sensitivity of mineralization is low. In this study, we overcame these difficulties by developing a Talbot-defocus multiscan method that consists of two imaging techniques based on X-ray microscope tomography with synchrotron radiation [3]. The method employing a Talbot interferometer enables highly sensitive observations via X-ray differential phase contrast [4]. With this technique, we can estimate the degree of bone matrix mineralization. Moreover, the method using defocus absorption contrast [5] allowed the visualization of the canalicular network and the entire cortical thickness from the endosteum to the periosteum. These two methods scan the same region of the specimen sequentially.

The Talbot-defocus multiscan X-ray microscope was constructed at the undulator beamline **BL20XU**. Imaging was performed using monochromatic 9-keV X-rays (Fig. 1(a)). An X-ray Fresnel zone plate (FZP) was used as an objective lens with a focal length of 261 mm. The sample was set 273 mm upstream of the FZP in the on-focus condition. Images were recorded using a CCD camera. The image detector was placed at the image plane 5.71 m downstream of the FZP. Therefore, the X-ray microscope magnification was 20.9 times,

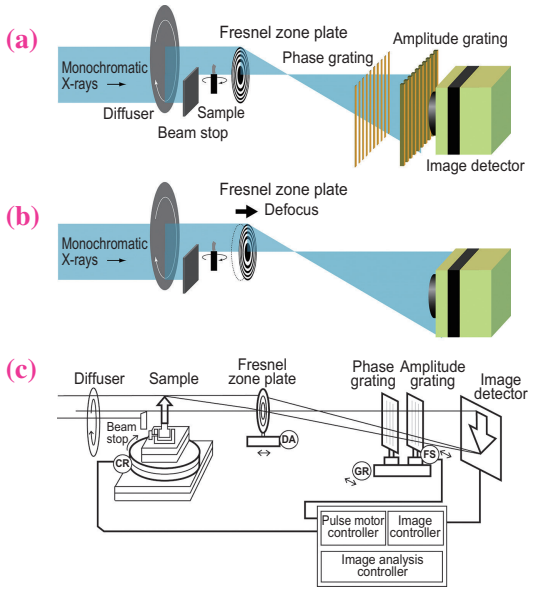

Fig. 1. Setup of multiscan X-ray microscope. **(a)** Differential phase-contrast mode in combination with a Talbot interferometer consisting of a phase grating and an amplitude grating. **(b)** Defocus absorption-contrast mode achieved by moving the Fresnel zone plate (thick arrow). **(c)** Block diagram of control system. FS, fringe scanning; GR, grating removal; DA, defocus arrangement; CR, CT scan rotation [3].

and the effective pixel size was 0.208 μm. The Talbot-defocus multiscan analysis was performed for each sample, as shown in Fig. 1(c). In the differential phase contrast method, CT scanning was performed with 500 projections over 180°. The total scan time was 6.5 h/sample.

In the defocus contrast method, the Talbot interferometer was removed from the optical axis. The FZP on the defocus stage was displaced 6 mm downstream along the optical axis in order to enhance the edge contrast of the object with Fresnel's diffraction effects. CT scan was performed with 1800 projections over 180°. The total scan time was 2.5 h/sample.

Tibias were isolated from euthanized 12–16-week-old female C57BL/6J mice (Clea, Tokyo, Japan). We applied the Talbot-defocus multiscan method to each cortical bone sample (Fig. 2).

Figure 3 shows a summary of the results. The Talbot phase tomogram revealed the degree of mineralization in the vicinity of osteocyte lacunae and canaliculi (Fig. 3(a)). The high mineralization zone observed near the periosteum and endosteum corresponds to the lamellar zone. The low mineralization zone located at the center of the cortical bone corresponds to the nonlamellar zone. The defocused setting image was reversed to demonstrate the osteocyte canalicular network (Fig. 3(b)). Canaliculi were enhanced as bright lines because of the defocus effect. In the lamellar zone, canaliculi ran parallel to each other, extending toward the bone surface (arrows). In contrast, at the middle of the cortical bone, the parallel arrangement of canaliculi was no longer apparent. Canaliculi corresponded precisely with each other in Figs. 3(a) and 3(b), as indicated by yellow arrows in Fig. 3(c). Thus, we detected the 3D structure of osteocyte canaliculi and the degree of mineralization in the vicinity of the osteocyte canalicular network in the merged image.

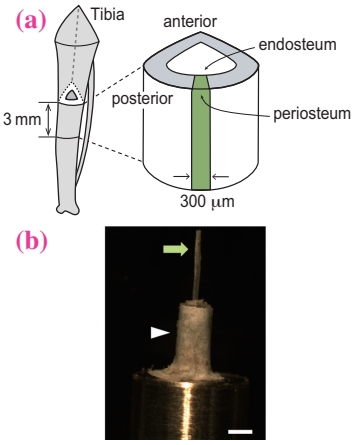

Fig. 2. Preparation of mouse bone sample. **(a)** Schematic presentation of tibia. The cortical bone sample used for imaging is represented in green. **(b)** The sample (green arrow)was attached to the holder using double-sided adhesive tape (arrowhead). Scale bar, 1 mm [3].

To detect the canaliculus, we employed a defocus absorption-contrast method to enhance the edge structure. Although the diameter of the canaliculus cannot be determined by this method, the location of abundant canaliculi was mapped as distinct lines in the tomogram. The Talbot phase tomogram revealed the distribution of mineralization, and combining the two tomograms allowed us to understand changes in mineralization in regions surrounding the osteocyte canalicular network. The spatial changes in mineralization suggest that osteocytes directly participate in mineral metabolism through the osteocyte canalicular network.

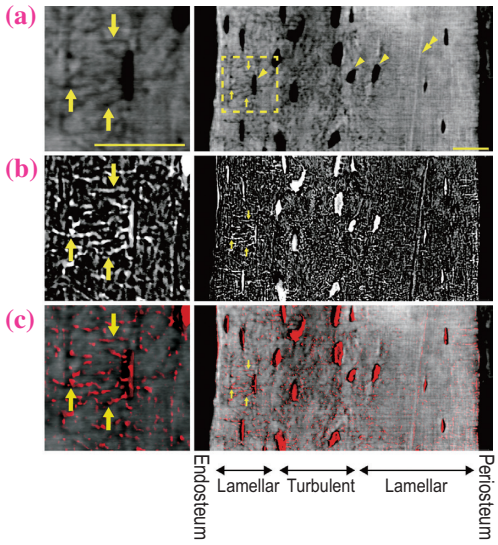

Fig. 3. Reconstructed tomograms. **(a)** Phase tomogram, in which gray scale indicates degree of mineralization (white, high; dark, low). Arrows, osteocyte canaliculi; Arrowheads, osteocyte lacunae; Double arrowhead, cement line. **(b)** Tomogram with defocus edge enhancement. The outer edges of the lacunae and canaliculi are enhanced. Note that black and white are reversed. **(c)** Combined image of (a) and (b). The defocus image is pseudocolored red. Scale bars, 25 μm. The dotted rectangle in (a-c) is magnified in the left image [3].

Nobuhito Nango[a,*], Koichi Matsuo[b] and Atsushi Momose[c]

[a] Ratoc System Engineering Co., Ltd.
[b] School of Medicine, Keio University
[c] Institute of Multidisciplinary Research for Materials, Advanced Tohoku University

*E-mail: nango@ratoc.co.jp

References

[1] L.F. Bonewald: J. Bone Miner. Res. **26** (2011) 229.
[2] T. Nakashima *et al.*: Nat. Med. **17** (2011)1231.
[3] *N. Nango, S. Kubota, A. Tkeuchi, Y. Suzuki, W. Yashiro, A. Momose and K. Matsuo: Biomed. Opt. Express* ***4*** *(2013) 917.*
[4] Y. Takeda *et al.*: Appl. Phys. Express **1** (2008) 117002.
[5] A. Snigirev *et al.*: Rev. Sci. Instrum. **66** (1995) 5486.

NRVS definition of the non-heme $Fe^{IV}=O$ intermediate in a halogenase and its control of reactivity

Mononuclear non-heme iron (NHFe) enzymes catalyze a wide array of biologically-relevant reactions, including H-atom abstraction, hydroxylation, halogenation, desaturation, and aromatic ring cleavage. They are important in neurotransmitter, antibiotic, and natural product biosynthesis, bioremediation, hypoxic regulation, and DNA cleavage in anticancer activity [1]. An α-ketoglutarate (αKG) dependent NHFe enzyme, syringomycin halogenase (SyrB2), which has an active site with 2-histidine 1-halide (Br^- or Cl^-) facial triad ligation rather than the more common 2-histidine 1-carboxylate facial triad found in most of NHFe enzymes, is involved in the biosynthesis of the phytotoxin syringomycin E. SyrB2 catalyzes chlorination of L-threonine (L-Thr) through a key, highly reactive, chloroferryl (Cl-Fe^{IV}=O) intermediate that activates the unreactive aliphatic C-H bond. For the non-native substrate L-norvaline (L-Nva) this enzyme was found to hydroxylate rather than halogenate (Fig. 1) [2]. Therefore, understanding the nature of this Fe^{IV}=O intermediate and its reaction mechanism for halogenation *versus* hydroxylation is key in the development of efficient catalysts for a range of important chemistries.

The first nuclear resonance vibrational spectroscopy (NRVS) study for an Fe^{IV}=O intermediate in a non-heme Fe enzyme is reported in Ref. [3]. The combination of NRVS coupled to density functional theory (DFT) calculations was applied in order to elucidate the geometric structure of the Fe^{IV}=O intermediate in SyrB2 and determine the factors that govern its reactivity and selectivity. NRVS is a technique that probes the vibrational sidebands of the 14.4 keV ^{57}Fe Mössbauer transition using third-generation synchrotron radiation. It is selective only for vibrations involving iron displacement, making it an ideal tool for studying the vibrational modes of a biological NHFe enzyme active site.

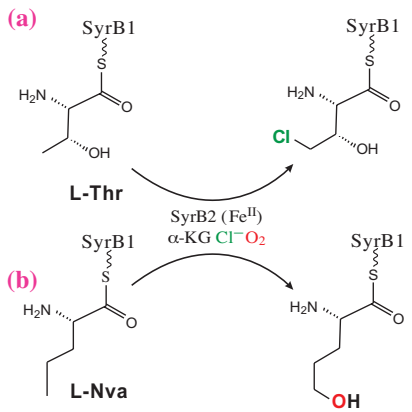

Fig. 1. SyrB2 catalyzes both chlorination of the native substrate L-Thr **(a)** and hydroxylation of a non-native substrate L-Nva **(b)**. [2]

The SyrB2 Fe^{IV}=O intermediate was generated and trapped with both Br^- and Cl^- ligated to the Fe (for a mass perturbation to aid in the assignment of the NRVS data). This intermediate could be trapped at the necessary purity and concentration by using a slow non-native substrate (L-cyclopropylglycine [L-Cpg]) attached to the non-native carrier protein CytC2. NRVS data for both samples were collected at beamline **BL09XU** at SPring-8 (as well as beamline 3-ID-D at APS). The partial vibrational density-of-states spectra for both halide bound forms of the intermediate are shown in Fig. 2(a) [3]. Both spectra show three peaks, with a shift in intensity from the higher energy modes to the lower energy modes when Cl^- is replaced by Br^-.

NRVS data on structurally-defined model complexes were used to calibrate DFT calculations to determine the computational method that best reproduces experiment. This experimentally-calibrated DFT method was then applied to possible Cpg-bound structures of the intermediate (with substrate positioning taken from Ref. [4]). It was found that only a 5-coordinate, trigonal bipyramidal (TBP) geometry, with the Fe=O oriented along the ~C_3 axis (Fig. 2(c)), reproduced the 3 peak pattern and the Cl^- to Br^- intensity shift (a mass effect, but one that shifts Fe motion into lower energy modes).

We then used the O_2 activation reaction coordinate calculation we developed for αKG-dependent NHFe enzymes in Ref. [5] to define the structure of the Fe^{IV}=O intermediate generated with the native substrate L-Thr bound. This had a similar structure to that of the Cpg-bound intermediate defined above (TBP geometry) with the Fe-oxo vector oriented perpendicular to the C-H bond of the substrate. The NHFe^{IV}=O enzyme intermediates have an S=2 ground state, and we have shown that an S=2 Fe^{IV}=O species has two frontier molecular orbitals (FMOs; low-lying unoccupied orbitals with significant oxo character) available for reactivity: a σ-FMO oriented along the Fe-O bond and a π-FMO perpendicular to the bond. The perpendicular orientation of the Fe=O vector relative to the H-substrate bond requires that the π-FMO is active for H-atom abstraction. Interacting with the π-FMO, the substrate H-atom is able to be transferred to the oxo group with a barrier consistent

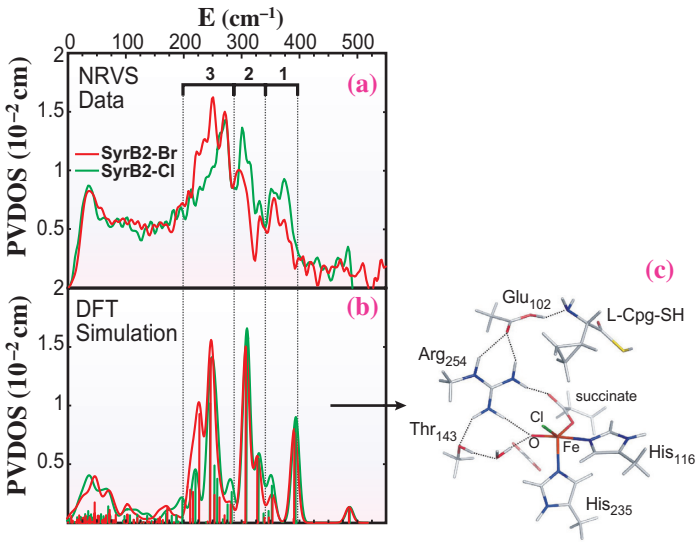

Fig. 2. NRVS data **(a)** and DFT simulations **(b)** for the SyrB2-Cl and SyrB2-Br intermediates. **(c)** DFT-derived structure of the SyrB2-Cl intermediate. [3]

with the experimental value (Fig. 3) [3]. The resulting Cl-Fe^{III}-OH species has the OH^- positioned away from the substrate carbon radical but the chloride is well-oriented towards the substrate radical for Cl• rebound and halogenation. Employing the same reaction coordinate as above with the alternative substrate L-Nva can lead to a H-bonding interaction with the O_2 intermediate along the reaction coordinate. This again results in a TBP intermediate but with its Fe=O vector oriented toward the substrate C-H bond.

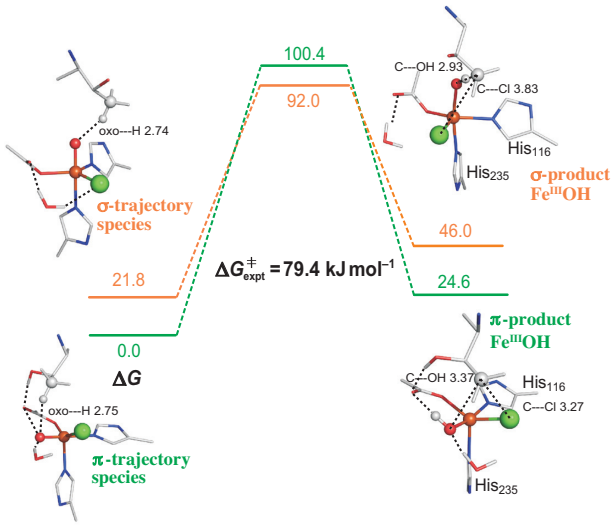

Fig. 3. Computational evaluation of the SyrB2 H-atom abstraction reaction coordinates for the π-trajectory (green text and energy levels) and the σ-trajectory (orange text and energy levels). Reactant energies are on the left, transition state energies are in the center, and product energies are on the right. The π-trajectory has a higher barrier than the σ-trajectory, consistent with experiment [2], with the π product well-oriented for halogenation while the σ product is oriented for rebound hydroxylation. [3]

This performs an H-atom abstraction using the σ-FMO of the Fe^{IV}=O that is oriented along the Fe-O bond (Fig. 3). This calculated reactivity was found to have a lower barrier than the π-pathway reactivity, consistent with experiment. For the σ attack, the resultant Fe^{III}-OH species has its OH^- group, rather than its Cl^-, aligned toward the substrate radical, thus favoring OH• over Cl• rebound, consistent with the observed hydroxylation reactivity for L-Nva (Fig. 1).

Thus, our combined NRVS and DFT methodology allowed the first elucidation of the structure of an Fe^{IV}=O intermediate in a NHFe enzyme and provided insight into the orientation dependence of the FMOs that govern halogenation *versus* hydroxylation reactivity in this class of enzymes.

E. I. Solomon*, M. Srnec, S. D. Wong, K. D. Sutherlin

Department of Chemistry, Stanford University, USA

*E-mail: edward.solomon@stanford.edu

References

[1] E.I. Solomon *et al.*: Acc. Chem. Res. **46** (2013) 2725.
[2] M.L. Matthews *et al.*: Proc. Nat. Acad. Sci. USA **106** (2009) 17723.
[3] *S.D. Wong, M. Srnec, M.L. Matthews, L.V. Liu, Y. Kwak, K. Park, C.B. Bell III, E.E. Alp, J. Zhao, Y. Yoda, S. Kitao, M. Seto, C. Krebs, J.M. Bollinger Jr and E.I. Solomon: Nature* ***499*** *(2013) 320.*
[4] T. Borowski *et al.*: J. Am. Chem. Soc. **132** (2013) 12887.
[5] A.R. Diebold *et al.*: J. Am. Chem. Soc. **133** (2011) 18148.

Materials Science :

"What is not fully understood is not possessed."
by Johann Wolfgang von Goethe

To control the properties/functions of a material, visualization of key structural characteristics is crucial. In 2013, outstanding research unveiled structures related to phase changes (by Yamada *et al.*), superconductivity (by Fujihisa *et al.*), antiferroelectricity (by Vakhrushev *et al.*), chirality (by Ohsumi *et al.*), proton conductivity (by Kitagawa *et al.*), and drug delivery (by Sakurai *et al.*).

Controlling the phase of matter is essential approach to create novel properties/functions in materials science. Phase change (PC) materials are widely used as optical storage media, and have been intensively studied for larger capacities and higher recording rates. Based on the in situ micro-diffraction technique, Yamada *et al.* successfully revealed the rapid crystallization of $Ge_{10}Sb_{90}$ nanodots with a 50-nm diameter, which have potential for next-generation optical storage media. The appearance of a superconducting phase in an element has yet to be demonstrated. Fujihisa *et al.* investigated X-ray diffraction under a high pressure of 241 GPa for phase VII calcium, which shows the highest T_c among all the elements (29 K at 216 GPa), and found a complex host-guest structure with two kinds of guest Ca chains.

Structure

Symmetry breaking is one way to create functions. An intriguing antiferroelectric transition of $PbZrO_3$ has been suggested to occur by an antiparallel shift of lead ions with the tilt of an oxygen octahedron, but its mechanism remains controversial. Vakhrushev *et al.* found that the phase transition originates from flexoelectric coupling between the transverse acoustic (TA) and transverse optical (TO) modes by means of high-resolution inelastic scattering measurements. Chirality, which is a typical example of symmetry breaking, plays an important role in biological activity, optical properties etc. However, identification and control of chiral-domains in crystals are quite difficult. Ohsumi *et al.* successfully visualized the three-dimensional distribution of the chiral domain in a racemic mixed crystal of $CsCuCl_3$ by scanning scattering measurements using circularly polarized X-rays.

In many fields, self-assembly is common for sophisticated structure/function control. Metal-organic frameworks (MOFs), whose structure can be precisely controlled by chemical design, have offered a wide range of applications, such as gas-sorption, catalytic reaction and proton conductivity. Kitagawa *et al.* found an unusually high proton-conductivity on the surface of a highly oriented MOF nanosheet, whose structure can be characterized only by high brilliance synchrotron X-ray diffraction. To develop a drug delivery system (DDS), the design of complexes for drug and delivery carriers and characterization of these complexes are quite important. Sakurai *et al.* fabricated self-assembled DDS nanoparticles, and successfully constructed a structural model based on the results of anomalous small-angle scattering (ASAXS) and light scattering.

All the highlighted research papers in "Materials Science I: Structure" in 2013 deal with key structural characterizations for novel properties and functions. This trend suggests the importance of synergic development of synthesis/growth of matter and characterization using synchrotron radiation to create new functions.

Akihiko Fujiwara

Laser pump and synchrotron radiation probe microdiffraction of $Ge_{10}Sb_{90}$ phase-change nanometer-sized dots

Digital versatile discs (DVDs) and Blu-ray discs are two of the most convenient optical storage devices for large amounts of information such as that in videos and digital photographs. These storage devices were realized owing to the extensive efforts and developments that have been made in the progress of phase change (PC) technologies. Reportedly, practical PC material films complete the reversible structure changes with 20 ns laser irradiation. However, the continuous development of PC devices is still a major concern: the aim is to realize a new class of storage devices with a large capacity and a high recording rate corresponding to the huge amount of digital data explosively increasing yearly. Among many candidates, the combination of PC nanometer-sized dots (nanodots, hereafter) and near-field optics has noticeably high potential (ideally more than 100 times larger capacity), since it may overcome the issues regarding the optical diffraction limit. One essential point to note here is whether the crystallization speed, which limits the recording rate, will be maintained for the nanodots.

To examine this point, it is crucial to precisely observe the crystallization process of the nanodot materials in real time. We previously developed a time-resolved X-ray pinpoint measurement system to observe the structural changes of PC materials on a nanosecond time scale using synchrotron radiation (SR) at beamline **BL40XU** [1,2]. The system coupled with an *in situ* optical reflectivity monitor demonstrated a strong correlation between crystal growth and optical reflectivity [1]. Using this system, we successfully observed the crystallization processes of some PC material films with a rather large thickness of 300 nm on a SiO_2 glass substrate. Nevertheless, doubt remained as to whether the observed crystallization behavior would be the same as that of a much thinner PC material film in real recording devices or that of future nanometer-sized dot materials, where the diffraction intensity will be lower and the background noise will increase owing to additional layers, e.g., a metal layer beneath the PC material layer. We therefore developed a new experimental system for laser-pump and SR-probe microdiffraction (Fig. 1) [3] by combining (i) a pump laser system (pulse width: 300 ps; repetition rate: 1 kHz), (ii) a highly brilliant focused microbeam with peak-energy width ($\Delta E/E \sim 2\%$) accomplished by focusing helical undulator radiation without monochromatization, and (iii) a precise sample disc rotation stage with a position feedback system for repetitive measurements. We then applied the system to observe the laser-induced structural changes of 50-nm-class $Ge_{10}Sb_{90}$ nanodots embedded in a thermally managed multilayered structure (Fig. 2) [4].

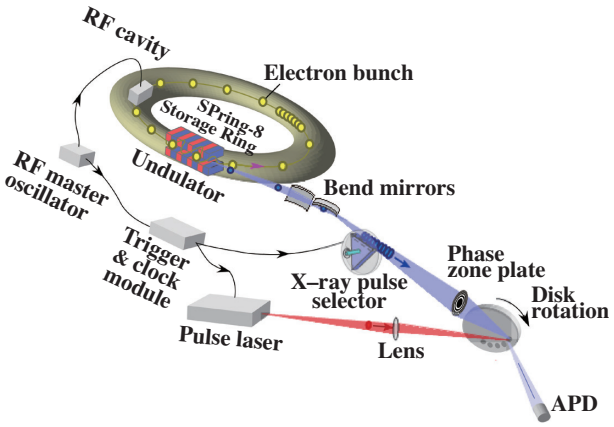

Fig. 1. Schematic of setup for laser-pump and synchrotron radiation (SR)-probe microdiffraction. The sizes of the pump laser and probe SR beams on the sample surface were optimized according to the sample shape: approximately 10×100 μm^2 (laser) and 1.98×16.6 μm^2 (SR).

The nanodot specimens were fabricated by successively sputtering multilayers on a patterned glass disc substrate with a diameter of 64 mm (HOYA Corp., Japan); on the glass substrate, UV-resin nanopillars with a diameter of 50 nm and a height of 100 nm were formed with a 100 nm pitch using the nanoimprinting technique. The layer stack was designed to imitate the structure of a commercial phase-change optical disc; it was optically optimized to exhibit a large change in reflectivity that corresponds to the amorphous-to-crystalline phase transition. Sb-based phase-change alloys, including $Ge_{10}Sb_{90}$, were characterized by growth-dominant crystallization processes owing to their relatively low nucleation rates but high growth rates [5]. To overcome the low nucleation rates, pure Sb layers were inserted as seed layers, which were crystallized during or immediately after deposition and serve as a precursor for the $Ge_{10}Sb_{90}$ layer. A silver layer with a thickness of 40 nm was used to enhance optical absorption in the $Ge_{10}Sb_{90}$ layer and also to protect the resin pillars from thermal damage. The multilayers were deposited almost exclusively on top of the nanopillars to successfully form nanodot recording elements.

Because the size of the SR probe beam was large (approximately 1.98 × 16.6 μm^2) compared with that of the nanodots (φ50 nm for each), we simultaneously observed diffractions from approximately 1200 to 1300 nanodots with one laser shot. Furthermore, since the diffraction intensity from one shot was very low, we compiled cumulative diffraction data by changing the measuring position on the sample for every shot.

Figure 3 shows the results of time-resolved diffraction intensity measurements of the 012$_H$ peak, the most intense peak, of crystalline $Ge_{10}Sb_{90}$ with rhombohedral symmetry *R*-3*m* resembling pure Sb. As seen in the figure, we could successfully detect the structural change from an amorphous state to a crystalline state as the variation in diffraction intensity on the nanosecond scale. All diffraction intensity profiles began to increase with a delay of approximately 70–100 ns and saturated at approximately 150 ns after laser pumping for 300 ps. By comparing curves (a) to (d), it is seen that the time delay before the start of crystallization becomes slightly shorter as the laser power decreases from (a) to (d). This indicates that setting the pumping laser power to slightly above the threshold of crystallization is effective for minimizing the crystallization time.

In conclusion, we successfully revealed the rapid crystallization of 50-nm-class $Ge_{10}Sb_{90}$ nanodots embedded in a multilayered structure in response to a short laser excitation of not more than 300 ps. This indicates the high potential of the nanodot material for use in next-generation ideal 'green data storage' systems with ultrahigh density and high recording speed.

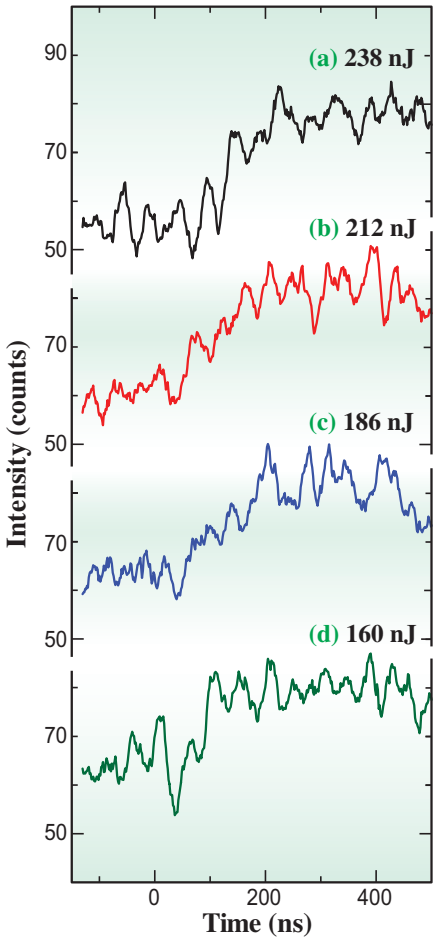

Fig. 3. Experimental results of the time-resolved diffraction intensity due to crystallization of the $Ge_{10}Sb_{90}$ nanodots with various pump powers of **(a)** 238, **(b)** 212, **(c)** 186, and **(d)** 160 nJ. Each curve was obtained by accumulating data from approximately 100,000 shots and plotted by averaging ten adjacent data, meaning that the time resolution was 16 ns, to smooth the curves.

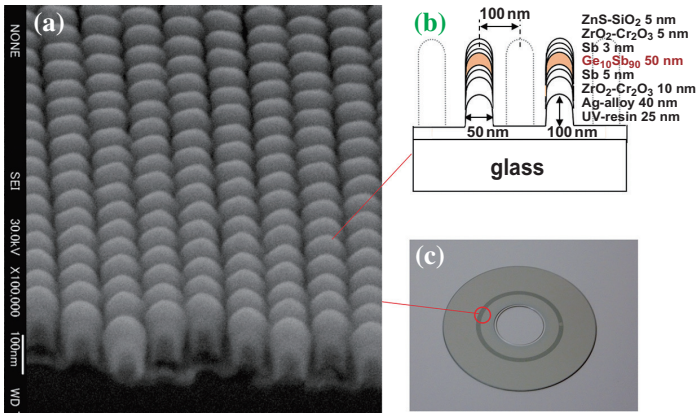

Fig. 2. SEM photograph **(a)** and schematic of cross section **(b)** of nanodot specimens. Approximately 2.4 × 10^{10} nanodots were formed in a zone (φ33.0–35.4 mm) on a sample disc **(c)**.

Noboru Yamada[a,*], Toshiyuki Matsunaga[b] and Shigeru Kimura[c]

[a] Dept. Materials Science and Engineering, Kyoto University
[b] R&D Division, Panasonic Corporation
[c] SPring-8/JASRI

*E-mail: yamada.noboru.4z@kyoto-u.ac.jp

References

[1] Y. Fukuyama *et al.*: Appl. Phys. Express **1** (2008) 045001.
[2] Y. Tanaka *et al.*: Jpn. J. Appl. Phys. **48** (2009) 03A001.
[3] *N. Yasuda, Y. Fukuyama, S. Kimura, K. Ito, Y. Tanaka, H. Osawa, T. Matsunaga, R. Kojima, K. Hisada, A. Tsuchino, M. Birukawa, N. Yamada, K. Sekiguchi, K. Fujiie, O. Kawakubo and M. Takata: Rev. Sci. Instrum.* ***84*** *(2013) 063902.*
[4] *N. Yamada, R. Kojima, K. Hisada, T. Mihara, A. Tsuchino, N. Fujinoki, M. Birukawa, T. Matsunaga, N. Yasuda, Y. Fukuyama, K. Ito, Y. Tanaka, S. Kimura and M. Takata: Adv. Opt. Mat.* ***1*** *(2013) 820.*
[5] L. van Pieterson *et al.*: J. Appl. Phys. **97** (2005) 083520.

Complex host-guest structure of calcium phase VII at high pressure

Thirty elements are known to show superconductivity at atmospheric pressure. Another 23 elements are currently known to show superconductivity at high pressures. The superconductivity transition temperature (T_c) increases with the pressure in some of these elements. Among these elements, Li, Ca, Y, and Sc have high T_c values near 20 K, and their highest T_c values are observed at high pressures. The highest T_c of the alkaline earth elements Sr and Ba are observed when these elements have a complex host-guest structure. The relation between the crystal structure and T_c is very interesting. As shown in Fig. 1, six crystalline phases of calcium, phases I (fcc), II (bcc), III (simple cubic, sc), IV ($P4_12_12$), V (*Cmca*), and VI (*Pnma*), have been found to exist at room temperature at ambient pressure and high pressures of 20 GPa, 32 GPa, 119 GPa, 143 GPa, and 158 GPa, respectively [1]. Superconductivity for Ca was first reported at about 44 GPa and 2 K. The T_c of Ca has been predicted to increase with the occupancy of *d*-electrons and would continue to occur with successive phase transitions. The T_c of phases IV and V increased with pressure and reached 25 K at 161 GPa and exceeded the previous highest recorded values of 20 K for Li at 48 GPa, 17.2 K for V at 120 GPa, and 19.5 K for Y at 115 GPa.

Recently, Sakata *et al*. have performed an X-ray powder diffraction experiment and discovered a new phase VII at around 210 GPa [2]. They measured the electrical resistance at low temperatures and found that phase VII has the highest T_c among all the elements at 29 K and 216 GPa. Its crystal was thought to have a typical host-guest structure as predicted by some theoretical studies [3,4]; however, the structure did not provide good quality upon Rietveld refinement. The purpose of this study is to clarify the fascinating structure of phase VII using the data obtained by synchrotron X-ray diffraction and density functional theory (DFT) calculation, and then to compare it with the previous host-guest structure to understand the relation between the crystal structure and its highest T_c.

Powder diffraction patterns of calcium samples up to 241 GPa were measured by using a diamond-anvil high-pressure cell (DAC) with a beveled diamond anvil of 100 μm inner diameter and 300 μm outer diameter and an imaging plate detector (IP) at beamline **BL10XU**. The X-ray wavelength was 0.41231 Å. The X-ray beams were collimated using a 10-μm-diameter pinhole. The typical exposure time was 10 min. A one-dimensional powder pattern was obtained by averaging all the intensities along the Debye-Scherrer rings recorded on the IP. Peak indexing and Rietveld analysis were performed with the Materials Studio (MS) software of Accelrys, Inc. DFT calculations for structural optimizations and enthalpies were carried out using the MS CASTEP program.

Structure analysis was performed on the pattern obtained at 241 GPa. Some tetragonal candidates were obtained by indexing 14 strong peaks from this pattern. However, none of these candidates were found to be appropriate since they could not fit the observed pattern. Instead of these candidates, the theoretically predicted model of *I*4/*mcm*-32 [3,4] with a=5.51 Å and c=9.18 Å shown in Fig. 2 fitted the observed strong peaks; however, some weak peaks remained unfitted. We attempted to fit these peaks with the *I*4/*mcm*(00γ) model by adjusting the incommensurability γ using Jana2006 software, but were unable to fit them. We tried to expand the cell size of the *I*4/*mcm*-32 model in the *ab*-plane and created tetragonal supercells. Finally, all diffraction peaks were fitted successfully in a 2×2×1 model by optimizing the *z*-coordinates of the guest chains. The converged structure has two *z*-coordinates as shown in Fig. 3. Since this model, which is assumed to be

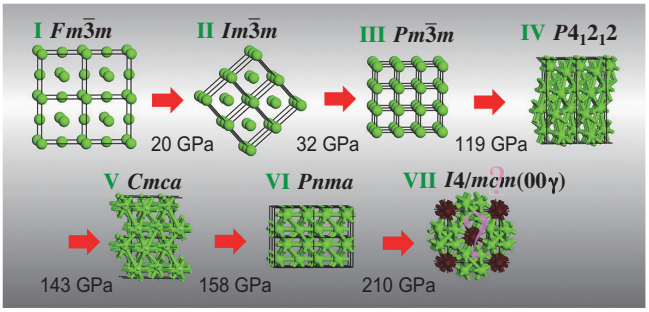

Fig. 1. Successive phase transitions of calcium under pressure [1]. The question marks in the crystal structure of phase VII [2] indicate that its structure is theoretically predicted but not established yet.

commensurate (host:guest=4:3), could fit all the peak positions perfectly, the host-guest ratio might be truly commensurate. The incommensurability γ fitted by using Jana2006 software converged to 1.333 and could also be regarded as 4/3. This supercell can be assigned to the 3-dimensional space group $P4_2/ncm$. The model containing 128 atoms is called $P4_2/ncm$-128. Its atomic coordinates for all 12 sites were refined by Rietveld analysis and DFT calculation. The refined coordinates closely matched and the structure was confirmed to be a valid energy minimum. The calculated stress and its anisotropy ratio became $\sigma_{xx} = \sigma_{yy} = 212.8$ GPa, $\sigma_{zz} = 211.4$ GPa, and $\sigma_{xx}/\sigma_{zz} = 1.006$. These values matched the experimental pressure of 241 GPa very well. Our phonon calculation for the $P4_2/ncm$-128 model confirmed the absence of an imaginary frequency.

Although all guest chains of the previous model aligned similarly, as shown at the bottom of Fig. 2, there are two guest chains that can be distinguished by their *z*-coordinates as shown by brown and blue atoms in Fig. 3. We can conclude that the appearance of the different chains is the origin of the 2×2×1 supercell. It would be very difficult to predict the $P4_2/ncm$-128 model only by theoretical calculation since the difference in enthalpy from that of the $I4/mcm$-32 model is too small and the number of atoms of 128 is too large for *ab initio* structure prediction. The volume per atom decreased by 22% from phase I at 1 bar to phase VII at 241 GPa. The corresponding first nearest interatomic distance decreased from 3.92 Å to 2.10 Å.

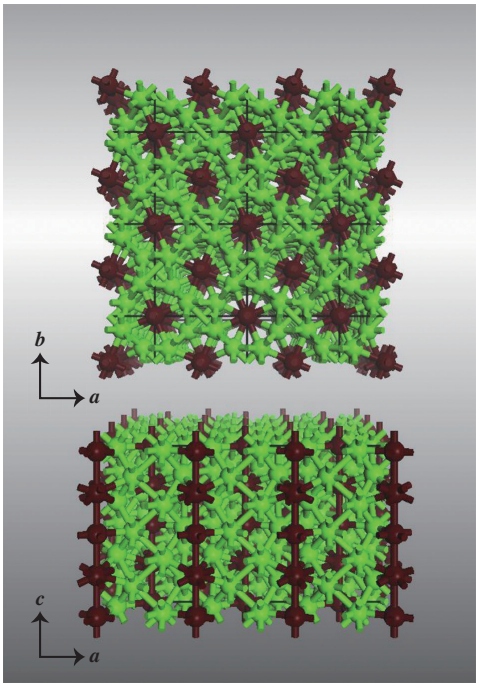

Fig. 2. Known and theoretically predicted host-guest structures [3,4] such as that observed in potassium phase III. The top and bottom figures show different views of the same structure. All spheres indicate calcium atoms; the atoms forming the host structure are in green and those forming the guest structures are in brown.

Our present work [5] is expected to stimulate theoretical investigations such that the T_c value of calcium phase VII may be calculated using this novel $P4_2/ncm$-128 model. Calcium, while being a single element, was found to show a new complex host-guest structure. The results of this study will lead to the design of new high-temperature superconducting materials.

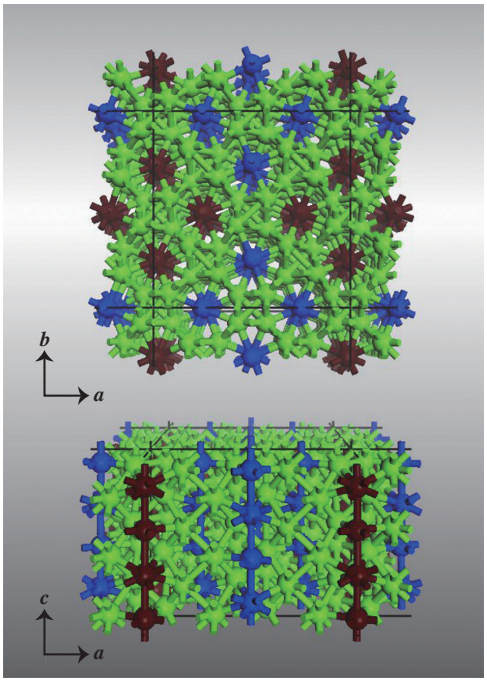

Fig. 3. Crystal structure of phase VII calcium at 241 GPa analyzed in this study [5]. All spheres indicate calcium atoms; the atoms forming the host structure are in green and those forming the guest structures are in blue and brown.

Hiroshi Fujihisa[a,*], Yuki Nakamoto[b] and Masafumi Sakata[b]

[a] National Institute of Advanced Industrial Science and Technology
[b] Center for Quantum Science and Technology under Extreme Conditions, Osaka University

*E-mail: hiroshi.fujihisa@aist.go.jp

References

[1] Y. Nakamoto *et al.*: Phys. Rev. B **81** (2010) 140106(R).
[2] M. Sakata *et al.*: Phys. Rev. B **83** (2011) 220512(R).
[3] S. Arapan *et al.*: Proc. Natl. Acad. Sci. USA **105** (2008) 20627.
[4] T. Ishikawa *et al.*: Phys. Rev. B **81** (2010) 092104.
[5] *H. Fujihisa, Y. Nakamoto, M. Sakata, K. Shimizu, T. Matsuoka, Y. Ohishi, H. Yamawaki, S. Takeya and Y. Gotoh: Phys. Rev. Lett.* ***110*** *(2013) 235501.*

The origin of antiferroelectricity in $PbZrO_3$

Lead zirconate, $PbZrO_3$ (PZ) is an intriguing antiferroelectric material, and has been extensively studied [1]. The properties of this crystal are determined by the strong competition between ferroelectric and antiferroelectric ordering. The structure of the low-temperature phase is described by a combination of the order parameters that correspond to R (½ ½ ½) and Σ (¼ ¼ 0) points. In Ref. 2, it was demonstrated that phase transition in PZ can be considered as a sequence of the transitions related first to the condensation of R-component and then to that of the Σ-component. Structural analysis demonstrated that antiferroelectricity in PZ is described by antiparallel shifts of lead ions accompanied by oxygen octahedral tilts, suggesting condensation of three soft modes at the same time. However, such a situation is very unlikely, and is inconsistent with the idea of a single irreducible representation describing the structural change.

Using beamline **BL35XU**, we investigated the dispersion of the low-frequency phonon modes to gain understanding of this phase transition. Previous phonon work [3] had only looked at phonons at q=0. Combining our phonon dispersion measurements with diffuse scattering maps, we were able to propose a model of the phase transition in this material that is driven by flexoelectric coupling [4].

The phonon spectra are extremely anisotropic. In the case of the excitations propagating in the [1 1 0] direction and polarized in the [1 $\bar{1}$ 0] direction (in-plane polarization), extremely low-lying transverse acoustical (TA) phonon resonances were observed together with a broad central peak and weak transverse optical (TO) phonon resonances (Fig. 1). The central peak can be identified with the central mode reported by Ostapchuk *et al.* [3]. The excitations propagating in the [1 1 0] direction and polarized in the [0 0 1] direction (out-of-plane polarization), are well resolved (Fig. 1(d)). Below the transition temperature, the frequency of the TA mode jumped up and the central peak practically disappeared (Fig. 1(b)).

Figure 2(a) shows the phonon dispersion surface for the TA phonons propagating and polarized in the (1 1 0) plane. A deep valley for q along the (1 1 0) direction is observed. Phonon dispersion curves along this direction demonstrate anomalously low frequencies and pronounced softening upon approaching the transition temperature. We found no features of the phonon frequencies or damping constant around the Σ-point, as confirmed by the diffuse scattering measurements [4]. In Fig. 3, the surface plot of the central peak intensity is presented. No singularity is observed around q=(¼ ¼ 0). We also carefully measured R-point spectra, which also consisted of broadened, temperature-independent phonon resonances and a central peak demonstrating traceable temperature dependence with critical temperature of about 100 K. Thus, the R-point phonon mode or central peak cannot be considered as the relevant excitation for the phase transition at around 500 K.

We were able to describe the phonon dispersion using a model that includes flexoelectric coupling of the acoustic and the TO modes [4]. Only three adjustable parameters are needed: the isotropic and anisotropic slopes of the TO branch, and isotropic flexoelectric constant. The results of the model calculations are shown in Fig. 2(b): the TA mode frequency is strongly lowered and the temperature evolution of the TA dispersion is completely governed by the softening of the TO mode. At a certain soft mode frequency, the TA mode may lose its stability at some arbitrary q_i and transform to an incommensurate phase. Our calculations demonstrate that $PbZrO_3$ is indeed close to such a stability limit, and that the softening of the

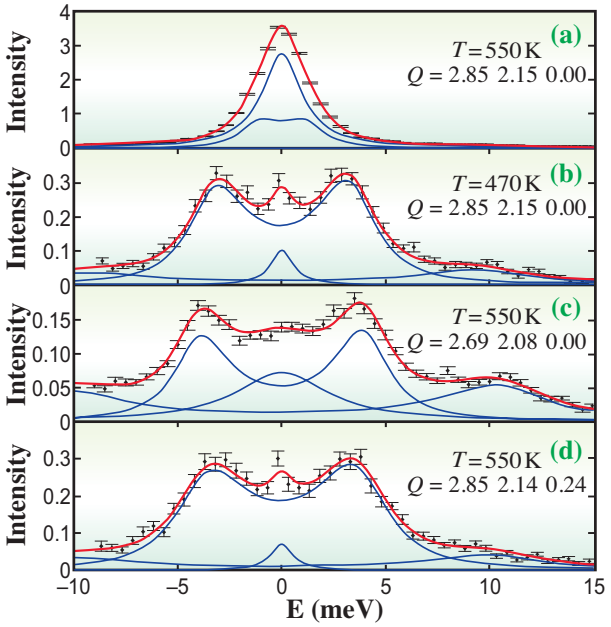

Fig. 1. Phonon resonances for Q in the (320) Brillouin zone: **(a)** q along (110) in-plane polarized above T_c; **(b)** q along (110) in-plane polarized below T_c; **(c)** in-plane polarized q tilted from (110); **(d)** q along (110) out-of-plane polarized above T_c.

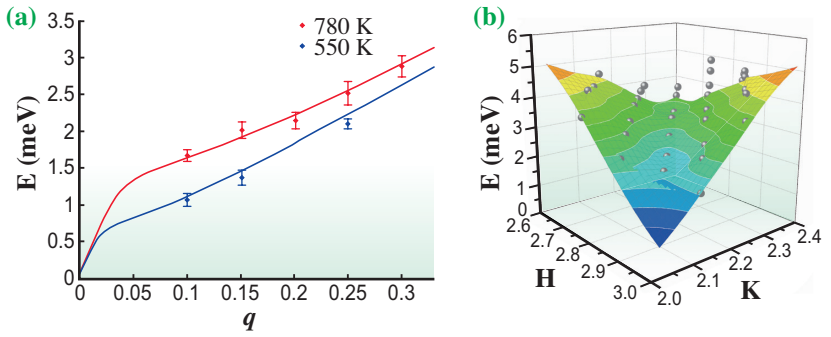

Fig. 2. **(a)** Phonon dispersion curves for in-plane polarized TA phonon branch at T=780 K and 550 K (dots: experimental data; solid lines: calculation results). **(b)** Experimental phonon dispersion surface for in-plane polarized TA phonons; gray spheres are experimental points.

TO mode is responsible for both the critical growth of the dielectric susceptibility in the paraelectric phase and the loss of the stability (softening) of the whole TA branch.

The antiferroelectric phase transition can then be considered as an incomplete incommensurate phase transition resulting from the flexoelectric coupling between the TA and TO modes. Fixing the wave vector at the commensurate Σ-point is the result of the *umklapp* term in the free energy. Formation of the R-type order parameter is triggered by the appearance of the Σ-type one and can be described in terms of the Holakovsky-type instability [5], resulting from biquadratic coupling between these two parameters [4].

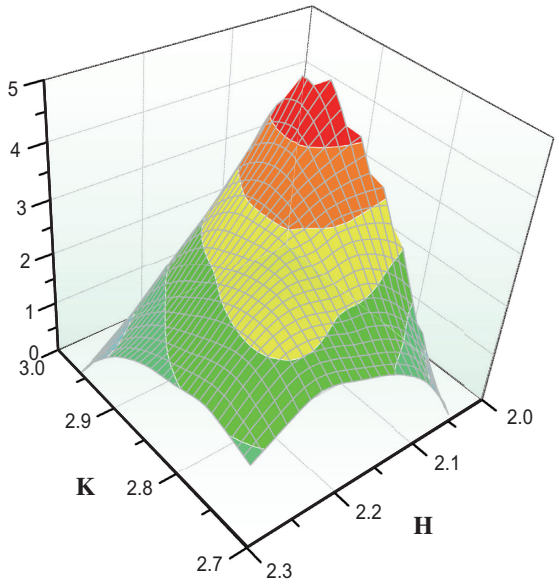

Fig. 3. Surface plot of the central peak intensity at 550 K.

Sergey Vakhrushev[a,b,*], R. Burkovsky[a,b,c] and Alfred Q. Baron[d]

[a] Ioffe Physico-Technical Institute, Russia
[b] St. Petersburg State Polytekhnical University, Russia
[c] European Synchrotron Radiation Facility, France
[d] SPring-8/RIKEN·JASRI

*E-mail: s.vakhrushev@mail.ioffe.ru

References

[1] H. Maniwa *et al.*: Phys. Rev. **83** (1951) 1078.
[2] H. Fujishita and S. Hoshino: J. Phys. Soc. Jpn. **53** (1984) 226.
[3] T. Ostapchuk *et al.*: J. Phys.: Cond Matter **13** (2001) 2677.
[4] *A.K. Tagantsev, K. Vaideeswaran, S.B. Vakhrushev, A.V. Filimonov, R.G. Burkovsky, A. Shaganov, D. Andronikova, A.I. Rudskoy, A.Q.R. Baron, H. Uchiyama, D. Chernyshov, A. Bosak, Z. Ujma, K. Roleder, A. Majchrowski, J.-H. Ko and N. Setter: Nat. Commun.* ***4*** *(2013) 2229.*
[5] J. Holakovsky: Phys. Status Solidi **56** (1973) 615.

Imaging chirality-domain morphology in racemic mixed crystal of $CsCuCl_3$

Chirality is the property of having non-superimposable mirror images such as human hands. Since molecular handedness determines biological activity, discrimination of molecular handedness is indispensable for drugs used in medicines, food additives, and so forth. Hence, the handedness-selective synthesis of molecule-based materials has been extensively studied and become a common practice. On the other hand, the chiral crystallization of non-molecular materials is attracting considerable attention as a method for obtaining potential materials for spintronics because a non-centrosymmetric electrostatic potential induces Rashba-type spin-orbit coupling or the Dzyaloshinskii-Moriya interaction. However, no universal guiding principles exist for growing a single-handed crystal consisting of achiral atomic components.

Interpretation of the chirality-domain morphology is essential for finding key factors controlling the handedness of an atomic arrangement and for establishing regulations for single-handed crystal growth. However, there is no appropriate technique for observing the chirality-domain morphology. In contrast to that observed in an aqueous solution, optical rotation also arises from crystal anisotropy (linear birefringence), which obscures the chiral effect (circular birefringence). Owing to Friedel's law, diffraction experiments are also not suitable for the discrimination of handedness in an atomic arrangement. However, the X-ray screw-axis ATS reflection (here, ATS represents the anisotropy of the tensor of susceptibility) may enable us to discriminate crystal handedness [1]. Near X-ray absorption edges, the intensity of the reflection depends on the handedness of both the atomic arrangement and the circular polarization. Thus, one can examine crystal handedness by measuring the flipping ratio and the namely, difference-over-sum ratio between reflection intensities for right- and left-handed circularly polarized incident X-rays [2]. Dark-field scanning X-ray microscopy with the screw-axis ATS reflection and a depth-profiling technique allow us to reconstruct a three-dimensional image of the chirality-domain distribution [3].

A schematic of the chirality-domain imaging experiment at beamline **BL39XU** is shown in Fig. 1. Linearly polarized X-rays from a planar undulator were converted to circularly polarized X-rays by using a diamond phase retarder. Kirkpatrick-Baez (KB) mirrors focused the circularly polarized X-ray beam to 2.7 × 2.7 μm^2 at the sample position. A cleaved (001) $CsCuCl_3$ surface was raster-scanned and the flipping ratio of the screw-axis ATS reflection $00l$ ($l = 14$) at each point was measured to construct an image of the chirality-domain distribution. $CsCuCl_3$ is a hexagonal perovskite system belonging to a chiral space group of $P6_122$ or $P6_522$ (Fig. 2) and crystallizes as a racemic mixed crystal from an aqueous solution. The obtained raster image of the flipping ratio revealed that the typical chirality-domain size was several tens of microns in the lateral direction. To realize three-dimensional imaging, we have developed the new nondestructive depth profiling technique shown below.

The penetration depth of X-rays varies with the photon energy especially near absorption edges. Figure 3(a) shows the penetration depth for the Bragg condition of the $00l$ ($l = 14$) reflection around the Cu *K*-edge. Flipping ratio maps of the same area, which are shown as top surfaces in Figs. 3(b)–3(e), were measured with X-rays having various photon energies of (b) 8.992 keV, (c) 8.987 keV, (d) 8.985 keV, and (e) 8.984 keV. Differences among them are attributed to the variation in penetration depth, from which one can determine the depth profile of handedness in an atomic arrangement. The reconstructed three-dimensional image of the

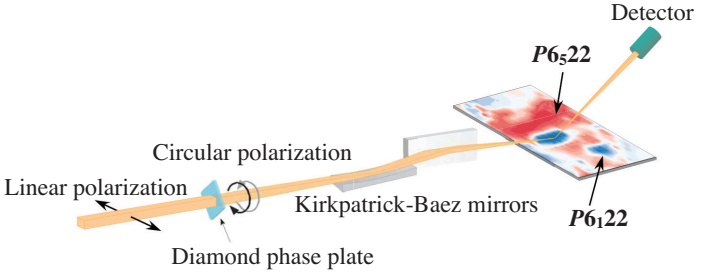

Fig. 1. Schematic of chirality-domain imaging experiment on a $CsCuCl_3$ racemic mixed crystal. An X-ray phase plate converted linear polarization to circular polarizations. KB mirrors focused a circularly polarized X-ray beam on the sample. The sample surface was raster-scanned through the beam.

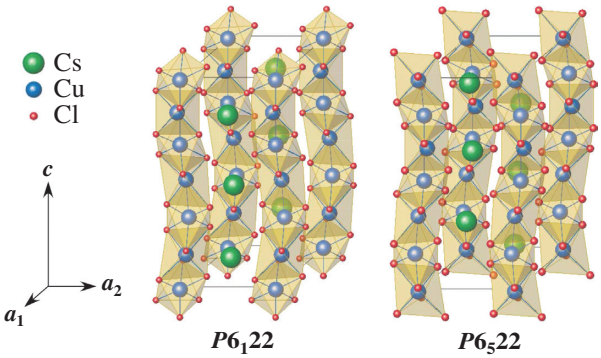

Fig. 2. Crystal structures of $CsCuCl_3$. Green, blue, and red spheres represent Cs, Cu, and Cl, respectively.

chirality-domain distribution revealed the following morphological features in $CsCuCl_3$: a chirality-domain boundary is preferentially formed parallel to the hexagonal *c*-plane; the typical domain is only a few microns thick with a size of several tens of microns in the lateral direction. The observed shallow chirality-domain shape suggests that relatively high in-plane cooperativity of the Jahn-Teller distortion of $CuCl_6$ octahedra is the predominant factor that determines the chirality-domain morphology in this material. This three-dimensional imaging technique facilitates the observation of the chirality-domain morphology and the understanding of the underlying twinning mechanisms, which will provide support to the increasing demand for improvement of the inorganic chiral crystal engineering.

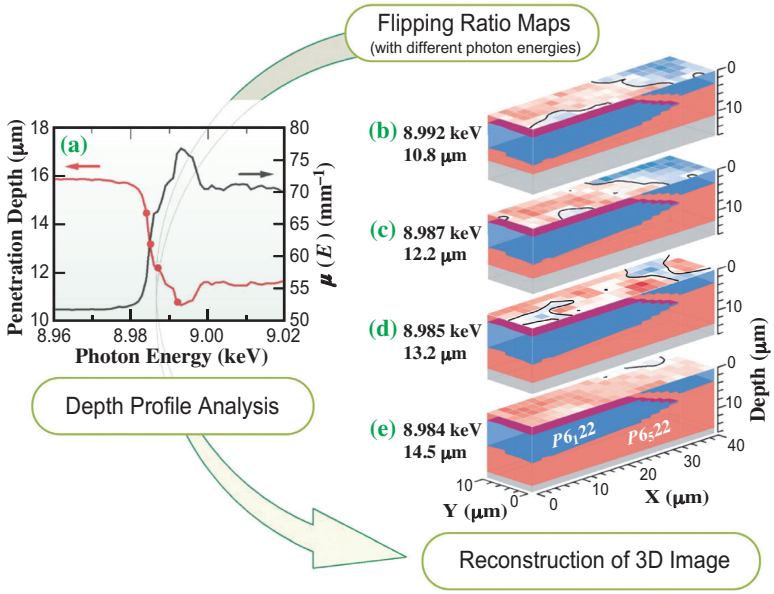

Fig. 3. Schematic illustration of three-dimensional imaging procedure of chirality-domain morphology. Raster images of the flipping ratio are measured using different photon energies. The variation in X-ray penetration depth allows us to analyze the depth profile. The chirality-domain morphology is visualized by reconstructing a three-dimensional image of the flipping ratio.

Hiroyuki Ohsumi[a,*], Yusuke Kousaka[b] and Taka-hisa Arima[a,c]

[a] SPring-8/RIKEN
[b] Department of Physics and Mathematics, Aoyama-Gakuin University
[c] Department of Advanced Materials Sciences, The University of Tokyo

*E-mail: ohsumi@spring8.or.jp

References

[1] V.E. Dmitrienko: Acta Crystallogr. Sect. A **39** (1983) 29.
[2] Y. Kousaka *et al.*: J. Phys. Soc. Jpn. **78** (2009) 123601.
[3] *H. Ohsumi, A. Tokuda, S. Takeshita, M. Takata, M. Suzuki, N. Kawamura, Y. Kousaka, J. Akimitsu and T. Arima: Angew. Chem. Int. Ed.* ***52*** *(2013) 8718.*

Clarification of proton-conducting pathway in a highly oriented crystalline metal-organic framework nanofilm

Metal-organic frameworks (MOFs), which are crystalline polymeric materials composed of metal ions and multidentate organic ligands, have provided a wide range of science-rich applications, such as those for deriving gas-sorption, catalytic, conducting, and electronic properties from their large porosity and the designability of their structures [1]. One of the challenging tasks in this research area is fabrication of porous MOFs as a thin film for the development of future important nanomaterials such as electronic and catalytic devices. At present, studies of MOF nanofilms are rare; the preparation of highly oriented crystalline MOF nanofilms is difficult, and investigations into the physical properties of MOF thin films are in their infancy [2]. Proton-conducting materials play a key role in some solid-state electrochemical devices such as batteries and fuel cells. Recently, research into the proton conductivity of MOF materials has been attracting significant attention, as MOFs offer great potential for the systematic design and modification of proton conducting properties [3]. Although some of the reported MOF materials have exhibited high proton-conductivity, some questions about proton transport still require answers. For example, in addition to the channels inside a MOF, can the surface of a MOF crystal act as an efficient pathway for protons? To answer this question, we have studied the electrical properties of a highly oriented and crystalline MOF nanofilm, because the size of the MOF crystal decreases to the nanoscale and the outer surface area of nanocrystals increases markedly.

The MOF nanofilm used for electrical measurement was constructed by a previously reported "modular assembly" method [4]. Briefly, a MOF (Cu-TCPP) nanosheet with a high aspect ratio (thickness: around 15 nm; diameter: around 400 nm) was synthesized by the reaction of $Cu(NO_3)_2$ and 5,10,15,20-tetrakis (4-carboxyphenyl)porphyrin (H_2TCPP), and then the product was deposited layer by layer onto a pre-prepared patterned Cr/Au (30/120 nm) electrode on a SiO_2 (300 nm thick)/Si wafer to form a thin film channel between electrodes (Figs. 1(a) and 1(b)). The present Cu-TCPP nanosheet has a two-dimensional (2D) layered structure, where the 2D reticulation along the *ab* plane is constructed with Cu-centered TCPP units connected by binuclear $Cu_2(COO)_4$ paddle wheels, and 3D packing is achieved along the *c*-axis as shown in Fig. 1(c). The Cu-TCPP nanofilm remains crystalline and highly oriented on the substrate. From the results of an X-ray study, the MOF nanosheets are considered to lie along the *ab* plane parallel to the SiO_2/Si substrate (Fig. 1(b)) [4].

The electrical properties of the highly oriented MOF nanofilm in this work were determined by depositing the nanofilm between two electrodes, and then performing alternating current (AC) impedance analysis with a quasi-four-probe method. The proton conductivity was estimated from Nyquist plots. The proton conductivity at 25°C at varying relative humidity (RH) is shown in Fig. 2 (inset). The nanofilm has a low conductivity of 3.2×10^{-8} S·cm^{-1} at 40% RH, which markedly increases by three orders of magnitude to 6.2×10^{-5} S·cm^{-1} at 90% RH, and then further increases to 3.9×10^{-3} S·cm^{-1} at 98% RH. It is worth noting that this value at 98% RH is high value for hydrated MOF sample and also comparable to the proton conductivity of an acid-impregnated MOF material [5].

We next analyzed the conductivity (log σ) *versus* the amount of water adsorbed on this nanosheet by water sorption measurement. As shown in Fig. 2, when RH increases from 40% to 90%, 4 mol of water is adsorbed by 1 mol of the TCPP unit, resulting in an increase in conductivity by 3.5 orders of magnitude. At this stage, the water molecule only adsorbs on the surface of the nanosheet, far from the area of multilayer adsorption or condensation at 96% RH.

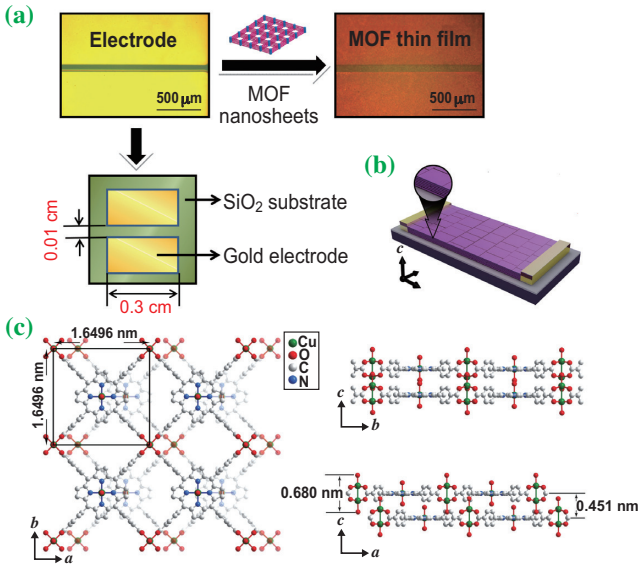

Fig. 1. **(a)** Experimental procedure of electrical measurement using "modular assembly" method. **(b)** Schematic of the Cu-TCPP nanosheet on the SiO_2 substrate, and **(c)** the modeled crystal structure of the Cu-TCPP nanofilm revealed by previous study [4].

In the RH range of 90% – 96%, the uptake of water suddenly increases to 34 H_2O/TCPP unit. At this high uptake, the conductivity reaches saturation and the conductivity increases slightly by about 1 order of magnitude. Considering that the proton conductivity strongly depends on RH and water adsorbs on the mesopores or macropores in the nanosheets, we may deduce that the hydrogen bonding network that acts as the pathway for proton transport is created by the water adsorbed, dangling coordination water, and dangling carboxyl groups of the nanosheets (Fig. 1(c)); therefore, it should be located within the mesopores or macropores, and/or on the surfaces of the nanosheets.

To clarify the proton-conducting pathway of the present Cu-TCPP nanosheet, *in situ* synchrotron X-ray diffraction (XRD) measurements under varying RH conditions were carried out at beamline **BL13XU**. Figure 3 shows synchrotron XRD patterns (λ = 1.550 Å, rt) of the Cu-TCPP nanosheet both in the horizontal (in-plane, grazing-incidence mode (GIXRD); Fig. 3(a)) and vertical (out-of-plane, $\theta-2\theta$ mode (XRD); Fig. 3(b)) directions relative to the substrate under varying RH conditions. As shown in Fig. 3, no significant changes under varying humidity were observed in both the GIXRD and XRD patterns of the nanofilm, indicating that the nanofilm remains intact at a high humidity. The constant GIXRD patterns with varying RH also exclude the possibility of a "gate-opening" effect in this 2D MOF under high humidity condition.

The results of synchrotron X-ray studies clearly indicate that the small amount of water adsorbed before 90% RH is sufficient to create an efficient pathway on the surface of the nanosheet for proton transport, exerting control over most of the change in proton conductivity. Hence, the surface of the Cu-TCPP nanosheet, which contains numerous dangling groups (Fig. 1(c)), should play a dominant role in constructing the proton pathway.

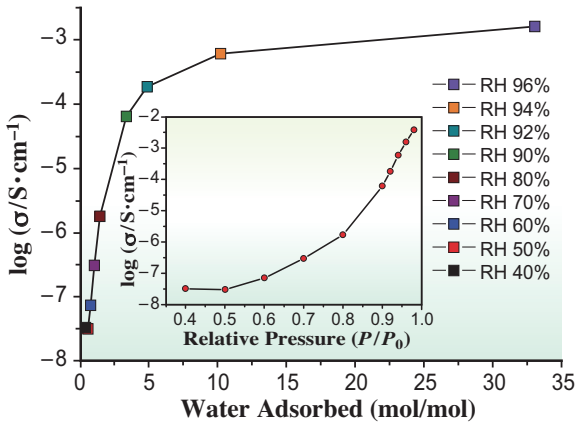

Fig. 2. Proton conductivity of the MOF nanofilm *versus* adsorbed water conditions. (Inset) Proton conductivities at various RH values.

The unusually high conductivity of this MOF thin film may arise from the numerous dangling groups on the surface of the nanosheet and the highly oriented crystalline morphology of the thin film. The size effect of the nanosheets used to fabricate the thin film should also be considered. The dimensions of the Cu-TCPP crystal are within the nanoscale; hence, there are numerous groups on the surface of the nanosheet, such as acidic coordinated waters on the Cu atom and noncoordinated carboxyl groups (Fig. 1(c)). These dangling groups can act as a Lewis acid. They have been reported to be effective proton donors and can be utilized to design MOF materials with high proton conductivity.

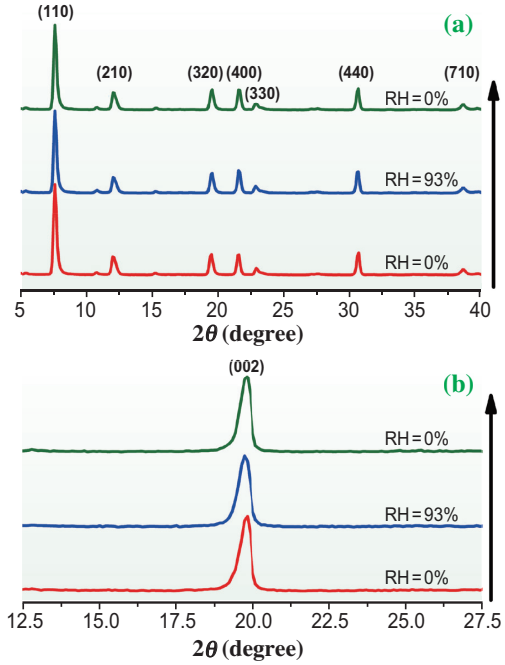

Fig. 3. Synchrotron XRD (λ = 1.550 Å) patterns of the MOF nanofilm: **(a)** in-plane and **(b)** out-of-plane. The patterns were measured first at RH = 0% for 10 min (red), then at RH = 93% for 10 min (blue), and finally at RH = 0% again for 10 min (green).

Kazuya Otsubo[a,b], Gang Xu[a] and Hiroshi Kitagawa[a,b,*]

[a] Division of Chemistry, Kyoto University
[b] JST/CREST

*E-mail: kitagawa@kuchem.kyoto-u.ac.jp

References

[1] S. Kitagawa *et al.*: Angew. Chem. Int. Ed. **43** (2004) 2334.
[2] O. Shekhah *et al.*: Chem. Soc. Rev. **40** (2011) 1081.
[3] M. Sadakiyo *et al.*: J. Am. Chem. Soc. **131** (2009) 9906.
[4] *G. Xu et al.: J. Am. Chem. Soc.* ***134*** *(2013) 16524.*
[5] *G. Xu, K. Otsubo, T. Yamada, S. Sakaida and H. Kitagawa: J. Am. Chem. Soc.* ***135*** *(2013) 7438.*

Characterizing self-assembled nanoparticles employed in drug delivery

Many biologically active compounds such as peptides and antibiotic molecules are hydrophobic or incompatible with water. To use these compounds as pharmaceutical drugs, they must be dispensed in aqueous solutions. The resultant solutions must be stable for at least a few months and their biological activity should not change at all during that period. Additionally, some of them are not stable in the body since they can be susceptible to enzymatic degradation or removed from the blood by the liver and other organs. Drug delivery using nanoparticles that encapsulate hydrophobic pharmaceutical compounds can dramatically improve their therapeutic effects as their well as stability under biological conditions. This technology is called a drug delivering system (DDS), and it is considered that nanotechnology and the integration of scientific fields, including biology, chemistry, and polymer science, are important in designing and characterizing DDS nanoparticles. The current trend of drug delivery aims at the development of targeted delivery, in which the drug is delivered to the target (such as a specific protein or DNA) with sustained release in a controlled manner. When the target is present inside cells such as in the cytosol or nucleus, the delivering vehicle must accomplish multiple tasks including cellular uptake through receptor recognition, endosomal escape, drug release, and nucleic entrance, as illustrated in Fig. 1.

Using beamline **BL40B2**, we have been studying small-angle X-ray scattering (SAXS) from DDS nanoparticles and the relationship between their structure and biological performance for DNA/polysaccharide [1-3] and hydrophobic-drug/polymer micelles [4,5].

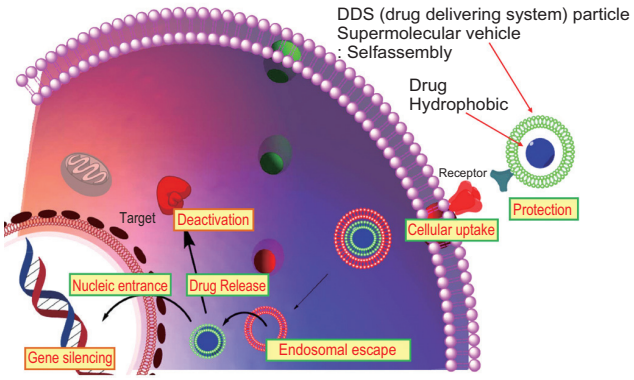

Fig. 1. Major barriers to overcome for cellular targeting delivery.

Polysaccharide/DNA Complexes

We have studied schizophyllan (SPG), a member of the β-1,3-glucans, as a delivery carrier of oligonucleotides, since SPG can complex with nucleotides such as poly(dA) (polyadenine) (Fig. 2(a)). The complex can be recognized by dectin-1 on antigen-presenting cells (APCs) and thus it is expected that β-glucans can specifically deliver the bound oligonucleotides to APCs. In fact, we have found that the complex can induce efficient gene silencing in animal models of fulminant hepatitis and bowel disease. It should be noted that we could observe therapeutic effects even when we applied the complexed antisense oligodeoxynucleotides (AS-ODN) at doses two orders of magnitude less than the reported dose because of the specific targeting. In order to use SPG as a DDS material, it is important to characterize its complex with therapeutic DNA in-site, i.e., in solution [1-3].

Figure 2(b) presents a typical SAXS profile from dA60/SPG (a complex of 60-base polyadenine with SPG), after combining data obtained with two different camera lengths (4.3 and 0.7 m) and extrapolating them to the zero concentration. The data shows the relation of $I(q) \sim q^{-1}$ in the middle range (0.08 nm^{-1} < q < 0.8 nm^{-1}), which is expected for rigid thin rods, and the intensity deviates upward in the low-q region and downward in the high-q region. The former deviation is ascribed to chain flexibility and the latter downward deviation is caused by the finite size of the cross section of the chain. From these deviations, the persistence length (pe) and the diameter of the worm-like cylinder (d) can be determined. By fitting the data with the Norisuye-Nakamura theory, pe and d were determined to be 45 ± 5 nm and 2.6 ± 0.2 nm, respectively.

Amphipathic block-copolymer micelles

Amphipathic block copolymers in aqueous solution undergo microphase separation into hydrophobic and hydrophilic domains [4,5]. When the hydrophilic block is long enough, stable spherical micelles consisting of a hydrophobic core and a hydrophilic shell are obtained. Polymeric micelles have great potential as DDS, because the core can encapsulate hydrophobic drugs and the shell can provide biocompatibility. Knowing how the drugs are distributed inside the core will help us understand the drug-releasing mechanism and increase the drug loading ratio. However, such information is hard to obtain since the core size is normally less than 100 nm and the drug concentration

is normally less than about 10 wt%, which makes it difficult to observe by electron microscopic techniques.

Recently, we have chosen the hydrophobic compound tetrabromocathecol (TBC) as a drug-equivalent model molecule. The bromine atoms in TBC act as probes in anomalous small-angle X-ray scattering (ASAXS), allowing us to find its localization in the polymeric micelles, the shape and size of which were determined by normal SAXS, as illustrated in Fig. 3. Light scattering measurements coupled with field flow fractionation were also carried out to determine the aggregation number (the number of polymer molecules in each micelle). A core-corona spherical model was used to explain the shape of the micelles, and the distribution of bromine atoms was explained with a rigid sphere model. Interestingly, the radius of the spherical region populated with bromine atoms was larger than that of the sphere corresponding to the hydrophobic core of the micelle. This result suggests that the TBC molecules infiltrate the polyethylene glycol (PEG) hydrophilic domain in the vicinity of the core/shell interface. The results of light scattering and SAXS indicate that the PEG chains in the shell region are densely packed and thus the PEG domain close to the interface has enough hydrophobicity to tolerate the presence of hydrophobic compounds.

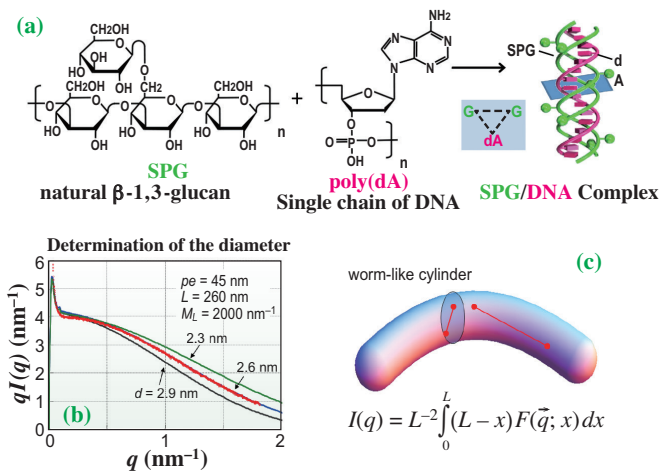

Fig. 2. **(a)** Repeating units of schizophyllan (SPG) and poly(deoxyadenylic acid) (dA_X) and an illustration of their complexation and stoichiometric structures of the triple helix of SPG and the complex, denoted SPG and dA_X/SPG. **(b)** Holtzer plots for the SAXS data of dA60/SPG, compared with results obtained adopting the Norisuye-Nakamura theory with different parameters. **(c)** Scattering function (so-called form factor) of a worm-like cylinder where $F(\vec{q}, x)$ is the Fourier transform of the probability density function that represents the probability that the contour point x is found at a specified point (which can be related to $\vec{q}$), as theoretically proposed by Nakamura and Norisuye.

Our group also carried out an SAXS study of a series of polymeric micelle samples and found that the major factor determining the aggregation number was the hydrophobicity of the chain, and that a high aggregation number induces overcrowding of the tethered PEG chains at the core/shell interface by 2-3 times. Thus, the control of the hydrophobicity may be important for designing more efficient DDS micelles.

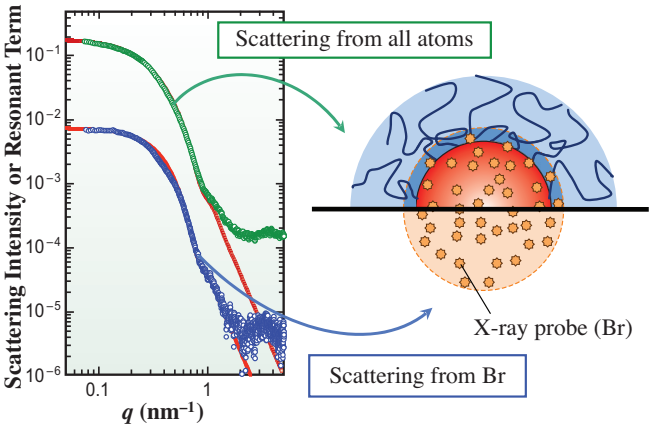

Fig. 3. SAXS and ASAXS profiles from TBC-incorporated polymeric micelles and their interpretation, showing the TBC distribution in the micelle. The red region represents the hydrophobic core, the blue lines represent PEG chains, and the orange polygons represent TBC.

Kazuo Sakurai

Department of Chemistry and Biochemistry, University of Kitakyushu

E-mail: sakurai@kitakyu-u.ac.jp

References

[1] S. Koyama *et al.*: J. Sci. Transl. Med. **2** (2010) 25ra24.
[2] Y. Sanada *et al.*: J. Phys. Chem. B **116** (2012) 87.
[3] S. Mochizuki *et al.*: J. Control Release **151** (2011) 155.
[4] *Y. Sanada, I. Akiba, K. Sakurai, K. Shiraishi, M. Yokoyama, E. Mylonas, N. Ohta, N. Yagi, Y. Shinohara and Y. Amemiya: J. Am. Chem. Soc.* ***135*** *(2013) 2574.*
[5] Y. Sanada *et al.*: J. Phys. Chem. B **116** (2012) 8241.

Materials Science :

To investigate the electronic and magnetic structures of various kinds of materials spectroscopic and scattering experiments are being conducted at the beamlines. Because relatively high-energy photons with a high-energy-resolution are used for spectroscopy research at SPring-8, the intrinsic bulk and buried interface properties can be precisely investigated. A recent trend is measurements in operand (i.e., studies for device materials under operating conditions, such as when a bias voltage and magnetic field are applied). Hard-X-ray photoemission spectroscopy (at BL15XU, BL29XU, BL46XU and BL47XU) (i.e., so-called HAXPES) provides bulk and interface information about materials. Recently, HAXPES studies at BL09XU have started. In the present chapter, recent achievements regarding the electronic and magnetic proprieties of materials are discussed.

Y. Yamashita *et al.* applied HAXPES at BL15XU to study the interface states of silicon under a bias voltage.

F. Bonel *et al.* showed the X-ray magnetic circular dichroism (XMCD) results for an electric field-driven chemical reaction at the buried FeCo/MgO interface. Experiments were performed at BL25SU, and the results shed a new light on the voltage-control of magnetism. Several mechanisms (charge accumulation or oxidoreduction) lead to magnetoelectric functionalities in solid-state devices.

Electronic & Magnetic Properties

The new soft X-ray beamline BL07LSU, which is operated by The University of Tokyo, has began started to produce promising results using time-resolved photoemission, three-dimensional nano-photoemission, and soft-X-ray emission spectroscopies. Using a soft-X-ray emission spectrometer, an energy resolution over $E/\Delta E \sim 10000$ has been achieved, and the electronic structures of polymer electrolyte fuel cells under operating conditions were reported by H. Niwa *et al.*

In addition, the activity from BL12XU, which operated by the National Synchrotron Radiation Research Center in Taiwan, has been fruitful. A. Severing *et al.* performed non-resonant inelastic scattering (NIXS) experiments on the heavy fermion compound, $CeCu_2Si_2$. By comparing the experimental data with theoretical simulations, they succeeded to determine the orbital orientation of the 4*f* ground state.

Other scattering methods are also actively utilized. K. Ohgushi performed resonant X-ray diffraction measurements at beamline BL19LXU for post-perovskite iridate, $CaIrO_3$. They argued that a quantum compass interaction occurs between the spins in $CaIrO_3$. M. Ito succeeded to introduced a rather bulk sensitive spin and orbital magnetization loops using magnetic Compton scattering. Their experiments were conducted at BL08W, and this method may be complementary to the XMCD method.

These pioneering results will significantly contribute to advancing the field of materials science.

Toyohiko Kinoshita

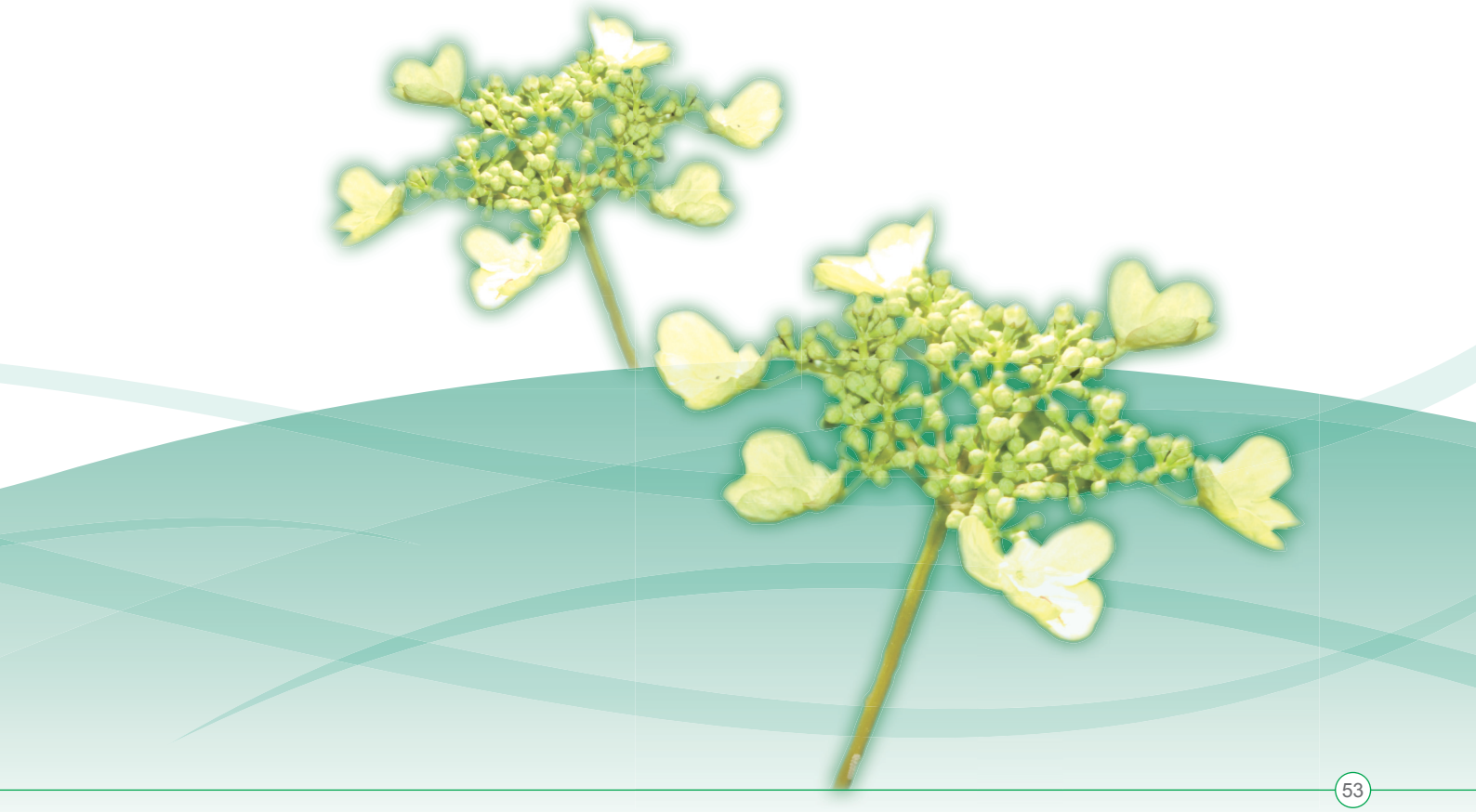

Bias-voltage application in a hard X-ray photoelectron spectroscopic study of the interface states at oxide/Si(100) interfaces

In the development of modern technologies, such as semiconductor and molecular electronics, optoelectronics, and fuel cells, a comprehensive knowledge of the electronic states in condensed matter systems is pertinent. Consequently, elucidating the electronic states in operational devices is indispensable. For the interface states at ultrathin oxide/Si interface, obtaining energy distribution interface states using a metal/ultrathin oxide/Si structure is difficult with electric measurements because the tunneling current flowing through the thin oxide layer interrupts electrical measurements. To solve this issue, we employed a bias application in hard X-ray photoelectron spectroscopic measurements (BA-HAXPES) [1,2] and evaluated the energy distribution of the interface states at the oxide/Si interface. This method is based on hard X-ray photoelectron spectroscopic (HAXPES) measurements under a bias between a metal layer and silicon substrate [1]. In the present study, we elucidated effects of the nitrogen atoms at the ultrathin SiO_2/Si interface on the interface states spectra and the density in the Si band-gap using BA-HAXPES.

The experiment employed three types of 3 nm-thick oxide layers on p-type Si(100): a SiO_2 layer, 1.2 and 1.8% SiON layers. Angle resolved photoelectron spectroscopy revealed that the nitrogen atoms were predominantly localized at the SiON/Si interface. After forming the oxide layers, a 10 nm-thick Ru film was deposited on the oxide. For the BA-HAXPES measurements, a bias voltage was applied to the backside silicon, and the metal Ru layer was grounded. The BA-HAXPES measurements were performed using **BL15XU**. For BA-HAXPES measurements, the incident X-ray energy was 5.95 keV, while the total energy resolution was 240 meV. Figure 1 schematically depicts the experimental setup for BA-HAXPES.

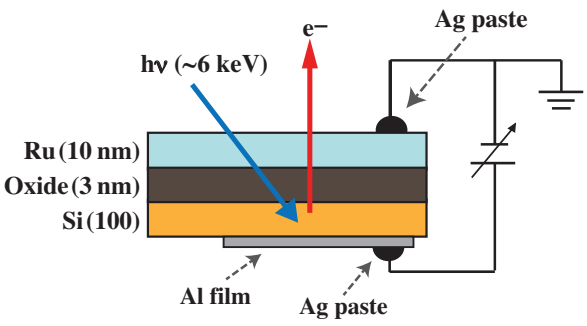

Fig. 1. Schematic of the experimental setup for BA-HAXPES.

Figure 2 shows the Si 1*s* spectra in the Si substrate region for the Ru/1.8% SiON/Si(100) structure as a function of bias voltage. Applying a positive bias voltage of 0.2 V to Si with respect to the Ru overlayer shifts the Si 1*s* substrate peak toward a higher binding energy by 0.085 eV. On the other hand, applying a −1.0 V negative voltage shifts the Si 1*s* peak toward a lower binding energy by 0.374 eV. These bias-induced shifts are completely reversible; that is, the shift diminishes upon removing the bias voltage. Therefore, these shifts are not due to a bias-induced chemical reaction of the Si substrate, but are caused by the accumulation or release of charge in the electronic states by the bias. By analyzing the energy shift of Si 1*s* level of the substrate as a function of bias voltage, the interface states in the Si band-gap are obtained.

Figure 3 shows the energy distribution of the interface states for the SiO_2/Si(100) interface as well

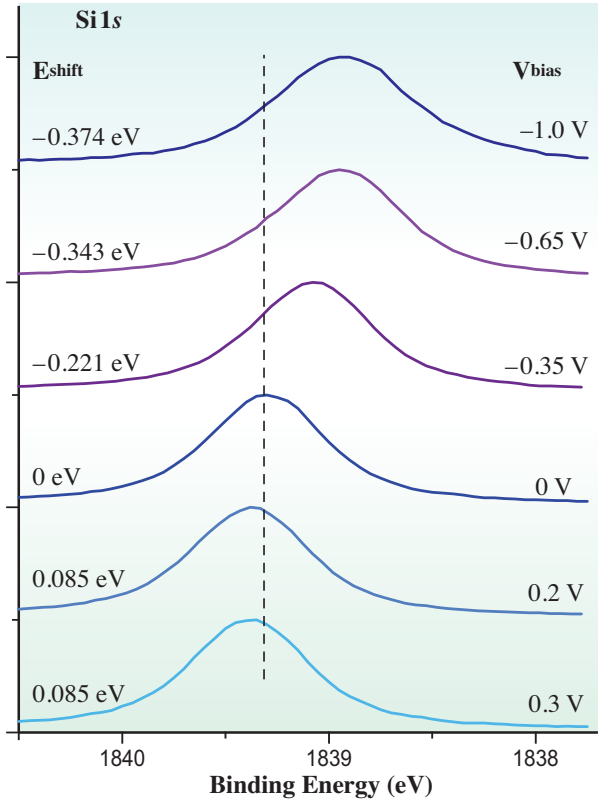

Fig. 2. Bias-dependent Si 1*s* spectra in the Si substrate region for the 1.8% SiON/Si(100) structure. Each bias voltage is applied to Si with respect to the Ru metal layer. Incident photon angle is 5° from the surface normal and the take-off angle is 85°.

as the 1.2 and 1.8% SiON/Si(100) interfaces. Note that the principle for the determination of the interface state spectra is given in our previous paper [1]. For the SiO_2/Si(100) interface (Fig. 3(a)), interface states are observed around the mid-gap, and the total interface state density is as low as ~10^{10} cm^{-2}. On the other hand, the interface states near the mid-gap increase for the 1.2% SiON/Si(100) interface and two new peaks appear near the conduction band minimum (CBM) and valence band maximum (VBM) compared to the SiO_2/Si(100) interface. The 1.8% SiON/Si(100) interface has the highest density of the three samples. Additionally, the 1.8% SiON/Si(100) and 1.2% SiON/Si(100) interfaces exhibit similar spectra. Thus, incorporating nitrogen atoms at the interface (Figs. 3(b) and 3(c)) increases the interface state densities around the mid-gap and forms the interface states near CBM and VBM.

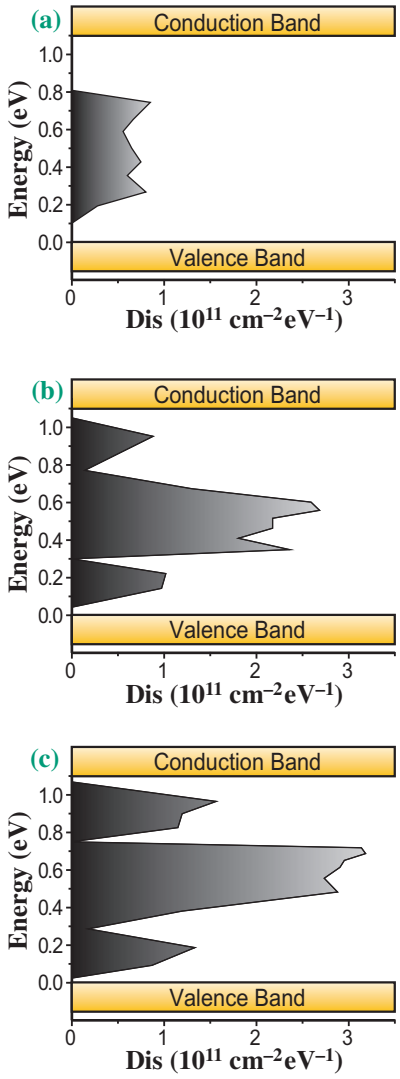

Fig. 3. Energy distribution of the interface states for **(a)** SiO_2/Si(100), **(b)** 1.2% SiON/Si(100), and **(c)** 1.8% SiON/Si(100) deduced from BA-HAXPES . Valence band maximum is set to the energy origin.

To assign the observed interface states, theoretical calculations for the SiO_2/Si system were referred [3]. The interface states near the mid-gap are attributed to isolated Si dangling bonds, whereas the interface states near VBM and CBM are due to weakened bonding and anti-bonding Si–O and/or Si–Si states, respectively. It should be noted that N related gap states are not formed in the Si band gap according to the theoretical calculation.

Next, we examined the origin of the increase in the interface state density as the nitrogen concentration increased. According to a previous study, N–O species at the SiO_2/Si interface induce inhomogeneous sites at the interface; the inhomogeneous sites consist of Si_2–N–O and Si–N–O_2 states at the interface [4]. The inhomogeneity should break (forming Si dangling bonds) and weaken Si–O bonds at the interface. Consequently, the interface states around the mid-gap increase and new states form near CBM and VBM as nitrogen atoms are inserted at the SiO_2/Si interface. Because the 1.8% SiON/Si(100) structure has more N–O species than the 1.2% SiON/Si(100) structure [1], the 1.8% SiON/Si(100) structure may possess more inhomogeneous sites at the interface. Thus, 1.8% SiON/Si(100) interface exhibits a higher interface state density than 1.2% SiON/Si(100) interface, although both show similar interface state spectra (Figs. 3(b) and 3(c)).

Yoshiyuki Yamashita[a,b,*], Toyohiro Chikyow[b] and Keisuke Kobayashi[c]

[a] Synchrotron X-ray Station at SPring-8, National Institute for Material Science
[b] Advanced Electronic Materials Center, National Institute for Material Science
[c] SPring-8/JAEA

*E-mail: yamashita.yoshiyuki@nims.go.jp

References

[1] *Y. Yamashita, H. Yoshikawa, T. Chikyo, K. Kobayashi: J. Appl. Phys.* ***113*** *(2013) 163707.*
[2] Y. Yamashita *et al.*: Jpn. J. Appl. Phys. **52** (2013) 108005.
[3] H. Kobayashi *et al.*: Appl. Surf. Sci. **252** (2006) 7700.
[4] Y. Yamashita *et al.*: Jpn. J. Appl. Phys. **46** (2007) L77.

Electric field-driven chemical reaction at the buried FeCo/MgO interface for potential use in low power spintronics devices

A challenging goal of spintronics is to manipulate electrically the magnetization direction in ferromagnets. In particular, this is a critical issue for the industrial development of magnetic random-access memories (MRAMs) composed of arrays of magnetic tunnel junctions (MTJs), the magnetization direction in each MTJ coding one bit of information. The usual way to switch the magnetization of a ferromagnetic layer is by using *current*-based methods: traditionally with the Oersted field generated by a current and recently with spin-transfer, by passing a large current through an MTJ. Interest on *voltage*-based methods is currently growing as these methods would require a much lower power consumption. We have recently shown that the perpendicular magnetic anisotropy (PMA) of ultrathin FeCo can be tuned with an electric field, leading to a reorientation of the easy magnetization axis from in-plane to out-of-plane under opposite voltages [1]. With this effect, precessional magnetization switching in MTJs could be induced by application of voltage pulses [2].

However, results that may seem inconsistent have been reported. The sign of the anisotropy change strongly depends on the ferromagnetic material and the nature of underlayers, and different time scales have been reported as well [1,3]. Actually, an electric field near a metal/insulator interface can have a variety of consequences on the properties of the metallic layer. First, capacitive charge accumulation modifies the density of states at the Fermi level and alters the electronic structure. Lattice distortions can also occur, as well as oxidoreduction and electromigration effects, with exchange of atoms between the metal and the insulator. When the metal is a ferromagnet, these effects may involve the electron spin, leading to magnetoelectric functionalities.

Investigation of these effects with spectroscopic techniques offers the opportunity to shed some light on the microscopic mechanisms occurring under voltage application. In particular, X-ray absorption near-edge spectroscopy (XANES) is particularly sensitive to the oxidation state, whereas X-ray magnetic circular dichroism (XMCD) is known to be a powerful tool for probing the atomic magnetic moment. In this paper, we report on the first XANES/XMCD measurements of an ultrathin FeCo film subjected to an electric field [4].

We studied multilayers with the following stacking: Au(50)/$Fe_{0.9}Co_{0.1}$(0.5)/MgO(1.8)/Cr(2)/Au(5) (*as-grown sample*) and Au(50)/$Fe_{0.9}Co_{0.1}$(0.5)/MgO(1.8)/SiO_2(5)/Cr(2)/Au(5) (*patterned sample*), grown on MgO(001) by molecular beam epitaxy and SiO_2 sputtering (thicknesses are in nanometers). Pillars with a diameter of 200 μm were patterned by electron beam lithography and ion etching. XANES measurements at the Fe $L_{2,3}$ edges were performed at the soft X-rays beamline **BL25SU**, with a beam diameter smaller than 200 μm and partial fluorescence detection. For XMCD measurements, a 0.5 T magnetic field was applied at 30° from the normal of the sample surface.

Figures 1(a) and 1(b) show the Fe $L_{2,3}$ XANES and XMCD spectra of the as-grown and patterned samples (sketched in Fig. 1(d)). The spectra of the as-grown sample show line shapes similar to those of pure Fe. Microfabrication induces marked changes in these spectra. Namely, both L_2 and L_3 peaks present a shoulder on their high energy side (indicated by arrows in Fig. 1(a)), while the XMCD signal is markedly reduced. These features are characteristic of a nonmagnetic FeO oxide. This partial oxidization of Fe is actually due to an etching step necessary to obtain the MgO/SiO_2 bilayer. From the XMCD reduction, we estimated that 1.8±0.5 monolayers (MLs) at the FeCo/MgO interface are oxidized. This corresponds to half of the grown 3.5 ML-thick FeCo film.

We measured the XANES/XMCD spectra of a pillar

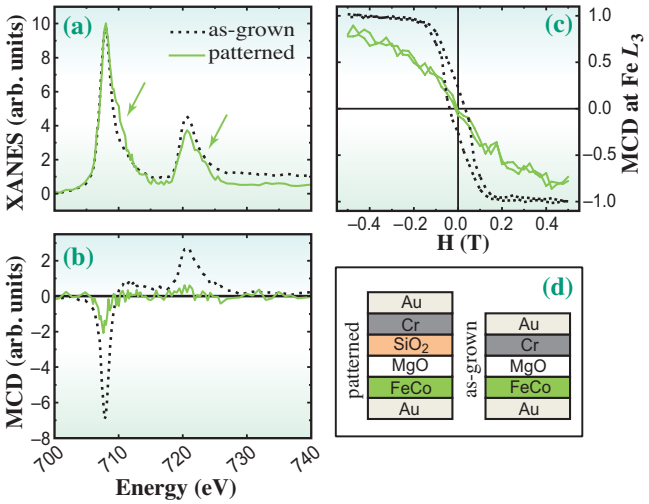

Fig. 1. **(a)** XANES and **(b)** XMCD spectra at the Fe $L_{2,3}$ edge for the as-grown and patterned samples, indicating Fe oxidation after microfabrication. **(c)** XMCD loops of the two samples with a magnetic field oriented at 30° from the surface normal and with a reduction in perpendicular anisotropy due to oxidation. **(d)** Sample structures.

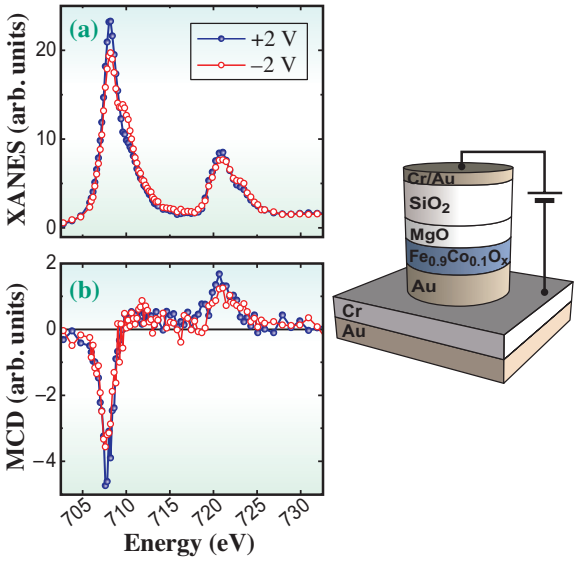

Fig. 2. **(a)** Fe $L_{2,3}$ XANES and **(b)** XMCD spectra of a pillar under a voltage of ±2 V. Variations in XANES line shape and XMCD amplitude indicate oxidoreduction.

while setting an electric field across the MgO/SiO_2 bilayer. The FeCo electrode was grounded and a voltage was applied to the Cr/Au electrode. The voltage was set to +2 V, then to −2 V, three times repeatedly. The results presented in Fig. 2 were obtained by averaging the spectra acquired separately at +2 V and −2 V. Varying the voltage induces a change in the relative weight of the main peaks and oxide-related shoulders. This means that the oxidation (reduction) of Fe is favored by an outward (inward) electric field with respect to the FeCo electrode. The XMCD change under ±2 V, and therefore the change in the magnetic moment, reaches a large value of 25%, which corresponds to the oxidoreduction of approximately 0.26 ML of Fe at the interface. Interestingly, the reaction is found to be reversible. This can be confirmed in Fig. 3, which displays the XANES variations at the L_3 energy when cycling the voltage ten times between +2 V and −2 V. Averaging over all voltage cycles yields the voltage dependence given in Fig. 3(c).

From the polarity of the voltage leading to oxidation/reduction, it can be inferred that the driving force is the electrostatic force, and not the "wind force" due to momentum transfer from the flowing electrons. This is at odds with the previous observation of electromigration in MTJs, which was driven by the current (10^6 A/cm^2) and occurred through nanoconstrictions in the insulator [5]. In our case, the current density and electric field reach at most 20 A/cm^2 and 0.14 V/nm, respectively. Together with the reversibility of the reaction, these observations suggest that in our experiments, the oxidoreduction originates from small changes in the positions of ions at the FeCo/MgO interface, uniformly over the surface.

The XMCD loops measured on the as-grown and patterned samples indicate that Fe oxidation, and therefore a negative applied voltage, reduces the PMA (Fig. 1(c)). This is opposite to the results reported in Ref. [1], in which a negative voltage induced an increase in PMA. Note that those studies dealt with as-grown films, showing no oxidization. This is an important result that sheds a new light on the voltage control of magnetism and clearly shows that several mechanisms (e.g., charge accumulation and oxidoreduction) can lead to magnetoelectric functionalities in solid-state devices. In future investigations, XANES/XMCD measurements will be performed to study the effect of charge accumulation on the magnetic anisotropy of these films.

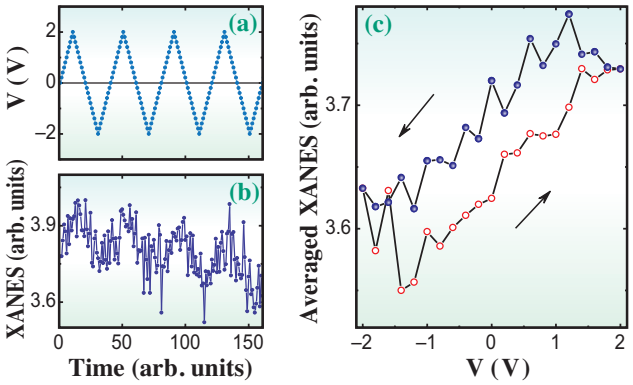

Fig. 3. Time traces of **(a)** the applied voltage and **(b)** fluorescence yield for an excitation of 708 eV (Fe L_3) while cycling the voltage between +2 V and −2V. **(c)** Voltage dependence of the fluorescence yield after averaging ten voltage sweeps.

Frédéric Bonell* and Yoshishige Suzuki

Graduate School of Engineering Science, Osaka University

*E-mail: bonell@spin.mp.es.osaka-u.ac.jp

References

[1] Y. Shiota *et al.*: Appl. Phys. Exp. **2** (2009) 063001.
[2] Y. Shiota *et al.*: Nat. Mater. **11** (2012) 39.
[3] A. Rajanikanth *et al.*: Appl. Phys. Lett. **103** (2013) 062402.
[4] *F. Bonell, Y.T. Takahashi, D.D. Lam, S. Yoshida, Y. Shiota, S. Miwa, T. Nakamura, Y. Suzuki: Appl. Phys. Lett.* ***102*** *(2013) 152401.*
[5] J. Ventura *et al.*: Phys. Rev. B **72** (2005) 094432.

Operando soft X-ray emission spectroscopy of iron phthalocyanine-based oxygen reduction catalysts

Polymer electrolyte fuel cells (PEFCs) have attracted much attention as clean and high efficient electrochemical devices for energy conversion. Conventionally, Pt-based materials are used as cathode catalysts for slow oxygen reduction reaction (ORR). Alternative ORR catalysts of low cost and high activity are desired because Pt is expensive and their resources are limited. Carbon-based materials are expected to be cathode catalysts alternative to conventional Pt catalysts for PEFCs. Carbon-based catalysts are usually synthesized by pyrolyzing precursors such as metal-phthalocyanine or metal-porphyrine with/without other carbon resources such as resins [1,2]. Accordingly, carbon-based catalysts are generally composed of C, N, O, H, and 3*d* transition metals. Thus, elucidation of ORR active sites is strongly required for further improving the ORR activity. There are two major candidates for the ORR active site, i.e. *TM*-N_x sites (*TM*: Fe or Co, x: 2 or 4), and nitrogen functional groups. In order to discuss the active site of carbon-based catalysts, their electronic structure has been investigated under *ex situ* conditions [2]. However, to further explore the ORR mechanism, study in *operando* condition is strongly required.

We have developed a novel electrochemical cell system for *operando* soft X-ray emission (SXE) spectroscopy of cathode catalysts for polymer electrolyte fuel cells at **BL07LSU** [3]. Incorporating a membrane electrode assembly (MEA) on a vacuum compatible flange, the system enables direct observation of element-specific electronic structure that changes with gaseous and potential conditions. SXE essentially provides element specific information involving transition within a particular element and is sensitive to valence electronic states of transition metals and light elements due to dipole-allowed transition at *L*-edge of transition metals and at *K*-edge of light elements.

A carbon-based catalyst was prepared by pyrolyzing a mixture of iron phthalocyanine and phenolic resin using a multi-step pyrolysis method (multi-FePc/PhRs). 0.4 mg·cm^{-2} of PtRu/C (TKK) and 4 mg·cm^{-2} of multi-FePc/PhRs were used as the anode and cathode catalysts of the MEA, respectively.

Operando SXE measurements were performed at **BL07LSU** using an ultrahigh resolution SXE spectrometer [4]. The gas flow rates were the same as those for CV measurements except for the introduction of N_2 and O_2 to the cathode with the rates of 45 and 5 mL·min^{-1}, respectively.

Figure 1 shows a schematic view of the MEA cell system. The vacuum environment is separated by a 150 nm-thick SiC membrane from the MEA in the atmosphere. An O-ring, SiC membrane, PTFE gasket sheets with Au foils as current collectors, and the MEA are sandwiched between a vacuum flange and the MEA cell. The electric potential between both electrodes can be manipulated by a Potentio/Galvanostat.

Figure 2 shows the H_2-O_2 fuel cell polarization plots obtained by measuring stable current densities at each potential. The gas flow rates were regulated to 10 mL·min^{-1} H_2 flow to the anode and 50 mL·min^{-1} N_2 or a mixture of 40 mL·min^{-1} N_2 and 10 mL·min^{-1} O_2 flow to the cathode. Only H_2 was humidified. The shape of the polarization plots of the MEA cell was similar to that of a standard fuel cell, demonstrating that the system can stably produce electricity by H_2 and O_2 gases. From Fig. 2, working voltage of the

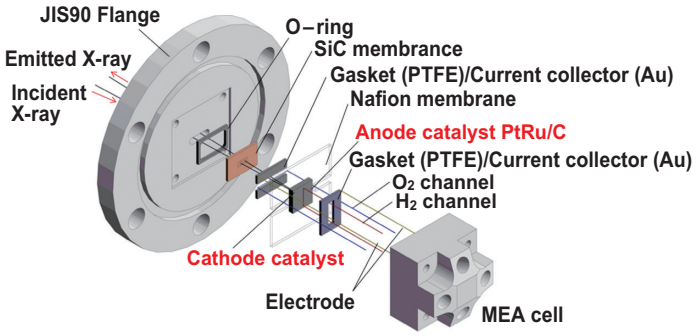

Fig. 1. Schematic view of the MEA cell for *operando* SXE measurements.

fuel cell was selected to 0.4 V. Also, 1.0 V, which is slightly above the open circuit voltage was chosen for SXE measurements.

The excitation energy for Fe 2*p* SXE was tuned to the Fe L_3 resonance at 710.0 eV. Figure 3 shows a comparison of *operando* Fe 2*p* SXE spectra of the MEA sample under various gaseous and operating conditions. Broad SXE features appear below an intense elastic line at 710.0 eV, reflecting energy loss due to Fe 3*d*-related states. The appearance of the energy-loss feature around 1.5 eV below the elastic peak is characteristic for iron species with planar ligand coordination, rather than typical iron oxides having larger *dd* excitation energies. The intensity of the 1.5 eV peak is significantly reduced when N_2 gas in the cathode is replaced by the mixture of N_2 and O_2 gases (lower panel of Fig. 3(b)). This change implies that oxygen may adsorb on an iron site with planar ligand coordination, such as Fe-N_x embedded into the sp^2 carbon network [1] considering the structure of the precursor.

As shown in upper panel of Fig. 3(b), it is noted that the shape of the Fe 2*p* SXE spectra does not change with the cell voltage under both gas conditions. This result can be explained by either of the following; that the Fe sites in the multi-FePc/PhRs catalyst are not ORR active because they adsorb oxygen too strongly to release oxygen, or the Fe sites are still ORR active where the rate-determining step of ORR is desorption of intermediates (such as H_2O_2) and/or reaction product (H_2O). However, it is difficult to exclude either of the above interpretations only using the present SXE results.

The experimental system developed in this study can also be applied to observe the electronic structure of solid-gas and solid-liquid interfaces under potential control, such as PEFC anode catalysts, metal-air battery electrodes and lithium-ion battery electrodes.

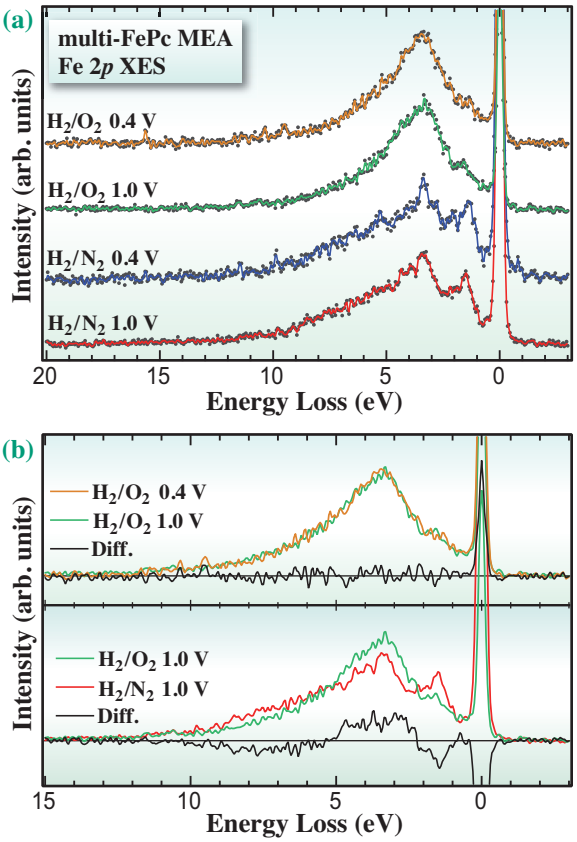

Fig. 3. **(a)** *Operando* Fe 2*p* SXE spectra of the multi-FePc/PhRs catalyst. Dotted lines are raw data. Solid lines are smoothed data as an eye guide. **(b)** Smoothed Fe 2*p* SXE spectra compared with 1.0 V (lower panel) and the same gas conditions (upper panel). Black solid lines are difference spectra.

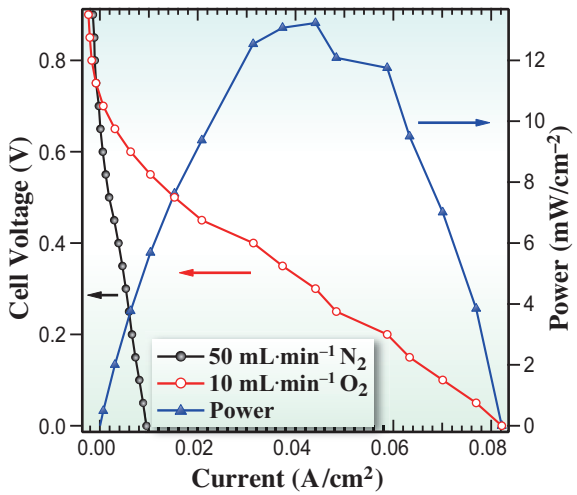

Fig. 2. H_2-O_2 fuel cell polarization plots.

Hideharu Niwa[a,b,*], Yoshihisa Harada[a,b] and Masaharu Oshima[b]

[a] Institute for Solid State Physics, The University of Tokyo
[b] Synchrotron Radiation Research Organization, The University of Tokyo

*E-mail: hniwa@issp.u-tokyo.ac.jp

References

[1] M. Lefèvre *et al.*: Science **324** (2009) 71.
[2] H. Niwa *et al.*: J. Power Sources **223** (2013) 30.
[3] *H. Niwa, H. Kiuchi, J. Miyawaki, Y. Harada, M. Oshima, Y. Nabae, T. Aoki: Electrochem. Commun.* ***35*** *(2013) 57.*
[4] Y. Harada *et al.*: Rev. Sci. Instrum. **83** (2012) 013116.

Orbital orientation of the *4f* ground state in $CeCu_2Si_2$

Heavy fermion compounds are rare earth or actinide materials where the *f* electrons hybridize with the conductions electrons. Due to the hybridization the charge carriers have enhanced effective masses which can be up to a thousand times larger than the free electron mass, giving the name to this class of materials. The hybridization of *f* and conduction electrons competes with the RKKY interaction so that quantum critical transitions from local magnetism to itinerant *f* electron behavior take place when the exchange interaction is increased with external parameters such as pressure, field or doping. Often unconventional superconductivity occurs in the vicinity of the quantum critical point. $CeCu_2Si_2$ was the first heavy fermion compound where this proximity of magnetism and superconductivity was observed [1].

The key to understanding heavy fermion compounds is linked to the ground state wave function of the *f* electrons. In a crystalline environment an ion experiences a so-called crystalline electric field (CEF) caused by the charges of the surrounding ions and the degeneracy of the Hund's rule ground state is lifted. The resulting CEF 4*f* states are highly anisotropic (see Fig. 1). However, as the wave functions cannot be calculated *ab initio*, they have to be determined experimentally. Single crystal magnetization measurements, inelastic neutron scattering and more recently also soft X-ray absorption spectroscopy at the $M_{4,5}$ edges ($3d \rightarrow 4f$) have been very successful in determining the 4*f* wave function. However, none of the established methods is able to determine the *orientation* of the 4*f* orbital in the tetragonal (a=b≠c) structure of $CeCu_2Si_2$. Figure 1 shows the ground state orbital of $CeCu_2Si_2$ for two possible orientations with loops in [100] direction (left) or [110] direction (right). The established techniques rely on dipole transitions, thus cannot distinguish these two fourfold orbitals. Hence an experiment which goes beyond the dipole limit is required.

Simulations of the scattering function $S(q,\omega)$ have shown that Inelastic X-ray Scattering (IXS) with hard X-rays has the potential to reach non-dipole allowed transitions when working at large momentum transfers. In order to mark the difference to resonant techniques the method is called non-resonant IXS, in brief NIXS. The left panel of Fig. 2 shows at the example of the cerium $N_{4,5}$ edge ($4d \rightarrow 4f$) the different multipole contributions to the radial parts of $S(q,\omega)$ as function of the momentum transfer $|\vec{q}|$. Already at 10 $Å^{-1}$ the scattering due to quadrupolar transitions (k=3) is quite substantial with respect to the dipole transitions (k=1). The simulation of the angular parts of $S(q,\omega)$ shows further that extra transitions appear, which are not allowed in the dipole approximation (see Fig. 2(b)).

We adapted these simulations of $S(q,\omega)$ at the cerium $N_{4,5}$ edge to our crystal-field problem by implementing the vector $\vec{q}$ dependence in addition to the absolute size of the momentum transfer $|\vec{q}|$. The direction of $\vec{q}$ gives the sensitivity to the shape of the orbital. Our simulation shows that NIXS is first of all, like inelastic neutron scattering and other methods, sensitive to the orbital shape out-of-plane. On top of this, and this is the intriguing novelty, the same simulation for two different directions within the tetragonal *ab*-plane ($\vec{q} \parallel [100]$ and $\vec{q} \parallel [110]$) shows that the NIXS intensity also depends on the $\vec{q}$ directions within the plane with fourfold rotational symmetry (Fig. 3, top graph). Hence NIXS should be able to tell us how the orbital is oriented.

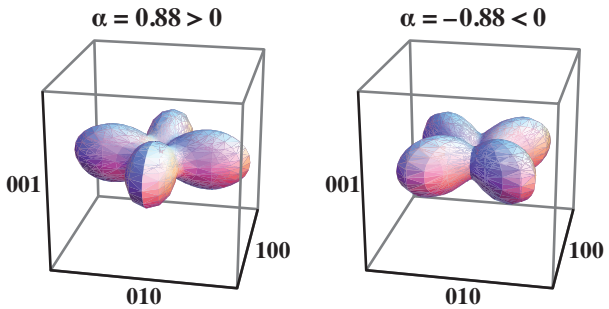

Fig. 1. Angular distribution of the *4f* electron in $CeCu_2Si_2$ corresponding to the wave function $\alpha\,|\pm 5/2> + \sqrt{(1-\alpha^2)}\,|\pm 3/2>$ with $\alpha = |0.88|$; on the left for $\alpha > 0$, on the right for $\alpha < 0$. Both orbitals are identical but rotated by 45° around the *c*-axis.

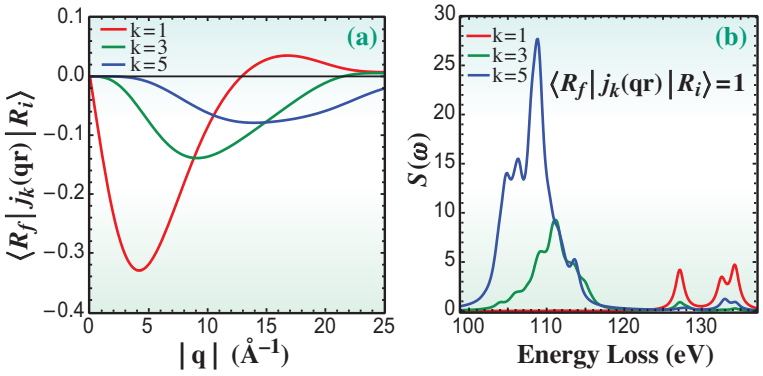

Fig. 2. **(a)** k^{th} order term of the radial part of the scattering function versus momentum transfer. **(b)** k^{th} order contribution of angular part of the scattering function as function of energy transfer.

Such a NIXS experiment was realized in a collaboration of the University of Cologne, Germany, the Max-Planck Institute for Chemical Physics of Solids in Dresden, Germany, and the National Synchrotron Radiation Research Center in Hsinchu, Taiwan. The experiment was carried out at the Taiwan beamline **BL12XU** at SPring-8 with 9.8 keV incident photons so that at a scattering angle of about 135° momentum transfers of 9.3 Å^{-1} could be achieved. This is well beyond the dipole limit. The bottom graphs of Fig. 3 show the NIXS data for momentum transfers in the two different in-plane directions, $\bar{q} \| [100]$ (blue dots) and $\bar{q} \| [110]$ (green dots). The error bars reflect the statistical error. Only a linear background has been subtracted. The comparison of simulation (top) and data (bottom) shows that the simulation for an orbital orientation with the loops along the [110] direction (see inset) reproduces the experimental data very well. We therefore conclude that we solved the long standing problem of the orbital orientation in the tetragonal heavy fermion system $CeCu_2Si_2$ and also opened up a new direction for studying the 4*f* orbitals of other heavy fermion systems. This work has been published in reference [2].

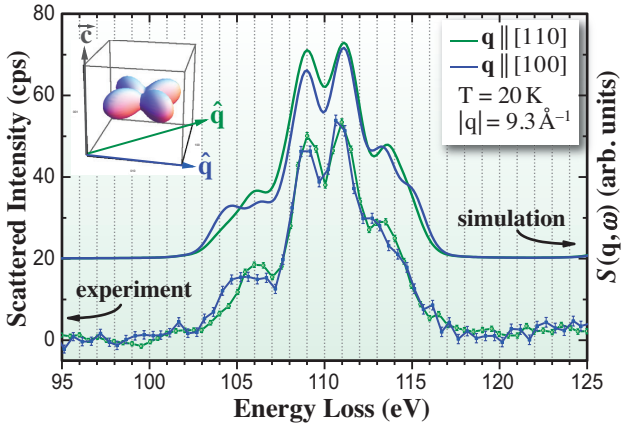

Fig. 3. Top: Simulation of $S(q,\omega)$ for the two in-plane directions assuming the orbital orientation as in the inset. The calculations are convoluted with a Lorentzian of FWHM = 0.3 eV and a Gaussian of FWHM=1.32 eV to account for lifetime broadening and instrumental resolution. Bottom: NIXS data of $CeCu_2Si_2$ single crystals for the two in-plane directions $\bar{q} \| [100]$ and $\bar{q} \| [110]$.

Andrea Severing[a,*], Liu Hao Tjeng[b] and Nozomu Hiraoka[c]

[a] Institute of Physics II, University of Cologne, Germany
[b] Max-Planck Institute for Chemical Physics of Solids, Germany
[c] National Synchrotron Radiation Research Center, Taiwan

*E-mail: severing@ph2.uni-koeln.de

References

[1] O. Stockert *et al.*: Nat. Physics **7** (2011) 119; and references therein.
[2] *T. Willers, F. Strigari, N. Hiraoka, Y.Q. Cai, M.W. Haverkort, K.-D. Tsuei, Y.F. Liao, S. Seiro, C. Geibel, F. Steglich, L.H. Tjeng and A. Severing: Phys. Rev. Lett.* ***109*** *(2012) 046401.*

Quantum compass interaction in post-perovskite iridate $CaIrO_3$

There is a new trend toward exploring Mott physics in 5*d* transition metal oxides with a strong spin-orbit interaction. Theoretical calculations using the Hubbard model revealed that the spin-orbit interaction drives a transition from a correlated metal to an insulator [1]. This novel Mott insulating state is actually realized in a layered perovskite, Sr_2IrO_4, including Ir^{4+} ions with a $(t_{2g})^5$ electronic configuration [2]. In this compound, one hole among t_{2g} manifolds takes a complex wavefunction with the spin and orbital magnetic moments of 1/3 and 2/3 μ_B, respectively, and this state is now called the $J_{eff}=1/2$ state.

The superexchange interaction across two Ir^{4+} ions in the $J_{eff}=1/2$ state is theoretically shown to be unique [3]. Although an antiferromagnetic Heisenberg interaction $J_1\mathbf{S}_i\cdot\mathbf{S}_j$ is dominant in a corner-shared IrO_6 bond, the magnetic interaction of the edge-shared IrO_6 bond becomes highly anisotropic and ferromagnetic, i.e., $-J_2\,\mathbf{S}_i^z\,\mathbf{S}_j^z$, where the *z* direction is perpendicular to the plane expanded by two Ir atoms and two O atoms responsible for the edge-shared bond. This interaction, which is called the quantum compass interaction owing to the analogy to the interaction between two compasses (Fig. 1), captures great interest since a quantum spin liquid is realized when this interaction occurs in the honeycomb lattice. To test the validity of this theory, it is necessary to elucidate the magnetic structure of an Ir oxide with both edge-shared and corner-shared IrO_6 bonds. We here focused on a post-perovskite-type compound, $CaIrO_3$, which exhibits both edge-shared and corner-shared IrO_6 octahedral bonds [4]. The compound shows a Mott insulating behavior characterized by a charge gap of ~0.17 eV and undergoes a transition to a canted antiferromagnetic state at 115 K [5].

Resonant X-ray diffraction measurements were performed at beamline **BL19LXU** (inset of Fig. 2(a)). An incident beam was monochromated by a pair of Si (1 1 1) crystals and irradiated on the (0 0 1) surface of the sample, which was placed in a ^{4}He closed-cycle refrigerator installed on a four-circle diffractometer with a vertical scattering plane geometry. The intensities of incident and scattered beams were detected by an ionization chamber and a Si PIN photodiode, respectively. The polarization of the incident beam was perpendicular to the scattering plane (σ) and that of the scattered beam was analyzed by using the (0 0 8) reflection of pyrolytic graphite.

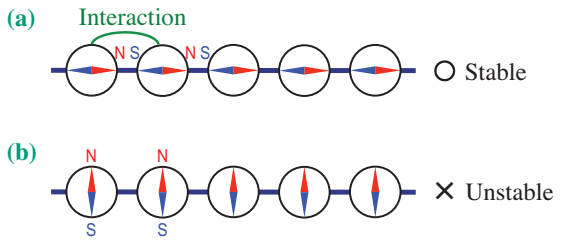

Fig. 1. Schematic of quantum compass model. When a number of compasses are placed in a line, they interact with each other, resulting in a stable state in which the N pole of a compass faces the S pole of the adjacent compass. The state in which the needles of the compasses point horizontally (Fig. 1(a)) is more stable in terms of energy than the state in which they point vertically (Fig. 1(b)). This anisotropic interaction is called the compass interaction. In the Heisenberg model, arrangement pattern **(a)** has the same energy as arrangement pattern **(b)**.

Figure 2(a) displays the absorption spectra obtained by fluorescence measurements at room temperature as well as the energy dependence of the scattered intensity of the (0 0 5) reflection at 10 K. We can observe a strong resonance peak at the L_3 edge of ~11.21 keV. The space group of $CaIrO_3$ is *Cmcm* with orthorhombic symmetry, where (0 0 2*n*+1) reflections are forbidden according to the *c*-glide reflection. The polarization analysis indicates the π' character of the scattered beam (Fig. 2(b)). The temperature variation of the integrated intensity follows well that of the weak ferromagnetic moment (Fig. 2(c)). Considering also that the anisotropic tensor of susceptibility (ATS) scattering is prohibited in the measured geometry, we conclude that the observed reflection originates from a commensurate antiferromagnetic ordering. The observed magnetic reflections are well accounted for by considering an antiparallel arrangement of two Ir spins (labelled 1 and 2 in Fig. 3(a)) in a primitive unit cell. We can also determine the spin direction by representation analysis. The parasitic ferromagnetism along the *b* axis can be permitted only when the antiferromagnetic moments are along the *c* axis. The obtained magnetic structure is schematically drawn in Fig. 3. It has a stripe-type order with a parallel alignment along the *a* axis and an antiparallel alignment along the *c* axis.

Importantly, the magnetic reflection cannot be detected within the experimental accuracy at the L_2-edge of ~12.82 keV, $I(L_2)/I(L_3)<0.3\%$. This large edge dependence of the magnetic scattering intensity is interpreted on the basis of the ligand field theory. When the tetragonal crystal field Δ and spin-orbit coupling ζ are present, sixfold degenerated t_{2g} orbitals are split into three doubly degenerated bands. At the ground state, one hole occupies one of the highest energy orbitals

$$|\varphi\pm\rangle=\frac{1}{\sqrt{A^2+2}}\left(A|xy\pm\rangle\pm|yz\mp\rangle+i|zx\mp\rangle\right).$$

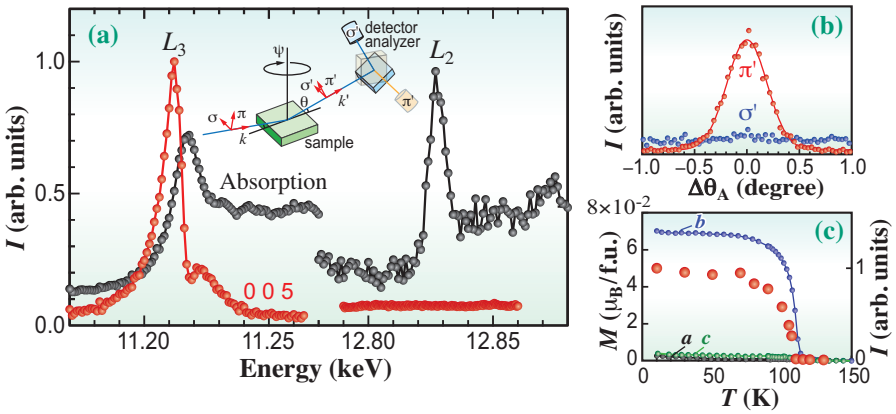

Fig. 2. **(a)** X-ray absorption spectra at room temperature and the magnetic scattering intensity (I) of the (0 0 5) reflection at 10 K near the Ir L-edge for $CaIrO_3$. The inset shows a schematic view of the experimental configuration. **(b)** Polarization analysis of the scattered light at the L_3 edge, where θ_A is the analyzer angle. **(c)** Temperature (T) dependence of the magnetization (M) at 0.1 T and the intensity (I) of the (0 0 5) reflection. (f.u. = formula unit)

When one electron is virtually excited from the Ir 2*p* orbitals in a resonant process, the t_{2g} bands are fully occupied; this simplicity enables us to calculate the atomic scattering tensor straightforwardly. By combining contributions of two Ir sites in a striped-ordered state, we obtain the scattering intensity as a function of the *A* parameter. The scattering intensity ratio between the L_2 and L_3 edges can be written as

$$\frac{I(L_2)}{I(L_3)} = \frac{(A-1)^4}{(A^2-2A-2)^2} \quad .$$

By comparing with the experimental results, we can give a constraint $A > 0.61$ (a constraint $A > 0.87$ is deduced from the results of ATS scattering analysis). This result indicates that the orbital state of the 5*d* hole is close to the $J_{eff}=1/2$ state.

The realization of the $J_{eff}=1/2$ state in $CaIrO_3$ enables us to discuss the magnetic structure in a theoretical framework. The observed antiferromagnetic (ferromagnetic) interaction through the corner-shared (edge-shared) bonds is totally consistent with the theoretical predictions. Moreover, the weak ferromagnetism can be successfully explained theoretically. The anisotropic axis *z* in the quantum compass model is tilted from the crystallographic axis *c* by $\pm\alpha$ and distinguished between the Ir(1)-Ir(1) and Ir(2)-Ir(2) bonds (see Fig. 3); this distinct local anisotropic axis leads to spin canting toward the *b* axis. We therefore safely state that the quantum compass interaction occurs between the spins in $CaIrO_3$. To the best of our knowledge, this is the world's first experimental demonstration of the quantum compass interaction for spins. Theoretically, arranging the spins that are subject to the quantum compass interaction in the honeycomb lattice is expected to enable the realization of Kitaev spin liquids, which can be used in quantum computers. The achievement of our research is expected to markedly increase the likelihood of realizing spin liquids.

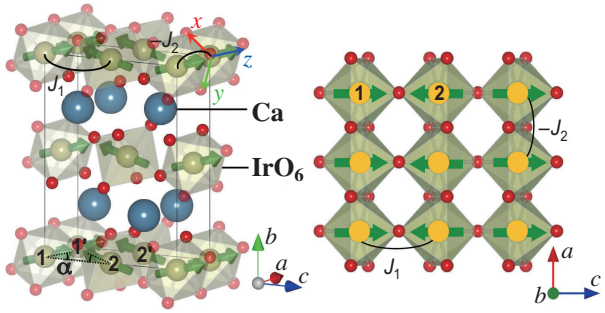

Fig. 3. Magnetic structure of post-perovskite-type compound $CaIrO_3$. The magnetic moment is ordered in an antiparallel arrangement by the Heisenberg interaction denoted as J_1 and in a parallel arrangement by the quantum compass interaction denoted as J_2. The magnetic moment is slightly tilted, which is caused by the anisotropy of the quantum compass interaction.

Kenya Ohgushi

Institute for Solid State Physics, The University of Tokyo

E-mail: ohgushi@issp.u-tokyo.ac.jp

References

[1] D. Pesin and L. Balents: Nat. Phys. **6** (2010) 376.
[2] B.J. Kim *et al.*: Science **323** (2009) 1329.
[3] G. Jackeli and G. Khaliullin: Phys. Rev. Lett. **102** (2009) 017205.
[4] *K. Ohgushi, J. Yamaura, H. Ohsumi, K. Sugimoto, S. Takeshita, A. Tokuda, H. Takagi, M. Takata and T. Arima: Phys. Rev. Lett.* ***110*** *(2013) 217212.*
[5] K. Ohgushi *et al.*: Phys. Rev. B **74** (2006) 241104(R).

Spin and orbital magnetization loops obtained using magnetic Compton scattering

The magnetic moment of a material is the sum of the spin (μ_S) and orbital moments (μ_L). Both are fundamental quantities for understanding the macroscopic magnetic properties of materials. However, there are very few experimental techniques that can be used to disentangle the spin and orbital contributions from the total magnetic moment. Most conventional magnetometer-based techniques, e.g., vibrating sample magnetometry (VSM) and superconducting quantum interference device magnetometry (SQUID), can only measure the total magnetic moment of the samples. X-ray magnetic circular dichroism (XMCD) is one of the useful tools that provide the ratio μ_L/μ_S within the framework called the sum rule procedure.

In this report, an X-ray magnetic Compton scattering (MCS) technique is described. MCS is one of the useful techniques for disentangling the spin and orbital contributions. Since MCS probes only the spin magnetization, it can provide the absolute value of the spin component of magnetization. Combined with conventional techniques, the orbital component of magnetization and its curve as a function of magnetic field can be uniquely deduced. Recent improvements of the MCS technique [1] can successfully separate the magnetic part from total Compton scattering as a function of magnetic field, enabling independent measurements in the positive and negative sides of spin magnetization curves. This development is useful for magnetic materials with exchange spring coupling, in which the magnetization curves show asymmetry with respect to the origin.

When the incident X-rays are circularly polarized, the cross section for Compton scattering is given as [2,3]

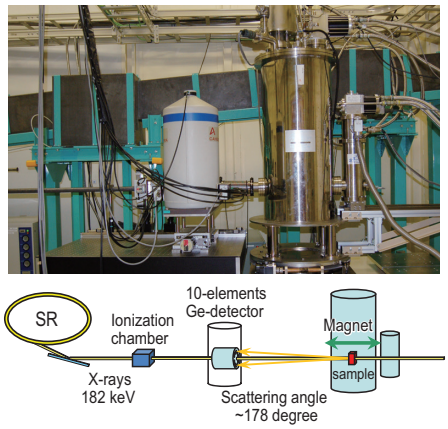

Fig. 1. Photograph and schematic drawing of MCS spectrometer.

$$\frac{d\sigma}{d\Omega} = \left(\frac{d\sigma}{d\Omega}\right)_{charge} + \left(\frac{d\sigma}{d\Omega}\right)_{spin}$$
$$= C_{charge}N + C_{mag}P_c\mathbf{S}\cdot(\boldsymbol{k}cos\theta + \boldsymbol{k}')\mu_S$$

where P_c is the degree of circular polarization of X-rays, $\mathbf{S}$ is the spin direction, $\boldsymbol{k}$ ($\boldsymbol{k}'$) is the wavevector of incident (scattered) X-rays, and θ is the scattering angle. C_{charge} and C_{mag} are constants. The first term, which contains the total number of electrons, N, corresponds to the charge Compton scattering. The second term is the magnetic term that contains the spin moment, μ_S.

The scattered X-ray intensity is proportional to the scattering cross section. To determine the absolute spin moment in a sample, we measure the intensities of Compton scattered X-rays from the sample under sampling condition (I) and non-magnetized condition (I_{non}). The magnetic effect R is defined by the following equation.

$$R = \frac{I - I_{non}}{I_{non}} = \frac{I_{spin}}{I_{charge}}$$
$$= \frac{C_{mag}P_c\mathbf{S}\cdot(\boldsymbol{k}cos\theta + \boldsymbol{k}')}{C_{charge}}\cdot\frac{\mu_s}{N} = A\left(\frac{\mu_s}{N}\right)$$

Once the coefficient A is given, the spin moment can be determined from the experimentally determined magnetic effect R, since the total number of electrons, N, is known. The coefficient A is usually determined by measuring a well-characterized material, such as Fe metal, the spin moment of which is already known.

The demonstrations [1] were carried out at the High Energy Inelastic Scattering beamline **BL08W**. Elliptically polarized X-rays emitted by the elliptical multipole wiggler are monochromatized to 182.6 keV with a degree of circular polarization of ~0.55. The spectrometer consists of a 3T-superconducting magnet, a sample cryocooler and a 10-element Ge detector. Compton scattered X-rays from a sample are detected by the detector at a scattering angle of 178 degrees.

Figure 2(a) shows the MCS intensity loop (filled circles) and VSM data (solid line) of $GdAl_2$ at 5 K. The total data acquisition time for MCS is ~14 h. The total count, which includes both the charge and magnetic contributions, is ~2×10^7 at each data point. The orbital moment of ferromagnetic $GdAl_2$ is almost quenched so that VSM can measure the response of the spin magnetic moment to the applied magnetic field. Thus, $GdAl_2$ is a good magnet for a feasibility test and the

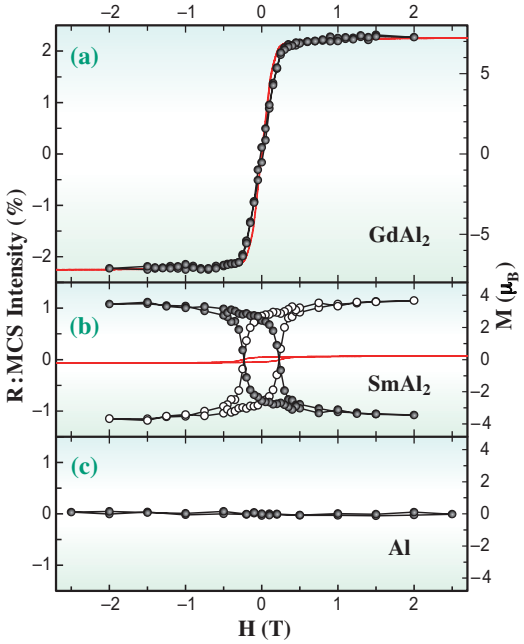

Fig. 2. MCS intensity loop (filled circles) and magnetization loops measured by VSM (solid line) of **(a)** $GdAl_2$, **(b)** $SmAl_2$ and **(c)** Al. The MCS intensity is corresponds to spin magnetization. The orbital magnetization loop (open circles in (b)) was obtained by subtracting the spin magnetization from the total magnetization data by VSM.

calibration of the MCS spectrometer. The left axis shows the magnetic effect R, which is the ratio of MCS intensity to charge Compton scattering intensity and the right axis shows the magnetization measured by VSM. The MCS spectrometer was calibrated by fitting the MCS intensity curve to the VSM data. Hence, the spin magnetization can be evaluated in the unit of Bohr magneton in later experiments using the spectrometer. The MCS intensity loop is in excellent agreement with the VSM data, demonstrating that the MCS loop captures the response of spin magnetization to the applied magnetic field.

Figure 2(b) shows the MCS intensity loop at 10 K (filled circles) as well as the VSM loop at 5 K (solid line) for $SmAl_2$. The total count is 2.6×10^7 at each point and the total data acquisition time is ~8 h. The MCS intensity is calibrated by $GdAl_2$ data, and the corresponding spin magnetization is given as μ_B in the right axis. In contrast to $GdAl_2$, the MCS intensity loop differs in its magnitude and sign from the VSM loop because of a large orbital magnetization in $SmAl_2$. The VSM data show a total magnetization of 0.2 μ_B at 2 T, while the MCS intensity loop reveals a spin magnetization of 3.5 μ_B. This leads to the orbital magnetization of 3.7 μ_B at 2 T. The spin and orbital magnetizations obtained here are in good agreement with the results of a previous work [4]. The orbital magnetization loop (open circles), obtained from the difference between the VSM and MCS intensity loops, shows an almost reverse hysteresis feature compared with the spin magnetization loop. This result confirms that the spin and orbital magnetization loops cancel each other out to make a small total magnetization loop in $SmAl_2$.

The sensitivity of the MCS spectrometer is estimated from the MCS intensity loop of Al. The intensity is almost constant because of its non-magnetic property (Fig. 2(c)). The standard deviation in the magnetic effects, R, is ~0.025%, which is equivalent to ~0.025 μ_B for Fe and ~0.07 μ_B for Gd as the minimum limit of spin magnetization measurement.

The temperature-dependent magnetization is also measured. Figure 3 shows the MCS intensity of $SmAl_2$ as a function of temperature at a magnetic field of 2.5 T. The MCS intensity starts to increase at around 100 K and then rapidly increases as the temperature decreases. The temperature dependences show almost the same curves with decreasing and increasing temperature.

Finally, the decomposition of total magnetization into spin and orbital contributions serves as a probe of atomic-level magnetic anisotropy and coupling, and plays an essential role in understanding the magnetization reversal process. This MCS technique is a new means for studying ferro- and ferrimagnetisms.

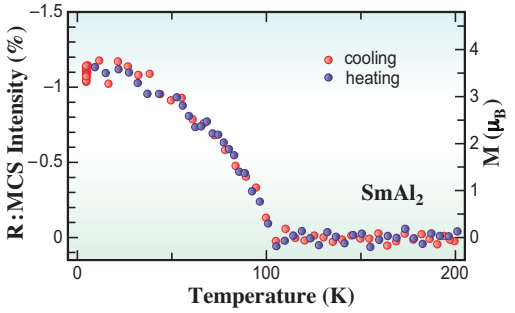

Fig. 3. Temperature dependence of MCS intensity of $SmAl_2$.

Masayoshi Itou

SPring-8/JASRI

E-mail: mito@spring8.or.jp

References

[1] *M. Itou A. Koizumi and Y. Sakurai: Appl. Phys. Lett.* ***102*** *(2013) 082403.*
[2] P. Platzman *et al.*: Phys. Rev. B **2** (1970) 3556.
[3] M. Cooper *et al.*: Ed., "X-ray Compton scattering," Oxford University Press, New York, 2004.
[4] H. Adachi *et al.*: Phys. Rev B **59** (1999) 11445.

Chemical

Here, outstanding chemical research is introduced as major achievements at SPring-8. The research areas include programmed arraying of metal complexes in supramolecular systems, Compton scattering of electrons in nanoconfined water, one-dimensional crystals inside carbon nanotubes, a new class of aluminum-based interstitial hydrides as a hydrogen storage material for fuel cell vehicles, and synchrotron infrared spectroscopy of water. Further remarkable research results achieved by applying SACLA (XFEL) to subjects concerning sequential multiphoton multiple ionization of atoms and attosecond X-ray interaction with core-hole atoms are also introduced.

Supramolecular systems, such as macrocyclic, tetrapyrroles have been studied with the aim of developing functionalized molecular assemblies due to high expectations from their photophysical, electrochemical, magnetic, and catalytic properties. X-ray crystal structure analyses of a facially stacked ionic complex between cyclic tetrapyroles, and a fourfold rotaxane were performed at the single crystal structure analysis beamline BL02B1. Emergent functions related to nanomagnetism, conductivity, or catalysis via intermolecular electronic communications among the stacked metal complexes should be developed.

Water molecules form a tetrahedral network in ice, and a distorted, slowly changing tetrahedral network in bulk water. The proton in a water molecule exists within a covalent bond in a nearly harmonic well. Since the potential well is due to the distribution of electrons, the valence electrons in nanoconfined water should be distributed very differently from the case of an individual molecule. This conjecture was tested using X-ray Compton scattering. Measurements of the momentum distribution of electrons at the high energy inelastic scattering beamline BL08W indicate that the ground states of electrons and protons in nanoconfined water qualitatively differ from the typical weakly interacting molecules.

Science

A physical problem found in free-standing 1D crystals is the metal-insulator transition, which is referred to as the Peierls transition. Suppression of the Peierls transition was tested by encapsulation of 1D crystals inside the cylindrical nanocavity of carbon nanotubes (CNTs), with the aim of preserving an enclosed 1D crystal as a 1D quantum conductor. The formation of unprecedented 1D crystals of elemental sulfur inside single-walled CNTs and double-walled CNTs was demonstrated at the powder diffraction beamline BL02B2. The most striking achievement in this study is that the 1D sulfur crystals exhibit a metallic character under ambient pressure, whereas bulk sulfur requires ultra-high pressures to become metallic.

To realize a hydrogen-based economy, safe and efficient hydrogen storage is a key technological challenge. For fuel cell vehicle applications, hydrogen storage materials should be mainly composed of light elements ($Z \leq 20$) to achieve a high gravimetric hydrogen capacity. Interstitial hydrides are favorable as hydrogen storage materials because the hydrogenation and dehydrogenation reactions should proceed simply, and their thermodynamic properties are tunable by the addition of other elements into the alloy. The synthesis of a new aluminum-based interstitial hydride, Al_2CuH_x, was achieved at the JAEA materials science beamline BL14B1. This finding may help to expand the diversity of aluminum-based hydrides and accelerate the development of practical hydrogen-storage materials.

Polymers chemically grafted to the surface of substrates, which are known as polymer brushes, are often used to modify surface properties such as hydrophilicity or hydrophobicity, friction, and adhesiveness. Superhydrophilic surfaces are particularly attractive due to their potential applications for self-cleaning, antifogging, antifouling, and water lubrication systems. The wettability of water on cationic poly(2-(methacryloyloxy) ethyl trimethylammonium chloride) (PMTAC) brush prepared on a silicon wafer was examined by synchrotron infrared (IR) spectroscopy at the infrared materials science beamline BL43IR. The structure of water existing under and even outside the droplet prevents the complete wetting of the highly hydrophilic polyelectrolyte brushes.

Since the detection of anomalous signals from naturally occurring sulfur atoms in a protein at an XFEL photon energy of 7.3 keV, which is far from the sulfur *K*-edge (~2.5 keV), the multiphoton ionization of the deep inner-shells and cascade decays has been investigated to reveal the pathways of multiphoton multiple ionization due to the newly developed XFEL at SACLA. Ionization of a heavy atom, Xe, progresses rapidly by repetition of the inner-shell photoionization and subsequent Auger/Koster-Kronig decay within the XFEL's short pulse duration. Understanding the ionization dynamics by high-intensity hard-X-ray beams may provide useful input for future molecular imaging experiments.

A similar phenomenon was observed in the photoabsorption processes of Kr gas. In addition to being of basic interest in the field of X-ray nonlinear optics, the X-ray interaction with core-hole atoms is very important for analysis of XFEL experiments. To investigate the X-ray interaction with the core-hole states, X-ray fluorescence from Kr atoms illuminated by the focused XFEL beam of SACLA was measured. A double core hole (DCH) is created, and the usefulness of DCH has been discussed to determine the pulse duration in the sub-10-femtosecond range.

Yuden Teraoka

Programmed arraying of metal complexes in a supramolecular system: Stacked assembly of porphyrin and phthalocyanine

Molecular materials comprising of organized assemblies of functional molecules occasionally demonstrate chemical and physical phenomena that are unpredictable from the sum of their individual molecular components. These phenomena are caused by intermolecular communications defined by their electronic states and relative spatial orientations, i.e., angle and distance. Supramolecular systems have been used for building the interconnections between the molecular components to develop such functionalized molecular assemblies with a synergetic effect, because supramolecular linkages are well suited to flexible control of the interactions between them. Macrocyclic tetrapyrroles, such as porphyrins and phthalocyanines and their metal complexes, have been used as key building blocks for a wide range of molecular materials owing to their unique photophysical, electrochemical, magnetic, and catalytic properties. Organized porphyrin assemblies are also showing promise for the construction of higher functionalized systems, whilst the arraying of multiple porphyrins has been investigated by employing bio-inspired templates and regulated stacking interactions.

We have recently reported supramolecular stacked arrays of porphyrins and phthalocyanines connected by two- or fourfold rotaxanes [1-4]. A fourfold rotaxane, **3**, was prepared from tetradactyl porphyrin with four alkyl ammonium chains, **2**, and phthalocyanine with four peripheral crown ethers, **1** (Fig. 1). A rotaxane consisting of a secondary ammonium ion and a crown ether has been recognized as a versatile building block for supramolecular systems. This complexation occurred as a result of electrostatic stabilization and hydrogen bonds between the negatively charged interior of the dibenzo-24-crown-8 ethers and the cationic ammonium $R_2NH_2^+$ moieties. Since the terminuses of the alkylammonium chains were locked by large phosphoramidate moieties, the porphyrin and phthalocyanine are inseparable, but their interactions are flexibly convertible. The interaction between the two metal complexes was interconverted between the protonation state and deprotonation state of the secondary amines in the middle of the alkyl chains. In the dinuclear Cu^{2+} complex of the fourfold rotaxane, the Cu^{2+}-porphyrin and the Cu^{2+}-phthalocyanine were stacked efficiently on one another to afford spin-spin communication. Spin states of the dinuclear complex were reversibly switchable between the protonated (doublet) and deprotonated forms (singlet) (Fig. 1(b)) [1]. This switchable communication between two

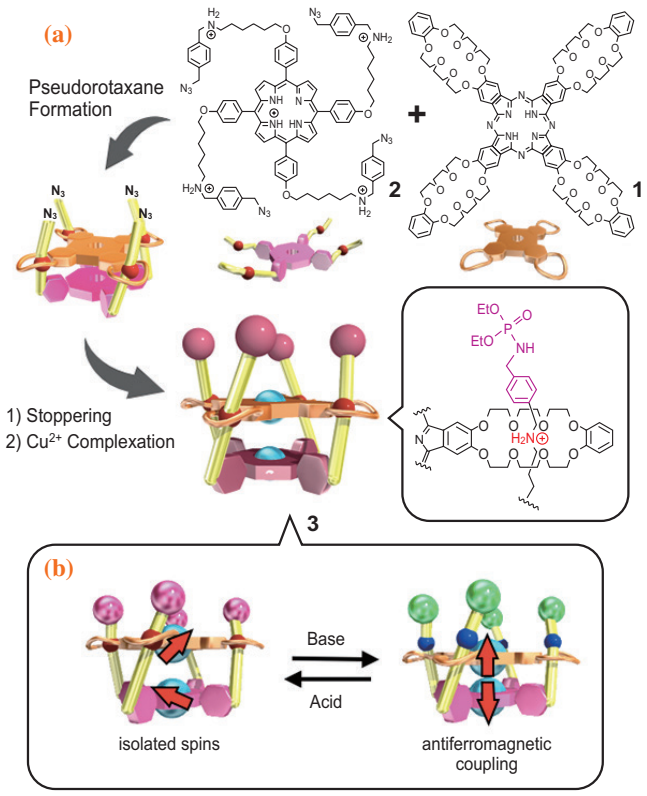

Fig. 1. **(a)** Synthesis of a dinuclear Cu^{2+} complex of the porphyrin/phthalocyanine fourfold rotaxane and **(b)** switchable spin-spin interaction between Cu^{2+} complexes in the fourfold rotaxane.

metal complexes demonstrated the obviously flexible character of the supramolecular rotaxane linkage. We also succeeded in the regioselective formation of the heterodinuclear complex in the fourfold rotaxane [2].

For the supramolecular architecture, ionic bonds as non-covalent interactions in molecular assemblies are usually categorized as relatively strong and nondirectional forces. However, they yield quite stable site- and configuration-specific molecular association by cooperation among multiple-ionic interactions and/or other intermolecular forces. For instance, there are many examples of intercalation phenomena of planar cationic dyes into polyanionic DNA duplexes through electrostatic and π-π interactions. From this viewpoint, the fourfold rotaxane would be a good platform for such a molecular association, because it has four cations as crown ether-wrapped ammonium ions standing in a square around the extended π-system of the phthalocyanine core. The structure of the molecular assembly is clear-cut and exhibits molecular

complementarity with tetraanionic porphyrins. The ionic complexation between the fourfold rotaxane and tetraanionic porphyrin (Cu^{2+}-$TPPS^{4-}$) was quite stable and stoichiometrically occurred even at a micromolar level in a solution, which was investigated by a photometric titration experiment (Fig. 2). However, without a crystallographic analysis, it is not possible to ascertain whether the Cu^{2+}-$TPPS^{4-}$ was stacked on top of the phthalocyanine ring or intercalated into the middle of the porphyrin and phthalocyanine.

Brown single crystals of **4** were obtained and the crystal structure revealed by synchrotron radiation at beamline **BL02B1** in collaboration with Dr. Kunihisa Sugimoto (JASRI) is shown in Fig. 3. We found a triply stacked structure of Cu^{2+}-$TPPS^{4-}$ on Cu^{2+}-porphyrin and Cu^{2+}-phthalocyanine in the fourfold rotaxane. The crystal structure clearly indicated that four alkylammonium chains of the porphyrin threaded into each crown ring attached to the phthalocyanine to form the fourfold rotaxane structure. Moreover, the Cu^{2+}-$TPPS^{4-}$ moiety was perfectly stacked on top of the phthalocyanine ring with a Cu–Cu distance of 3.6 Å as an *H*-aggregate, whereas the porphyrin ring and phthalocyanine ring of the fourfold rotaxane were stacked in a slightly slipped *J*-aggregation form. All phenyl rings of Cu^{2+}-$TPPS^{4-}$ intervened between adjacent crown ethers to stabilize the ionic complex. To our best knowledge, this is the first example of an X-ray crystal structure of a facially stacked ionic complex between cyclic tetrapyroles as well as that of a fourfold rotaxane. Recently, we found that Cu^{2+}-$TPPS^{4-}$ directly affects the electronic state of the phthalocyanine in the supramolecular assembly.

Since the electronic properties of porphyrin and phthalocyanine are tunable by complexation with metal ions and functionalization through diverse substitutions, this should allow the potential development of emergent functions related to nanomagnetism, conductivity, or catalysis via intermolecular electronic communications among the stacked metal complexes.

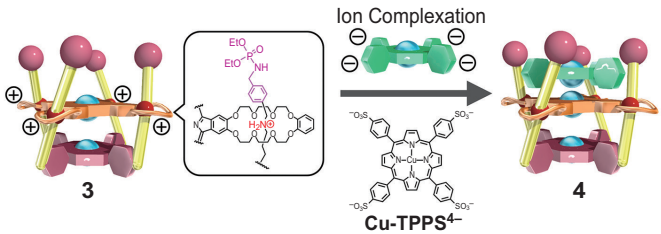

Fig. 2. Triply stacked array of Cu^{2+}-porphyrins, Cu^{2+}-phthalocyanine, and Cu^{2+}-$TPPS^{4-}$ formed via ionic complexation.

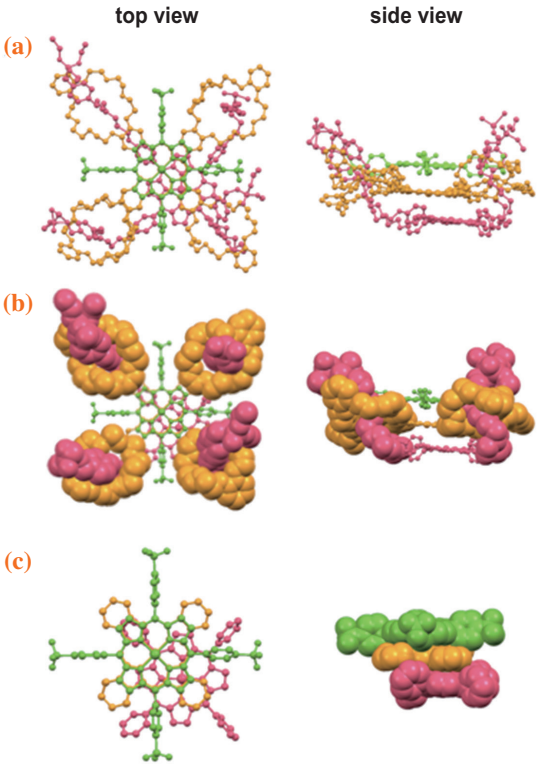

Fig. 3. Crystal structure of the triply stacked assembly: **(a)** the whole figure of the assembly, **(b)** the emphatic alkyl ammonium chains and the crown ether rings as a space-filling model to clarify the four rotaxane structures, and **(c)** the extracted porphyrin and phthalocyanine rings to show the stacking structure. Porphyrin and phthalocyanine of the fourfold rotaxane and Cu^{2+}-$TPPS^{4-}$ are represented in pink, orange, and green, respectively. Solvent molecules and hydrogen atoms have been omitted for clarity. [3]

Kentaro Tanaka[a,*] and Yasuyuki Yamada[a,b]

[a] Department of Chemistry, Nagoya University
[b] Research Center for Materials Science, Nagoya University

*E-mail: kentaro@chem.nagoya-u.ac.jp

References

[1] Y. Yamada *et al.*: Angew. Chem. Int. Ed. **51** (2012) 709.
[2] Y. Yamada *et al.*: Dalton Trans. **42** (2013) 15873.
[3] *Y. Yamada, N. Mihara, S. Shibano, K. Sugimoto and K. Tanaka: J. Am. Chem. Soc.* ***135*** *(2013) 11505.*
[4] Y. Yamada *et al.*: Chem. Commun. **49** (2013) 11053.

Compton scattering confirmation of the anomalous ground state of the electrons in nano-confined water

Water is usually viewed as a collection of molecules that remain intact at room temperature and atmospheric pressure, interacting weakly through the hydrogen bonds formed by the attraction of the electrons around the oxygen of one molecule with the protons on another. The water molecules form a tetrahedral network in ice, and a distorted, slowly changing, primarily tetrahedral network in bulk water. Within this picture, the proton in the water molecule exists within a covalent bond in a nearly harmonic well that is softened only slightly by the attraction of the neighboring oxygen.

With the advent of deep inelastic neutron scattering (DINS) it has become possible to observe the momentum distribution of the protons in water. The width and shape of this momentum distribution is due almost entirely, even at room temperature, to the confinement of the proton in the potential provided by its surroundings. The weakly interacting molecule picture above is qualitatively correct for bulk water. The momentum distribution is well approximated by a 3D anisotropic Gaussian, the momentum widths are consistent with the frequencies of oscillation of the proton observed with other techniques, and the width is approximately calculable from perturbation theories that begin with the isolated molecule as an unperturbed system [1]. However, deviations from the weakly interacting molecule model observed with DINS become extreme when water is confined to dimensions on the order of 20 Å. The proton is observed to delocalize coherently over distances of the order of 0.2-0.3 Å in a strongly anharmonic double well potential [2]. Since the potential well the proton sees, is due to the distribution of the electrons of the system, one would expect that the valence electrons in nano-confined water to be distributed spatially very differently than would be the case in individual molecules.

This conjecture was tested at the high energy inelastic scattering beamline **BL08W**, by using X-ray Compton scattering to measure the momentum distribution of the electrons for nano-confined water in conditions for which the proton was known to be delocalized [3]. Two systems were chosen, water in the single walled nano-tube (SWNT) as a function of temperature, and water in two forms of Nafion at room temperature. Nafion is the proton exchange membrane used in many commercial fuel cells because of its high conductivity. The protons are confined in irregular pockets in the polymer (Teflon) matrix, as shown in Fig. 1. The two materials differed in the length of the side chains (shown in the figure), which donate the proton to the water that makes it a conductor. We discuss only the Nafion results here. The conclusions from the nanotube data are the same.

We show in Fig. 2 the momentum distribution of the protons in the two forms of Nafion. The broad tails on the distribution and the appearance of oscillations demonstrate that the confining potential is far from the nearly harmonic wells of the covalent bond in the molecule. In Fig. 3, we show the results of the X-ray Compton scattering for the change in the momentum distribution for the valence electrons of the water for the two types of Nafion, obtained by subtracting the dry Nafion signal from the signal with water present, and removing the core electron contribution for the water. The amount of water in the Nafion is the same as that in the samples in Fig. 2. The curve in Fig. 3 is a phenomenological fit. Its shape was obtained from X-ray Compton measurements, by others at SPring-8 [4], of the change in the momentum distribution in bulk water when deuterium was substituted for hydrogen. The amplitude in Fig. 3, as measured by the $\Delta J(0)/J(0)$, however, is 46 times greater than observed in those measurements. It is also 17 times greater, by the same criterion, than the change observed as the hydrogen bond in bulk water is disordered by heating from 5° above melting to 5° below boiling at

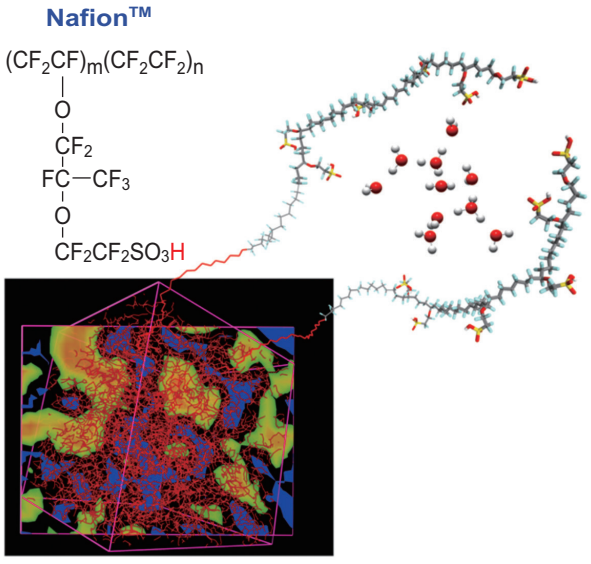

Fig. 1. Multiscale simulation of the structure of Nafion. Blue areas are primarily polymer, red orange primarily water. Samples differ in the length of the side chains.

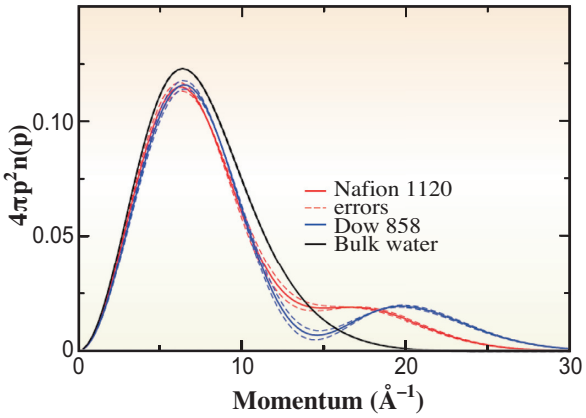

Fig. 2. Proton radial momentum distribution in water confined in two types of Nafion, compared with that of bulk water.

atmospheric pressure [5]. The changes observed here are far outside the range of what can be achieved by the weakly interacting molecule model. The changes in the electron distribution indicate the ability of the electron backbone for the hydrogen bond network to shift electrons around in order to create the Born-Oppenheimer potential that leads to the momentum distribution for the protons shown in Fig. 2.

These measurements demonstrate that the ground state of the electrons and protons in nano-confined water is qualitatively different from the usual weakly interacting molecule model. Presumably the frustration due to confinement of the geometric configuration preferred by the tetrahedral ordering raises the energy of that state, allowing an energetically nearby configuration of the electrons and protons, better adapted to the confinement, to become the ground state. In any case, the existence of this state has profound implications for biology. 20 Å is the characteristic distance between the elements of a biological cell. It is likely that evolution was making use of the properties of this state of water when life evolved, and that the functioning of cells depends on its properties.

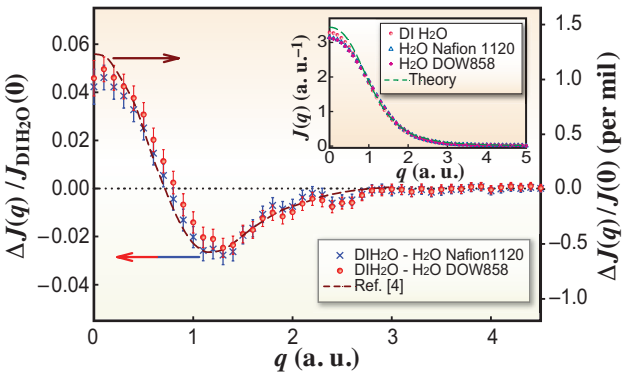

Fig. 3. The difference Compton profile (CP) of water in Nafion 1120 and Dow 858 subtracted from the CP of bulk water. The red dashed line is a fit to the difference (H_2O-D_2O) between H_2O and D_2O, rescaled to fit our data; a rescaling by a factor of 46 is needed. The inset shows the experimental CP for deionized (DI) water, confined water in two types of Nafion (Nafion 1120 and DOW 858) and theoretical CP (green dashed line) of isolated water molecule.

George F. Reiter[a,*], Aniruddha Deb[b] and Stephen J. Paddison[c]

[a] Physics Dept., University of Houston, USA
[b] Dept. of Chemistry, University of Michigan, USA
[c] Dept. of Chemical and Biomolecular Engineering, University of Tennessee, USA

*E-mail: greiter@uh.edu

References

[1] C. J. Burnham *et al.*: Chem. Phys. **135** (2011) 144502.
[2] G. Reiter *et al.*: Physical Review B **85** (2012) 045403.
[3] *G.F. Reiter, A. Deb, Y. Sakurai, M. Itou, V.G. Krishnan and S.J. Paddison: Phys. Rev. Lett. **111**(2013) 036803.*
[4] K. Nygård *et al.*: J. Chem. Phys. **126** (2007) 154508.
[5] M. Hakala *et al.*: J. Chem. Phys. **125** (2006) 084504.

A metallic phase of elemental chalcogens: One-dimensional crystals of sulfur inside carbon nanotubes

A one-dimensional (1D) crystal, the ultimate monatomic wire, is one of the most intriguing quantum systems in solid-state physics, and offers a rich potential to pave the way for next-generation electronic nanodevices. As clearly found in a hypothetical 1D hydrogen crystal, which is believed to exhibit a metallic character, synthesis of 1D crystals is a potentially promising approach for transformation of non-metals into metals.

A common problem found in free-standing 1D crystals is the metal-insulator transition, the so-called Peierls transition. It is well known that 1D conducting polymers (e.g., polyacetylene) undergo bond length alternation owing to the Peierls instability, so that the resulting material has a fundamental energy gap. Our strategy for suppressing the Peierls transition is to encapsulate 1D crystals inside the cylindrical nanocavity of carbon nanotubes (CNTs) in order to preserve the enclosed 1D crystal as a 1D quantum conductor.

Carbon nanotubes (CNTs) are ideal containers because of their inherent quasi-1D hollow structures with diameter of ~1 nm. The steric confinement effect due to the constraining nanospace of CNTs has enabled exotic atoms to form a unique nanostructure differing from the bulk structure. In addition, CNTs provide uniform interaction potential fields inside the cylindrical cavity since the lattice of CNTs consists of only carbon atoms. This is in stark contrast to other 1D porous materials, and results in stabilization of the enclosed 1D crystals without any local distortions by the host lattice.

Here, we demonstrate the formation of unprecedented 1D crystals of elemental sulfur inside single-walled CNTs (SWCNTs) and double-walled CNTs (DWCNTs) [1]. The most striking achievement in our study is that the 1D sulfur crystals exhibit a metallic character under ambient pressure, whereas the bulk sulfur requires ultrahigh pressures of above 90 GPa to become metallic. An important property of elemental sulfur is its ability to form covalently bonded 3D helical molecules. However, this fibrous allotrope is an insulator under ambient conditions (Fig. 1(a)). Even though the 1D zigzag and linear configurations have been predicted to show metallic behavior (Fig. 1(b)) [2], to the best of our knowledge, the experimental isolation of these 1D systems has eluded scientists.

As clearly visualized in Fig. 2, high-resolution transmission electron microscopy (HRTEM) revealed the formation of monatomic sulfur chains inside the hollow cores of an SWCNT (S@SWCNT) and DWCNT (S@DWCNT). Figure 2(a) displays an HRTEM image of two monatomic sulfur chains encapsulated inside an SWCNT with a diameter of 1.1 nm. However, because electron-beam irradiation activated the sulfur chains and induced their translational motion during imaging, the precise bonding configuration of the sulfur atoms inside the single carbon wall was obscured at atomic resolution. To identify the structure of sulfur chains, double carbon walls are useful because the surrounding carbon walls allow us to identify the encapsulated structure with atomic resolution not only by stabilizing the encapsulated sulfur chains, but also by protecting them from electron-beam damage. Here, we can identify a zigzag sulfur chain inside a DWCNT with an inner diameter of 0.7 nm (Fig. 2(b)) and a linear sulfur chain in a DWCNT with a narrower inner diameter of 0.6 nm (Fig. 2(c)). Our HRTEM analysis revealed that the periodic distance is 0.33 ± 0.03 nm for the zigzag sulfur chain and 0.18 ± 0.02 nm for the linear sulfur chain; the narrower the nanotube diameter, the more constrained the sulfur chain is along the tube axis.

One of our important results is the successful observation of X-ray diffraction (XRD) from the encapsulated 1D sulfur chains (Fig. 2(d)), measured at beamline **BL02B2**. The XRD result clearly indicates the presence of highly crystalline 1D phases of elemental sulfur in bulk quantity. The domain size of the 1D sulfur chains inside SWCNTs is 35-45 nm, and that in DWCNTs is 90-160 nm at 300 K, indicating that the long-range order and large domain size of 1D sulfur chains is likely to be due to the strong covalent bond within the 1D sulfur chains. In this sense, the "1D monatomic chains" of sulfur are no longer simple chains and we believe that the 1D sulfur chains can be regarded as a new phase of "1D crystals." Note that our XRD analysis showed good agreement with the periodic distances evaluated by HRTEM analysis. In addition, we found that the 1D sulfur crystals formed

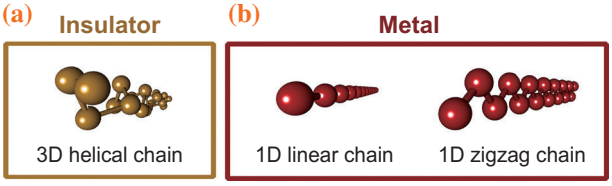

Fig. 1. Schematic illustrations of **(a)** 3D helical sulfur chain that behaves as an insulator and **(b)** 1D linear and zigzag sulfur chains. These 1D planar configurations exhibit metallic properties at ambient pressure [2].

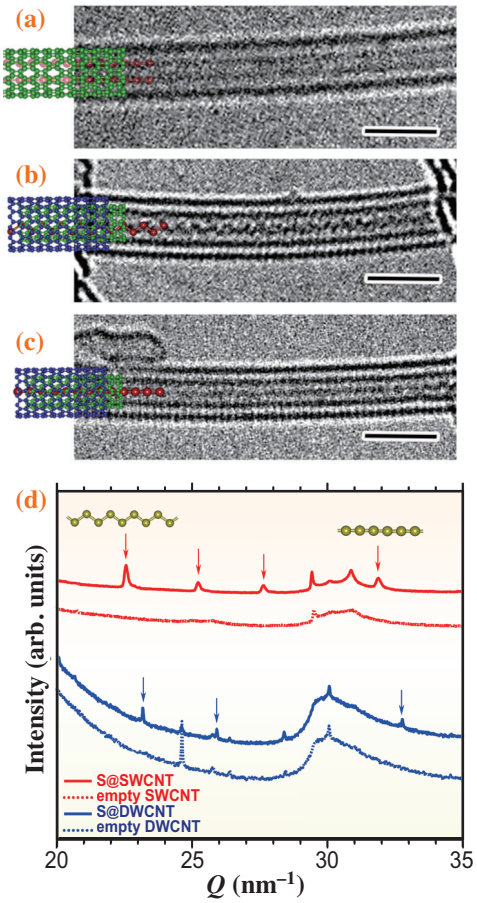

Fig. 2. HRTEM images of **(a)** S@SWCNT, **(b)** S@DWCNT with the 1D sulfur chain in the zigzag configuration, and **(c)** S@DWCNT with the 1D sulfur chain in the linear configuration. Scale bar: 2 nm. **(d)** XRD patterns of S@SWCNTs, empty SWCNTs, S@DWCNTs, and empty DWCNTs. Arrows indicate the Bragg peaks of 1D sulfur crystals.

inside SWCNTs and DWCNTs are similar to each other, except for slight axial compression inside the DWCNTs (e.g., the lattice constants *d* of the 1D linear sulfur are 0.197 nm and 0.192 nm inside SWCNTs and DWCNTs, respectively).

Most importantly, we verified that the 1D sulfur crystals indeed exhibit a metallic character, thus improving the electrical conductivity of CNT sheets (Fig. 3). Our temperature-dependent electric-resistance measurements clearly show that the presence of the 1D sulfur crystals reduces the electrical resistivity of both SWCNTs and DWCNTs in the whole temperature range measured here. For instance, we observed that the resistivity of SWCNTs decreases by one-half from 1.1×10^{-3} to 5.0×10^{-4} Ω·cm at 300 K, and the drop was more pronounced at 2 K (1.5×10^{-2} to 2.0×10^{-3} Ω·cm). We further evaluated the dimensionality of percolation paths due to electron hopping and found that the 1D sulfur crystals contribute to new conduction paths. These results led us to conclude that the 1D sulfur crystals act as a new metallic phase consisting only of elemental sulfur at ambient pressure.

We have also reported that not only sulfur but also selenium has the ability to form a 1D crystal inside the narrow cavity of DWCNTs [3]. Interestingly, this 1D phase of selenium exhibits the double-helix structure, and its electronic structure differs significantly from that of bulk selenium consisting of a 3-fold single helix. We foresee that the present findings will open new avenues leading to the discovery of new 1D systems, which is a promising way to transform non-metals into metals, resulting in a new branch of nanoscience in the area of exotic 1D crystals inside CNTs.

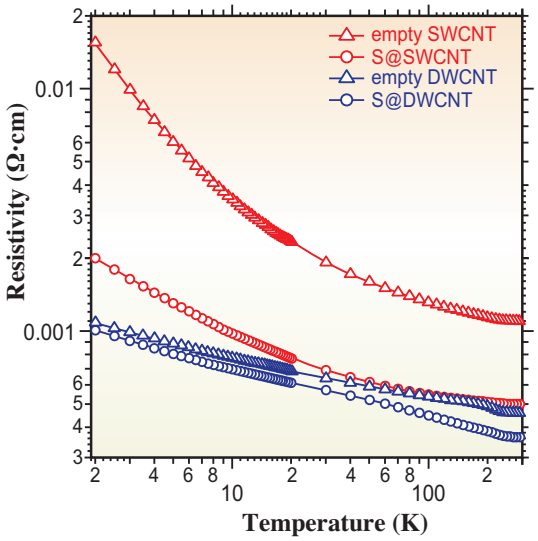

Fig. 3. Temperature-dependent electric resistivity curves of empty SWCNTs, S@SWCNTs, empty DWCNTs, and S@DWCNTs.

Toshihiko Fujimori[a,b]

[a] Center for Energy and Environmental Science, Shinshu University
[b] JST/PRESTO

E-mail: t_fujimori@shinshu-u.ac.jp

References

[1] *T. Fujimori, A. Morelos-Gómez, Z. Zhu, H. Muramatsu, R. Futamura, K. Urita, M. Terrones, T. Hayashi, M. Endo, S.Y. Hong, Y.C. Choi, D. Tománek and K. Kaneko: Nat. Commun.* ***4*** *(2013) 2162.*
[2] M. Springborg and R.O. Jones: Phys. Rev. Lett. **57** (1986) 1145.
[3] *T. Fujimori, R. Batista dos Santos, T. Hayashi, M. Endo, K. Kaneko and D. Tománek: ACS Nano* ***7*** *(2013) 5607.*

A new class of aluminum-based interstitial hydrides, Al_2CuH_x

Safe and efficient hydrogen storage is widely recognized as one of the key technological challenges to realize a hydrogen-based economy. Hydrogen can be stored as a pressurized gas, cryogenic liquid, and solid fuel via chemical or physical combination with other materials; hydrogen forms hydrides with some materials leading to solid-state storage, which provides an important safety advantage over pressurized gas and cryogenic liquid storage methods.

For automotive applications, materials should be mainly composed of light elements ($Z \leq 20$) to reach a high gravimetric hydrogen capacity. In this context, many studies of complex aluminum hydrides have been reported, in which aluminum and hydrogen atoms form complex anions as shown in Fig. 1(a). However, complex aluminum hydrides suited for practical application have not yet been developed. Apart from complex aluminum hydrides, aluminum-based alloy hydrides, i.e., aluminum-based interstitial hydrides (Fig. 1(b)), have not been reported. Pure aluminum and its alloys have low affinity for hydrogen and are difficult to hydrogenate, though their interstitial hydrides are expected to show excellent properties for hydrogen storage. In the present study, we demonstrate the formation of an aluminum-based interstitial hydride Al_2CuH_x [1], which belongs to a new class of aluminum-based hydrides. Its interstitial nature is investigated.

Figure 2(a) shows the crystal structure of the Al_2Cu alloy [2]. A square antiprism consisting of eight aluminum atoms and one copper atom is the structural unit of the crystal structure. One-dimensional chains created by the face-sharing antiprisms share edges to form the crystal structure with interstitial spaces. The starting material was Al_2Cu alloy powder. The sample was pressurized to 10 GPa and heated in hydrogen fluid at temperatures of up to 900°C. The structural changes and hydrogenation reaction of the sample were observed *in situ* by synchrotron radiation X-ray diffraction measurements at beamline **BL14B1** [3].

Figure 3 shows a series of X-ray diffraction profiles taken when the sample was heated at 10 GPa in hydrogen fluid. The Al_2Cu structure was maintained below 880°C. The sample decomposed into pure aluminum and Al_2Cu_3 at 880°C. No hydrogenation reaction occurred at this stage. The sample was cooled to 800°C after the decomposition reaction. The diffraction profile gradually changed as shown in Fig. 3; new Bragg peaks appeared as indicated by arrows in Fig. 3. They were indexed with an enlarged unit cell of the Al_2Cu alloy, suggesting volume expansion caused by the hydrogenation reaction of the Al_2Cu alloy.

The sample was recovered at ambient conditions. Hydrogen evolved at around 150°C when the recovered sample was heated at ambient pressure. After the hydrogen evolution, the sample had the original Al_2Cu structure. Here, it was confirmed that the aluminum-based hydride Al_2CuH_x was formed by the hydrogenation reaction at 10 GPa and 800°C. The hydrogen content was roughly estimated to be $x \approx 1$ on the basis of mass measurements performed during the dehydrogenation reaction.

It is worth mentioning that the hydrogenation reaction proceeded only after the decomposition reaction at 10 GPa and 880°C. The Al_2Cu alloy was not hydrogenated when the sample was heated from room temperature to 800°C at 10 GPa. The surface oxide layer on the alloy was considered to inhibit the hydrogenation reaction. The oxide layer was removed by the decomposition reaction, which allowed the hydrogenation reaction upon the subsequent cooling

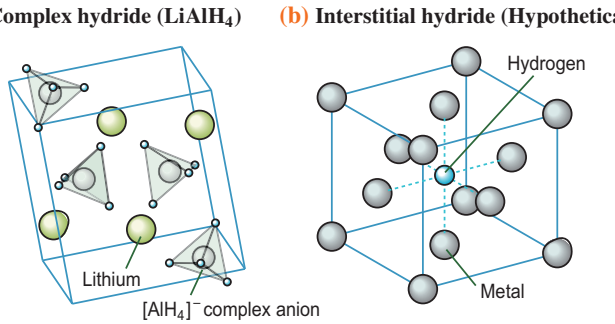

Fig. 1. Schematic of the crystal structure of **(a)** typical complex aluminum hydride ($LiAlH_4$) and **(b)** interstitial hydride (hypothetical). Aluminum and hydrogen atoms form complex anions in the complex aluminum hydride, whereas the metal lattice of the interstitial hydride remains intact during a hydrogenation reaction.

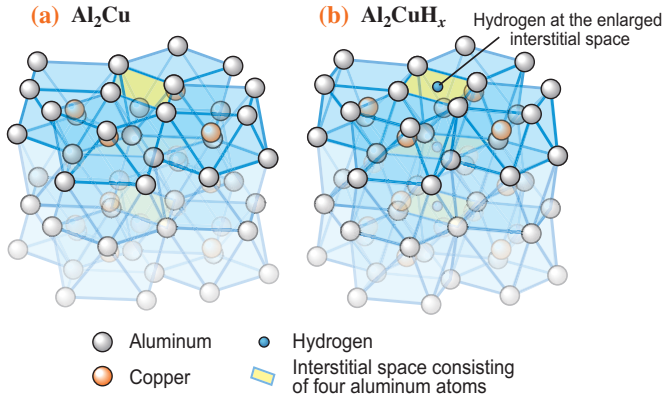

Fig. 2. Schematic of the crystal structure of **(a)** Al_2Cu alloy and **(b)** Al_2CuH_x. Positions of hydrogen atoms were determined only by first-principles calculations.

of the sample. Such a complex synthetic route is difficult to find without the aid of *in situ* synchrotron radiation X-ray diffraction measurement.

Figure 2(b) shows the crystal structure of Al_2CuH_x, which was determined by powder X-ray diffraction measurement and first-principles calculations (note that the positions of hydrogen atoms were determined only by first-principles calculations). The structural change of the Al_2Cu alloy caused by the hydrogenation reaction can be explained as follows. The Al_8Cu square antiprisms twist to enlarge the interstitial spaces consisting of four aluminum atoms. Hydrogen atoms are located at the center of the enlarged interstitial sites to form the interstitial hydride Al_2CuH_x. The electronic structure of Al_2CuH_x determined by first principles calculations also illustrates the interstitial nature of the hydride [1].

The aluminum-based interstitial hydride Al_2CuH_x (x~1) has been successfully synthesized by hydrogenating Al_2Cu alloy at high temperatures and pressures. Al_8Cu square antiprisms in Al_2Cu twisted during the hydrogenation reaction, which enlarges the interstitial spaces enabling the accommodation of hydrogen atoms. The properties of interstitial hydrides are favorable for hydrogen storage materials because the hydrogenation and dehydrogenation reactions should proceed simply and their thermodynamic properties are tunable by the addition of other elements to the alloy. Both the experimentally and theoretically obtained results in the present study will be useful for exploring other aluminum-based interstitial hydrides. These findings will help expand the variety of aluminum-based alloy hydrides, which, in turn, will help in developing practical hydrogen-storage materials.

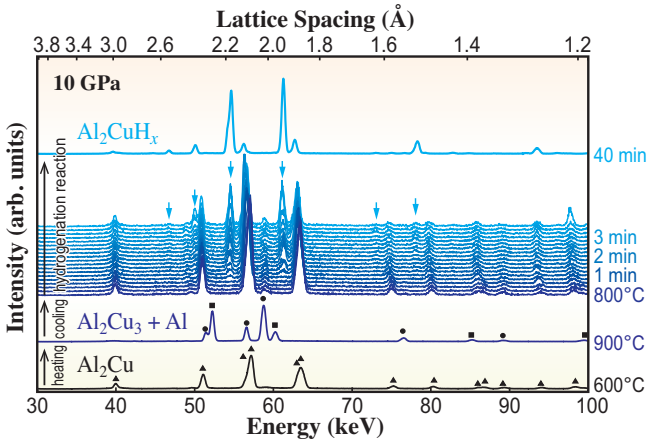

Fig. 3. Series of *in situ* synchrotron radiation X-ray diffraction profiles of the sample during heat treatment at 10 GPa. Bragg peaks denoted by triangles, circles, and squares originated from Al_2Cu, Al_2Cu_3, and pure aluminum, respectively. Arrows indicate Bragg peaks originated from the formed hydride.

Hiroyuki Saitoh

SPring-8/JAEA

E-mail: cyto@spring8.or.jp

References

[1] *H. Saitoh, S. Takagi, N. Endo, A. Machida, K. Aoki, S. Orimo and Y. Katayama: APL Mater. **1** (2013) 032113.*
[2] A. Meetsma *et al.*: J. Solid State Chem. **83** (1989) 370.
[3] W. Utsumi *et al.*: J. Phys. Condens. Matter **14** (2002) 10497.

Synchrotron infrared spectroscopy of water on polyelectrolyte brush surface

Polymers chemically grafted to the surface of substrates, known as polymer brushes, are often used to modify surface properties such as hydrophilicity or hydrophobicity, friction, and adhesiveness. Superhydrophilic surfaces are particularly attractive because of their potential applications to self-cleaning, antifogging, antifouling, and water lubrication systems. In this work, we examined the wettability of water on a cationic poly(2-(methacryloyloxy)ethyl trimethylammonium chloride) (PMTAC) brush prepared on a silicon wafer by contact angle measurement and synchrotron infrared (IR) spectroscopy [1].

The wettability of solids can be characterized by the spreading coefficient. The initial spreading coefficient, S_0, is defined as

$$S_0 = \gamma_{sv} - \gamma_{lv} - \gamma_{sl} \qquad (1)$$

Here, γ_{sv}, γ_{lv}, and γ_{sl} are the interfacial tension at the solid/vapor, water/vapor, and solid/water interfaces, respectively. When S_0 is positive, a water droplet deposited on a dry surface spreads and completely wets the surface. In contrast, a negative S_0 value indicates partial wetting. A positive S_0 value and, accordingly, the complete wetting state are expected for polyelectrolyte brush surfaces because they exhibit the extremely high γ_{sv} and quite low γ_{sl} values.

The contact angle measurement was carried out by reflection interference contrast microscopy. Monochromatic light (λ = 546 nm) vertically irradiated onto a water droplet was reflected at the air/water surface or at the water/substrate interface. These two types of reflection create interference at the water surface, which enabled us to calculate the drop shape profile and determine the contact angle of water on the PMTAC brush (Fig. 1). The contact angle was extremely small but remained finite at 0.95°, contrary to our expectation based on the spreading coefficient.

The above results led us to a fundamental question: why is complete wetting not achieved, even with superhydrophilic polyelectrolyte brushes? To answer this question, we performed synchrotron IR spectroscopy at beamline **BL43IR**. A fine-focused IR beam from the synchrotron radiation was narrowed to 10 μm × 10 μm through an aperture. A small amount of water was deposited on the polyelectrolyte brush surface and dry air was gently passed around it to purge water vapor from the beam path. The IR spectra were obtained from the beam reflected from the inside and outside of a water droplet approximately 10–50 μm away from the boundary (crosses in Fig. 1(a)). The representative spectra of water on the PMTAC brush are shown in Fig. 2. Inside the droplet, the spectrum had a broad peak centered at around 3450 cm^{-1}, which arose from the O–H stretching vibration (filled circles). This is a typical IR spectrum for water, and the broad shape reflects the diversity of the hydrogen bond network. Figure 2 also shows the spectrum obtained from the outside of the droplet (filled triangles). Intriguingly, even though the water phase was not visible under the microscope, weak O–Hstretching absorption was detected. This was not from the vapor phase, which we confirmed was removed by purging with dry air in exactly the same setup. Furthermore, this small absorption was not seen at points sufficiently far from the droplet. Therefore, the absorption peak suggested the presence of a microscopic amount of water at the surface only in the vicinity of the droplet. Even more noteworthy is that, the position of the O–H stretching peak shifted from 3450 cm^{-1} to around 3200 cm^{-1}. This small peak was visible, even inside the droplet, as a slight shoulder on the main peak (arrow in Fig. 2). The peak shift to the lower wavenumber implied that the hydrogen bonds between the water molecules became shorter and that

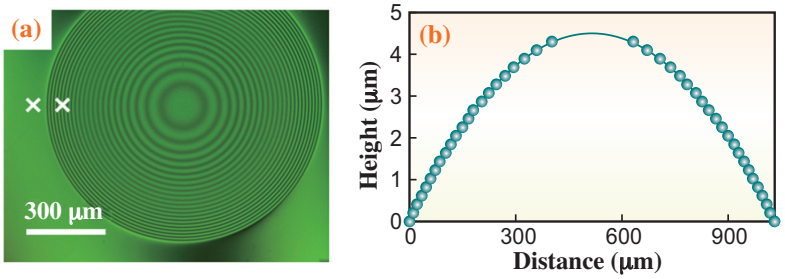

Fig. 1. **(a)** Interference rings of a water droplet on the surface of PMTAC brush. The crosses indicate the points measured by IR spectroscopy. **(b)** Drop profile calculated from the interference.

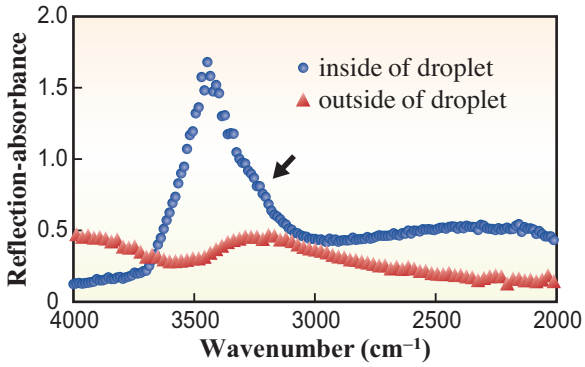

Fig. 2. IR spectra of water on the PMTAC brush: (●) inside and (▲) outside of the water droplet (see the crosses in Fig. 1). The outside spectrum is shown at 2× magnification for clarity.

the entire network became more rigid [2]. The peak at around 3200 cm^{-1} has previously been observed for amorphous solid water [3]. We conclude that a thin layer of water, which included highly structured water, existed beneath and around the water droplet. The structuring of the water molecules can be attributed to both the spatial confinement in the thin layer and the hydration effect around the ionic species.

A schematic model of the wetting of the polyelectrolyte brushes is shown in Fig. 3. The initial spreading coefficient, S_0, is not valid for the wetting of a polyelectrolyte brush, because it assumes that the surface is dry and does not take the spreading and structuring of the water into consideration. Thus, we used the local equilibrium spreading coefficient, S, for the coexisting thin film.

$$S = \gamma_{sv}^{eq} - \gamma_{lv} - \gamma_{sl}^{eq} \qquad (2)$$

The spontaneous penetration of water into the brush layer implied that the surface tension of the wet brush, γ_{sv}^{eq}, is lower than that of the dry surface, γ_{sv}. This is mainly due to the enthalpy and entropy of the mixing of the polymer and water, and the surface rearrangement of α-methyl groups, which have relatively low surface energy, caused by the high flexibility of polymer chains in the wet brush. Furthermore, the solid/water interfacial tension after the structuring of water, γ_{sl}^{eq}, should be much higher than γ_{sl}, which is expected to be extremely low because the thermodynamic properties of structural water resemble those of ice rather than liquid water. It has been reported that the interfacial tension at the ice/water interface is fairly [4]. These two effects result in $S < S_0$ and an increase in the contact angle, which breaks the conditions for complete wetting. Therefore, we concluded that a thin layer composed of the swollen polymers and the structural water existed under and even outside the droplet, and prevented the complete wetting of the highly hydrophilic polyelectrolyte brushes.

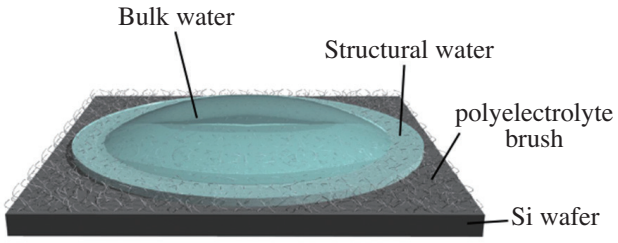

Fig. 3. Schematic illustration of the wetting of a polyelectrolyte brush.

Daiki Murakami and Atsushi Takahara*

JST ERATO Takahara Soft Interfaces Project
Institute for Materials Chemistry and Engineering,
Kyushu University

*E-mail: takahara@cstf.kyushu-u.ac.jp

References

[1] *D. Murakami, M. Kobayashi, T. Moriwaki, Y. Ikemoto, H. Jinnai, A. Takahara: Langmuir* ***29*** *(2013) 1148.*
[2] K. Nakamoto *et al.*: J. Am. Chem. Soc. **77** (1955) 6480.
[3] S.A. Rice *et al.*: J. Phys. Chem. **87** (1983) 4295.
[4] A. Adamson *et al.*: J. Colloid Interface Sci. **34** (1970) 461.

Sequential multiphoton multiple ionization of xenon atoms by intense X-ray free-electron laser pulses from SACLA

In early 2012, a new XFEL facility, the SPring-8 Angstrom Compact free electron LAser (SACLA) [1], started user operation. One of the first experiments at SACLA was to detect anomalous signals of naturally occurring sulfur atoms in a protein (lysozyme microcrystal) at a photon energy of 7.3 keV, set far from the sulfur *K*-edge (~2.5 keV) to suppress electronic damage [2]. Although the attempt to clarify the anomalous substructure failed, the results demonstrated that anomalous data can indeed be obtained by serial femtosecond crystallography (SFX). As a next step, we have investigated dynamical behaviors, i.e., deep inner-shell multiphoton ionization and cascade decay, of heavy Xe atoms exposed to high-intensity X-ray pulses at 5 and 5.5 keV [3,4].

Multiphoton processes are well-known phenomena in the optical regime and have been investigated for decades. The advent of extreme ultraviolet (EUV) FELs with femtosecond pulse widths has led to renewed interest in multiphoton ionization processes in the EUV regime. The objective of these studies was mainly to reveal the pathways of multiphoton multiple ionization newly opened up by these light sources. Multiphoton processes at higher photon energies discussed in the present work are of particular importance because of their direct relevance to electronic damage in high-resolution X-ray imaging measurements.

The experiment was carried out at the experimental hutch 3 (EH3) of beamline 3 (BL3) of SACLA [5]. The XFEL beam was focused by a Kirkpatrick-Baez mirror system to a focal diameter of ~1 μm (FWHM). Xe gas was introduced as a pulsed supersonic gas jet to the focal point of the XFEL pulses in an ultrahigh-vacuum reaction chamber. The XFEL pulse energies were measured by a beam-position monitor located upstream of the beamline. The relative X-ray pulse energy passing through the interaction point was also measured shot-by-shot by a PIN photodiode.

Ions produced in the source volume were extracted towards an ion time-of-flight (TOF) spectrometer equipped with microchannel plates (MCP) and a delay-line anode (Roentdek HEX80). Signals from the delay-line anode and MCP were recorded by a digitizer and analyzed by a software discriminator. The arrival time and arrival position of each ion were determined. The position information was used to compensate the TOF, which varied with the departure position perpendicular to the spectrometer axis [4]. Figure 1 depicts the TOF spectrum for Xe ions measured at a photon energy of 5.5 keV after TOF compensation. We can clearly see ions with charge states of up to +26 and well-resolved isotopes at different charge states.

Figure 2 depicts the charge state distribution of Xe at photon energies of 5 and 5.5 keV. The peak fluence of the XFEL pulse determined by calibration using Ar [3,4] is 47 μJ/μm^2 for both photon energies. The charge state distribution varies with the peak fluence. The peak fluence dependence of the ion yield for each charge state indicates the contribution of multiphoton processes. Charge states of up to +22 are oserved at the photon energy of 5 keV, whereas charge states of up to +26 are observed at the photon energy of 5.5 keV. The binding energies of 2*s*, 2$p_{1/2}$, and 2$p_{3/2}$ of neutral Xe are 5.5, 5.1, and 4.8 keV, respectively. According to the calculated results [3,4], the 2*p* ionization thresholds become larger than 5 keV beyond the charge state of +11; thus, the sequential one-photon ionization ends at the charge state of +11 for the photon energy of 5 keV. On the other hand, the photon energy of 5.5 keV is above the ionization thresholds for charge states of up to +23. Thus, one-photon ionization is always induced at the charge states of up to +23 for the photon energy of 5.5 keV. Therefore, the maximum charge state at 5 keV is lower than that at 5.5 keV.

Theoretical charge state distributions [3,4] are also shown in Fig. 2. In the theoretical model, relativistic effects and shake-off are not included.

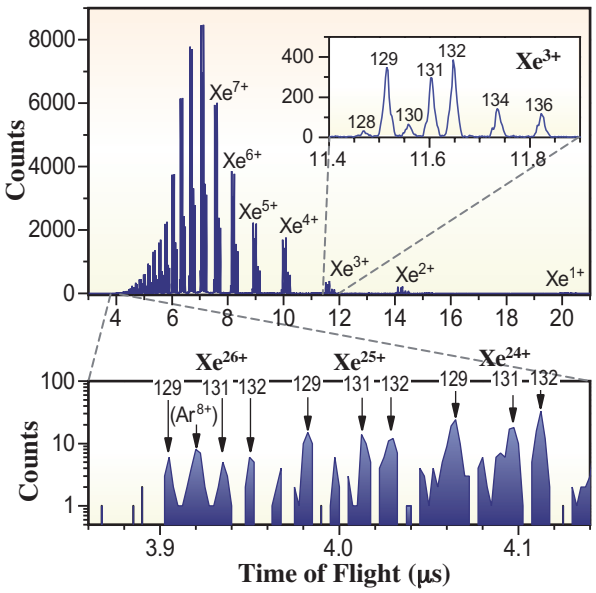

Fig. 1. Ion time-of-flight spectrum of Xe recorded at the photon energy of 5.5 keV [3].

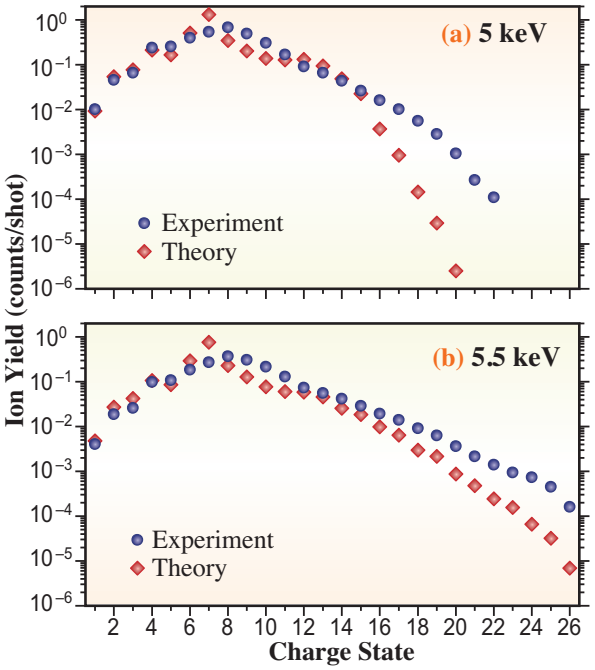

Fig. 2. Experimental and theoretical charge state distributions of Xe at the photon energies of 5 keV **(a)** [4] and 5.5 keV **(b)** [3]. The peak fluence is 47 μJ/μm^2 for both photon energies.

In spite of these limitations, the experimental and theoretical results are in reasonable agreement at 5.5 keV, at least semiquantitatively. In the charge state distribution at 5 keV, notable discrepancies between experimental and theoretical results appear above the charge state of +16 and increase with the charge state. The discrepancies, namely, significantly higher ion yields for high charge states and the highest charge state of +22 in the experiment, are interpreted on the basis of the resonant-enabled X-ray multiple ionization mechanism, where transient resonant excitation enhances the ionization process beyond the limit expected by the sequential ionization model. This feature is not shown at 5.5 keV, because 5.5 keV is above each ionization threshold.

Let us consider the pathways of multiphoton multiple ionization observed in this study. Figure 3 depicts one typical pathway yielding Xe^{24+} obtained by theoretical calculation [3]. The plot illustrates that the total energy of the system varies in the course of ionization. After L-shell photoionization, the energetically excited core-hole state relaxes via a series of Auger and Coster-Kronig decays and/or fluorescences. Note that another photoionization occurs before the atom fully relaxes to the ground configuration. For each photoionization, the deep single-core vacancy is rapidly filled up within sub-fs, and the time scale of the accompanying Auger and Coster-Kronig decay cascade ranges from a few fs to tens of fs. The time scale of fluorescences at the highest charge state is about 0.7 ps. In the present calculations, the pulse shape is assumed to be a Gaussian with an FWHM of 30 fs. In the case of sequential multiphoton absorption, the results are not sensitive to the pulse shape or spikiness of individual pulses, unless the pulse duration is much shorter than the decay time scale.

In conclusion, we have clarified that the ionization of heavy atoms irradiated by intense XFEL pulses rapidly progresses with the repetition of inner-shell photoionization and following Auger/Coster-Kronig decay within the XFEL pulse duration. Understanding the ionization dynamics of heavy atoms exposed to high-intensity hard-X-ray beams will provide useful input for future molecular imaging experiments using XFELs.

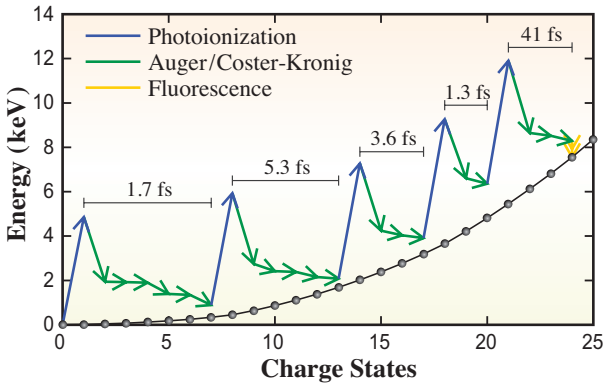

Fig. 3. Exemplar pathway of multiphoton multiple ionization of Xe at 5.5 keV [3]. The black solid line with dots indicates the ground-configuration energy for the given charge states, and the energy of neutral Xe is set to zero.

Hironobu Fukuzawa[a,b,*], Koji Motomura[a] and Kiyoshi Ueda[a,b]

[a] Institute of Multidisciplinary Research for Advanced Materials, Tohoku University
[b] SPring-8/RIKEN

*E-mail: fukuzawa@tagen.tohoku.ac.jp

References

[1] T. Ishikawa *et al.*: Nat. Photonics **6** (2012) 540.
[2] T.R.M. Barends *et al.*: Acta Cryst. D **69** (2013) 838.
[3] *H. Fukuzawa, S.-K. Son, K. Motomura, S. Mondal, K. Nagaya, S. Wada, X.-J. Liu, R. Feifel, T. Tachibana, Y. Ito, M. Kimura, T. Sakai, K. Matsunami, H. Hayashita, J. Kajikawa, P. Johnsson, M. Siano, E. Kukk, B. Rudek, B. Erk, L. Foucar, E. Robert, C. Miron, K. Tono, Y. Inubushi, T. Hatsui, M. Yabashi, M. Yao, R. Santra, K. Ueda: Phys. Rev. Lett.* ***110*** *(2013) 173005.*
[4] *K. Motomura et al.: J. Phys. B* ***46*** *(2013) 164024.*
[5] K. Tono *et al.*: New J. Phys. **15** (2013) 083035.

Attosecond X-ray interaction with core-hole atoms

We assume implicitly that X-rays interact with atoms in their ground state when we analyze data obtained by X-ray diffractometry or spectroscopy. Now, the success of X-ray free-electron lasers (XFEL) challenges this "common sense." A femtosecond flush of XFEL provides X-ray photons comparable to those generated by SPring-8 undulator beamlines over one second. Such high intensity X-rays may be able to excite most atoms in the beam section several times. Furthermore, the interval of the successive excitations may be shorter than the lifetime of the core-hole states. Since the X-ray property in the core-hole states differs considerably from that in the ground state, the X-ray interaction with the core-hole atoms is very important for the analysis of XFEL experiments as well as the basic interest in the field of X-ray nonlinear optics.

To investigate the X-ray interaction with the core-hole states, we measured X-ray fluorescence from krypton gas illuminated by focused XFEL beam of SACLA [1]. When X-rays photoionize an atom, the $K\alpha$ fluorescence is emitted from the atom with a core hole in the K shell. When X-rays photoionize the single core-hole (SCH) atom again before the fluorescence decay, it becomes a double core-hole (DCH) state. The fluorescence from the DCH state is called the hypersatellite $K^h\alpha$, giving evidence of X-ray interaction with SCH atoms. The incident photon energy of 15 keV is sufficiently high to create the DCH state by sequential photoionization, and is considerable lower than the threshold of the shake-off process of around 29 keV. A Kirkpatrick-Baez mirror system [2] focused X-rays down to 1.2 × 1.3 μm^2, increasing the peak intensity.

Figure 1 shows the fluorescence spectrum with clear hypersatellite peaks on the higher photon energy side [3]. Both $K\alpha$ and $K^h\alpha$ are doublets because of splitting of the L shell into the L_2 and L_3 subshells. We emphasize that the lifetime of the SCH state is only 170 attoseconds. Nevertheless, the focused XFEL beam photoionizes the SCH atom again to create the DCH atom, providing evidence of the attosecond X-ray interaction with SCH atoms.

Since the DCH creation is a two-photon process, the $K^h\alpha$ yield is expected to depend quadratically on the pulse energy. However, the measured dependence appears to be just superlinear (Fig. 2). The milder dependence is due to the linear contribution from the $K\alpha$ tail. The measured dependence can be fitted by a sum of linear and quadratic terms.

Now, we discuss a possible application of the DCH creation. The different pulse-energy dependence between the $K\alpha$ and the $K^h\alpha$ fluorescence yields allows us to estimate the pulse duration. Such estimation is not straightforward because of the temporal pulse shape. First, the DCH creation is a sequential process; thus, its efficiency depends on the pulse duration. For example, it is suppressed as the pulse duration approaches the SCH lifetime. Fortunately, the SCH lifetime of 170 attoseconds is considered to be much shorter than the expected pulse duration. Accordingly, the pulsed effect is

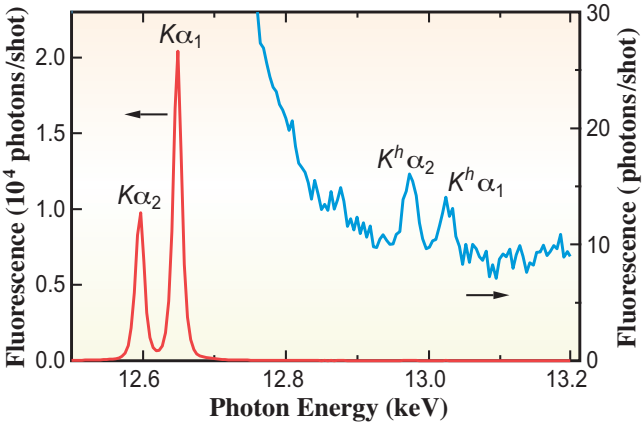

Fig. 1. X-ray fluorescence spectrum of krypton. Hypersatellite peaks $K^h\alpha$ are observed on the higher photon-energy tail of the $K\alpha$ lines.

not important in the present case. Second, the spiky temporal structure due to the self-amplified spontaneous-emission operation can increase the rate of DCH creation, because the instantaneous intensity is higher than that expected from an averaged smooth profile. The effect can be included statistically in the estimation as the degree of second-order coherence, $g^{(2)}(\tau)$.

At present, there is no experimental technique that can be used to determine $g^{(2)}(\tau)$. Thus, we employ an XFEL simulation code, SIMPLEX [4]. The parameters, such as emittance and peak current of the electron beam, are determined from the measured FEL gain curve. Then, we refine these parameters so that the degree of the first-order coherence, $g^{(1)}(\tau)$, calculated from the simulation results agrees with that determined from measured single-shot spectra. Using the calculated $g^{(2)}(\tau)$ and assuming a Gaussian pulse shape, we analyze the ratio between the $K\alpha$ and the $K^h\alpha$ fluorescence, and determine the pulse duration to be 2.5-2.8 fs (FWHM). Our estimation is found to be consistent with the electron bunch length deduced from the measured FEL gain length.

In conclusion, we successfully observed, for the first time, the DCH creation by sequential X-ray two-photon ionization and showed that intense X-rays can interact with atoms in the core-hole states. Here, we briefly discuss the impact on the structural analysis using an XFEL. When an atom becomes the SCH state, the absorption edge shifts to higher photon energies, and the anomalous scattering factor changes drastically. Since the anomalous phasing method widely used in protein crystallography relies on the physical property at the *K* edge of atoms in the ground state, it would be important to know how much X-rays are scattered by the SCH atoms. We also show that the DCH creation is useful for determining the pulse duration in the sub-10-femtosecond range. Compared with other two-photon processes, such as two-photon absorption and second-harmonic generation, we consider that the DCH creation is more efficient and suitable for XFEL beam characterization. Combined with X-ray optical delay, one will be able to construct an X-ray autocorrelator with a femtosecond resolution.

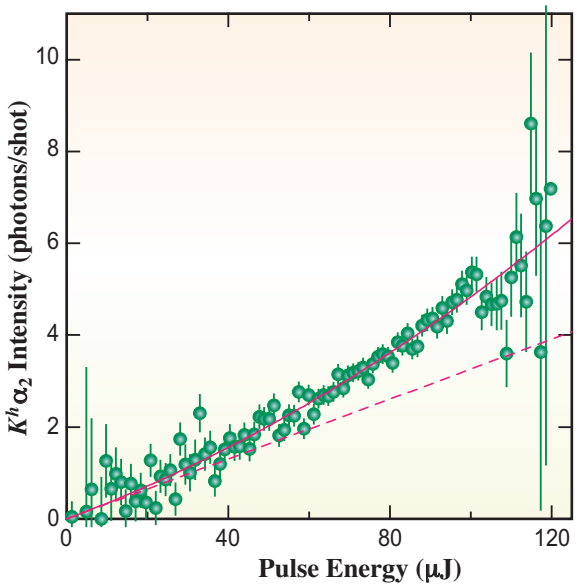

Fig. 2. Pulse-energy dependence of the $K^h\alpha_2$ fluorescence. Circles indicate the measured fluorescence intensity. Vertical bars indicate the standard error of the mean. Solid line shows the fitting with a sum of linear (dashed line) and quadratic terms.

Kenji Tamasaku

SPring-8/RIKEN

E-mail: tamasaku@riken.jp

References

[1] T. Ishikawa *et al.*: Nat. Photonics **6** (2012) 540.
[2] H. Yumoto *et al.*: Nat. Photonics **7** (2013) 43.
[3] *K. Tamasaku, M. Nagasono, H. Iwayama, E. Shigemasa, Y. Inubushi, T. Tanaka, K. Tono, T. Togashi, T. Sato, T. Katayama, T. Kameshima, T. Hatsui, M. Yabashi, T. Ishikawa: Phys. Rev. Lett.* ***111*** *(2013) 043001.*
[4] T. Tanaka: Proc. FEL Conf. 2004 (Comitato Conferenze Elettra, Trieste, 2004) p. 435.

Earth & Planetary

It is not an exaggeration to say that expansion of high-pressure generation conditions, which can be achieved by advances in high-pressure generation techniques using diamond-anvil cell (DAC) and large volume press (LVP) apparatuses, is the engine for development in Earth and planetary sciences. In 2010, advances in a combination technique of a diamond-anvil cell and laser heating successfully simulated high-pressure and high-temperature conditions corresponding to the center of the Earth (6400 km beneath the surface). These innovative techniques allows *in situ* X-ray diffraction studies of pure iron at such extreme conditions, enhancing the understanding of the state and evolution of the Earth's core and providing new knowledge about the Earth's deep interior. Here, two highlights by a brilliant X-ray source and the DAC technique will be first presented.

Ozawa *et al.* performed *in situ* X-ray diffraction experiments of iron sulfide at pressures and temperatures characteristic of the Earth's core and found that Fe_3S decomposes into Fe and FeS. They have suggested that sulfur may be an unlikely major light element in the Earth's core. Moreover, to learn about how iron behaves under extreme conditions like those at the Earth's core, Ohtani *et al.* determined the density and the vibrational properties of compressed pure iron by X-ray diffraction and inelastic X-ray scattering. Comparing their new data to seismic observations of the core, they discussed the composition of the Earth's core and showed the importance of information about both the density and the sound velocity in constraining the composition of the Earth's core.

Science

Although the pressure range attainable by the LVP apparatus is limited compared to that by the DAC, many unique studies have been carried out due to the larger sample space in LVP. Kawamoto *et al.* observed separation of a supercritical fluid with the composition of water-rich slab-derived components using an *in situ* X-ray radiographic method in LVP, and determined the second critical endpoint of two magmatic-hydrothermal systems. They showed that the existence of the critical endpoints plays a particularly important role on how various types of magma are generated in the subduction zones. Sakamaki *et al.* investigated the density, viscosity, and structure of molten basalt under high-pressure and high-temperature conditions in subduction zones. They concluded that ascending basaltic magma would have accumulated extensively in the pressure and temperature conditions corresponding to the boundary between the lithosphere and the asthenosphere due to the difference in melt mobilities.

Finally, new results of high-pressure generation over 100 GPa using LVP will be reported. Using X-ray source and a Kawai-type multi-anvil high-pressure apparatus with large sintered diamond anvils, Yamazaki *et al.* probed silicon dioxide (SiO_2) at extreme pressures and temperatures up to 109 GPa and 900 K, and observed the structural phase transition of stishovite, a high-pressure phase of SiO_2, to the $CaCl_2$-type phase. This technical evolution contributes to the understanding of the whole Earth's mantle and plays major roles in the advancement of high-pressure research.

Yasuo Ohishi

Separation of supercritical slab-fluids to form aqueous fluid and melt components in subduction zone magmatism

Subduction-zone magmatism is triggered by the addition of H_2O-rich slab-derived components such as aqueous fluid, hydrous partial melts, or supercritical fluids from the subducting slab. Whether the slab-derived component is an aqueous fluid, a partial melt, or a supercritical fluid persists as an open question. In general, with increasing pressure, aqueous fluids dissolve more silicate components and silicate melts dissolve more H_2O. Under low-pressure conditions, these aqueous fluids and hydrous silicate melts are divided by an immiscibility gap. The highest temperature of the immiscibility gap between the fluids and the melts is designated as a critical point. The temperature of the critical point decreases concomitantly with increasing pressure and finally reaches the H_2O-saturated solidus temperature. Under this pressure and temperature condition, no difference exists between hydrous silicate melts and aqueous fluids. This point is designated as a critical end point. Geochemical analyses of island arc basalts suggest the two slab-derived signatures of a melt and a fluid [1]. These two liquids unite to a supercritical fluid under P-T conditions beyond the critical end point.

X-ray radiography experiments [2,3] were conducted using the SPEED1500 Kawai-type multi-anvil apparatus installed at beamline **BL04B1** to examine unmixing and mixing behavior of a sediment melt and aqueous fluids, and of a high-Mg andesite (HMA) melt and aqueous fluids under high-pressure and high-temperature conditions. When we heated the sample at low pressures with various H_2O concentrations, we observed one round material in another material with different X-ray absorbance. We interpreted these to be coexisting silicate melt and aqueous fluid (Fig. 1(a)). At high pressures, we observed no such coexisting phase, but found gold powders, which was added to facilitate visualization of the boundary, falling during heating (Fig. 1(b)). Two phases were observed during heating and cooling in radiography images at pressures lower than 2.8 GPa in HMA–H_2O and 2.5 GPa in sediment-H_2O [4]. At higher pressures, only a single phase was recognized. The radiography results are also shown in pressure-temperature diagrams at constant bulk H_2O, in which critical curves and the H_2O-saturated solidus temperature meet at critical end points in HMA–H_2O and sediment-H_2O. These results show that the pressure of the second critical end point can be at 2.8 GPa (92 km depths) and 750°C for HMA–H_2O, and 2.5 GPa (83km depths) and 700°C for sediment-H_2O.

These depths are within the mantle wedge underlying volcanic arcs, which are formed 90–200 km above subducting slabs. These data suggest that sediment-derived supercritical fluids, which are fed to the mantle wedge from the subducting slab, react with mantle peridotite to form HMA supercritical fluids. Such HMA supercritical fluids separate into aqueous fluids and HMA melts at 92 km depth during ascent. The aqueous fluids are fluxed into the asthenospheric mantle to form arc basalts, which are locally associated with HMAs in hot subduction zones. The separated HMA melts retain their composition in limited equilibrium with the surrounding mantle. The separation of slab-derived supercritical fluids into melts and aqueous fluids can explain the two slab-derived components observed in subduction zone magma chemistry.

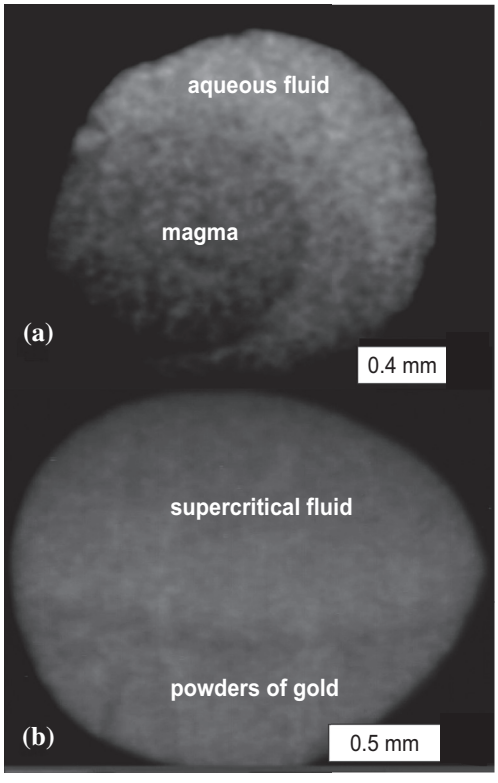

Fig. 1. Snapshots of radiography.
(a) X-ray radiograph shows unmixing between HMA (dark circle) and aqueous fluid (matrix) at 1011°C and 1.5 GPa (run 2234).
(b) X-ray radiograph shows the gold-powder-rich portion (lower dark half) falling in a uniform single supercritical fluid in the sediment with 50% (wt) H_2O at 953°C and 2.6 GPa (run 1536).

The newly determined critical end points suggest that slab-derived fluids are expected to be under supercritical conditions in the slab sediment layer and at the base of the mantle wedge, where HMA-bearing supercritical fluid is presumably formed by a reaction between sediment-derived supercritical fluids and peridotite, beneath the volcanic arcs. Therefore, no isolated fluid/melt phase exists, but there is a single supercritical fluid phase (with a continuum characteristic between aqueous fluid and hydrous melt in the downgoing sediments) at least > 83 km, and the base of the mantle wedge (underneath volcanic arcs) at least > 92 km.

Elliott *et al.* [1] recognized two slab-derived components in basalt chemistry: a partial melt from the subducting sedimentary layer and an aqueous fluid from the subducting basaltic layer. In our hypothesis (Fig. 2) [4,5], the melt and the fluid components can coexist in the mantle wedge if the supercritical slab-fluids supplied from the downgoing slabs separate into a melt and an aqueous fluid. Two such distinct slab-derived components have also been suggested to explain the chemistry of many arc basalts. Separation of slab-derived supercritical fluids into melts and aqueous fluids can commonly occur in most subduction zones.

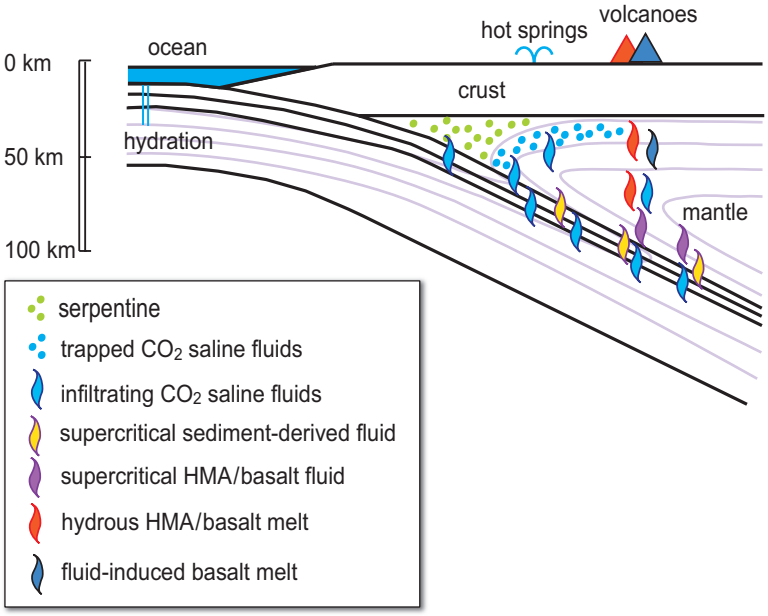

Fig. 2. Schematic illustration showing separation of supercritical fluids into aqueous fluid and hydrous melt. When a sediment-derived supercritical fluid enters the overlying mantle, the fluid will react with the peridotite to become HMA-bearing supercritical fluid. This HMA-bearing supercritical fluid migrates upwards and meets the critical end point. Then it will separate into a melt phase and a fluid phase. The HMA or basalt melt will continue to react with mantle to form a melt-derived magma or a Mg-rich andesitic magma. The fluid will trigger hydrous partial melting of the ambient mantle peridotite to form a fluid-derived magma. [4,5]

Tatsuhiko Kawamoto[a,*], Masami Kanzaki[b] and Kenji Mibe[c]

[a] Graduate School of Science, Kyoto University
[b] Institute for Study of the Earth's Interior, Okayama University
[c] Earthquake Research Institute, The University of Tokyo

*E-mail: kawamoto@bep.vgs.kyoto-u.ac.jp

References

[1] T. Elliott *et al.*: J. Geophys. Res. **102** (1997) 14991.
[2] M. Kanzaki *et al.*: High-Pressure Research in Mineral Physics, edited by M.H. Manghnani and Y. Syono. American Geophysical Union, Washington (1987) pp. 195.
[3] K. Mibe *et al.*: Proc. Natl. Acad. Sci. USA **108** (2011) 8177.
[4] *T. Kawamoto, M. Kanzaki, K. Mibe, K.N. Matsukage, S. Ono: Proc. Natl. Acad. Sci. USA* ***109*** *(2012) 18695.*
[5] *T. Kawamoto, M. Yoshikawa, Y. Kumagai, Ma.H.T. Mirabueno, M. Okuno and T. Kobayashi: Proc. Natl. Acad. Sci. USA* ***110*** *(2013) 9663.*

A magma "traffic jam" between lithosphere and asthenosphere

Along the axial zone of mid-ocean ridges (MOR), the asthenospheric mantle rises in response to the diverging motion of the oceanic lithosphere and experiences decompression melting. Depending on the volatile content and temperature of the upper mantle, peridotite partial melting initiates at depths of about 80 to 130 km. The resulting basaltic magmas are buoyant and mobile, percolating upward to form the crust, and leaving a refractory residuum that forms the oceanic lithosphere.

Structural changes in basaltic magmas with pressure (or depth) play a central role in the control of melting and magma mobility. Density measurements of basaltic magmas have thus far been carried out by the sink-float method [1]. Here, we apply X-ray absorption [2,3], an alternative method that enables the determination of liquid density under desired conditions. Furthermore, we use *in situ* falling-sphere viscometry and *in situ* X-ray diffraction [4,5] to measure magma viscosity and magma structure, respectively. The resulting complete and detailed dataset allows us to examine pressure-dependent changes in magma density, viscosity, and structure in unprecedented detail.

X-ray absorption measurements were performed up to 4.5 GPa and 2000 K at beamline **BL22XU**. We find that the density of basaltic magmas increases rapidly at pressures of ~4 GPa (Fig. 1(a)). Such rapid densification is consistent with previous studies on quenched aluminosilicate melts, which showed that Al coordination number increase rapidly between 3 and 5 GPa.

We further conducted *in situ* viscosity measurements by the falling-sphere method with X-ray radiography at beamline **BL04B1**. For basaltic magma, the isothermal viscosity first decreases and then increases with pressure. Viscosity minima are clearly discernible, both along the 1900 and 2000 K isotherms (Fig. 1(b)). The pressure of the viscosity minimum further coincides with that of rapid densification, suggesting that both are related to the same pressure-induced structural changes in the basaltic magma.

In order to clarify the nature of the structural changes, we performed X-ray diffraction experiments from 1.9 to 5.5 GPa at 1800 to 2000 K at beamline BL04B1. The X-ray diffraction interference functions, *Qi(Q)*, and its Fourier transform *G(r)*, i.e., the radial distribution function, are determined. The first peak at r = 1.6-1.7 Å in *G(r)* corresponds to the average T-O bond length, i.e., the length between tetrahedrally coordinated cations (T = Si^{4+}, Al^{3+}) and oxygen.

The T-O bond length is a characteristic parameter of the network structure of magmas. Figure 1(c) shows the T-O length of basaltic magma as a function of pressure, along with those of $MgSiO_3$ and $CaSiO_3$ melts, and corundum. No experimental data for the structure of basaltic magma at ambient pressure are available as a benchmark. For reference, we use the T-O length of anorthite melt at zero pressure. The T-O bond length in basaltic magma at ambient pressure may be shorter than that of anorthite melt because of the smaller Al_2O_3 content. We find that, for basaltic melt, the T-O length decreases between 1.9 and 4.3 GPa, and then increases between 4.3 and 5.5 GPa. Only the initial decrease is consistent with the simple compression of magma. As the T-O lengths in TO_6 octahedrons are generally longer than those in TO_4 tetrahedrons, the extension of the T-O length at high pressures is consistent with an increase in cation coordination. Between 4 and 6 GPa, the increase in Al^{3+} coordination is generally more extensive than that in

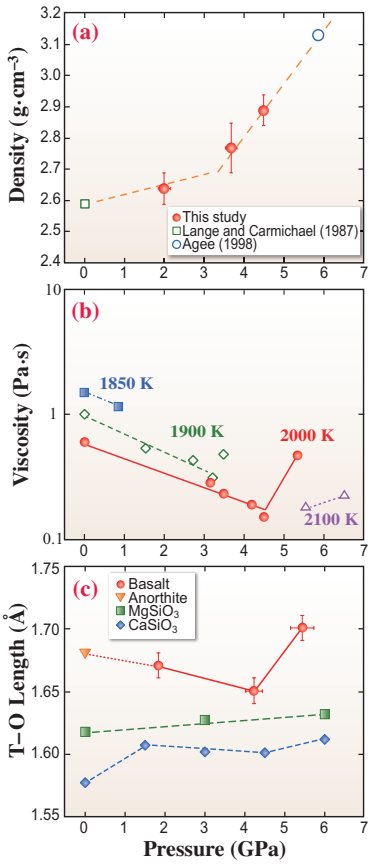

Fig. 1. Results of the experimental study. **(a)** Density of basaltic magma as a function of pressure at 2000 K. Anomalous densification occurs between 4 and 6 GPa. **(b)** Viscosity of basaltic magma at high pressure and temperature. **(c)** Pressure dependence of the T-O bond length of basaltic magma from this study, and other silicate melts from previous studies.

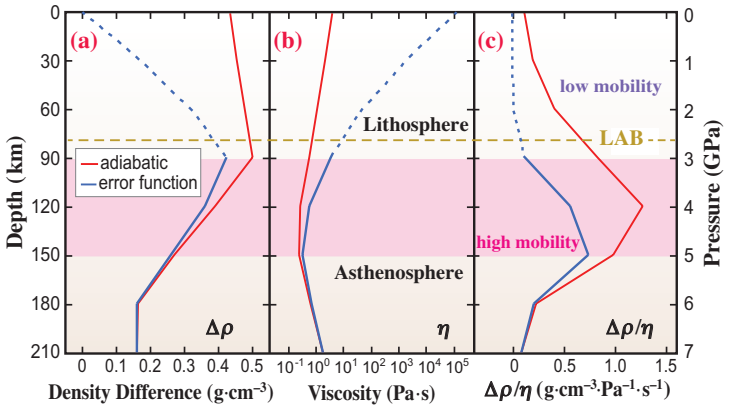

Fig. 2. Magma properties and mobility as a function of depth. **(a)** Density difference between basaltic magma and olivine ($\Delta\rho$) as a function of depth (and pressure). The red and blue lines are based on an adiabatic temperature gradient, and a realistic error-function temperature profile for mature oceanic lithosphere, respectively. The potential temperature is 1623 K. Pink shading highlights the depth range with anomalous physical properties of basaltic melts owing to the structural transition in Al coordination. **(b)** Viscosity (η) of basaltic magma along the same two profiles. Hypothetical subsolidus density and viscosity profiles are shown by dashed lines. **(c)** Mobility $\Delta\rho/\eta$ of basaltic magma along the same two profiles.

Si^{4+} coordination. Therefore, the rapid density increase of basaltic magma at these pressures is attributed to an increase in Al^{3+} coordination. This behavior is unique compared with other silicic melts: T-O lengths have been reported to only modestly increase with pressure for $MgSiO_3$ and $CaSiO_3$ melts (Fig. 1(c)).

Gravity-driven separation of buoyant magma from partially molten rock is proportional to the "hydrostatic magma mobility" (defined as $\Delta\rho/\eta$) in addition to the permeability. Here, η is the melt viscosity, and $\Delta\rho$ is the density difference between the magma and the surrounding solid rock (for which we take olivine Fo_{90} as representative). Figure 2(a) shows that, for any plausible choice of geotherm, $\Delta\rho$ decreases rapidly from 100 to 180 km depth (i.e., ~3.5 to ~6 GPa). This transition is caused by a coordination change of Al in the melt with an unusually large compressibility of almost five times higher than usual above and below this depth range. Also, $\Delta\rho$ slightly decreases from a depth of ~100 km to the surface (Fig. 2(a)). This slight decrease in $\Delta\rho$ is a conservative estimate as we do not consider the effects of the successive removal of garnet and clinopyroxene, nor those of an increase in Mg# (in olivine) in the residual MOR melting column (i.e., the oceanic lithosphere). The resulting maximum $\Delta\rho$ at 3-4 GPa, in combination with minimum η at 4-5 GPa (Fig. 2(b)), results in a peak in magma mobility at ~120-150 km depth in the Earth's mantle (Fig. 2(c)).

The peak in melt mobility at ~120-150 km depth carries important implications for the nature of Earth's shallow mantle. The decreased mobility of melt as magma ascends from a partially molten asthenosphere gives rise to the tendency of excess melt accumulation at 80-100 km depth (Fig. 3). Unless vertical dikes or channels form in the lithosphere that would otherwise allow the melts to escape, magma generated at depth would accumulate atop the asthenosphere. Indeed, a recent magnetotelluric study suggests such a scenario beneath the edge of the Cocos plate. Excessive melt accumulation at these depths may also lead to rheological weakening, enhanced shear deformation, and the formation of sub-horizontal melt bands that would further decrease vertical melt mobility. However, this excess magma may also be cooled by heat conduction to the overlying lithosphere, which would cause it to freeze, further restricting permeability and possibly giving rise to the formation of an extensive network of basaltic sills at the base of the lithosphere. Excess melt accumulation at 80-100 km depth may help explain the origin of the seismically observed Gutenberg discontinuity, as well as its geographical correlation with features suggestive of recent partial melting of the mantle.

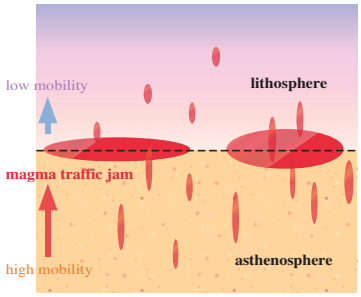

Fig. 3. Schematic illustration of the lithosphere and asthenosphere boundary (LAB). Magma mobility is faster between 120 km and 150 km, causing relative magma depletion. The LAB at around 80 km depth can be a zone of excessive melt accumulation, since it can be fluxed at higher rates from below where mobility is higher, but is removed at much slower rate above where mobility is lower.

Tatsuya Sakamaki

Dept. of Earth and Planetary Materials Science,
Tohoku University

E-mail: sakamaki@m.tohoku.ac.jp

References

[1] T. Sakamaki *et al.*: Nature **439** (2006) 192.
[2] T. Sakamaki *et al.*: Earth Planet. Sci. Lett. **287** (2009) 293.
[3] T. Sakamaki *et al.*: Am. Mineral. **95** (2010) 144.
[4] T. Sakamaki *et al.*: J. Appl. Phys. **111** (2012) 112623.
[5] *T. Sakamaki, A. Suzuki, E. Ohtani, H. Terasaki, S. Urakawa, Y. Katayama, K. Funakoshi, Y. Wang, J. Hernlund, M. Ballmer: Nat. Geosci.* ***6*** *(2013) 1041.*

Sound velocity of hexagonal close-packed iron up to core pressures

Measurement of sound velocities of metallic iron under extreme conditions is crucial for understanding the Earth's core. Figure 1 shows a one-dimensional seismic profile of the Earth's interior, the Preliminary Reference Earth Model, PREM [1]. The density and seismic velocities of the core-forming materials are essential in clarifying the constituent of the Earth's core. In pioneering works, Fiquet *et al.* [2] and Mao *et al.* [3] used X-ray scattering techniques to measure the velocities of metallic iron at extreme pressures in order to discuss the compositions and properties of the Earth's inner core. There are longstanding controversies regarding Birch's law, i.e., the V_p and density relation and its temperature dependence. Fiquet *et al.* [2] determined the seismic velocity of hcp-Fe to 112 GPa at room temperature by the inelastic X-ray scattering method, IXS. Their V_p-density relation overlapped with that determined by shock experiments along the Hugoniot [4]. This coincidence of the ambient temperature data with those determined by the high temperature shock compression experiment along the Hugoniot implies that there is no temperature effect on Birch's law. On the other hand, Mao *et al.* [3] determined the seismic velocity of hcp-Fe up to 153 GPa using nuclear inelastic scattering (NIS), and reported higher V_p compared with the shock compression data. The V_p-density relations of the Birch's law determined by these works are shown in Fig. 2. The discrepancy between these two works is significant. Without solving this inconsistency, it is impossible to argue the composition of the inner core using the sound velocity of hcp-Fe. In order to determine a reliable V_p-density relation for hcp-Fe at ambient temperature and at high temperatures, we measured the P-wave velocity of hcp-Fe to 174 GPa, the maximum pressure using IXS, at room temperature, and up to 1000 K in a wide pressure range up to 100 GPa [5].

Inelastic X-ray scattering spectra were taken at the high-resolution inelastic X-ray scattering beamline **BL35XU**. The energy longitudinal acoustic (LA) mode of the hcp-Fe was precisely determined by fits to the IXS spectra. All results from one set of thermodynamic (P, T) conditions, with the error bars from the spectral fits, were then fitted to a sinusoidal dependence of the LA mode energy on momentum transfer. The NaCl pressure medium was used in most runs, excepting runs made at high temperature. Pre-compressed rhenium foil was used for the gasket for confining pressure. Density was measured from the X-ray diffraction of the sample using the flat panel image plate detector before and after the IXS measurements. In some runs made in the early stage the X-ray powder diffraction of the same sample in the same DAC was taken at **BL10XU** beamline before or after the experiments. The two unit cell volumes determined by the two procedures were consistent with each other. The results of our measurements at room temperature and up to 174 GPa, and those up to 1000 K at high

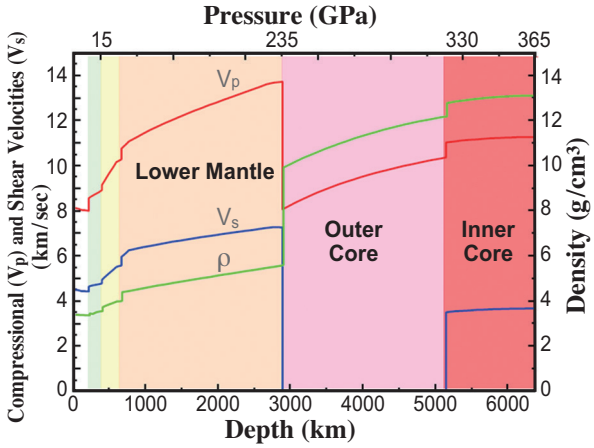

Fig. 1. Preliminary Reference Earth Model, PREM [1]. V_p is the compression and Vs is the shear velocity.

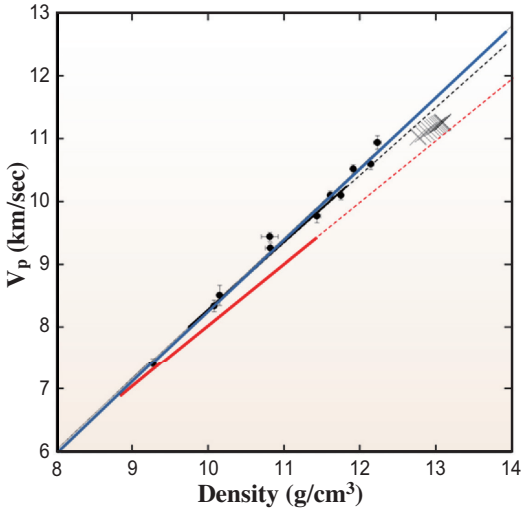

Fig. 2. Birch's law, the compressional velocity-density relation, of hcp-Fe at ambient and high temperatures determined in this study. All present data at 300 K and high temperatures up to 1000 K are shown as solid circles. Crosses, X, are V_p and density for the PREM inner core. All of the data at 300 K and high temperature determined here are fitted by the single blue line of V_p (km/s) = 1.126(±0.042) ρ (g/cm^3) −2.969(±0.466) (R^2 = 0.988). The IXS [2] and NIS [3] data are shown as black and red curves, respectively.

pressures to 100 GPa are summarized in Fig. 2. Our high-temperature compressional velocities, as seen in Fig. 2, fall on the same linear velocity *vs* density line, V_p [km/s] = 1.126(±0.042)ρ [g/cm^3] – 2.969(±0.466) (R^2 = 0.988), as those at room temperature, indicating that Birch's law is valid for hcp-Fe at least up to 1000 K [5].

In previous works, two methods have been used to investigate sound velocities in hcp-Fe at high pressure: nuclear inelastic scattering (NIS) and IXS as used here [2,3]. The NIS technique [3] provides spectra from which, within a harmonic approximation, the phonon density of states may be extracted, and from this DOS, the Debye velocity, and, eventually, the sound velocity, V_p, may be isolated. Our results are in good agreement with the NIS results obtained by Mao *et al.* at pressures up to 153 GPa [3]. Thus, we solved the longstanding controversy of Birch's law of hcp-Fe in the present experiment. Although we could detect almost no temperature dependence in Birch's law for hcp-Fe, it is likely that there is a large temperature dependence at temperatures above 1000 K in Birch's law. Recent *ab initio* calculations showed that it has a negligible temperature effect below 1000 K, whereas a large effect at higher temperatures as shown in Fig. 3. A large temperature effect in Birch's law above 1000 K is consistent with the shock compression data determined along the Hugoniot [4]. The recent results on the thermal state of the outer core based on melting experiments of iron-light element systems propose that the temperature at the ICB is around 5500 K [5]. The P-wave velocity and density values at temperatures around 5500 K for the shock experiment and theoretical calculations are shown as large red circles in Fig. 3. The isothermal Birch's law at 5500 K may have a slope similar to that at 300 K obtained in the present study. Assuming the isothermal slope of Birch's law at 300 K holds even at high temperatures, we can estimate the P-wave velocity of hcp-Fe at 330 GPa and 5500 K, using the isothermal Birch's law at 5500 K and the thermal equation of state of hcp-Fe. The isothermal Birch's law at 5500 K may be expressed as follows: V_p [km/s] = 1.174ρ[g/cm^3] – 4.230(±0.032) (R^2 = 0.988) [5]. The density and P-wave velocity of hcp-Fe under the ICB condition, 330 GPa and 5500 K, are calculated to be 13.3(5) g/cm^3 and 11.4 km/s, respectively. Thus, hcp-Fe has a density about 4% higher and P-wave velocity about 3% higher than those in the seismological model, PREM, 12.76 g/cm^3 and 11.03 km/s at ICB (see Fig. 3), respectively.

On the basis of the arguments above, we can conclude that the light elements or the combination of the light elements and nickel decreases both the density and compressional velocity of hcp-Fe simultaneously under the inner core conditions, accounting for the seismic observations of the inner core. This conclusion is in striking contrast to the properties of the outer core, i.e., the outer core contains light elements, which reduces the density and increases the sound velocity of the outer core by forming molten iron alloy. The sound velocity of hcp-Fe under the inner core conditions is a key to clarifying the composition of the inner core.

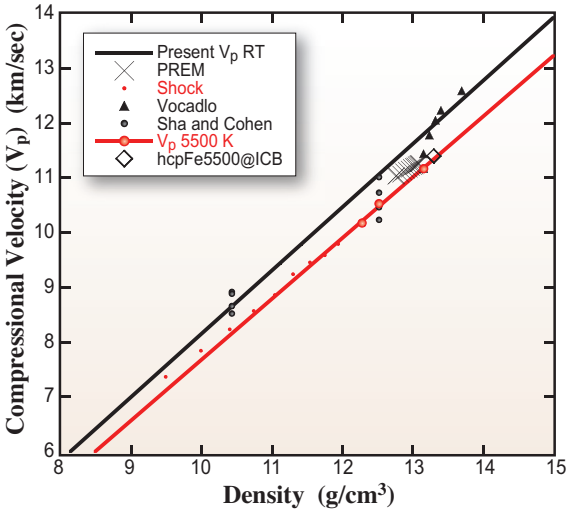

Fig. 3. Compressional velocity and density of hcp-Fe at 300 and 5500 K [5]. Small red circles, black triangles, and black circles are the shock compression data along the Hugoniot and the results of *ab initio* calculations [5]. The compressional velocity *versus* density of the PREM inner core is shown as large crosses [1]. Large red circles are V_p and density at 5500 K estimated by extrapolation of the shock compression and those calculated by the *ab initio* methods. The relation for hcp-Fe at 5500 K is V_p (km/s) = 1.174ρ (g/cm^3) –4.230(±0.032), assuming that the slope of the line is the same as that at 300 K [5]. Open diamond shows the compressional velocity and density of hcp-Fe under the inner core boundary condition, 330 GPa and 5500 K.

Eiji Ohtani

Department of Earth Science, Tohoku University

E-mail: ohtani@m.tohoku.ac.jp

References

[1] A.M. Dziewonski and D.L. Anderson: Phys. Earth Planet. Inter. **25** (1981) 297.
[2] G. Fiquet *et al.*: Science **291** (2001) 468.
[3] H.K. Mao *et al.*: Science **292** (2001) 914.
[4] J.M. Brown, R.G. McQueen: J. Geophys. Res. **91** (1986) 7485.
[5] *E. Ohtani, Y. Shibazaki, T. Sakai, K. Mibe, H. Fukui, S. Kamada, T. Sakamaki, Y. Seto, S. Tsutsui, A.Q.R. Baron: Geophys. Res. Lett.* ***40*** *(2013) 1.*

Decomposition of Fe_3S above 250 GPa

The Earth's core includes substantial amounts of light elements in addition to iron and nickel. Sulfur is one of the candidates for such a light element. A phase diagram of the Fe–FeS system, particularly for the high-pressure and high-temperature (*P-T*) conditions of the core, is needed to understand the composition and state of the Earth's core. Fe and FeS exhibit a simple binary eutectic system at ambient pressure. Previous experimental studies revealed the formation of the intermediate compounds Fe_3S_2, Fe_2S, and Fe_3S at high pressures [1]. Earlier experiments showed that tetragonal Fe_3S, known as the most iron-rich Fe–S compound, is stable at least up to 220 GPa and 3300 K [2]. In contrast, theoretical calculations predicted a continuous solid solution between Fe and FeS under inner core boundary (ICB) conditions [3]. In this study [4], we examine the subsolidus phase relations of iron–sulfur alloys up to 271 GPa by a combination of *in situ* synchrotron X-ray diffraction (XRD) measurements and chemical analyses on recovered samples.

All high *P-T* experiments were conducted at beamline **BL10XU**. High *P-T* conditions were generated in a laser-heated diamond-anvil cell (DAC). We prepared the starting materials by mixing FeS powder and metallic iron. In addition, the high-pressure Fe_3S phase was used as the starting material in run #2. The samples were heated with a couple of 100 W single-mode Yb fiber lasers by a double-side heating technique. The temperature was measured by using a spectroradiometric method. Angle-dispersive XRD spectra were collected on a charge-coupled device or an imaging plate detector. A monochromatic incident X-ray beam with a wavelength of 0.41332–0.42342 Å was collimated to approximately 6 μm (full width at half maximum). In addition to the XRD measurements, chemical analyses were also carried out on samples recovered from runs #1 and #2, using an analytical transmission electron microscope.

Five separate sets of experiments were conducted at pressures between 226 and 271 GPa and temperatures up to 3100 K. In the first set of experiments with Fe (+20 atm% S), the starting material was initially compressed to 238 GPa at room temperature. Broad diffraction peaks from hcp Fe, B2-FeS, and rhenium were observed before heating (Fig. 1(a)). We subsequently heated the sample to 2510 K at 241 GPa and observed the appearance of Fe_3S diffraction peaks [1] (Fig. 1(b)). The Fe_3S peak intensities increased at 2130 K and 226 GPa, indicating its stability under these *P-T* conditions. Chemical analyses also indicated the presence of Fe_3S in the recovered sample. In the second run, we used the tetragonal Fe_3S phase as the starting material. It was compressed in the DAC and heated to 2530 K at 271 GPa for 3 h. The XRD pattern obtained before heating showed only MgO peaks; however, two weak reflections appeared at d = 1.70 and 1.65 Å, which can be attributed to the B2 110 and hcp 101 peaks. The chemical analysis suggests the coexistence of sulfur-rich and sulfur-poor particles (Fig. 2), which most likely correspond to the B2 and hcp phases, respectively, as observed in the XRD pattern. Point analyses suggest

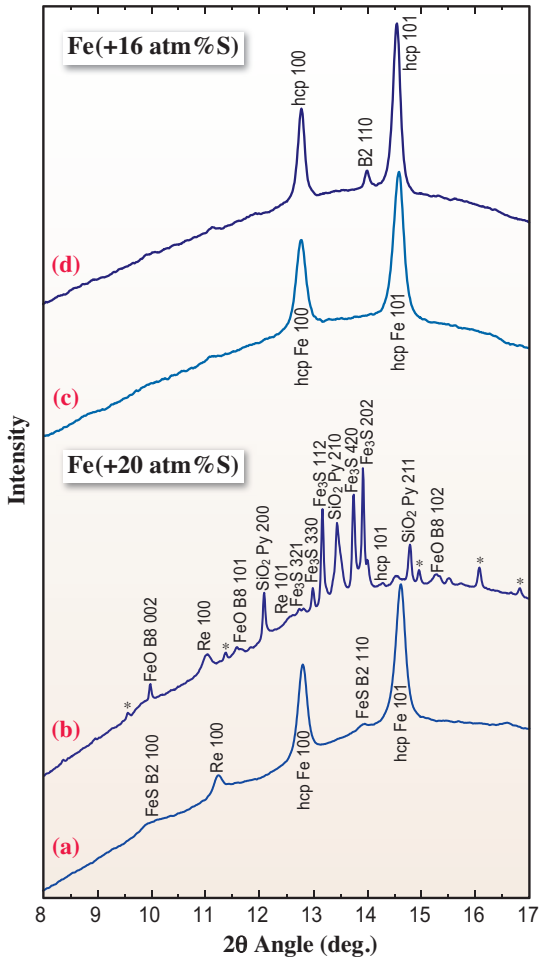

Fig. 1. XRD patterns **(a)** at 238 GPa and 300 K before heating and **(b)** after heating at 236 GPa and 2980 K in the first run, and at **(c)** 259 GPa and 300 K before heating and **(d)** 269 GPa and 2700 K in the fourth run. Peak broadening due to nonhydrostatic stress before heating and the smaller amount of FeS likely resulted in the absence of peaks from FeS in (c). SiO_2 Py stands for the pyrite-type SiO_2 insulation material and Re for the rhenium gasket. The peaks marked with an asterisk are likely from the Fe_2S phase.

a lower limit of 33.5 atm% S for the S-rich phase and an upper limit of 12.4 atm% S for the S-poor phase. These results clearly indicate the decomposition of Fe_3S into two phases. In run #3, the Fe (+20 atm% S) sample was squeezed to 255 GPa and subsequently heated. Whereas only diffraction peaks of hcp Fe were observed before heating, two new peaks appeared upon heating to 3100 K at 251 GPa and were assigned to the 100 and 110 lines of the B2 structure. In addition, the spots appeared on the Debye rings of hcp iron, indicating grain growth and thus the stability of hcp under this *P-T* condition. In the fourth set of experiments with the Fe (+16 atm% S), the sample was first compressed to 259 GPa at 300 K (Fig. 1(c)). On subsequent heating, the diffraction lines from hcp became sharper, and the B2 110 peak appeared at 2540 K and 264 GPa and further grew at 2700 K and 269 GPa (Fig. 1(d)). Similarly, in the fifth run using the Fe (+10 atm% S) sample, we originally compressed it to 268 GPa at 300 K. The B2 110 peak appeared during heating to 1630 K at 267 GPa. These results are summarized in Fig. 3.

The coexistence of hcp Fe and Fe_3P-type Fe_3S was previously reported at 220 GPa and 3300 K [2]. In agreement with the earlier experiments, we observed the formation of Fe_3S from a mixture of Fe and FeS up to 241 GPa and 2510 K (Fig. 3). On the other hand, the Fe_3S starting material decomposed into Fe-rich and Fe-poor phases at 271 GPa and 2530 K (Fig. 2). Furthermore, the XRD measurements in this study repeatedly confirmed that tetragonal Fe_3S did not form, and alternatively, hcp Fe and B2 coexisted above 251 GPa and 3000 K (Fig. 3). Previous first-principles calculations [3] predicted that Fe and FeS exhibit a continuous solid solution at ICB pressures, and that coexisting solid and liquid contain very similar amounts of sulfur. This suggests that the observed density jump across the ICB cannot be reconciled with the difference in sulfur content between the inner and outer core; therefore, sulfur is not likely the predominant light element in the core. However, we have demonstrated that the compositional range of the solid solution is limited at 271 GPa and 2530 K, where Fe_3S decomposes into mixed phases. Recent laser-heated DAC experiments have revealed that both Fe and Fe (+10% Ni) alloy adopt the hcp structure under inner core *P-T* conditions. However, theoretical calculations suggested that a small amount of sulfur impurity in iron stabilizes the bcc rather than the hcp structure under the inner core conditions. The present experimental results suggest that the hcp phase forms in the S-bearing system at 2700 K and 269 GPa.

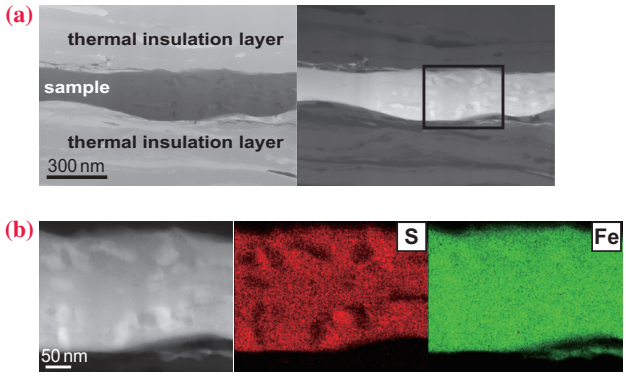

Fig. 2. **(a)** STEM bright-field (left) and dark-field (right) images of the recovered sample in the second run. In the bright-field image, the light domains represent the thermal insulation layers, which consist of SiO_2 and MgO, and the dark region shows the assemblage of the iron–sulfur alloys. The dark-field image gives the atomic number contrast (*Z*); the bright areas correspond to high *Z* values. **(b)** Magnified image of the boxed area in (a) (left). Sulfur (middle) and iron (right) maps in the same area.

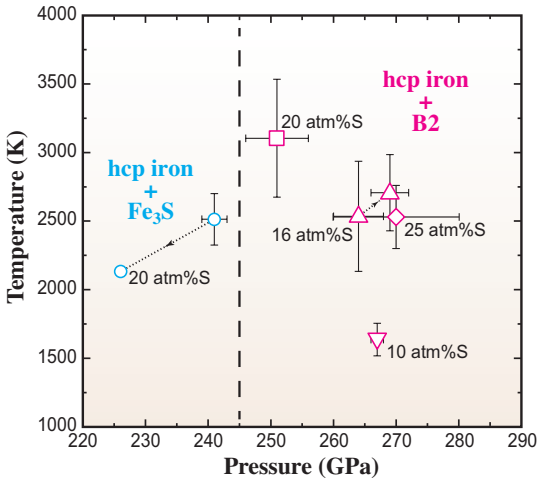

Fig. 3. Experimental conditions and results. Blue and red symbols represent the stabilities of the hcp and Fe_3S, and hcp and B2 phases, respectively. The sequential changes in *P-T* conditions are illustrated by the arrows. The starting bulk compositions are indicated by the numbers: run #1 (circles); run #2 (diamonds); run #3 (squares); run #4 (triangles); and run #5 (downward triangle).

Haruka Ozawa [a,b,c]

[a] Institute for Research on Earth Evolution, Japan Agency for Marine-Earth Science and Technology
[b] Dept. of Earth and Planetary Sciences, Tokyo Institute of Technology
[c] Earth-Life Science Institute, Tokyo Institute of Technology

E-mail: h-ozawa@jamstec.go.jp

References

[1] Y. Fei *et al.*: Am. Mineral. **85** (2000) 1830.
[2] S. Kamada *et al.*: Earth Planet. Sci. Lett. **294** (2010) 94.
[3] D. Alfè *et al.*: Earth Planet. Sci. Lett. **195** (2002) 91.
[4] *H. Ozawa, K. Hirose, T. Suzuki, Y. Ohishi, N. Hirao: Geophys. Res. Lett.* ***40*** *(2013) 4845.*

Generation of pressure over 1 Mbar in the Kawai-type multianvil apparatus

High-pressure experiments are one of the most useful methods for studying the earth's interior, meaning that the generation of pressure is of essential importance. In earth science, the Kawai-type multianvil apparatus has been widely employed in the clarification of the structure and state of the deep Earth (cf. [1]). The most marked advantage of the Kawai-type multianvil apparatus is the capability to compress a large volume sample (>1 mm^3) in an octahedral pressure medium under a quasi-hydrostatic environment through compression with eight cubic anvils. Moreover, by adopting an internal heating system, the sample can be heated homogeneously and stably, which make it possible to obtain qualitative physical and chemical properties of minerals under high-pressure and -temperature conditions. In the conventional Kawai-type multianvil apparatus, in which tungsten carbide (WC) is used as second-stage anvils, however, the attainable pressure has been limited to ~28 GPa. In the late 1980s, sintered diamond, which is two times harder than WC, became available for the second-stage anvils of the Kawai-type multianvil apparatus instead of WC [2]. In the early 1990s, therefore, the experimental pressure was raised to slightly higher than 30 GPa by using cubic sintered diamond anvils with an edge length of ~10 mm. In 1998, sintered diamond cubes with an edge length of 14 mm were introduced, which made it possible to squeeze the Kawai-cell of eight cubic anvil assembly at a load two times higher than when using 10 mm edge cubes. Through the use of 14-mm-edge-length sintered diamond anvils and the optimization of the pressure medium and the gasket, the attainable pressure has been expanded to higher than 40 GPa (e.g., [3]). As shown in Fig. 1, the pressure range has been significantly increased since 2004. The discovery of post-perovskite phase strongly motivates our technique of pressure generation using the Kawai-type multianvil apparatus.

The high-pressure and high-temperature *in situ* X-ray diffraction experiment was conducted at the white X-ray beamline **BL04B1** to test the pressure generation. The Kawai-type high-pressure cell composed of eight sintered diamond cubic anvils with an edge length of 14 mm and truncated edge length (TEL) of 1.0 mm was set in the DIA-type press (SPEED-Mk.II/Madonna). Two types of sintered diamond anvils were tested: one is the "C-grade" sintered diamond anvil with 8% Co as a binder and the other is the "C2-grade" sintered diamond anvil with 7.5% Co as a binder (both sintered diamond anvils are supplied by Sumitomo Electric Industries, Ltd.). The strength of the C2-grade anvil is slightly higher than that of the C-grade. The fracture strength (TRS) and Young's modulus of C2-grade anvil are reported to be 1.25 GPa and 941 GPa, respectively, whereas those of the C-grade anvil are 1.15 GPa and 893 GPa, respectively (informed from Sumitomo Electric Industries, Ltd.). As illustrated in Fig. 2, a cylindrical TiB_2+BN+AlN heater was placed in the octahedral pressure medium of MgO+5% Cr_2O_3 with an edge length of 4.1 mm. Pressure was determined from the volume of Au mixed into the sample, using the equation of state for Au [3].

Pressures up to ~110 GPa were successfully generated using the cell assembly shown in Fig. 2 with the C2-grade anvils. The attainable *P-T* range of the Kawai-type apparatus has been extended in the present study, which is ~15 GPa higher than

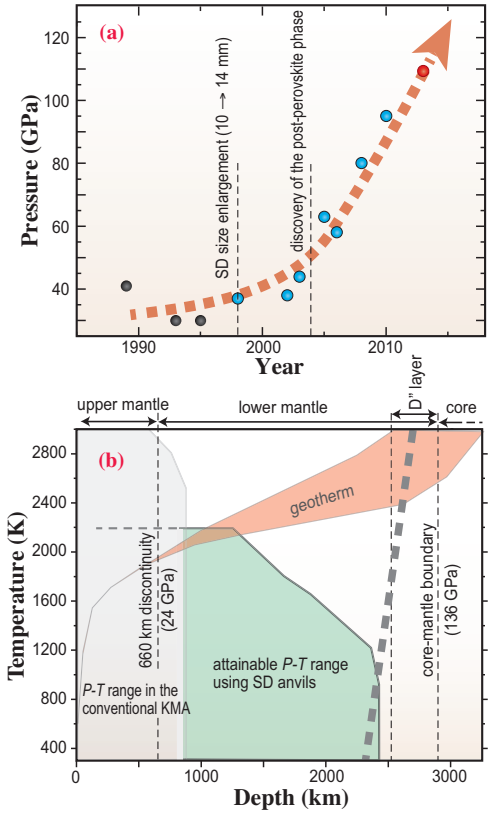

Fig. 1. **(a)** Evolution of the attainable pressure in the Kawai-type multianvil apparatus using sintered diamond for second-stage anvil (thick dotted line). **(b)** Depth-temperature diagram showing the attainable pressure and temperature range of the Kawai-type multianvil apparatus, together with the phase boundary between perovskite and post-perovskite in $MgSiO_3$ (thick solid line).

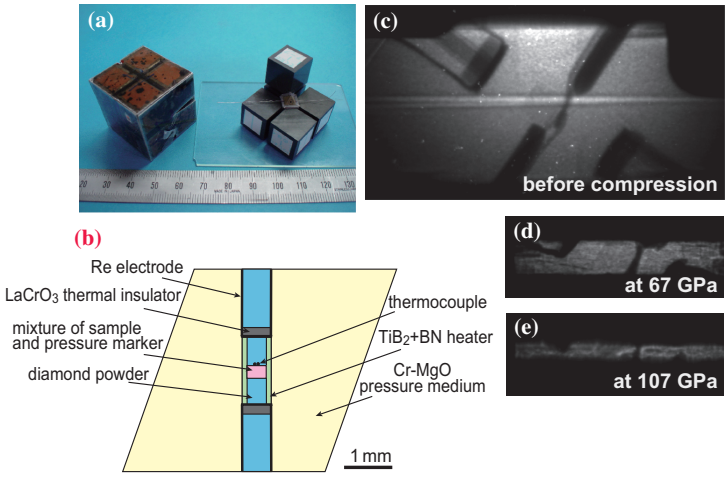

Fig. 2. **(a)** Kawai-type high-pressure cell comprising of eight sintered diamond cubic anvils. **(b)** Schematic illustration of furnace assemblies used in the present study. **(c)-(e)** X-ray radiographs showing the inside of cell assembly through anvil gap before compression, at 67 GPa, and at 107 GPa, respectively.

in the previous study, as shown in Fig. 1. This pressure range is now close to those of the D" layer (Fig. 1). In order to generate higher pressure, high-quality sintered diamond is of essential importance. In addition, enlargement of the sintered diamond anvil size is demanded because a load more higher press than 10 MN should be applied in the present cell assembly. At present, the maximum press load for a 14 mm cube is limited to ~10 MN owing to the limitation of the strength of WC of the first-stage anvils. Another key point may be further optimization of the cell assembly. For example, Tange *et al.* [4] showed that the use of Al_2O_3 as a pressure medium generates pressure more effectively than when using the Cr-doped MgO adopted in the present study.

Stishovite was compressed in the pressure generation test. During compression, the second-order structural transition from stishovite ($P4_2/mmm$) to the $CaCl_2$-type ($Pnnm$) phase was observed. The transition is shown in the diffraction patterns in Fig. 3. A peak assigned to be (211) line of stishovite split into a doublet with peaks assigned to the (121) and (211) lines of the $CaCl_2$-type phase. The splitting, however, was not clear at pressures around 55 GPa. Assuming the ambiguity is due to the coexistence of both phases, the transition pressure is estimated to be ~55 GPa. From the change in the axial ratios of stishovite to the $CaCl_2$-type phase, the transition pressure is also estimated to be ~55 GPa. The transition boundary in this study is consistent with the results previous studies (e.g., [5]).

In SiO_2, the α-PbO_2 structure (*Pbcn or Pnc2*) was reported as the next high-pressure polymorph of the $CaCl_2$-type. Murakami *et al.* [6] showed the stability of the α-PbO_2-type phase to be higher than ~100 GPa, and determined the phase boundary to be P (GPa) = 98 + (0.0095 ± 0.0016) × T (K). In the compression experiment on stishovite, the sample was annealed at 109.0 GP and 900 K for 15 min. Although the annealing pressure was 2.5 GPa higher than that at the phase boundary proposed in the previous study, no sign of transition to the α-PbO_2 type was observed. This indicates that the annealing temperature and duration are not sufficient to promote the phase transition because of slow transition kinetics, or the real phase boundary is higher than that reported in the previous study.

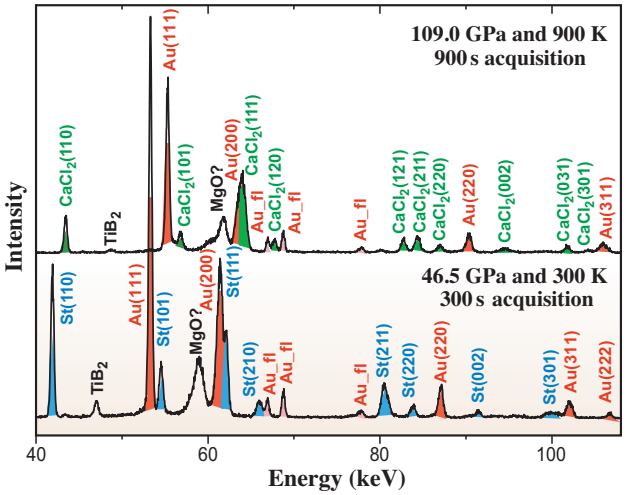

Fig. 3. Representative diffraction profiles for stishovite (st) at 46.5 GPa and 300 K (bottom profile) and the $CaCl_2$-type phase ($CaCl_2$) at 109 GPa and 900 K (upper profile).

Daisuke Yamazaki

Institute for Study of the Earth's Interior,
Okayama University

E-mail: dy@misasa.okayama-u.ac.jp

References

[1] E. Ito: Treatise on Geophysics, Vol. 2, Mineral Phys. (2007) 197.
[2] E. Ohtani *et al.*: Rev. Sci. Instrum. **60** (1989) 922.
[3] *D. Yamazaki, E. Ito, T. Yoshino, N. Tsujino, A. Yoneda, X. Guo, F. Xu, Y. Higo, K. Funakoshi: Phys. Earth Planet. Inter.* ***228*** *(2014) 262.*
[4] Y. Tange *et al.*: High Press. Res. **28** (2008) 245.
[5] R. Nomura *et al.*: Phys. Earth Planet. Int. **183** (2010) 104.
[6] M. Murakami *et al.*: Geophys. Res. Lett. **30** (2003) 11.

Environmental


"Nemunoki" - *Silk tree*

SCIENCE

SR-based XRF and XAFS methods are frequently used for investigations in environmental science, such as element mapping and speciation of environmental samples because research targets are often very dilute and amorphous forms with complex composition.

At SPring-8, XRF and XAFS studies were mostly conducted in hard X-ray beamlines. In 2011, XRF and XAFS measurement systems in the soft X-ray region, including scanning microscopy, were installed at BL27SU. New findings using these measurement systems are now being published.

Here we highlighted four topics. Yoshimura *et al.* investigated element profile and chemical state of sulfur in shells in relation to seasonal changes in the environment over long periods using μ-XRF and S *K*-edge XANES. Using XAFS, Takahashi *et al.* examined the seasonal changes in the species and concentration of Fe in an aerosol, which is a significant factor for the amount of soluble Fe in the North Pacific region and may affect the carbon cycle on the Earth's surface. Yokoyama *et al.* clarified the immobilization mechanism of As by calcite in the groundwater by determining the oxidation state and local structure of As using XAFS. Additionally, Fujimori *et al.* investigated the thermochemical behavior of Pb in fly ash during formation of chlorinated aromatics in solid waste incinerators by XAFS at combustion temperatures.

Tomoya Uruga

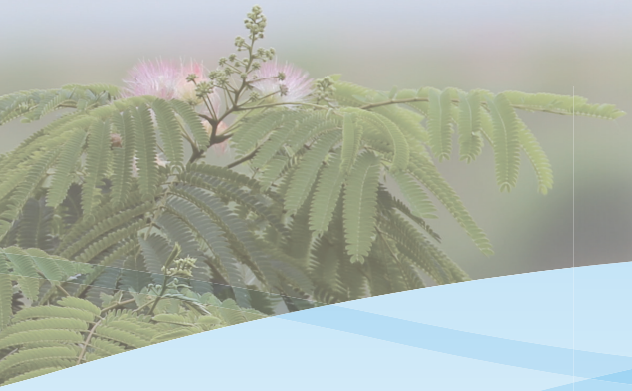

Environmental and biological influence on seasonal fluctuations of sulfur in a giant clam shell

Bivalves, the shells of which are composed of calcium carbonate ($CaCO_3$), are a geologically important producer of biominerals. The characteristic variations of element profiles in shell $CaCO_3$ are a widely used approach for identifying differences in biological processes and environmental changes associated with element partitioning. A long-lived bivalve, particular giant clams present several advantages for palaeoclimate research, and provide long-term records (up to ~100 years) of the environmental conditions in tropic and sub-tropic oceans [1]. Recently, the dynamics of sulfur incorporation in clam shells are of interest in relation to environmental and physiological parameters.

Sulfate in seawater is the third most abundant ion and sufur concentrations in biogenic $CaCO_3$ range from several hundred to several thousand ppm (e.g., [2]). Sulfur is regarded as an important element in relation to organic compounds, and Cuif *et al*. [3] has proposed a close relationship between skeletal micro-structure and organic matrices. Contrary to the situation with S content in biogenic carbonates which might reflect contamination with organic substances, sulfur in $CaCO_3$ is present as structurally substituted sulfate governed thermodynamic and/or kinetically controlled partitioning [2]. Clarification of how sulfur is hosted in the bivalve shell should elucidate how element incorporation into bivalve shells relates to environmental and biological studies. Furthermore, little attention has been paid to intra-shell seasonal variations of sulfur. Evaluation of the chemical speciation of sulfur is needed to establish reliable paleoenvironmental reconstructions and to better understand details of biomineralization mechanisms.

For this study, we collected a live specimen of the strawberry clam *Hippopus hippopus* (Fig. 1) from Ishigaki Island, Japan (24°33'N, 124°16'E), located in the subtropical northwestern Pacific Ocean. *H. Hippopus* has an aragonitic shell [4]. X-ray absorption near-edge structure (XANES) and μ-X-ray fluorescence analysis (μ-XRF) measurements were carried out at the b-branch of the soft X-ray photochemistry beamline **BL27SU**. μ-XRF mapping data for each element was obtained by using a silicon drift detector. For μ-XRF measurements, the polished slab was fixed on an aluminum sample holder that was then installed in a vacuum chamber and fixed on a motorized XYZ stage. The horizontal and vertical beam size at focus point were 16.3 and 13.7 μm, respectively. The μ-XRF measurements for sulfur and strontium were taken at a photon energy of 2481.3 eV along a transect from the inner shell layer at 8 μm intervals with an acquisition time of 1 s. The spectra of S *K*-edge XANES collected from bivalve shells and S-bearing organic and inorganic reference materials (Fig. 2) indicated that inorganic sulfate was present in marine aragonitic and calcitic bivalve shells (strawberry clam and Japanese scallop *Mizuhopecten yessoensis*). The selected energy range for S XANES measurements was 2460–2510 eV with an energy step of 0.2 eV and an acquisition time of 4 s.

From XRF measurements, we had little direct evidence of the cyclic changes of elements associated with organic components such as phosphorus, with some varying by approximately one order of magnitude (up to >1000 ppm) as observed in sulfur, however. The stacked S *K*-edge XANES spectra collected from reference materials and bivalve shells (Fig. 2) exhibited several features that varied among inorganic and organic reference compounds. The main peaks of the organic reference materials showed large shifts toward higher energies with increasing oxidation state of sulfur. Moreover, the XANES spectra of various inorganic sulfate compounds exhibited a pronounced peak appearing around 2481.5 eV and some small peaks can be confirmed on the higher energy side of main peak. The spectra of the two bivalve shells exhibited similar spectral features to those of sulfate compounds, and the spectrum of the *H. hippopus* and *M. yessoensis* shells showed a significant resonance. A sub-peak at 2484.4 eV that appeared on the high-energy side of the main peak near 2481.5 eV was also apparent in the spectrum of $CaSO_4$ (Fig. 2).

The comparison between the shell structure and the sea surface temperature record shows

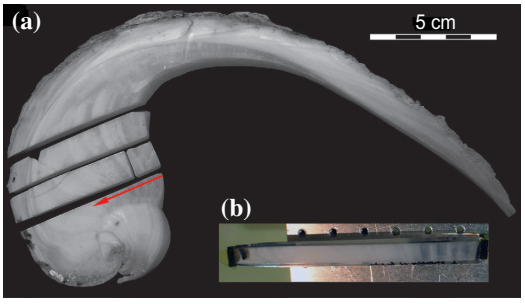

Fig. 1. **(a)** A slab of the *Hippopus hippopus* specimen. A polished slab obtained from the inner shell layer was used for μ-XRF/XAS measurements. The red arrow indicates the measurement transect. **(b)** The polished slab was fixed in an aluminum sample holder with conductive double-sided carbon tape and inserted into the vacuum chamber.

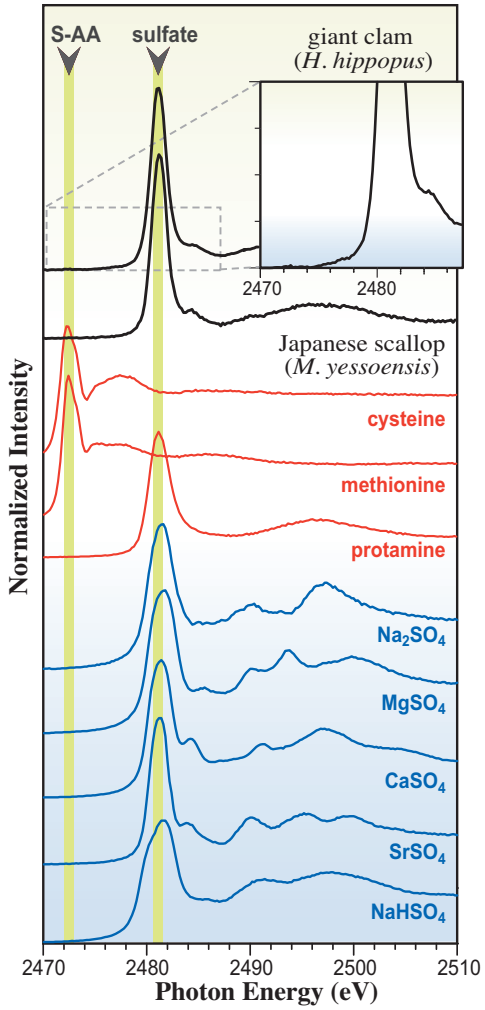

Fig. 2. S *K*-edge XANES spectra of a giant clam shell aragonite (*H. hippopus*), Japanese scallop shell calcite (*M. yessoensis*), and S-bearing reference materials.

that the large increments of light bands correspond to the summers and the thin increments of main dark bands to the winters in *H. hippopus*. Sulfur concentrations in the specimens showed clear annual fluctuations and varied by approximately one order of magnitude, and S maxima and minima of *H. hippopus* shells were associated with the dark and bright bands, respectively, an indication of a negative correlation between sulfate concentrations and water temperature. Supplementary sources of nutrients from symbiotic algae can also maintain the characteristic fast growth of tropical clam shells. The translocation of photosynthates from zooxanthellae, phototrophy is the most significant source of energy to clams, and this source provides sufficient C for growth and metabolic requirements in *H. hippopus* (e.g., [5]). During higher growth periods, carbonate ions (CO_3^{2-}) in calcifying fluids is increased, and at the same time the increased calcium carbonate saturation state induces the higher calcification rates. This process is promoted enzymatically in the calcifying space. The increases in CO_3^{2-} concentrations would negatively influence the sulfate incorporation into $CaCO_3$ by reducing the relative activity of sulfate ions to carbonate ions in the calcifying fluids, with sulfur concentrations being lower during periods of faster growth (Fig. 3). If the seasonal skeletal growth rate and the changes in carbonate ion concentrations in calcifying fluids were positively correlated, it is suggested that environmental factors such as insolation or some influencing factors of shell growth affected sulfate concentrations in their shells.

The large seasonal changes of sulfate concentrations can potentially be an archive of cyclic changes of shell crystallization, which is related to environmental factors (e.g., insolation) and bivalve physiology. In contrast to element partitioning of cations, the mechanisms controlling inorganic anion incorporation are poorly understood. Our analysis and the previous studies suggest that the possible strong controls of crystal structure and aqueous chemistry on sulfate incorporation into $CaCO_3$.

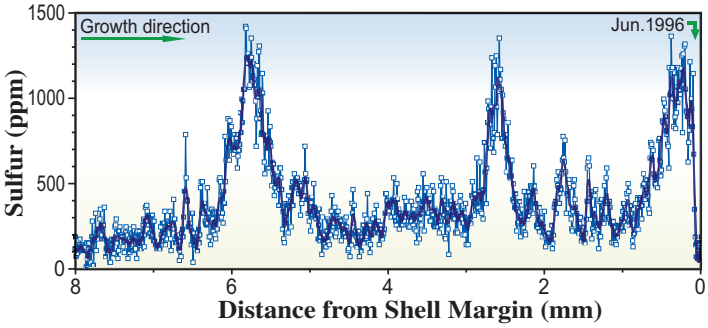

Fig. 3. Sulfur profile from the inner shell layer of *H. hippopus* obtained by the μ-XRF measurement at 8-μm intervals. The spatial resolution of μ-XRF allows the variations of the S content to be examined at a daily timescale (300-850 points per year). The moving average trend (blue line) was calculated by using a 15-point smoothing window.

Toshihiro Yoshimura

Japan Agency for Marine-Earth Science and Technology

E-mail: yoshimurat@jamstec.go.jp

References

[1] M. Elliot *et al.*: Palaeogeogr. Palaeoclimatol. Palaeoecol. **280** (2009) 132.
[2] E. Busenberg and L.N. Plummer: Geochim. Cosmochim. Acta **49** (1985) 713.
[3] J.P. Cuif *et al.*: Geochim. Cosmochim. Acta **67** (2003) 75.
[4] *T. Yoshimura, Y. Tamenori, A. Suzuki, R. Nakashima, N. Iwasaki, H. Hasegawa and H. Kawahata: Chem. Geol. **352** (2013) 170.*
[5] D.D. Klumpp and C.C. Griffiths: Mar. Ecol. Prog. Ser. **115** (1994) 103.

Seasonal changes in Fe species and soluble Fe concentration in the atmosphere in the Northwest Pacific region based on results of the speciation analysis of aerosols collected in Japan

Oceanic areas where phytoplankton growth is limited by iron (Fe) concentration are called "high-nutrient, low-chlorophyll (HNLC)" regions [1], which account for 20% to 30% of the world's oceans [2]. The concentration of bioavailable Fe in the euphotic zone in the ocean can affect the photosynthesis of phytoplankton in HNLC regions, which can consequently affect the carbon cycle on the Earth's surface. Moreover, the amount of Fe in remote oceans can increase the production of dimethyl sulfide and/or organic carbon from microorganisms in the ocean, which in turn can affect the radiative forcing in the atmosphere [2]. Thus, understanding the processes of Fe supply and the dissolution of Fe from the atmosphere into the ocean is essential for estimating the impact of Fe on the Earth's climate.

The bioavailability of Fe in aerosols depends mainly on the fraction of soluble Fe (=$[Fe_{Sol}]/[Fe_{Total}]$, where $[Fe_{Sol}]$ and $[Fe_{Total}]$ are the atmospheric concentrations of soluble Fe and total Fe, respectively). However, numerous factors affecting the soluble Fe fraction have not been fully elucidated. In this study, the Fe species, chemical composition, and soluble Fe concentration in aerosols collected in Tsukuba, Japan over a year (nine samples from December 2002 to October 2003) were investigated to identify the factors affecting the amount of soluble Fe supplied into the ocean. The soluble Fe concentration in aerosols correlates with the concentrations of sulfate and oxalate originating from anthropogenic sources, suggesting that soluble Fe is mainly derived from anthropogenic sources. Moreover, the soluble Fe concentration correlates with the enrichment factors of vanadium and nickel emitted by fossil fuel combustion. These results suggest that the degree of Fe dissolution is affected by the magnitude of anthropogenic activity, such as fossil fuel combustion.

Hence, X-ray absorption fine structure (XAFS) spectroscopy was performed in this study at beamline **BL01XU** to identify the Fe species in aerosols [3]. The speciation of various elements in aerosols has been successfully conducted for calcium, zinc, and iron [4,5]. In Figs. 1 and 2, examples of X-ray absorption near-edge spectroscopy (XANES) profiles and extended X-ray absorption fine structure (EXAFS) spectra are respectively shown with the fitting results obtained by a linear combination of the spectra of possible Fe species. The fitting of XANES profiles and EXAFS spectra coupled with the results of micro-X-ray fluorescence analysis (μ-XRF; data not shown) revealed the main Fe species in the aerosols collected in Tsukuba to be illite, ferrihydrite, hornblende, and Fe(III) sulfate (Fig. 3). In particular, the illite fraction increases in spring, possibly due to the illite contributed by the arid area in East China, which can be transported to Japan via dust events that often occur in spring (Fig. 3).

On the other hand, the Fe(III) sulfate fraction reached about 15-20% of the total Fe from May to August (Fig. 3). On the basis of the results of backward trajectory analyses, the air mass in Tsukuba during that period came from the south part, or from industrial areas in Tokyo, which was supported by the increase in Zn and Cu concentrations during the period. Moreover, the soluble Fe fraction in each sample measured by leaching experiment was also

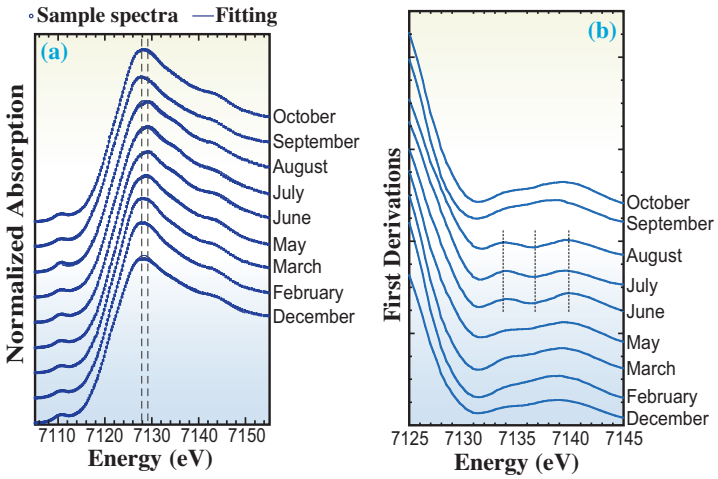

Fig. 1. **(a)** Fitting of Fe *K*-edge XANES spectra of aerosols collected in various months and **(b)** their first-derivative spectra.

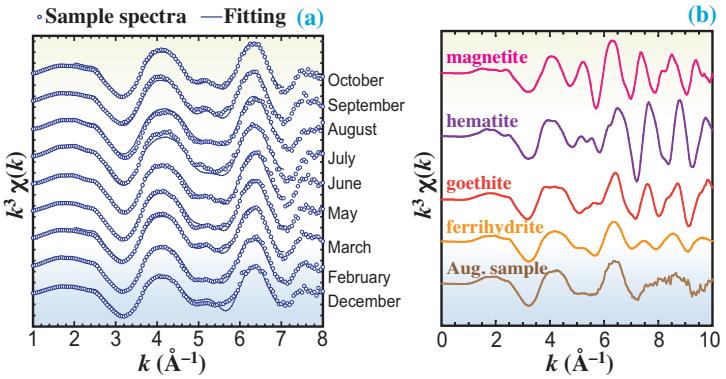

Fig. 2. **(a)** Fitting of Fe *K*-edge EXAFS spectra in k space of aerosols collected in various months with **(b)** the reference spectra for various Fe oxide species.

high during the period, which closely correlated with the Fe(III) sulfate fraction determined by the XAFS spectrum fitting, suggesting that Fe(III) sulfate is the main soluble Fe species from aerosols that is dispersed into the ocean.

Another possible factor that can control the amount of soluble Fe dispersed into the ocean is the total Fe(III) concentration in the atmosphere, which was high in spring owing to the high mineral dust concentrations during the period (= i.e., March in Fig. 4(a-1)). However, this factor does not contribute to the amount of soluble Fe to a larger degree than the effect of Fe speciation. The contribution of each species to the total amount of Fe during the whole year was largest for ferrihydrite, whereas the contribution to soluble Fe was largest for Fe(III) sulfate (Fig. 4(b)). As a result, the amount of soluble Fe is larger in May, June, and July owing to the presence of Fe(III) sulfate during this period (Fig. 4(a-2)).

On the basis of the above results, it was concluded that the most significant factor influencing the amount of soluble Fe in the North Pacific region is the concentration of anthropogenic Fe species, such as Fe(III) sulfate, that emitted from megacities in East Asia.

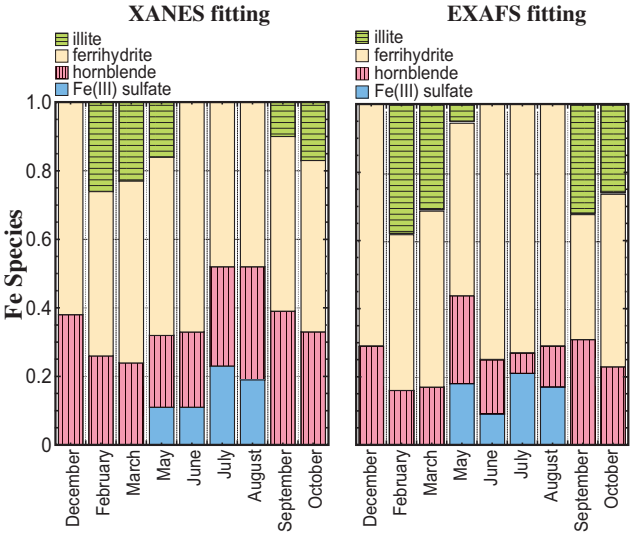

Fig. 3. Iron species in aerosols estimated by **(a)** XANES fitting and **(b)** EXAFS fitting.

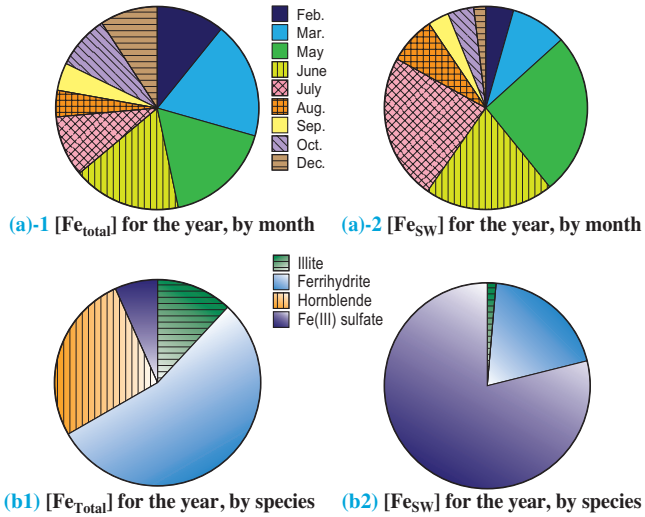

Fig. 4. **(a)** Contribution of each month to (a)-1 total [Fe_{Total}] and (a)-2 total [Fe_{SW}] for the year and **(b)** contribution of each species for (b)-1 total [Fe_{Total}] and (b)-2 total [Fe_{SW}] in the year. Note that the sampling was conducted only in February, March, May, June, July, August, September, October, and December.

Yoshio Takahashi

Department of Earth and Planetary Systems Science, Hiroshima University

E-mail: ytakaha@hiroshima-u.ac.jp

References

[1] J.H. Martin and S.E. Fitzwater: Nature **331** (1988) 341.
[2] J.D. Jickells *et al.*: Science **308** (2005) 67.
[3] *Y. Takahashi, T. Furukawa, Y. Kanai, M. Uematsu, G. Zheng and M.A. Marcus: Atmos. Chem. Phys.* ***13*** *(2013) 7695.*
[4] T. Furukawa and Y. Takahashi: Atmos. Chem. Phys. **11** (2011) 4289.
[5] Y. Takahashi *et al.*: Atmos. Chem. Phys. **11** (2011) 11237.

Differences between immobilizations of arsenite and arsenate by calcite

Arsenic (As) is a highly toxic element. Drinking As-rich groundwater has led to serious health problems in some areas in the world, particularly in Bangladesh and West Bengal. The most common and widely accepted mechanism of As release to groundwater in Bangladesh is the reduction of iron (Fe) hydroxides containing a large amount of As under anoxic condition [1]. However, in general, there is a poor correlation between the concentrations of As and Fe in As-contaminated groundwater, indicating that this mechanism does not fully explain the heterogeneous As contamination in groundwater found in Bangladesh [2]. In anaerobic sediments where Fe hydroxides are unstable, several Fe secondary minerals, clay minerals, carbonate minerals, and sulfide minerals could be present. Recently, the water–mineral interaction for these minerals has received much interest as the key reaction for further investigation of As behavior in As-contaminated groundwater. Calcite ($CaCO_3$) is the most stable polymorph of calcium carbonate under ambient condition and ubiquitously found in various surface environments. Many As-contaminated groundwater sources are slightly saturated with calcite, suggesting that calcite precipitates in groundwater. Furthermore, once As is incorporated into calcite, a serious environment pollution caused by the leaching of As from calcite could not easily occur, because calcite is unaffected by redox changes unlike Fe minerals. Therefore, calcite has recently received much interest as an effective scavenger of As leached from Fe oxyhydroxides in As-contaminated groundwater.

Arsenic is mostly found in the forms of inorganic oxyanions, i.e., As(III) (arsenite, AsO_3^{3-}) or As(V) (arsenate, AsO_4^{3-}) in natural water. The toxicity and geochemical behavior of As depend markedly on the oxidation state of As. Thus, As interaction with calcite must be investigated with consideration of the dependence of As reactivity on the oxidation state of As. However, few studies have compared arsenite to arsenate in terms of the scavenging ability of calcite. Previous studies have shown that arsenate could be retained in calcite through sorption and coprecipitation [3]. On the other hand, it remains controversial whether calcite can immobilize arsenite [3,4]. To resolve this controversy, the investigation of the distribution behavior of As between water and calcite needs to be coupled with the determination of the As oxidation state in both water and solid phases.

In this study, laboratory experiments simulating the distribution of As to calcite were conducted for arsenite and arsenate to determine each species' distribution coefficient for calcite [5]. To determine the oxidation state of As in calcite and water, we employed the X-ray absorption near edge structure (XANES) technique and high-performance liquid chromatography-ICP-MS (HPLC-ICP-MS), respectively. In addition, we evaluated the local structure of As in calcite using atomic-scale structural information obtained by extended X-ray absorption fine structure (EXAFS) analysis. Arsenic *K*-edge XANES and EXAFS experiments were performed at beamline **BL01B1**.

The results of the coprecipitation experiment of As and calcite indicated that arsenate is preferentially incorporated into calcite over a wide range of pHs (7–12), whereas the incorporation of arsenite into calcite

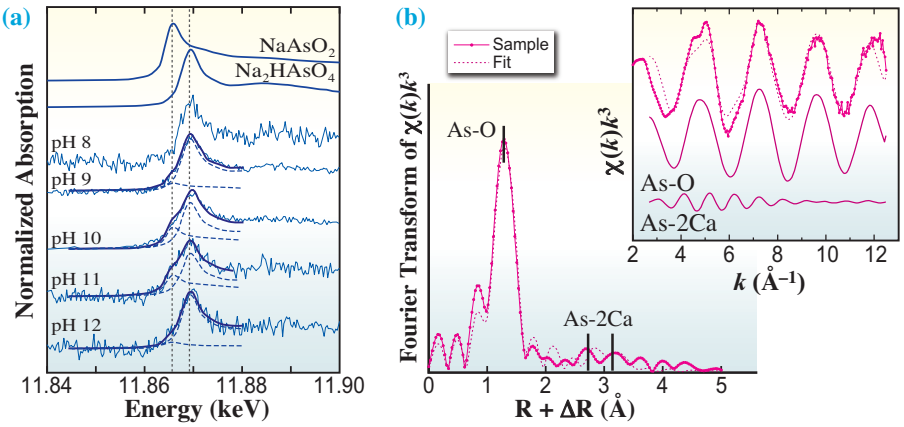

Fig. 1. **(a)** Normalized As *K*-edge XANES spectra for calcite precipitated in arsenite system at pHs 8 to 12. The spectra obtained by simulation are shown as solid curves, whereas the contributions of arsenite and arsenate are shown as dashed curves. **(b)** Normalized k^3-weighted EXAFS spectrum and its Fourier-transformed spectrum for the arsenate incorporated into calcite. Dotted lines are fitted FEFF simulations with an As-O shell and two As-Ca shells.

is not confirmed at circumneutral pH (Fig. 1(a)). This difference between arsenite and arsenate is attributed to the fact that their dissolved species are negatively charged and neutral, respectively, at circumneutral pH (arsenite as H_3AsO_3; arsenate as $H_2AsO_4^-$ or $HAsO_4^{2-}$). The ratio of the distribution coefficients of arsenite and arsenate to that of calcite was $K_{As(V)}/K_{As(III)} > 2.1\times10^3$ (pH 7). As pH increases (> 9), up to 33% of As(III)/As_{total} ratio is partitioned into calcite. The stronger interaction of arsenite with calcite at an alkaline pH compared with at circumneutral pH is due to the negative charge of arsenite at alkaline pH ($H_2AsO_3^-$). The local environment of arsenate in calcite revealed by EXAFS analysis shows that the AsO_4 tetrahedron is bound to six Ca atoms. This suggests that an arsenate oxyanion is substituted into the carbonate site in calcite during the coprecipitation (Fig. 1(b)).

In the system spiked only with arsenite (arsenite system), the XANES analysis detected arsenate in calcite (Fig. 1(a)), indicating that the oxidation of arsenite to arsenate occurred during the coprecipitation with calcite. To clarify the arsenate-incorporation mechanism in the arsenite system, the stabilities of arsenite and arsenate in the calcite-supersaturated solution were electrochemically investigated using cyclic voltammetry (CV). The oxidation of arsenite to arsenate appears as peak A in the voltammograms of the arsenite solutions in Fig. 2. Peak A shifts to a more negative potential with an increase in Ca concentration, which indicates a decrease in the apparent oxidation potential of arsenite to arsenate in the presence of Ca^{2+}. As a result, it was found that the complexation of Ca^{2+} and arsenate makes arsenate more stable in the solution. This stabilization could induce the oxidation of arsenite to arsenate, which is considered to result in the preferential incorporation of arsenate into calcite in the arsenite system (Fig. 3). The finding of this complexation-induced redox reaction suggests that the immobilization of As to calcite can occur even under reducing condition via arsenite oxidation to arsenate, although arsenite is hardly distributed to calcite.

The degree of As distribution to calcite may markedly depend on the arsenite/arsenate ratio in solution because of the large difference between the distribution coefficients of arsenite and arsenate, suggesting that the oxidation state of As is a significant issue in considering the scavenging ability of calcite for As in groundwater. In As-contaminated groundwater, arsenite is usually the main dissolved species. Although arsenite is hardly distributed to calcite, the immobilization of As to calcite can occur in groundwater by complexation with Ca^{2+} and the stabilization of arsenate. Considering the high abundance of Ca in natural water, the promotion of arsenite oxidation in the presence of Ca^{2+} is important as a (geo)chemical reaction, which may have been overlooked until recently.

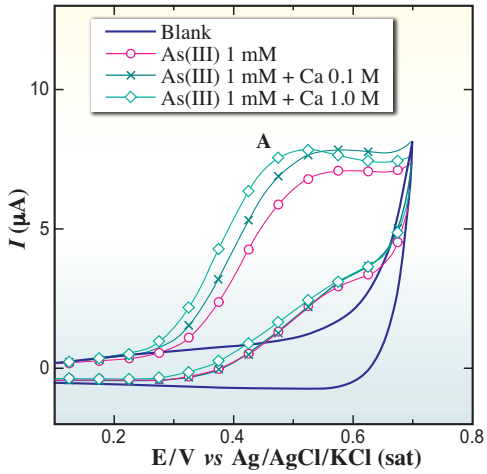

Fig. 2. Cyclic voltammograms for arsenite solution at different Ca concentrations in comparison with a blank solution.

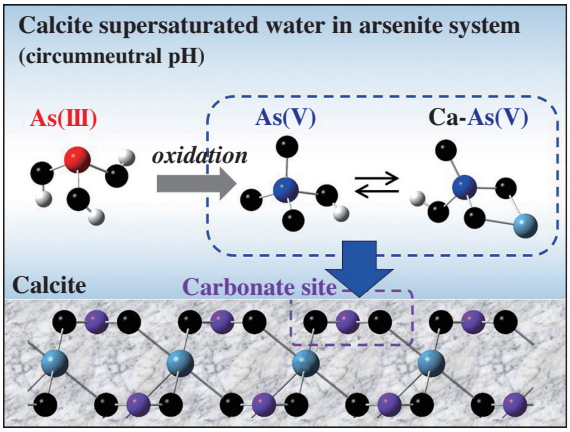

Fig. 3. Conceptual model of the complexation-induced arsenite oxidation and coprecipitation of arsenate with calcite in the arsenite system.

Yuka Yokoyama[a,*], Kazuya Tanaka[b] and Yoshio Takahashi[a]

[a] Department of Earth and Planetary Systems Science, Hiroshima University
[b] Institute for Sustainable Sciences and Development, Hiroshima University

*E-mail: yoshiyuka@hiroshima-u.ac.jp

References

[1] R. Nickson *et al.*: Nature **395** (1998) 338.
[2] A. van Geen *et al.*: Geochim. Cosmochim. Acta **68** (2004) 3475.
[3] Y. Yokoyama *et al.*: Chem. Lett. **38** (2009) 910.
[4] G. Román-Ross *et al.*: Chem. Geol. **233** (2006) 328.
[5] *Y. Yokoyama, K. Tanaka and Y. Takahashi: Geochim. Cosmochim. Acta* ***91*** *(2012) 202.*

Thermochemical behavior of lead during formation of chlorinated aromatics determined by X-ray absorption spectroscopy

Regarding the toxicity and resource recovery of lead, various speciation studies have revealed the redox chemical state of lead in postcombustion fly ash from thermal processes such as municipal solid waste (MSW) incineration and coal combustion. A large amount of lead exists as chloride, oxide, or sulfide in the thermal solid phase. Lead chloride ($PbCl_2$) promotes the formation of toxic chlorinated aromatic compounds (aromatic-Cls), such as polychlorinated dibenzo-*p*-dioxins (PCDDs), furans (PCDFs), biphenyls (PCBs), and benzenes (CBzs). In contrast, lead oxide (PbO) inhibits the formation of aromatic-Cls. Lead metallurgical processes can also be used to generate PCDDs, PCDFs, and PCBs. The thermochemical behavior of metals in the solid phase likely plays a role in aromatic-Cl formation and inhibition, which is supported by the results of our recent mechanism-based thermochemical studies of strong metal catalysts (Cu [1,2] and Fe [3]) and a metal inhibitor (Zn [4]). In the present study [5], we evaluated the thermochemical behavior of lead using quantitative and X-ray spectroscopic techniques.

Real fly ashes (RFAs) from municipal solid waste incinerators (MSWIs) were used to determine the major chemical forms and thermal behavior of lead. We prepared model fly ashes (MFAs) to understand the thermochemical interaction between lead and metal chlorides ($CuCl_2$ and $FeCl_3$). Gas chromatography/mass spectrometry (GC/MS) experiments provided quantitative information on aromatic-Cls such as PCBs and CBzs. The thermochemical state of lead was analyzed by X-ray absorption near-edge structure (XANES) measurements at beamline **BL01B1**. During the Pb L_3-edge XANES measurement, the sample disk was heated from room temperature to 300°C and 400°C in a T-type *in situ* cell under a flow of 10% oxygen/90% nitrogen delivered at 50 mL/min. After background removal and normalization, spectral analyses were performed by a linear combination fit (LCF) using reference materials of Pb [Pb, $PbCl_2$, PbO, Pb_3O_4, $PbO{\cdot}Pb(OH)_2$, and PbS].

The chemical states of Pb in three raw RFAs (at room temperature) were analyzed on the basis of the spectral shapes and LCFs of the Pb L_3-edge XANES spectra. The XANES spectral shape of Pb in each RFA was similar to that of the reference chloride ($PbCl_2$), as shown in Fig. 1. Pb existed mainly as a combination of chloride and oxide according to the LCFs of the XANES spectra (Table 1). Only RFA-B contained a notable quantity of lead sulfide (31%). According to previous studies, the three RFAs were representative mixtures of Pb chemical forms in MSW fly ash.

We prepared simplified MFAs admixed with $PbCl_2$ (1.0% Pb) and PbO (1.0% Pb) with KCl (10% Cl), activated carbon (3.0%), and SiO_2 (remainder), denoted as MFA-$PbCl_2$ and MFA-PbO, respectively, to examine the thermochemical behaviors of the two major Pb compounds in MSW fly ash. We observed small changes of MFA-$PbCl_2$ in the spectra from room temperature to 300°C and 400°C, as shown in Fig. 1. The LCF results indicated that the $PbCl_2$ composition at room temperature (60%) decreased slightly to 55–56% at higher temperatures. Therefore, the thermochemical oxidation of trace $PbCl_2$ in the model solid phase could promote the chlorination of the carbon matrix. Heating at 300°C and 400° lifted the characteristic spectrum dip of MFA-PbO at ~13067 eV, as shown in Fig. 1. The analysis of

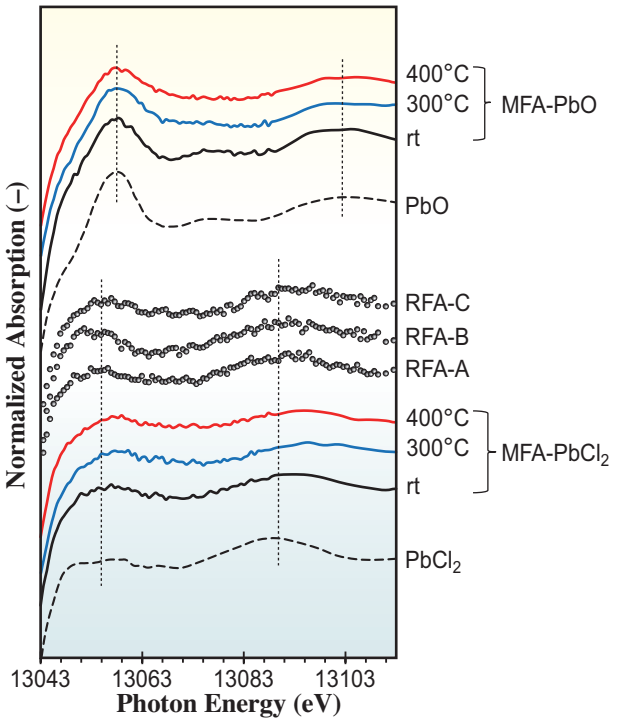

Fig. 1. Pb L_3-edge XANES spectra of RFAs and MFAs containing $PbCl_2$ and PbO.

spectra by LCF indicated that lead oxide in MFA-PbO was partially chlorinated to 25–28% $PbCl_2$ (Table 1). Inorganic chloride (KCl) functioned as a chlorine source for lead oxide. The reduced thermochemical chlorination of carbon by inorganic chloride might be due to the suppression of aromatic-Cls resulting from the prior partial chlorination of PbO using an inorganic chlorine source in the solid phase.

There is a large elemental composition gap between MFA-$PbCl_2$ and RFA. Thus, using RFA-A (which contained 89% $PbCl_2$ as the major Pb chemical form at room temperature) (Table 1), we performed *in situ* Pb L_3-edge XANES analysis. The L_3-edge spectrum of Pb at room temperature (rt), similarly to that of $PbCl_2$, shifted its peak positions to higher energies, such as in the PbO spectrum, upon heating (Fig. 2). The LCF results indicated that the 89% $PbCl_2$ content in RFA-A decreased to 44–59% after heating at 300°C and 400°, as shown in Table 1. Because the complex solid phase contributed largely to the thermochemical oxidation of $PbCl_2$, the formation of aromatic-Cls was promoted.

In real MSW fly ash, Pb exists in both oxide and chloride forms. Aromatic-Cl formation depends on the balance between the inhibition by lead oxide and the promotion by lead chloride. Because Pb coexists with other metal catalysts in real MSW fly ash, the coexistence effect of $PbCl_2$ has to be considered. Overall, our mechanism-oriented study suggests that Pb in MSW fly ash functions as an "adjuster" in the generation of aromatic-Cls, depending on the lead oxide/chloride ratio and conditions of coexistence with metal catalysts.

Table 1. Lead chloride, oxide, and sulfide components (%) in RFAs and MFAs based on LCF of Pb L_3-edge XANES.

Pb samples		Chloride (%)	Oxide (%)	Sulfide (%)
RFA-A	rt	89	11	
	300°C	44	56	
	400°C	59	41	
RFA-B	rt	26	43	31
RFA-C	rt	47	53	
MFA-PbO	rt		100	
	300°C	25	75	
	400°C	28	72	
MFA-$PbCl_2$	rt	60	40	
	300°C	55	45	
	400°C	56	44	

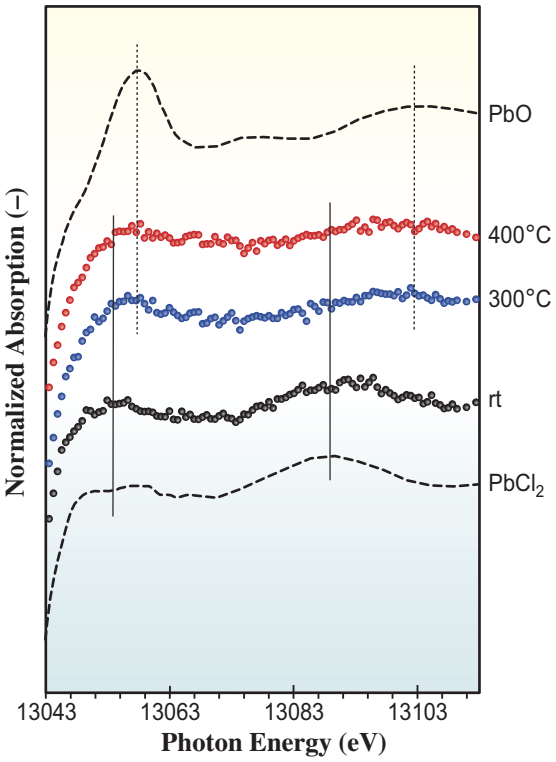

Fig. 2. *In situ* Pb L_3-edge XANES spectra of lead chloride-rich RFA-A heated from room temperature (rt) to 300°C and 400°C.

Takashi Fujimori[a,b,*] and Masaki Takaoka[a,b]

[a] Department of Global Ecology, Kyoto University
[b] Department of Environmental Engineering, Kyoto University

*E-mail: fujimori.takashi.3e@kyoto-u.ac.jp

References

[1] M. Takaoka *et al.*: Environ. Sci. Technol. **39** (2005) 5878.
[2] T. Fujimori *et al.*: Environ. Sci. Technol. **43** (2009) 8053.
[3] T. Fujimori *et al.*: Environ. Sci. Technol. **44** (2010) 1974.
[4] T. Fujimori *et al.*: Environ. Sci. Technol. **45** (2011) 7678.
[5] *T. Fujimori, Y. Tanino and M. Takaoka: Environ. Sci. Technol.* ***47*** *(2013) 2169.*

Industrial

Industrial use of SPring-8 is quite unique in the global SR community in terms of the scope of industrial areas and the number of industrial users. Reflecting the industrial structure of Japan, companies in electronics, automobile, hard/soft materials, energy & environment, pharmaceutical, and consumer goods conduct experiments for their critical research programs at various beamlines in SPring-8. The latest statistics for FY2012 indicate that 32% and 20% of research proposals conducted at contract and public beamlines, respectively, are submitted by leading researchers from the private companies. In addition, researchers from public and academic entities lead joint projects with their industrial partners, and actively conduct measurements at SPring-8 beamlines. The following five articles illustrate such activities.

Organic Semiconductors: H. Fukidome, M. Kotsugi, and H. Hibino, from Tohoku University, SPring-8/JASRI, and NTT Basic Research Laboratories, respectively, studied graphene epitaxy intensively at BL07SU, BL17SU, and BL23SU to develop graphene-silicon fusion devices. They conducted microscopic X-ray absorption spectroscopy (μ-XAS) measurements using a photoemission electron microscope (PEEM) at BL17SU on an operating graphene transistor to understand the electronic structure of the device. They also developed 3D Nano ESCA of the graphene transistor at BL07SU to elucidate the charge-transfer region at the interface of graphene and the source/drain electrodes.

Applications

Greenhouse Gas Control: To understand hydration structures around carbon dioxide molecules captured in aqueous amine solutions, H. Deguchi, N. Yamazaki, and Y. Kameda, from Kansai Electric Power Co., Mitsubishi Heavy Industries, and Yamagata University, respectively, applied an X-ray scattering capability at the leading industrial contract beamline BL16XU. Detailed analyses of the distribution function revealed hydrogen bond formations in solution. This work would contribute to the development of chemical absorption plants for large-scale CO_2 sources.

Automotive Catalysts: Catalysts composed of abundant base metals are highly demanded due to global concerns about the consumption of precious metals and to strengthen emission control. Y. Nagai from TOYOTA Central R&D Laboratories demonstrated the efficiency of an *operando* XAFS method, which is based on the quick-scanning XAFS (QXAFS) capability at their own contract beamline BL33XU. He discovered that simultaneous valence changes of copper and cerium atoms in Cu/CeO_2 of a three-way catalyst contribute to the improved reduction performance of nitrogen oxide in a rich/lean cycling condition.

Iron and Steel: D. Seo and M. Kobayashi from Toyohashi University of Technology and H. Toda from Kyushu University collaborated to successfully visualize a dual-phase structure of ferrite-austenite stainless steel using a phase contrast technique, namely, propagation-based imaging followed by a phase retrieval process. Their technique of 3D volumetric analysis is promising for a variety of duplex steel, such as ferrite-martensite and ferrite-cementite.

Electric Power Supply: The recent incidents in the aircraft industry have drawn public attention to the safety of lithium ion batteries when used improperly. K. Ohara, K. Fukuda, and E. Matsubara from Kyoto University developed two techniques of *in situ* XRD measurements of commercially available LIBs in normal use and have modeled cells in the extra-overcharge state at their contract beamline BL28XU.

SPring-8 would like to expand its application opportunities to include industrial areas that currently do not employ SR in Japan (e.g., food processing, agricultural and marine products, construction material, metal processing, and mineral resources).

Norimichi Sano

Soft X-ray spectromicroscopic study on graphene toward device applications

Graphene, the honeycomb network of carbon atoms, is promising for electronics, photonics and even spintronics owing to its excellent electronic properties, such as linear band dispersion and giant carrier mobilities arising from the fact that the behaviors of charged carriers are governed by relativistic quantum mechanics. As shown in Fig. 1, we have developed epitaxy of graphene on 3C-SiC thin films on Si substrates (GOS) toward graphene-Si fusion devices with the aid of surface science techniques, such as X-ray photoelectron spectroscopy and spectroscopic photoelectron and low-energy electron microscopy, at beamlines **BL23SU** and **BL17SU** [1]. Note that GOS has the unique property of the face-specific-dependent electronic band structure, which can offer multifuctionality in GOS-based devices [1]. In combination with surface micromachining techniques [2], 3D nanoscale multifunctioned GOS (3D-GOS) will be realized in the near future.

However, there are practical issues toward the realization of graphene-based integrated devices. One of the practical issues is device isolation. Site-selective epitaxy of GOS (SSE-GOS) before device fabrication is efficient because this simplifies device fabrication processes and can prevent sample damage and contamination during processing. Consequently, we have developed SSE-GOS by spatially controlling the defect density of a 3C-SiC(111) thin film on a Si(111) substrate [3].

The SSE-GOS production method is schematically shown in Fig. 2. First SiO_2 micropatterns on the Si(111) substrate were formed as a mask for SiC patterning. Then 3C-SiC(111) thin films were grown on both the bare Si and SiO_2-covered surface regions by gas-source molecular beam epitaxy with monomethylsilane as a gas source, followed by lifting the 3C-SiC(111) thin films off the SiO_2-covered regions using a dilute HF aqueous solution. Again, 3C-SiC(111) thin films were grown on the sample. Finally, the sample was annealed at 1523 K for 30 min in ultrahigh vacuum for graphitization.

To verify SSE-GOS, we have characterized the sample surface by microscopic low-energy electron diffraction (μ-LEED) and microscopic X-ray absorption spectroscopy (μ-XAS). The μ-LEED observation was performed by low-energy electron microscopy (LEEM) at the NTT Basic Research Laboratories. In Fig. 3, graphene (1×1) spots are visible in region A but are absent in region B. However, the (1×1) spots of the base SiC(111) thin film are visible. These results suggest the site-selective formation of graphene in region A.

μ-XAS near the Si *K*-edge (μ-Si-*K* XAS) was carried out by photoemission electron microscopy (PEEM) at **BL17SU** to elucidate the cause of the site-selectivity of GOS epitaxy. The μ-Si-*K* XAS spectra obtained from regions A and B are shown in Fig. 3. These spectra were similar to the previously reported Si-*K* XAS spectra of SiC. Note that the peak D (~1847 eV), which is related to Si vacancies [3] can be observed. The reduced intensity of peak D in the spectrum from region B indicates a higher density of Si vacancies in the SiC thin film in region B. It is concluded from the μ-LEED and μ-Si-*K* XAS results that the formation of Si vacancies suppresses the graphitization since the intensity of peak D is reduced by increasing the

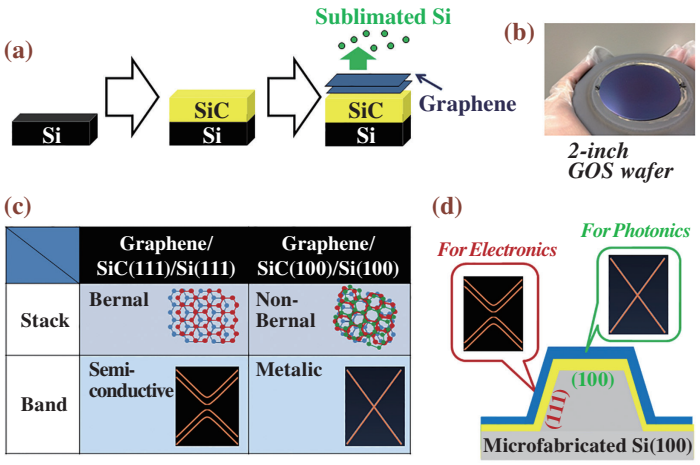

Fig. 1. **(a)** Schematics of GOS production process. **(b)** Optical micrograph of 2 inch GOS wafer. **(c)** Face-specific dependence of electronic structure of GOS. **(d)** Conceptual drawing of 3D-GOS.

density of Si vacancies, maybe because the increased Si vacancy density can increase the Si partial pressure near the surface that inhibits graphitization. The Si vacancy formation is ascribable to the increased surface roughness in region B during the removal of the SiC thin film before the second SiC growth. Intelligent microscopic control techniques for Si vacancies such as ion implantation shall be useful for precise device isolation for graphene-based integrated circuits.

Unlike ordinal device materials, such as Si, charged carriers in graphene follow relativistic quantum mechanics. This can make the graphene device operation mechanism reasonably specific. Definite clarification of the device operation mechanism requires direct nanoscopic observation techniques for electronic states under operating conditions, such as gate bias control, in addition to (macroscopic) electrical measurement.

For this purpose we have carried out operando observation of a graphene transistor using μ-XAS with PEEM at BL17SU [4]. In the graphene transistor, many-body effects, such as excitonic effects and Anderson orthogonality catastrophe, are remarkable and depend on the molecular orbital (π^* *vs* σ^*). The magnitudes of many-body effects are controllable by gate bias and contact with source/drain electrodes, which vary the position of the Fermi level in graphene, because of the disappearance of density of states near the Dirac point. This PEEM study is interesting. However, the exact Fermi level position cannot be inferred, which makes it difficult to unambiguously relate information on electronic states with device characteristics. For this reason, 3D Nano ESCA at BL07SU has been developed. The 3D Nano ESCA observation of the graphene transistor in fact made it possible to elucidate the charge transfer region between graphene and source/drain electrodes [5]. Furthermore, the 3D Nano ESCA operando observation, involving the addition of the gate-biasing function, is also now in progress [6]. The combination of PEEM and 3D Nano ESCA must be a novel way to fully understand device physics.

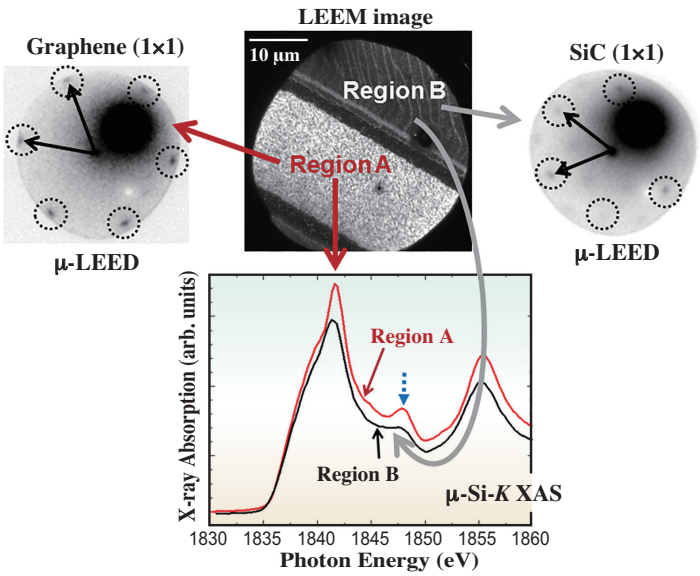

Fig. 3. Analyses of SSE-GOS using a LEEM image, μ-LEED, and μ-Si-*K* XAS.

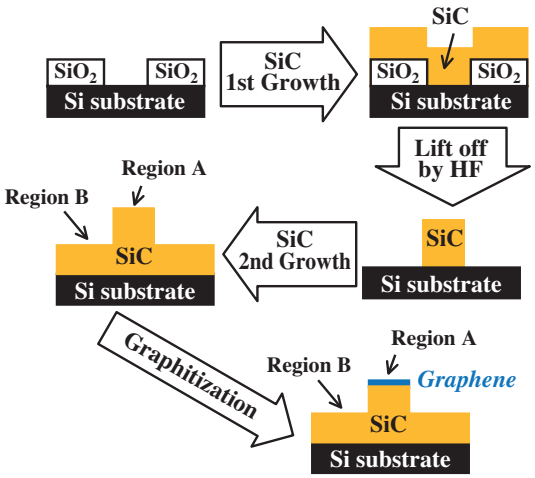

Fig. 2. Schematic drawing of production method of SSE-GOS.

Hirokazu Fukidome[a,*], Masato Kotsugi[b] and Hiroki Hibino[c]

[a] Reseach Institute of Electrical Communication, Tohoku University
[b] SPring-8/JASRI
[c] NTT Basic Research Laboratories

*E-mail: fukidome@riec.tohoku.ac.jp

References

[1] H. Fukidome *et al.*: J. Mater. Chem. **21** (2011) 17248.
[2] H. Fukidome *et al.*: Appl. Phys. Lett. **101** (2012) 041605.
[3] *H. Fukidome, Y. Kawai, H. Handa, H. Hibino, H. Miyashita, M. Kotsugi, T. Ohkochi, M.-H. Jung, T. Suemitsu, T. Kinoshita, T. Otsuji and M. Suemitsu: Proc. IEEE* ***101*** *(2013) 1557.*
[4] H. Fukidome *et al.*: Scientific Reports **4** (2014) 3713.
[5] N. Nagamura *et al.*: Appl. Phys. Lett. **102** (2013) 246104.
[6] H. Fukidome *et al.*: Scientific Reports **4** (2014) 5173.

Hydration structure around CO_2 captured in aqueous amine solutions observed by high energy X-ray scattering

Carbon dioxide is widely recognized as a major greenhouse gas that causes the global warming problem. One approach to reducing CO_2 emission is CO_2 capture at thermal plants. Among various technologies for CO_2 capture, the chemical absorption method [1] using aqueous amine solutions is the closest to commercialization for large-scale plants.

The chemical absorption method is based on a reversible chemical reaction between CO_2 and an aqueous amine solution. CO_2 in flue gas is separated into the solution by contact with the CO_2-lean solution. After absorption, CO_2 is released from the CO_2-rich solution by heating. Then, the regenerated solution is used again in the absorption process.

Although some chemical absorption plants for factory-scale CO_2 emission sources have been under commercial operation, plants for large-scale CO_2 emission sources such as thermal plants are still under development. One significant way to improve chemical absorption is to develop a more efficient solution to be realized by such characteristics as high absorption capacity, a high absorption rate and a small thermal energy for regeneration. These properties depend on the hydration structure of chemical species bound with CO_2. Better understanding of the structure can bring a new insight into the improvement of the solution performance. However, the analysis of the hydration structure has some difficulties because the materials for the analysis are liquid systems.

We have been applying the high energy X-ray scattering method using SPring-8 to the analysis of the hydration structure and conformation of amine molecules [2-4]. Compared with spectroscopic methods, the X-ray scattering method has an advantage of the capacity to derive molecular structure directly through a distribution function. In this report, we describe the results obtained using 30 wt% monoethanolamine (MEA) aqueous solution before and after CO_2 absorption. MEA is a primary amine expressed in the chemical formula of $NH_2CH_2CH_2OH$, and is a typical and fundamental amine used for the chemical absorption method.

Measurements were carried out at the undulator beamline **BL16XU**. The incident X-ray wavelength was 0.3356 Å (36.94 keV). The scattered X-ray intensity from the sample solution was measured over a 2θ range of $0.5 \leq 2\theta \leq 80°$. The molar fractions of the sample solutions before and after CO_2 absorption were $(MEA)_{0.112}(H_2O)_{0.888}(CO_2)_x$ (x=0 and 0.058, respectively). The sample solution was sealed in a flat plate acrylate resin cell with a thickness of 2 mm, which had X-ray transmission windows, each made of a Kapton film with a thickness of 25 μm. An empty cell was also measured for background intensity correction. The total exposure time was about 4–5 h for each sample solution.

Figure 1 shows the observed distribution function $g(r)$ of the sample solutions. In Fig. 1, the distribution function of a water sample is also shown for comparison. Three dominant peaks at r = 1.0, 1.5, and 2.8 Å are observed in $g(r)$ for the amine solution samples. The peak at r = 1.0 Å can mainly be ascribed to the intramolecular interaction of O–H within the water molecule. The peak at r = 1.5 Å is attributed to intramolecular interactions (mainly C–C, C–N, and C–O) in the amine (carbamate) molecule. The peak at r = 2.8 Å can be attributed mainly to the intermolecular hydrogen–bonded O···O interaction between the nearest neighbor water molecules. This peak also involves hydrogen–bonded O···O and N···O interactions concerning the nearest neighbor intermolecular amine···amine and amine···water interactions. Thus, atom pairs of the molecules existing in the sample solutions are clearly observed.

However, variations before and after CO_2 absorption are not clear. In order to clarify structural information on the captured CO_2, we derived a difference distribution function between before and after CO_2 absorption, $\Delta g_{CO_2}(r)$, as shown in Fig. 2. Peaks at r = 1.2 Å and 2.2 Å are obviously observed in the difference distribution function. These peaks

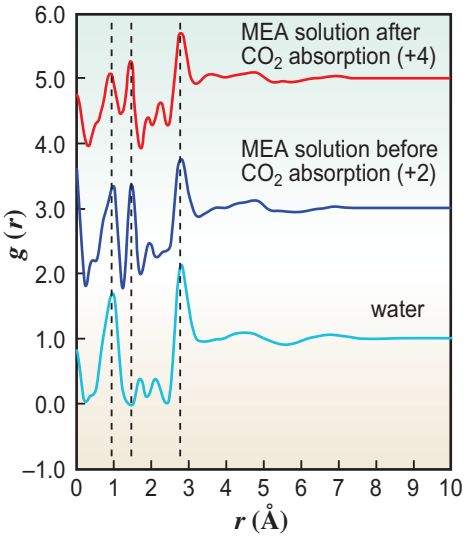

Fig. 1. Observed distribution functions.

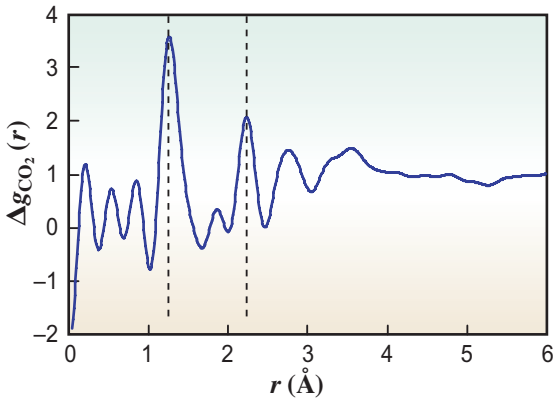

Fig. 2. Difference distribution function observed between before and after CO_2 absorption.

are mainly attributed to the intramolecular C–O and nonbonding O···O interactions of captured CO_2, respectively.

The difference distribution function in Fig. 2 involves both intramolecular interactions within molecules that bind the captured CO_2 and intermolecular interactions between the captured CO_2 and its neighboring molecules. By subtracting the intramolecular contributions from the total distribution function, the intermolecular distribution function can be obtained. An NMR analysis showed that absorbed CO_2 molecules in the sample exist as MEA carbamate of 86 mol%, HCO_3^- /CO_3^{2-} of 13 mol%, and MEA carbonate of 1 mol%. The molecular structure of MEA carbamate was calculated theoretically using DFT calculation. Five stable carbamate structures were obtained. Although the molar ratio between HCO_3^- and CO_3^{2-} is unknown, we considered the HCO_3^- molecule only and used the structure in a single crystal of $NaHCO_3$. The amine carbonate molecule was ignored because of its low molar ratio. From these molecular structures, we calculated the intramolecular interactions. By subtracting the intramolecular interactions from the total interactions, we obtained the intermolecular distribution function, $\Delta g^{inter}_{CO_2}(r)$, as shown in Fig. 3. The distribution functions in Fig. 3(a–e) were derived from the MEA carbamate structures (a)–(e), respectively. On the basis of any MEA carbamate structure, a broad peak at around r = 0.35 nm can be observed. By the detailed analysis, it was revealed that this peak originated from water molecules that formed hydrogen bonds with the captured CO_2. This result suggests that new hydrogen bonds are formed between the captured CO_2 molecules and the neighboring water molecules. Further study on other amine solutions showed that CO_2 captured as either amine carbamate or HCO_3^-/CO_3^{2-} formed hydrogen bonds with water molecules. Understanding of the hydrated structure at the molecular level will contribute to the development of new absorbing solutions with higher performance.

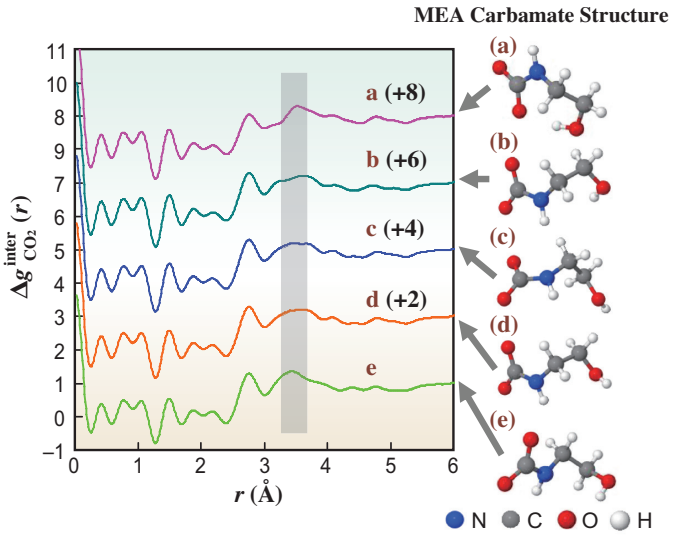

Fig. 3. Intermolecular distribution functions around captured CO_2. The distribution functions a–e were derived from the MEA carbamate structures **(a)–(e)**, respectively.

Hiroshi Deguchi[a,*], Noriko Yamazaki[b] and Yasuo Kameda[c]

[a] Power Engineering R&D Center, Kansai Electric Power Co., Inc.
[b] Advanced Technology Research Center, Mitsubishi Heavy Industries, Ltd.
[c] Dept. of Material and Biological Chemistry, Yamagata University

*E-mail: deguchi.hiroshi@c4.kepco.co.jp

References

[1] J.D. Figueroa *et al.*: Int. J. Greenhouse Gas Control **2** (2008) 9.
[2] H. Deguchi *et al.*: Ind. Eng. Chem. Res. **49** (2010) 6.
[3] *H. Deguchi, Y. Kubota, H. Furukawa, Y. Yagi, Y. Imai, M. Tatsumi, N. Yamazaki, N. Watari, T. Hirata, N. Matubayasi, Y. Kameda: Int. J. Greenhouse Gas Control* ***5*** *(2011) 1533.*
[4] Y. Kameda *et al.*: Bull. Chem. Soc. Jpn. **86** (2013) 99.

Operando XAFS study of Cu/CeO_2 for automotive three-way catalysts

Three-way catalysts (TWCs) can promote the simultaneous purification of three harmful gas emissions, that is, carbon monoxide (CO), unburned hydrocarbons (HCs), and nitrogen oxides (NOx), from automotive engines. The TWCs are placed under the floor and/or beside the engine, and their devices are installed in exhaust pipes. Each TWC comprises (i) precious metals such as platinum (Pt), rhodium (Rh), and palladium (Pd), (ii) supports for dispersing these precious metal particles on the nanometer scale, and (iii) catalytic promoters. In particular, the precious metals are pivotal components since they function as a source of catalytic active sites that detoxify harmful components. Recently, owing to the rising concern for global environmental protection, emission regulations have been strengthened step by step on a world scale. In line with this trend, the demand for automotive catalysts has been increasing yearly, increasing the consumption of precious metals. Therefore, the finite availability of precious metals has inspired us to develop catalysts comprising base metals, which are economical and abundantly available.

This study is intended to clarify a catalytic mechanism of NO reduction over a base metal catalyst and an optimum reaction condition for maximizing the catalytic activity for NO reduction, utilizing *operando* XAFS (X-ray absorption fine structure) analysis. The NO reduction reaction is considered as the most difficult reaction in three-way conversions. Herein, we show an important mechanism of an improved NO reduction reaction over the base metal catalyst Cu/CeO_2 under a periodic (rich/lean cycling) reaction condition [1].

Operando XAFS analysis provides the chemical states and molecular structures of catalysts in their working states as well as their catalytic activities. This methodology has been well established along with the use of intense synchrotron radiation sources. Figure 1 shows the high-speed *operando* XAFS system that we are using for catalysis at the Toyota beamline **BL33XU**. The gas transfer unit comprises three independent gas supply lines using 15 types of gas cylinders. The high-speed gas switching system is used to rapidly change between three gas lines, in order to simulate actual auto exhausts that always vary with the engine operation. The mass analyzer can analyze 5 gas species every 50 ms. We evaluated the catalytic activity on-line using the gas analyzer. The *operando* cell was specially designed for transient X-ray detection while minimizing the dead volume. A combination of a servo-motor-driven Si channel-cut monochromator with a tapered undulator enables rapid acquisitions of high-quality data of quick-scanning XAFS (QXAFS) [2]. The beamline covers an energy range from 4.0 to 46.0 keV. We applied the *operando* XAFS technique at both the Cu *K*-edge (8.98 keV) and Ce *K*-edge (40.45 keV) in order to clarify the Cu-Ce interaction in Cu/CeO_2 catalysts under reaction conditions. We performed an *operando* time-resolved QXAFS analysis at both high and low X-ray energies with a temporal resolution of one second, and revealed a unique dynamic behavior of synergistic redox properties of Cu and Ce species.

In this work, 6 wt% Cu/CeO_2 was used. Figure 2 shows changes in the Cu and Ce *K*-edges absorption edge energy under the static and periodic reaction conditions at temperatures ranging from 50 to 600°C.

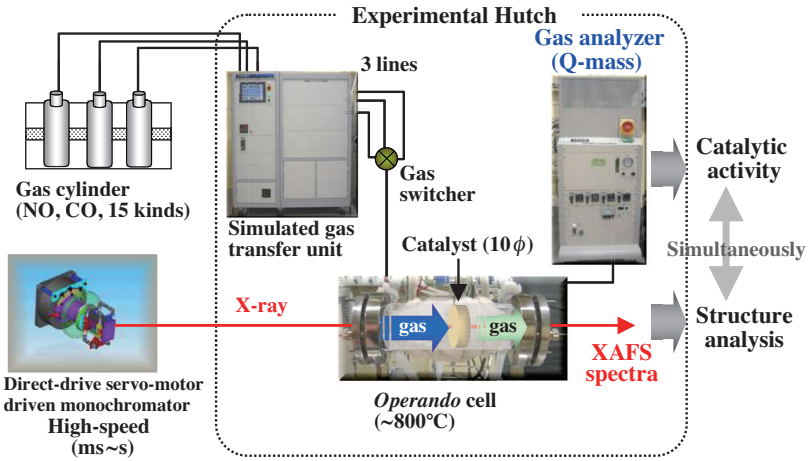

Fig. 1. Experimental setup for *operando* XAFS in transition mode.

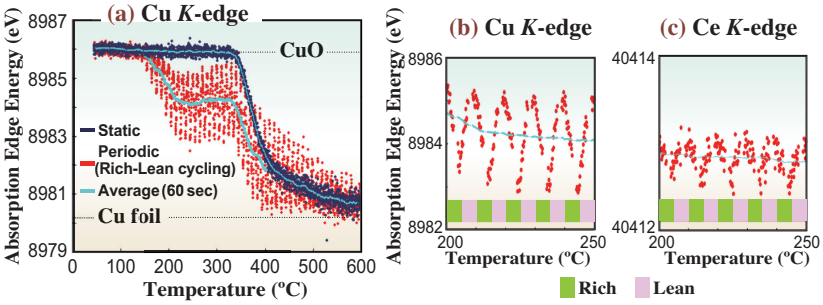

Fig. 2. **(a)** Energy shift of Cu *K*-edge as a function of temperature for the Cu/CeO_2 under the static and periodic reaction conditions. Magnified views of **(b)** Cu *K*-edge and **(c)** Ce *K*-edge absorption edge energy under the periodic condition. [1]

The static condition was obtained using a reactant gas stream consisting of 0.4% O_2, 0.65% CO, 0.15% NO, 0.1% C_3H_6, *ca.* 3% H_2O, and He balance. On the other hand, under the periodic condition, a lean stream (oxygen excess) consisting of 0.8% O_2, 0.65% CO, 0.15% NO, 0.1% C_3H_6, *ca.* 3% H_2O, and He balance or a rich stream (oxygen insufficient) with the same composition as the lean gas except for 0% O_2 was alternately introduced to the *in situ* cell every 30 s. The time-averaged O_2 concentration under the periodic condition was the same as that under the static condition. The Cu and Ce *K*-edges XAFS measurements were carried out under the same *operando* conditions, i.e., the catalyst weight, atmospheric condition, total flow rate, and temperature ramping rate. The Cu and Ce *K*-edges XAFS spectra were collected every one second. As shown in Fig. 2(a), the absorption edge energy of the Cu *K*-edge for Cu/CeO_2 at low reaction temperatures was the same as that for CuO powder used as a reference, indicating that the initial oxidation state was Cu^{2+}. The reduction of CuO under the static condition began to occur at 340°C. In contrast, the onset temperature of Cu reduction under the periodic condition was obviously low compared with that under the static condition. The Cu oxide species started to be reduced at 150°C along with the oscillation of the Cu oxidation state corresponding to the rich/lean cycling (Fig. 2(b)). In addition, the Ce oxidation state of the CeO_2 support also fluctuated under the periodic condition (Fig. 2(c)). It should be noted that the fluctuation period of the Cu oxidation state synchronized with that of the Ce oxidation state. Figure 3(a) shows the temperatures for 20% NO conversion under the static and periodic conditions. Cleary, the periodic condition leads to a significant increase in the catalytic reduction of NO. As for a conventional Cu/Al_2O_3 catalyst, an effective Cu reduction and an improvement in NO reduction were not seen under the periodic condition (data not shown). It was considered that the Cu oxide species in the Cu/CeO_2 catalyst under the periodic condition were easily reduced by synchronization with the valence change of Ce^{4+}/Ce^{3+} at the interface between the Cu particles and the CeO_2 support as shown in Fig. 3(b), and that this function improved the catalytic activity for NO reduction.

By the *operando* XAFS analysis, we discovered that the synchronization of the Cu and Ce valence change in Cu/CeO_2 under the periodic condition improves the catalytic activity for NO reduction.

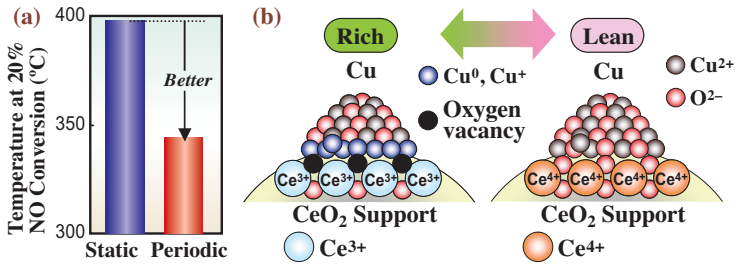

Fig. 3. **(a)** Temperatures for 20% NO conversion for the Cu/CeO_2 under the static and periodic reaction conditions. **(b)** Schematic representation of the oxidation state behavior of Cu and Ce under the periodic condition. [1]

Yasutaka Nagai

TOYOTA Central R&D Labs., Inc.

E-mail: e1062@mosk.tytlabs.co.jp

References

[1] *Y. Nagai, K. Dohmae, Y.F. Nishimura, H. Kato, H. Hirata, N. Takahashi: Phys. Chem. Chem. Phys.* ***15*** *(2013) 8461.*
[2] T. Nonaka *et al.*: Rev. Sci. Instrum. **83** (2012) 083112.

Visualization of dual-phase structure in duplex stainless steel

Since the discovery of X-rays by Röntgen [1] in 1896, absorption has been a dominant principle of X-ray imaging techniques. Conventional imaging techniques such as radiography and computed tomography (CT) rely on the decrease in X-ray beam intensity (attenuation) when traversing an object, which can be measured directly using an X-ray detector. As well known, however, this mechanism of image formation often provides poor contrast when imaging light-element materials such as polymers and biological tissues, as well as when imaging multiphase objects with a small difference in intensity between multi-composed structures such as the ferrite-austenite duplex stainless steel considered in this study. The difference in theoretical linear attenuation coefficient between two phases was only about 1.1 cm^{-1} (3.1% difference) at an X-ray energy of 37.7 keV owing to their quite similar chemical compositions. Various alternative methodologies have been developed to overcome such poor contrast [2]. Around the time of the development of laboratory-based micro-CT systems in the mid-1960s, in addition to absorption, creating X-ray images using the refraction of X-rays by matter was attempted [3]. This type of phase-contrast imaging (PCI) greatly enhances the visibility of weakly absorbing features in low density objects that barely absorb X-rays. PCI is different from the absorption contrast technique: It uses information concerning changes in the phase of an X-ray beam that passes through the object in order to create its images. Moreover, it enables the different phases to be distinguished even if their attenuation coefficients are very similar, which would be impossible with the absorption contrast technique alone.

Over the last several years, a variety of PCI techniques have been developed, all of which are based on the observation of interference patterns between diffracted and undiffracted waves. The most commonly used PCI techniques are propagation-based imaging, crystal interferometry, analyzer-based imaging, edge illumination and grating-based imaging. The propagation-based imaging is the most common name of the first technique and is also called in-line phase-contrast, in-line holography, refraction-enhanced imaging or phase-contrast radiography. A simple but powerful approach to realizing a higher imaging sensitivity when using synchrotron light sources is the propagation-based imaging method used in this study. Its experimental setup is basically the same as that of conventional radiography. It consists of an in-line arrangement of an X-ray source, a sample and an X-ray detector and no other optical elements are required (Fig. 1). By leaving an appropriate drift space between the sample and the imaging detector, interfaces within the probed sample can be visualized (Fig. 2(a)). If the X-ray wavefront distorted by the sample has a sufficient degree of transverse coherence, Fresnel diffraction on microscale structures will lead to interference fringes that enhance the edges and interfaces of the sample in the recorded radiograph. Compared with the conventional absorption contrast technique, PCI allows us to study samples either with negligible absorption or with many different components that show too similar degrees of absorption to be discriminated such as duplex metals.

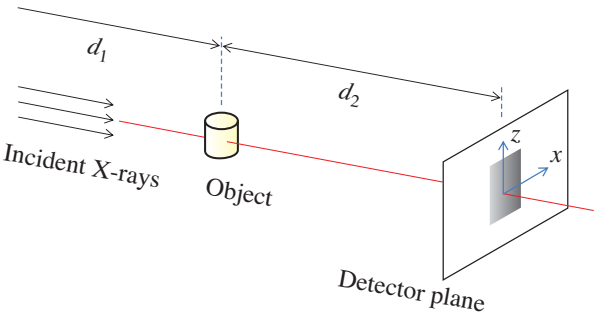

Fig. 1. Experimental setup of propagation-based imaging with single distance d_2 for duplex steel.

Owing to the weak refraction of X-rays compared with the light, specialized conditions are required to make use of X-ray refraction in the imaging. The X-ray beam should have a high spatial coherence and a significant distance between the sample and the detector d_2 is required. Experimental Hutch 2 of beamline **BL20XU**, which is used in this study, provides highly coherent beams sufficient for meeting the above first requirement, and the distance of the beam source from the sample, d_1, is 245 m. In the case of the parallel beam source used in this study, PCI fringe intensity increases with the propagation distance d_2, but the fringes broaden out. Therefore, a wide d_2 range from 8 to 1200 mm was considered to compare the visibility of fringes at the interfaces of duplex structures with the change in X-ray energy from 37.7 to 78 keV.

Although raw information on PCI is often useful for visual inspection with the naked eye like biomedical inspection, any further quantitative analysis, which is necessary for the segmentation of the tomographic

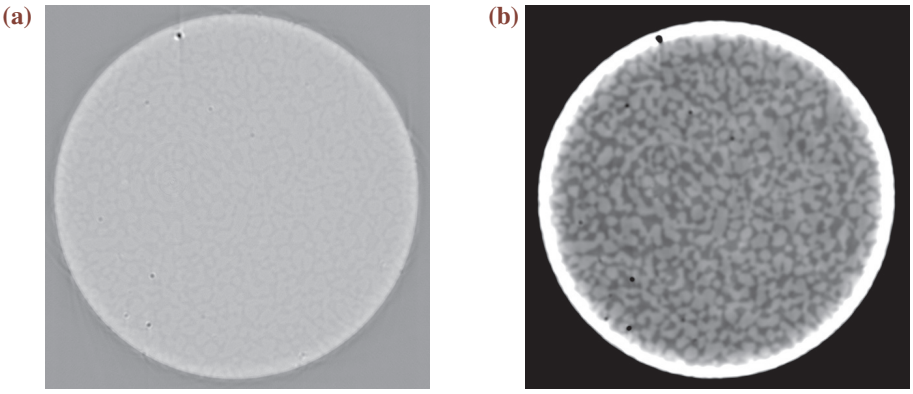

Fig. 2. Cross-sectional images of duplex steel **(a)** before and **(b)** after phase retrieval process at d_2 = 800 mm.

volume, is not easily possible using the raw information on PCI. This is because the gray levels in the multiple material regions are not too different to be divided into different segments; they only vary at the interfaces. However, if transmission radiographs are sent through an appropriate phase retrieval process, tomographic reconstruction can be performed and the tomograms will exhibit area contrast rather than edge-enhancing contrast (Fig. 2(b)). With subsequent post-processing such as noise filtering, a virtual 3D structure consisting of a complex dual-phase microstructure was successfully reconstructed, as shown in Fig. 3.

A variety of phase retrieval methods for PCI data have been developed since the mid-1990s. Although their algorithms are iterative or use analytical approaches, many methods require a large number of raw images obtained at different distances d_2 as well as numerous restrictions [3]. A single-distance phase-retrieval method developed by Paganin *et al.* [4] was chosen in this study, which is relatively simple and widely used in practical imaging. This particular algorithm retrieves the phase from radiographs obtained at a single distance d_2. Through a well-established multistage process of PCI mentioned above, 3D volumetric analysis for many types of duplex steels, such as ferrite-martensite, ferrite-cementite, and ferrite-austenite steels, has entered a new phase. The CT technique as an analytical tool for engineering takes a step forward once more via the success of this application, but many challenges still lay ahead, for example, PCI of heterogeneous metals consisting of more than two phases or improving the phase retrieval algorithm to fix dummy artifacts occurring at interfaces of defects inside samples.

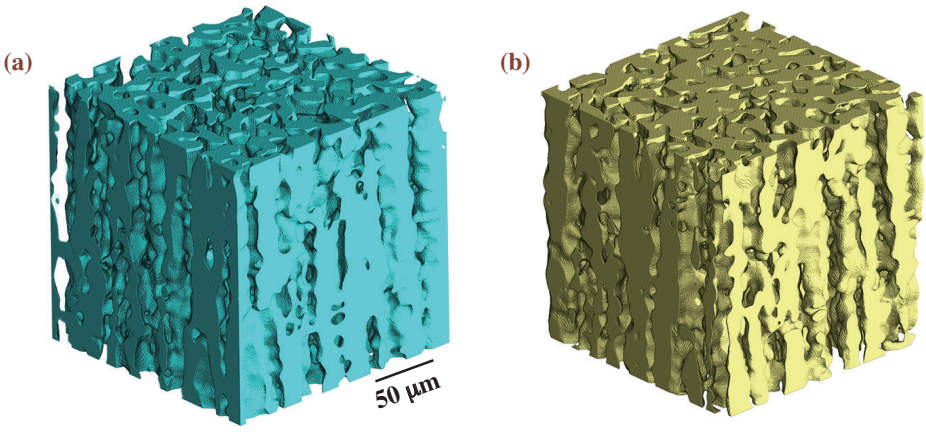

Fig. 3. Virtual 3D structures of duplex steel consisting of **(a)** ferrite and **(b)** austenite phases were reconstructed by a single-distance phase retrieval process.

Dowon Seo[a,*], Hiroyuki Toda[b] and Masakazu Kobayashi[a]

[a] Dept. of Mech. Eng., Toyohashi University of Technology
[b] Dept. of Mech. Eng., Kyushu University

*E-mail: seodwn@gmail.com

References

[1] W.C. Röntgen: Nature **53** (1896) 274.
[2] H. Toda *et al.*: Metall. Mater. Trans. **37A** (2006) 1211.
[3] P. Cloetens *et al.*: J. Appl. Phys. **81** (1997) 5878.
[4] D. Paganin *et al.*: J. Microsc. **206** (2002) 33.

Tackling the safety issue of lithium ion batteries at Kyoto University & NEDO beamline

Lithium ion batteries (LIBs) have been widely used in power supply applications, e.g., mobiles, electric vehicles and renewable energy storage devices. Most LIBs use a variety of organic electrolytes because of a wide potential window despite rigorous reactivity with the atmosphere. Their safety in normal use is no longer questionable, but this is not true in cases of improper use as seen in the recent accidents in the aircraft industry. A real-time analysis of unexpected reactions occurring in the LIBs in overcharge states would contribute to the improvement of their safety, while many disassembly analyses have already provided limited information. In particular, it is still difficult to analyze active materials in commercial LIBs directly owing to thick outer cases. Therefore, *in situ* analyses of such commercial products seem challenging in various charge/discharge states including the overcharge region. In this article, we would like to introduce an *in situ* pinpoint XRD analysis system and a recently developed glove box-integrated diffractometer to deal with the safety problem latent in the commercial LIBs mentioned above.

In general, the electrochemical reaction in the LIBs can be understood by gradual or drastic changes in crystal structure associated with Li^+ insertion/desertion. Firstly, we developed an *in situ* XRD method with a confocal geometry to attain a spatial resolution of several tens of micrometers. A schematic drawing of the confocal method is shown in Fig. 1(a). Incident and receiving slits that collimate the incident and diffracted X-rays form a confocal area with a lozenge shape. Its spatial resolution h is given as:

$$h = w / \cos(2\theta/2)$$

where w and 2θ are the slit width and diffraction angle, respectively. This confocal setup with a highly penetrative X-ray realized a pinpoint XRD analysis, which allowed us to understand the crystal structure of sealed materials.

The commercial LIB investigated in this study consists of a $LiCoO_2$ layer on an Al current collector as a cathode, graphites on a Cu current collector as an anode, and probably conventional organic electrolytes. These components were wholly packaged in an Al container, the wall thickness of which is about 300 μm. The LIB package connected to a mobile phone was placed on a multi-axis diffractometer installed at beamline **BL28XU** [1], as shown in Fig. 1(b). The observation area, i.e., confocal area, is controlled by changing the position of the mobile phone. Figures 1(c) and 1(d) show *in situ* XRD patterns during 2 h charge and 5 h discharge reactions, respectively. The diffraction peak corresponding to the Al container on the surface of the LIB package remains unchanged during the charge and discharge reactions. On the other hand, the electrode deeply packed in the battery exhibits a distinct diffraction peak shift at 2θ = 4.9-5.0°, which is assigned to $LiCoO_2$-related compounds ($Li_{1-x}CoO_2$) during the operation of the mobile phone. This is due to a change in crystal structure associated

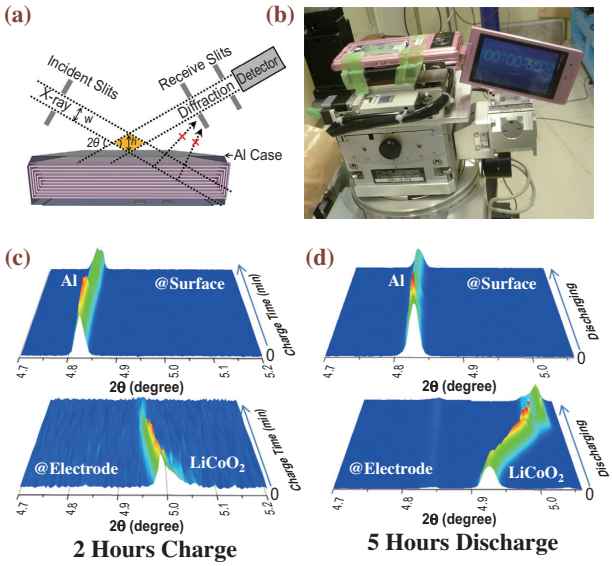

Fig. 1. **(a)** Schematic drawing of the confocal XRD analysis of the commercial LIB. **(b)** View of the measurement. *In situ* XRD patterns obtained on surface and electrode positions of the battery during **(c)** charge and **(d)** discharge process.

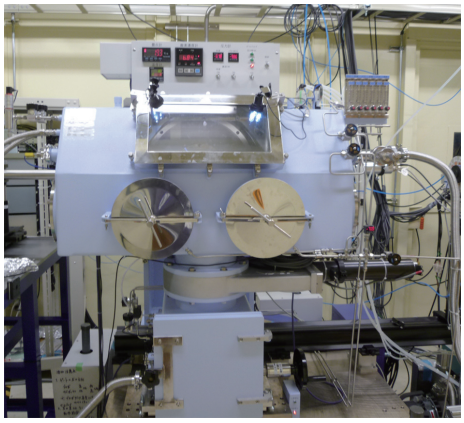

Fig. 2. Photograph of the glove box-integrated diffractometer developed through a collaboration with Rigaku-Aihara Corporation.

with the Li^+ insertion/desertion. Thus, our study demonstrates the great potential of confocal XRD as a time-resolved pinpoint analysis technique for commercial LIBs.

Secondly, as a fundamental study for the $LiCoO_2$ electrode in the overcharge state, a see-through cell convenient for examining a certain type of oxidation was prepared under inert atmosphere and subjected to the following analysis. The cell was preliminarily conditioned by performing charge/discharge cycles up to the second discharge process. A fast XRD analysis based on consecutive snapshots acquired from a one-dimensional pixel array detector was carried out using the glove box-integrated diffractometer (see Fig. 2) installed at BL28XU to prevent possible hazards, e.g., thermal runaway, fire and explosion, in the overcharge state. Figure 3 shows *in situ* XRD patterns of the cell during the third charge process. At the beginning of the charge process, two diffractions for Al and three diffractions for $Li_{1-x}CoO_2$ in the O3 structure were observed. Through charging the cell until 5.0 V indicated by the broken line, $Li_{1-x}CoO_2$ in the H1-3 structure appeared and finally transformed into $Li_{1-x}CoO_2$ in the O1 structure. This structural transformation induced by the electrochemical extraction of Li^+ from the $LiCoO_2$ active material is fairly consistent with the earlier studies reported in the literature. Interestingly, it is found that the diffraction peak at around 2θ = 9.7° continues to shift to a lower angle until the potential of 5.5 V (the so-called overcharge state in this material system), indicating that the $Li_{1-x}CoO_2$ in the O1 structure is still active in the potential region. At a potential higher than 5.5 V, the peak positions of the $Li_{1-x}CoO_2$ in the O1 structure become constant and noisy current is observed. This behavior can be explained by the inevitable decomposition of the electrolyte used at the high potential. To the best of our knowledge, this is the first *in situ* XRD study on $LiCoO_2$ electrodes in the extra-overcharge state (more than 5.5 V).

In conclusion, we showed two *in situ* analyses. The confocal XRD analyses carried out at BL28XU successfully visualized the phase transition behavior of the $LiCoO_2$ active material depending on the electrochemical potential in the commercial LIBs. Also, a $LiCoO_2$ electrode in the extra-overcharge state was investigated in detail by means of the glove box-integrated diffractometer. Further development of synchrotron-based analyses will strongly promote the wide spread use of the LIBs.

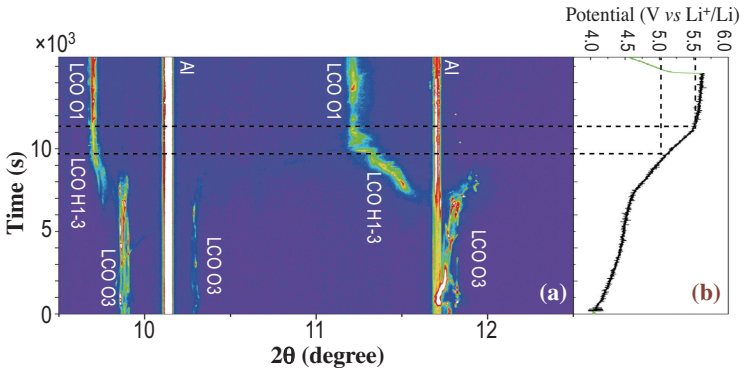

Fig. 3. **(a)** *In situ* XRD patterns and **(b)** charge curve for the LIB cell used in this study. "LCO" in the figure means $LiCoO_2$-related compounds.

Koji Ohara[a], Katsutoshi Fukuda[a] and Eiichiro Matsubara[b,*]

[a] Office of Society-Academia Collaboration for Innovation, Kyoto University
[b] Dept. of Materials Science and Engineering, Kyoto University

*E-mail: matsubara.eiichiro.6z@kyoto-u.ac.jp

References

[1] E. Matsubara: SPring-8 Research Frontiers 2011, p147.

Nuclear Physics

LEPS and LEPS2 Beamlines Overview

The linearly polarized photon beam produced by laser-induced backward Compton scattering from 8 GeV electrons has been used to study the quark-nuclear physics via the photoproduction of hadrons at BL33LEP (LEPS). This photon beam has a large polarization, nearly 100% at the maximum energy, which is a great advantage to elucidate the photoproduction mechanism. The photon energies above 1.5 GeV are tagged by detecting recoiled electrons.

The LEPS beamline has been upgraded in parallel to the experiments. An all-solid UV laser with a 355-nm wavelength (Paladin) was introduced instead of the previous Ar laser, and thanks to the low power consumption, we performed the simultaneous injection of two UV lasers. The gain of beam intensity was accomplished by a factor of 1.6. The maximum energy has also been extended up to 2.9 GeV by introducing 266-nm deep UV lasers (Frequad-HP). The photon intensities have reached 2.5×10^6 s^{-1} for the 2.4-GeV beam and 2.0×10^{-5} s^{-1} for the 2.9-GeV beam, respectively.

The upgraded high intensity beam has been utilized for the high-statistics experiments. The article by Tokiyasu *et al.* reports the results of the search for the K^-pp bound state through the $\gamma d \rightarrow K^+\pi^- X$ reaction. The kaonic nuclei like a K^-pp state are very exotic because they contain a real kaon as a nuclear component. The confirmation of the existence of such nuclei is one of the recent hot subjects in hadron physics and this is the first try using the photoproduction. The obtained missing mass spectrum has shown no peak structure corresponding to the K^-pp bound state in the expected mass region. The upper limit of the production cross section has been estimated.

The construction of a new laser-electron photon beamline, LEPS2, has started at **BL31LEP** in 2010. Based on the experience in the LEPS experiments, the LEPS2 project aims to improve the beam intensity one order of magnitude and to enable the installation of the large acceptance detector with high resolution. A new LEPS2 experimental building was constructed outside the experimental hall of the storage ring. Figure 1 shows the ribbon-cutting scene of the inauguration ceremony of LEPS2 performed in front

Fig. 1. Photograph of the inauguration ceremony of the laser-electron photon beamline LEPS2 (BL31LEP) held on February 21, 2013.

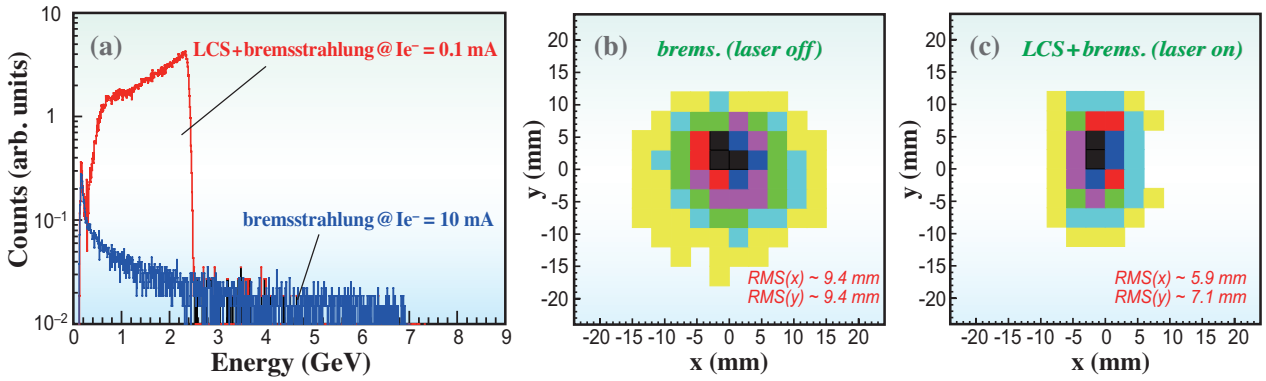

Fig. 2. **(a)** Energy spectra of the photon beam in the case of laser ON and OFF, respectively. The vertical scale is normalized by the electron beam current. **(b)** Beam profile for the Bremsstrahlung photon only (laser OFF). **(c)** Beam profile in the case of laser ON.

of the experimental building. By using one of four special beamlines with 30-m straight sections, which have the smallest beam divergence, the photon beam does not spread out even at the target position (135-m downstream of the collision point).

The LEPS2 project reached a milestone in 2013. On January 27, the first photon beam at BL31LEP was successfully observed in the measurements of energy spectrum, beam profile and beam intensity. In the beam commissioning, two 16-W lasers and a 24-W laser with the wave length of 355 nm were used and injected simultaneously. The energy spectrum measured with a BGO crystal calorimeter and beam profile measured by a position counter with scintillating fibers are shown in Fig. 2. The Compton edge of 2.4 GeV is clearly identified for the laser-Compton scattering (LCS) gamma rays and the small beam size (< 10 mm in RMS) was confirmed as expected. The Compton scattering rate was estimated to be about 7×10^6 s^{-1} for the 100-mA storage electron current.

In the LEPS2 experimental building, we have been preparing two detector systems. One is a large acceptance charged particle spectrometer using a large 1-T solenoid magnet transported from the Brookhaven National Laboratory (BNL) in U.S. Several chambers and counters which will be placed inside the solenoid are still under the construction. Another detector is an electromagnetic calorimeter, BGOegg, consisting of 1320 BGO crystals, which has been developed by the ELPH group in Tohoku University, and is now placed upstream of the solenoid magnet. A photograph of the inside of the LEPS2 experimental building is shown in Fig. 3. After many efforts for the setup of detectors and for the preparation of the data acquisition system, the commissioning run has just started with the BGOegg. The full-scale BGOegg experiment will be performed in 2014 to investigate the η' meson physics, etc.

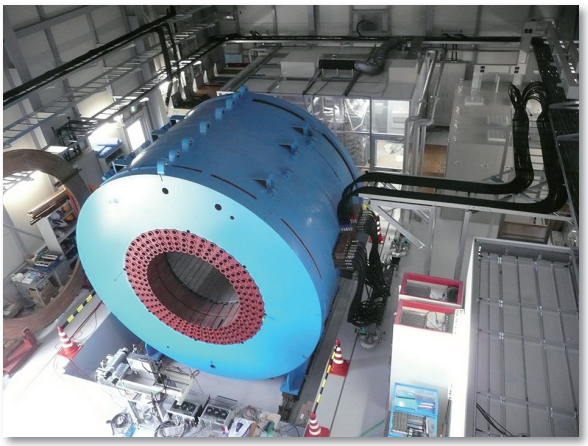

Fig. 3. Photograph of the inside of the LEPS2 experimental building. The BNL/E949 solenoid magnet is installed around the center of the room and the BGOegg is placed in the clean booth upstream of the magnet. The diameter of the magnet yoke is 5 m.

Masaru Yosoi for the LEPS Collaboration

Research Center for Nuclear Physics (RCNP), Osaka University

E-mail: yosoi@rcnp.osaka-u.ac.jp

Search for the K^-pp bound state using the photon induced reaction at BL33LEP

One of the missions of hadron physics is to investigate the interaction between hadrons and search for new types of nuclei within the framework of quantum chromodynamics. It is well known that π's exist as virtual particles in nuclei. However, the low-energy interaction between a π and a nucleon is repulsive, and π's are not bound in nuclei. In the case of antikaons, the interaction is highly complicated owing to the existence of $\Lambda(1405)$ below the K^-pp mass threshold. The interaction between an antikaon and a nucleon is strongly attractive if the isospin of the system is zero. This indicates the existence of a bound state of antikaons in nuclei called kaonic nuclei. Kaonic nuclei are a totally new type of nucleus and contain real mesons as components. If such nuclei exist, we can extract invaluable information on the properties of hadrons in nuclei. Intensive studies have been performed theoretically and experimentally to prove the existence of kaonic nuclei, especially the K^-pp bound state (the bound state of a K^- and two protons), the simplest kaonic nucleus. The structure of the K^-pp bound state has been studied by various theoretical approaches. The binding energy (B.E.) and width (Γ) were predicted to be 9 – 95 MeV and 34 – 110 MeV, respectively. The predicted B.E. is much larger than those of ordinary nuclei (~8 MeV per nucleon).

Experimental evidence of the K^-pp bound state was reported by the FINUDA collaboration (B.E. = $115^{+6}_{-5}(stat)^{+3}_{-4}(syst)$ MeV, $\Gamma = 67^{+14}_{-11}(stat)^{+2}_{-3}(syst)$ MeV) [1] and the DISTO collaboration (B.E. = 103 ± 3 $(stat)$ ±5 $(syst)$ MeV, $\Gamma = 118\pm8$ $(stat)$ ±10 $(syst)$ MeV) [2]. The measured B.E.'s and Γ's are different from each other, and measured B.E.'s are much larger than the values predicted using theoretical models. The experimental studies do not provide sufficient proof to conclude the existence of the K^-pp bound state, and search experiments with different reactions are awaited.

This situation has motivated us to perform a new experiment to search for the K^-pp bound state using a photon-induced reaction at the LEPS (Laser Electron Photon experiment at SPring-8) facility [3]. We adopted the $\gamma d \rightarrow K^+\pi^-X$ reaction using the photon beam with energies ranging from 1.5 to 2.4 GeV. We detected K^+ and π^- at forward angles, and searched for a peak structure corresponding to K^-pp bound state production in the missing mass spectrum. Figure 1 shows the schematic diagram of this reaction. In the effective Lagrangian approaches, a K^- or K^{*-} is exchanged if a K^+ is detected at very forward angles. The momentum transfer squared $|t|$ is sufficiently small that the exchanged K^- or K^{*-} is on mass-shell. From this point of view, the $\gamma d \rightarrow K^+\pi^-X$ reaction is regarded as the virtual $K^-d \rightarrow \pi^-X$ or $K^{*-}d \rightarrow \pi^-X$ reaction, which has not been used for the search for the K^-pp bound state up to now.

The experiment was performed at **BL33LEP**. A linearly polarized photon beam was produced by backward Compton scattering of an ultraviolet laser from 8 GeV electrons. The recoiled electrons were detected with a tagging counter, and the energies of the photon were measured with a resolution of 12 MeV when they are in the range from 1.5 to 2.4 GeV. The data used in this work was collected during 2002/2003 and 2006/2007 with a 150-mm-long liquid deuterium target. A total of 7.6×10^{12} photons were incident on the target. Charged particles produced in the target were detected with a spectrometer at forward angles. The spectrometer consists of a dipole magnet equipped with tracking devices and scintillation counters. The momenta were measured by track reconstruction with a resolution of 6 MeV/c for 1 GeV/c particles. The particle species were identified from the time-of-flight information, and K^+ and π^- were selected for analysis. The missing mass of the $\gamma d \rightarrow K^+\pi^-X$ reaction ($MM_d(K^+\pi^-)$) was calculated in the following kinematic region: $\cos\theta^{lab}_{K/\pi} > 0.95$, $0.25 < p_K < 2.0$ GeV/c, $0.25 < p\pi < 0.6$ GeV/c, where θ^{lab} and p are the scattering angle and momentum in the laboratory system, respectively. Then, the differential cross section was measured by applying acceptance correction for each event.

Figure 2 shows the differential cross section as a function of $MM_d(K^+\pi^-)$. The dominant features in the obtained spectrum are the Λ and Σ peaks, which are mainly due to the quasi-free $\gamma N \rightarrow K^+Y^*$ processes followed by $Y^* \rightarrow Y\pi^-$ decay. Here, N, Y^*, and Y respectively denote the nucleon (p/n), hyperon resonances (Λ^*, Σ^* and so on), and the hyperon

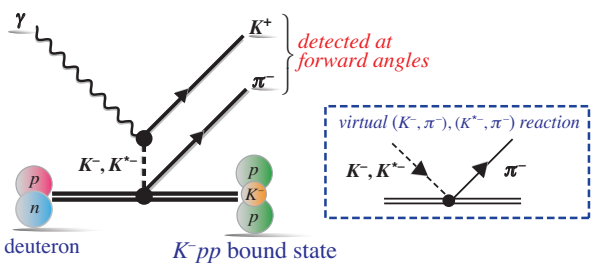

Fig. 1. Schematic diagram of the $\gamma d \rightarrow K^+\pi^-X$ reaction.

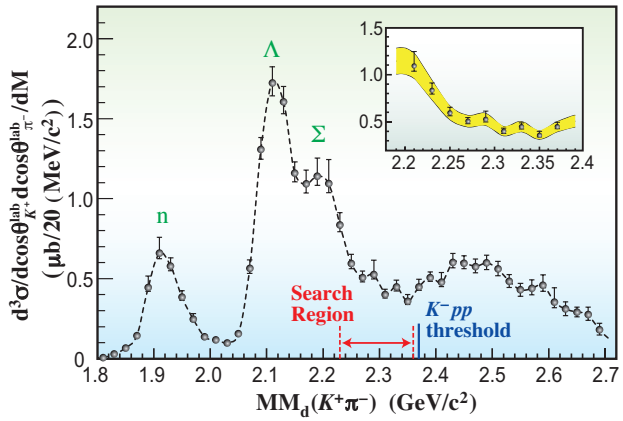

Fig. 2. Differential cross section of the $\gamma d \rightarrow K^+\pi^-X$ reaction as a function of $MM_d(K^+\pi^-)$. Inset: Differential cross section in the range from 2.2 to 2.4 GeV/c^2. The error band denotes the discrepancy between the 2002/2003 and 2006/2007 data sets.

(Λ/Σ). Quasi-free nucleons are actually bound in the deuteron. The peak around 1.9 GeV/c^2 is attributed to the $\gamma n \rightarrow K^+\Sigma^-$ process followed by $\Sigma^- \rightarrow \pi^- n$ decay. If the production cross section of the K^-pp bound state is large, a peak structure will appear in the mass region from 2.22 to 2.36 GeV/c^2. However, no peak structure was observed in the search region. More precise investigation revealed that the contribution in the search region was dominated by quasi-free processes such as $\gamma p \rightarrow K^+\Lambda(1520)$ or $\gamma p/n \rightarrow K^+\pi^-\Lambda/\Sigma$.

To quantify the search results, the upper limits of the cross section of the K^-pp bound state production were obtained under different B.E. and Γ assumptions. Figure 3 shows the upper limits of the production cross section of the K^-pp bound state for three Γ values as a function of assumed mass. The upper limits were determined as (0.17–0.55), (0.55–1.7), and (1.1–2.9) μb for signals with Γ = 20, 60, and 100 MeV, respectively. These values correspond to (1.5 – 5.0), (5.0 – 15), and (9.9 – 26)% of the production cross section of typical hyperon production as $\gamma N \rightarrow K^+\pi^- Y$.

In summary, we measured the differential cross section of the $\gamma d \rightarrow K^+\pi^-X$ reaction at BL33LEP. The peak structure corresponding to the K^-pp bound state was not observed in the mass region from 2.22 to 2.36 GeV/c^2 in the spectrum. The upper limits of the cross section of K^-pp bound state production were determined under various B.E.'s and Γ's. This work is the world's first search result of the K^-pp bound state using a photon-induced reaction. The production cross section in this reaction was found to be much smaller than those of typical hyperons.

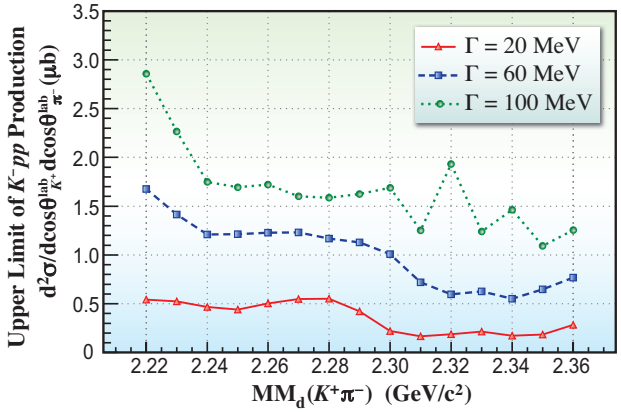

Fig. 3. Upper limit of the differential cross section of the K^-pp bound state in the $\gamma d \rightarrow K^+\pi^-X$ reaction as a function of assumed mass. Red, blue, and green lines are the results for Γ = 20, 60, and 100 MeV, respectively.

Atsushi Tokiyasu for the LEPS Collaboration

Research Center for Nuclear Physics (RCNP), Osaka University

E-mail: tokiyasu@rcnp.osaka-u.ac.jp

References

[1] M. Agnello *et al.*: Phys. Rev. Lett **94** (2005) 212303.
[2] T. Yamazaki *et al.*: Phys. Rev. Lett **104** (2010) 132502.
[3] *A. O. Tokiyasu et al.: Phys. Lett. B* ***728*** *(2014) 616.*

Accelerators & Beamlines Frontiers

SPring-8 Beam Performance

Developments and Upgrades of the Storage Ring and Linac

Lower Emittance Optics for User Operation

To provide brilliant photons at the SPring-8 storage ring, new optics has been available for the user operation since May 9, 2013. The main parameters of new optics are listed in Table I. The natural emittance of the new optics is reduced from 3.49 nm·rad to 2.41 nm·rad at 8 GeV by optimizing the quadrupole magnetic fields. Compared to the previous optics, SPECTRA [1] predicts that the new optics can provide 1.5-times higher brilliance and 1.25-times higher flux density for 10 keV photons with the SPring-8 standard undulator, and it was confirmed at the accelerator diagnostics beamline II (BL05SS) that the flux density of the new optics is 1.3-times higher than that of the previous ones (see Fig. 1).

Table 1. Main parameters of the new optics

	Previous Optics	New Optics
Beam energy	8 GeV	
Natural emittance	3.49 nm·rad	2.41 nm·rad
Energy spread σ_E/E	0.11%	
Tune (Q_x, Q_y)	(40.14, 19.35)	(41.14, 19.35)
Natural chromaticity (ξ_x, ξ_y)	(−88, −42)	(−117, −47)
(β_x, β_y, D) @ ID center	(22.5 m, 5.6 m, 0.11 m)	(31.2 m, 5.0 m, 0.15 m)

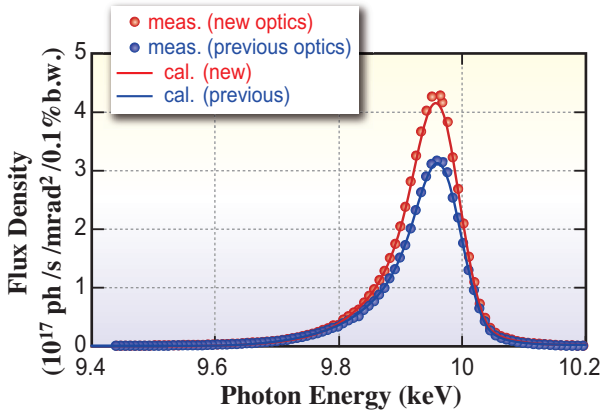

Fig. 1. Comparison of the photon flux density for the new and previous optics at diagnostics beamline II (BL05SS).

Cure for Impact of Insertion Devices

In recent light source rings the top-up operation, where the electron beam is injected into the storage ring during user experiment, is essential for improving the integral brilliance and the strength stability of the light source. In the top-up operation the electron beam is injected with beam shutters for the photon beam opened and the gaps of insertion devices (ID) closed. Hence electron loss should be as small as possible for radiation safety and to prevent demagnetization of the magnet array of ID's.

Usually, the injected electron beam has a large horizontal oscillation amplitude being injected in the horizontal plane. This horizontal oscillation with is converted into a vertical oscillation by coupling of the betatron motion. Consequently, the beam is lost at a vertical obstacle that is narrower than the horizontal aperture. In particular, when the gap of the in-vacuum undulator is closed, the vertical aperture increases beam loss, becoming much smaller.

In the SPring-8 storage ring, linear betatron coupling is well suppressed by tuning the skew quadrupole magnets. Consequently, linear coupling scarcely affects the beam loss. However, higher-order coupling resonance is excited through the skew octupole magnetic field of ID07, which is a complex of eight Figure-8 undulators, and hence enhances beam loss. Figure 2 shows the operation point and the resonance lines of the betatron motion. As the oscillation amplitude grows, the betatron tune shifts to

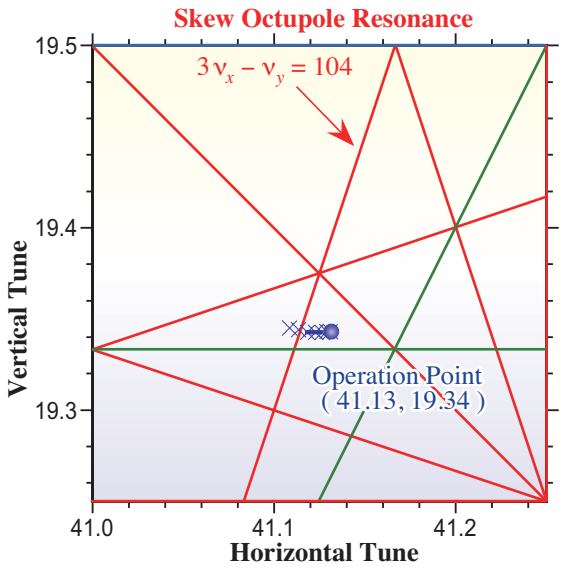

Fig. 2. Betatron tune and resonance lines in the tune diagram. Green and red lines denote the third and fourth order resonances, respectively.

the skew octupole resonance. Then electrons with a large amplitude like the injecting beam are lost due to the coupling resonance.

Octupole magnets installed to cancel the octupole magnetic field of ID07, improved the beam injection efficiency. Figure 3 shows the trend of the injection efficiency in user operation and the output current to the skew octupole magnets. The injection efficiency is recovered by exciting the octupole magnets.

Besides the skew octupole coupling resonance, the injection efficiency is degraded when the ID gaps are closed, especially that of ID19, which is a 25-m long in-vacuum undulator. Because the quadrupole magnetic field generated by ID19 shifts the betatron tune to approach the higher order coupling resonance according to the gap value, beam loss increases due to the resonance excitation. However, tuning the strength of neighboring quadrupole magnets can compensate for this tune shift and restore the injection efficiency. In user operations of the SPring-8 storage ring, the compensation for the effects of the insertion devices maintains the injection efficiency above 80%.

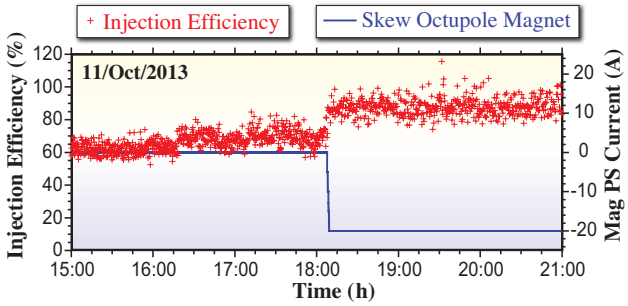

Fig. 3. Trend of the injection efficiency and the exciting current of the skew octupole magnet.

Upgrade of the Bunch Purity Monitor

The bunch purity monitor installed at the beam diagnostics beamline I (BL38B2) has been upgraded by introducing the fast time measurement system that employs a time to digital convertor (TDC; V1290N, CAEN) [2] and a hybrid photodetector (HPD; R7110UMOD, Hamamatsu) to detect photons with a high count rate.

HPD is a type of photomultiplier tube that incorporates a photocathode and an avalanche photodiode (APD) in an evacuated electron tube. In the HPD, a high electric field applied to the photocathode accelerates the photoelectrons emitted from the photocathode. These photoelectrons are bombarded onto the APD and deposit their kinetic energy in the APD to generate electron-hole pairs (electron bombardment gain). The secondary electrons are collected and further multiplied by the avalanche gain in the APD. These effects realize a total gain of 10^4 or higher, which is sufficient to detect single photons. Additionally, the R7110U series HPD has a sufficient time resolution to discriminate a bucket separation of 2 ns.

V1290N is a 16 ch, high performance multi-hit TDC with a time resolution of 25 ps and a double hit resolution of 5 ns. It has a full-scale range of 52 μs, which is sufficient to measure the whole 4.8 μs revolution period of the electron beam. An output signal of the HPD of about 500 kcps and a reference-timing signal, which is synchronized to the revolution of the electron beam (208.8 kHz), are fed into two of the TDC channels. The time difference between two signals is processed statistically by software controlling the TDC.

Development of the software, setup of the HPD and other hardware devices were completed in November 2013, and upgraded bunch purity monitor is operational. The result of a 20-min bunch purity measurement is shown in Fig. 4. The high count-rate detection of the HPD and high speed signal processing capacity of the TDC allow the bunch impurity to be evaluated on the 10^{-9} order within 20 seconds and enable an immediate bunch purity measurement of a topped up bunch at every top-up injection.

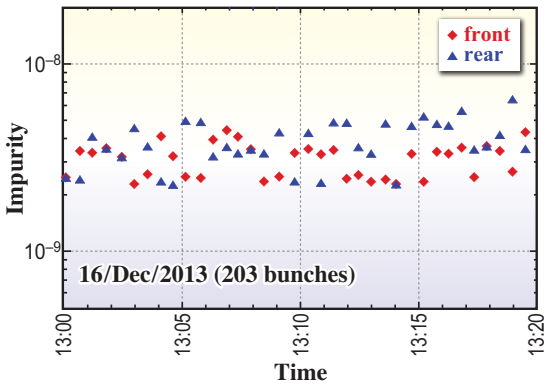

Fig. 4. Result of the bunch purity measurement. Measurements are successfully repeated at intervals of about 30 s after every topping-up injection.

Development of X-ray Fresnel Diffractometry to Measure the Light Source Size of Insertion Devices

A novel technique using X-ray Fresnel Diffractometry (XFD) has been developed to measure the micron electron beam size at a source point of an ID. An ID source size measurement using XFD

enables us to evaluate the brilliance of undulator radiation at each beamline. XFD uses monochromatic X-ray Fresnel diffraction via a single slit with an optimized width to create a double-lobed diffraction pattern as shown in Fig. 5. The principle is based on the correlation between the depth of the median dip in the double-lobed pattern and the source size at the ID; that is, the valley of the dip becomes shallower as the source size increases. XFD can be positioned as an evolutionary form of a conventional X-ray pinhole camera (XPC) because using monochromatic X-ray and optimizing the pinhole size improves the XPC resolution. XFD has the potential to measure a very small electron beam size less than 1 μm (r.m.s.) when the slit is placed a short distance (several meters) from the source point and the observing X-ray energy is several tens of keV. Therefore, the XFD should be useful for ultra-low emittance diagnostics of next generation light sources such as a diffraction limited storage ring.

A vertical source size measurement using XFD was demonstrated at the beam diagnostics beamline II (BL05SS)[3] with an ID (ID05) [4]. An undulator radiation of 7.2 keV was diffracted by a front-end 4-jaw slit with an optimized vertical width of 150 μm and a horizontal width of 200 μm. The Fresnel diffraction pattern was observed using a high-resolution X-ray imaging apparatus called beam monitor (HAMAMATSU) placed 65.4 m from the slit. Figure 6 shows the observed diffraction images at four operation points with different horizontal betatron tunes with and without skew quadrupole magnets for betatron coupling correction. The double-lobed structures are clearly observed in the vertical direction, but are smeared in the horizontal direction due to large horizontal emittance. The reduction in the contrast of the double-lobed patterns indicates growth of the vertical electron beam size at the ID05 source point due to the increased betatron coupling.

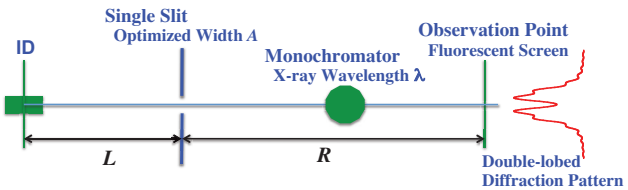

Fig. 5. Layout for the source size measurement of ID using X-ray Fresnel diffractometry.

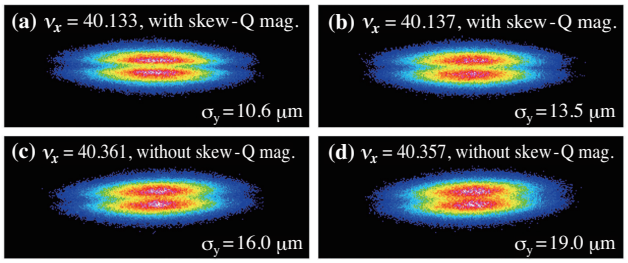

Fig. 6. Double-lobed Fresnel diffraction images observed at four operation points with different horizontal betatron tunes ν_x. Vertical betatron tune ν_y is fixed at 19.35. Image **(a)** and other three images **(b)**, **(c)**, **(d)** are observed with and without skew quadrupole magnets, respectively. Vertical beam sizes are evaluated from the depths of the median dips in the vertical line profiles.

Development of Ultra-fast Variable Field Kicker for Bucket-by-bucket Beam Handling

For the bucket-by-bucket handling of the muti-GeV beam in a few nano-second timescale, a variable field ultra-fast kicker has been proposed and developed [5,6]. The kicker is a TEM mode stripline type and the kick field distribution is continuously variable from a dipole to a quadrupole by changing the drive voltage of the two stripline electrodes as shown in Fig. 7. To realize a short kick duration of ~4 ns for 2 ns spacing bucket, the stripline is set to 0.2 m.

The quadrupole kick can be applied to an off-axis injection into the storage ring with a very narrow dynamic aperture of few mm, like future light sources, with smallest perturbation on stored beam. The dipole kick is for an on-axis swap injection ring with a much narrower dynamic aperture and enables100-mA average current operations by bucket-by-bucket base handling. Although fast dipole kickers with horizontally separated parallel plates have been proposed for damping rings for linear colliders, their narrower apertures causes issues with synchrotron radiation irradiation. On the other hand, our kicker has an unlimited horizontal aperture with a high and flat

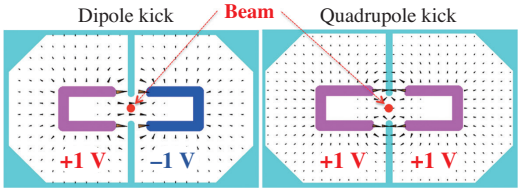

Fig. 7. Cross sectional view of kicker electrode and electric field. **(a)** Dipole kick field driven opposite polarity pulses for left and right stripline electrodes. **(b)** Quadrupole kick driven by the same polarity pulses.

dipole kick field distribution, which is one advantage compared to parallel plate types.

The beam test of the kicker was performed with a 1-GeV electron beam from the SPring-8 linear accelerator. The kick strength and the beam profile of the kicked beam were measured with two Ce:YAG screen beam profile monitors installed just after the kicker and its 8 m downstream. To measure the kick field distribution, the kicker was mounted on a horizontaly and vertically movable stage. At the beam test, just one electrode of the kicker was driven by a +50 kV 2 ns pulse generator. The time structure of the kick was measured by changing the timing between the kick pulse and the electron bunch (Fig. 8). The maximum kick angle is 0.6 m·rad, which is comparable to designed value that includes the cable loss of the kick voltage.

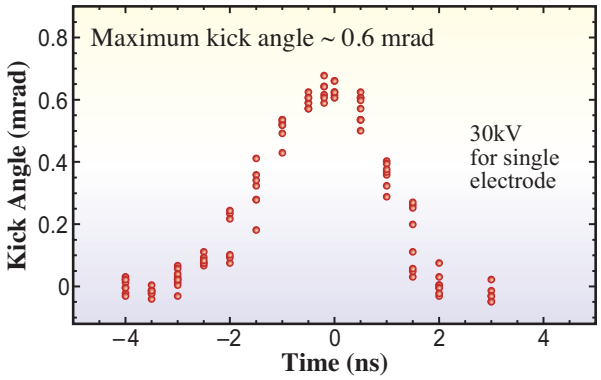

Fig. 8. Time structure of the kick. Maximum kick angle is 0.6 m·rad, which corresponds to 30 kV pulse, but degrades with the cable loss from the maximum available voltage of 40 kV at the pulse generator.

Improvement of Data Acquisition Scheme in the COD Measurement System

The beam position acquisition scheme was modified for the closed orbit distortion (COD) measurement system. The system modification effectively identifies the beam abort source during the user operation in some cases.

An interlock system is in operation which turns off RF acceleration signals and leads to beam abort when the beam orbits at the insertion devices exceed the pre-defined window. Although rare, beam abort events occurred several times in 2012 and 2013; in most cases problems originated from the source of the beam orbit shift the accelerator devices, but the cause could not be identified when the source of the orbit shift was restored by itself in short time. Thus, we have developed a scheme to modify the existing COD measurement system, which has been operating since 2008, to observe the beam orbit shift along the storage ring just prior to beam abort.

In the COD measuring system, beam position monitor (BPM) signals are switched sequentially and detected by ADC. A digital signal processor (DSP: Texas-Instruments C6713) controls the COD measurement scheme. There are 48 DSP throughout the ring, which are operated in parallel and roughly synchronized. Before the modification, it took about 15 ms to process all the BPM data by switching every BPM signal, this was too long to obtain the beam orbit just before the beam abort. Moreover, the DSP became idle after the COD measurement was finished until the supervising computer, which calculated the orbit correction parameters for the steering magnets, issued the next measurement command.

We shortened the switching time from 1 ms to 70 μs. Moreover, we made DSP not to enter an idle state. As a result, all the BPM positions are recorded every 1 ms in a ring buffer on the DSP board. When the stored beam is lost by the interlock system, the DSP detects a voltage drop in the BPM sum signal and stops the ring buffering update.

We can identify the source of beam orbit shift by analyzing the ring buffer data. Figure 9 shows the orbit shift obtained by the modified system when the beam is aborted by the interlock system. A particular COD pattern grows in 10 ms and the beam is lost. Figure 10 shows the analysis of the closed orbit correction just before the beam is lost. In this case, one of the steering magnets is the source of the beam orbit shift.

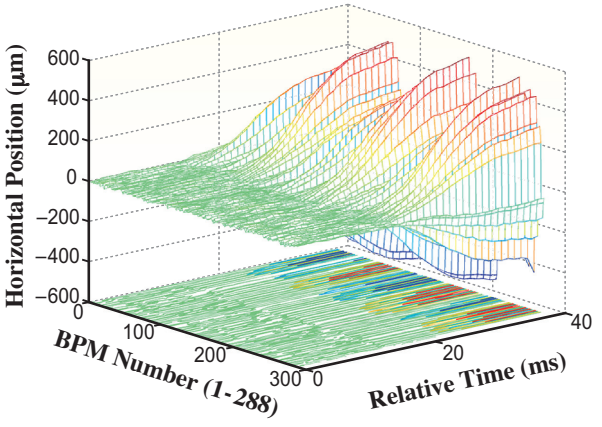

Fig. 9. Horizontal closed orbit grows more than 500 μm in 10 ms, and the beam is aborted by the interlock system. Closed orbit data is stored every 1 ms and used for the beam orbit shift analysis.

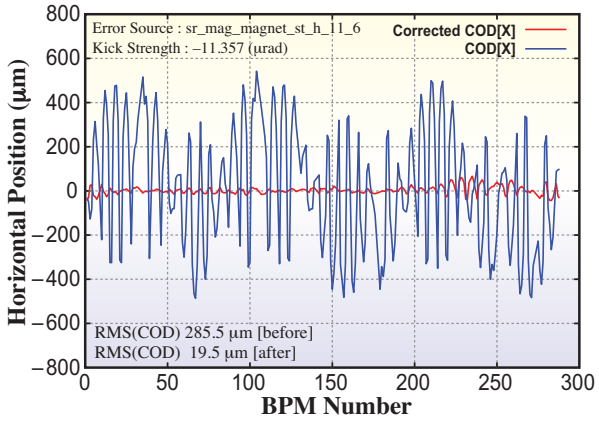

Fig. 10. Analysis of closed orbit just before beam is aborted. In this case, the steering magnet is the orbit shift source.

Suppression of Stored Beam Oscillation during Injection by Fast Kickers in the SPring-8 Storage Ring

The residual oscillations during injection to the storage ring are suppressed more significantly than before by adding a correction kicker magnet in 2013. The suppression of light axis oscillation was confirmed with TTPM (turn by turn beam profile monitor) [7].

Four pulsed bump magnets are used for injection into the storage ring. There are residual oscillations of the stored beam orbit due to imperfections of bump magnet pulse shape matching, such as timing jitters between the four pulses, pulse shape difference of the rising and falling part of the half sine pulses of 8-μs width, etc. The magnitude of amplitude oscillation is 0.4 mm (r.m.s.), but there are 400~700 ns wide spike-like oscillations due to at rising part mismatch and 0.25-mm amplitude with 1.4-μs width due to the falling part mismatch.

We started studies to suppress the residual oscillations using a correction kicker in 2010 [8,9]. The correction has been applied during user time since 2012 to suppress the spike-like oscillations due to the rising part mismatch. In 2013, an additional correction kicker was installed to suppress the broader part, due to the falling part.

We tuned the correction kickers by observing the suppression effect with SPBPM (single pass BPM). Figure 11 compares the oscillation amplitude with and without the correction observed with SPBPM, the horizontal axis is the turn number where zero indicates the injection time. The spike-like oscillation amplitude of 0.45 mm (r.m.s.) at the third turn is reduced by 90%. By adding the second correction kicker, the averaged oscillation amplitude is suppressed to a level less than 0.15 mm within fifth revolution of the stored beam.

Since light axis oscillation suppression is necessary from the viewpoint of synchrotron radiation usage, we confirmed that the light axis oscillation is suppressed with TTPM, which measures the monochromatic light beam profile of the insertion device radiation at the beam diagnostic beamline (Fig. 12). A huge light axis oscillation is generated and the data is saturated over the detection range up to the third turn after the injection. After applying the fast correction kicker at the third turn, the oscillation is reduced at least by 87%, down to 4 μrad. Without the kicker correction, it takes about 80 turns to reduce the oscillation, which was determined by the damping time with the bunch by bunch feedback system [10].

All data acquired by the SPBPM and TTPM system show a consistent result for the suppression effect. It is concluded that the residual oscillation in the horizontal direction at injection is reduced by a factor of five, within the fourth turn after injection by applying the correction scheme with the two kicker systems.

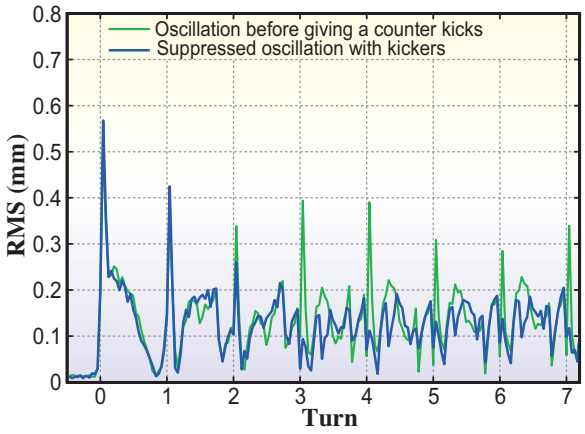

Fig. 11. R.M.S. values of the residual oscillation *vs* turn number after injection, where 0 corresponds to the injection time. Counter kick is applied at third and fourth turns for the primary and secondary kicker, respectively.

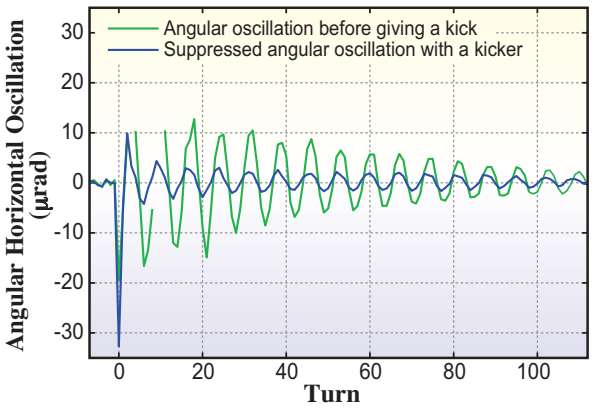

Fig. 12. Angular horizontal oscillation observed by TTPM. Oscillation data under 10 turns is saturated because the oscillation amplitude is more than 30 μrad.

Prototype Circuit using FPGA for Trigger Timing System in SPring-8 Linac

To easily setup a high-speed logic system, NIM modules are common in timing system for the injector linac. However, the large number of modules (more than 100) make it difficult to modify the timing system because the hundreds of cables outside already connect the modules and there is no more space to install additional modules for further improvements.

To fundamentally solve this problem, we have developed and tested a prototype circuit using an field-programmable gate array (FPGA). An FPGA is an LSI that we can reprogram to compose a complicated logic circuit. The prototype system is much smaller, and should have a higher functionality and reliability than the current complex system.

For the prototype, we adopted a Vertex-6 FPGA ML623 Characterization Kit produced by Xilinx as an FPGA board (Fig. 13). Re-clocking circuits were added to all output ports of the FPGA board to minimize the timing jitters.

In one FPGA, we create a program, which include half of the current timing system. This prototype circuit functions properly and results in output signals with jitters less than 2.5 ps, which is sufficient for electron gun trigger signals. However, the number of counter delay circuits in FPGA must be less than four at a clock frequency of 508 MHz due to the signal delay time, which limits the scale of the circuit in the FPGA. Thus, three PFGAs are necessary to replace all the current timing system. The prototype will be modified to replace the modulator trigger system, while another larger circuit with two or three FPGAs will be developed to replace all others in the future.

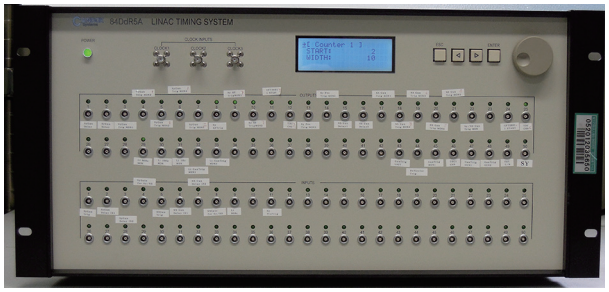

Fig. 13. Prototype of the trigger timing circuit with an FPGA. It has 50 NIM inputs, 50 NIM outputs, and 3 clock inputs. Half of the current timing system is programmed in the FPGA.

Haruo Ohkuma*, Shigeki Sasaki and Hirofumi Hanaki

SPring-8/JASRI

*E-mail: ohkuma@spring8.or.jp

References

[1] T. Tanaka and H. Kitamura: SPECTRA code ver. 9.02 (2012).
[2] A. Kiyomichi *et al.*: Proc. 9th Annual Meeting of Particle Accelerator Society of Japan, Osaka, Japan, 2012, p. 701 (in Japanese).
[3] S. Takano *et al.*: Proc. IBIC2012, Tsukuba, Japan, p.186.
[4] M. Masaki *et al.*: AIP Conf. Proc. **1234** (2010) 560.
[5] T. Nakamura: Proc. IPAC '11, San Sebastian, Spain, p.1230.
[6] T. Nakamura *et al.*: Proc. 9th Annual Meeting of Particle Accelerator Society of Japan, Osaka, Japan, 2012, p. 525 (in Japanese).
[7] M. Masaki *et al.*: Proc. IBIC2012, Tsukuba, Japan, 2012, p.492.
[8] C. Mitsuda *et al.*: Proc. IPAC'10, Kyoto, Japan, 2010, p.2252.
[9] C. Mitsuda *et al.*: Proc. of IPAC'13, Shanghai, China, 2013, p.666.
[10] T. Nakamura *et al.*: Proc. of IPAC'11, San Sebastian, Spain, 2011, p.493.

SPring-8
New Apparatus, Upgrades & Methodology

New protein crystal mounting method using humidity control and hydrophilic glue coating to improve X-ray diffraction experiments

Cryopreservation of protein crystals is essential for minimizing radiation damage from brilliant synchrotron beams. However, the treatment is often troublesome, because the crystals are fragile and contain moisture, which expands upon cooling, destroying their crystalline order. To prevent the freezing damage by vitrifying the moisture in the sample, the crystal mother liquor is replaced with an aqueous/organic mixture solution, the so-called "cryoprotectant." This method is quite simple and effective, but it sometimes affects protein structure and/or crystalline quality. Therefore, there is a need for testing it with various kinds and concentrations of cryoprotectant agents. On the other hand, non-cryogenic experiments are also important. For instance, the results of experiments performed at room temperature should be compared with cryogenic ones to estimate crystalline quality. Also, structures at ambient temperature do not have side-effects of cryocooling, such as molecular shrinkage.

However, there has been no versatile method for cryogenic and ambient experiments. The free-mount method, where protein crystals are exposed to controlled humid air, serve possibly the purpose and showed the ability to improve resolution of protein crystals [1]. However, most of protein crystals were heavily damaged, when their mother liquors were removed and the crystals were exposed to air.

To overcome this issue, we have developed a new crystal mounting method: humid air and glue-coating (HAG) mounting method at beamline **BL38B1**. This method involves a combination of controlled humid air and water-soluble polymer glue for crystal coating [2]. The experimental procedure for HAG method can be briefly described as follows (Fig. 1(a)):

(1) Glue preparation: 8 to 13% (w/w) polyvinyl alcohol (PVA) served as the aqueous glue solutions. The glue solutions vitrified successfully after exposure to wet gas of 92.0% RH or lower. Although the glue was adequate for many types of crystal mother liquors, it formed a physical ion-containing hydrogel in some conditions, especially for high concentrations of multivalent anions such as tartrate, phosphate and sulphate ions. The gel often had trouble thoroughly coating and cryoprotecting the crystals. However, we found that glycerol worked well to prevent gel formation, thus the crystals should be handled with glue or crystal mother liquor containing glycerol.

(2) Crystal handling: a small amount of the glue solution was applied to and spread over a crystal mounting loop with a typical diameter larger than the crystal (Fig. 1(a1)). A crystal was directly picked up from a crystallization droplet by the glue-coated loop, without removal of the mother liquor surrounding the crystal (Fig. 1(a2)). The scooped crystal was kept steady for a few seconds so that it could be thoroughly coated and covered by the glue on the loop (Fig. 1(a3)). Next, the loop was mounted on the diffractometer and exposed to the humid air (Figs. 1(a4) and 1(a5)).

(3) Optimized humidity: to search for a suitable humidity condition, the crystal quality was not only judged by visual inspection but also evaluated by taking diffraction images. We started experiments with an empirically determined humidity of 83.0% RH and changed it in steps of ±2–3% RH. Next, a coarse optimization with the steps of 1–2% RH was performed followed by a finer humidity optimization with the steps of 0.1–0.5% RH. Sample after optimized humidity condition are shown in Fig. 1(a6).

This method can be applied well to many types of protein crystals:

(i) Fragile crystals. The crystals of the bacterial hydrolase RsbQ are mechanically very fragile and sensitive to environmental changes. Thus, the conventional cryoloop mount with traditional cryoprotectant agents does not work (Fig. 1(b1)). Using the HAG method with 13% (w/w) PVA3500, we were able to obtain high resolution (1.4 Å) data after cryocooling without cryoprotectant agents (Fig. 1(b2)).

(ii) Preparation of isomorphous crystals. The changes of the lattice constants in tetragonal lysozyme crystals were reproducible, reversible and gradual for varying humidity, but these amounts were smaller than those in previous experiments without coating. The results suggest that this method can gently control the lattice constants of protein crystals. This advantage will also be useful for multi-crystal data collection.

(iii) Membrane proteins. The crystallization condition of the bacterial membrane protein *Blastochloris viridis* photoreaction center (*Bv*RC) contained high concentrations of sulphate ions (1.9 M). The glue prepared by mixing equal volumes of glycerol and 8% (w/w) PVA4500 was successfully subjected to cryocooling without ice formation. In the conventional cryoloop method, a *Bv*RC crystal soaked in cryoprotectant containing 30% (v/v) glycerol was damaged after only two minutes [3]. However, the glue of PVA and glycerol mixture preserved the crystals for over 20 minutes during a diffraction check at room temperature when mounted with the HAG method.

As stated above, the HAG method can handle crystals stable at room temperature and cryocooled without additional cryoprotectant agents. For users, the humidity control apparatus of HUM-1 (Rigaku Co.) and an automatic switching device of the gas nozzles have been installed at beamline BL38B1.

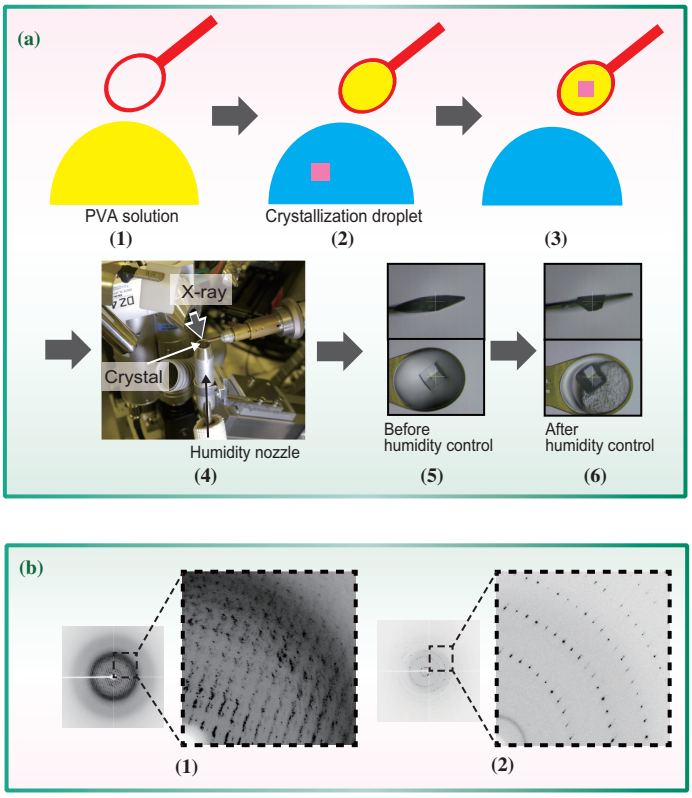

Fig. 1. Experimental procedure of HAG method and its practical example.
(a) Overview of the HAG method. (1) Crystal handling procedures. (1) Applying the PVA glue to a cryoloop. (2, 3) Picking up a crystal, and steeping the crystal to be coated by the glue. (4, 5, 6) The crystal mounted on the diffractometer and exposed to humid air. (5) Just before the lysozyme crystal was placed in the apparatus. (6) After the lysozyme crystal was exposed to 73.9% RH air.
(b) Diffraction images of bacterial hydrolase RsbQ crystals. (1) The crystal was flash-cooled by a cryoloop mount with a cryosolution composed of the reservoir solution supplemented with 25% (*v*/*v*) glycerol. (2) The crystal was mounted by the HAG method, using 13% (*w*/*w*) PVA3500 glue at 69.1% RH, then flash-cooled.

Seiki Baba* and Takashi Kumasaka

SPring-8/JASRI

*E-mail: baba@spring8.or.jp

References

[1] R. Kiefersauer *et al.*: J. Appl. Cryst. **33** (2000) 1223.
[2] S. Baba *et al.*: Acta Cryst. D**60** (2013) 1839.
[3] R.H.G. Baxter *et al.*: Acta Cryst. D**61** (2005) 605.

High repetition rate X-ray chopper for time-resolved measurements

Pump-probe time-resolved measurement using pulses of synchrotron radiation is a measurement technique that can achieve time resolution similar to the single-pulse width of synchrotron radiation. In order to perform pump-probe time-resolved measurements, it is necessary to select individual X-ray pulses, because the frequency of (probe) pulses is usually much higher than that of the stimulation to the sample (pump). As a means of selecting single X-ray pulses, X-ray choppers have been adopted at many synchrotron radiation facilities. They have the advantage that time resolution is not necessary for the detector in experiments using X-ray choppers, however, the repetition frequency of the X-ray single pulse obtained using the X-ray chopper installed in SPring-8 was limited to several kHz [1]. This is comparable to the repetition rates of typical regenerative amplifier femtosecond pulse lasers, and X-ray choppers have successfully been used for pump-probe experiments with femtosecond pulsed lasers. On the other hand, studies of electronic devices, e.g. next generation memory, that allow electrical stimulation at rates of 100 kHz have been proposed, and furthermore, femtosecond amplifier pulsed lasers with repetition frequencies of the order of 100 kHz have been realized in recent years, so X-rays choppers which can reach these repetition rates are required. In order to meet this demand, we have developed such a high repetition rate X-ray chopper.

High repetition rate X-ray choppers can be realized using X-ray diffraction [2], however this changes direction and position of the chopped X-rays. By contrast, blocking the X-rays except at specific times does not affect these properties and is the approach used here. Figure 1 shows three types of X-ray choppers [3-5]. Type A is similar to standard optical choppers, with a rotating slotted disc. The motor-axis is parallel to the X-ray beam and this type is referred to as "parallel." In contrast, the triangular chopper B rotates about an axis perpendicular to the beam, and is referred to as the "perpendicular type." For both A and B, each slit transmits one X-ray pulse each revolution. The perpendicular type blocks the X-rays at both the entrance and the exit, so for the same rotational speed and radius offers half the temporal width of the parallel type.

The chopping method which we adopted for our high repetition rate X-ray choppers described here is of type C. Similarly to type B, the axis of rotation is perpendicular to the beam, offering the advantage of short opening time. The chopper shape is a disc, similar to type A, but rather than using slits, the X-rays pass through grooves cut along radial lines on the surface of the disc. Since the X-rays pass through the center of the disc, this design offers twice the chopping speed of types A and B for the same rotating speed. Furthermore, the grooved design is of low fabrication cost, and is well suited to high chopping frequency applications, which require a large number of grooves.

Figure 2(a) shows a photograph of the chopper apparatus. The upper part is the chopper disk housing, which operates in vacuum to reduce friction, and the lower part contains the motor, which is an air-spindle design (ShinMaywa Industries, Ltd. SPM30). The speed and phase of the motor can be controlled by a phase-locked loop linking the SPring-8 RF pulse to the eight pulses per revolution required to control the motor. Figure 2(b) shows a photograph of the chopper disc. The X-rays pass along the direction shown through grooves in the 140-mm-diameter disc. To allow high rotation speeds the disc must be light, so that suitable materials are aluminum and titanium. To allow use at X-ray energies of up to 40 keV, titanium was chosen. As shown in Fig. 2(c), alternate grooves have different widths and depths, making up 54 pairs at regular intervals. The grooves labelled 'A' are 250 μm wide and 500 μm deep. Grooves B are 250 μm wide to a depth of 1 mm, with a further 110-μm-wide deep groove to a depth of 1.5 mm. When the disc rotates at 29,000 rpm and is

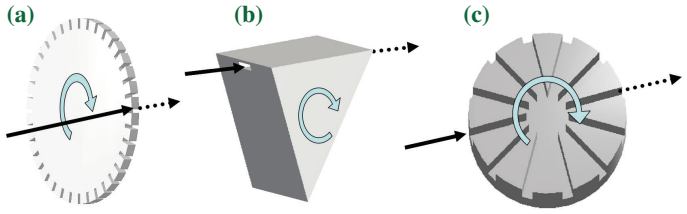

Fig. 1. Three types of X-ray chopping methods.

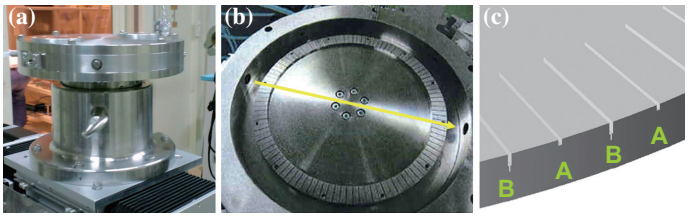

Fig. 2. Photograph of **(a)** the X-ray chopper apparatus and **(b)** the X-ray chopper disc. **(c)** Computer graphic diagram of the groove structure on the disc (b). The yellow arrow in (b) shows the X-ray pass.

synchronized to the SPring-8 RF signal, the 250-μm-wide grooves offer an opening time of 1.17 μs, and the 110- μm-wide grooves an opening time of 0.52 μs, respectively. These allow selection of single bunches in the '1 bunch + 11/19 filling', '5 bunch + 1/7 filling' and '12 bunch + 1/14 filling' modes. The different depths provide two different chopping frequencies. Using depths of up to 500 μm, both A and B grooves transmit the beam, giving a chopping frequency of 52.2 kHz, which corresponds to once every four full passes of the SPring-8 bunch structure. Using depths greater than 500 μm, only groove B transmits X-rays, giving a chopping frequency of 26.1 kHz (once every eight full passes of the bunch structure).

Figure 3 shows results from operating the chopper during the '5 bunch + 1/7 filling' mode. The test was carried out at **BL13XU**, using a 12.4 keV X-ray beam.

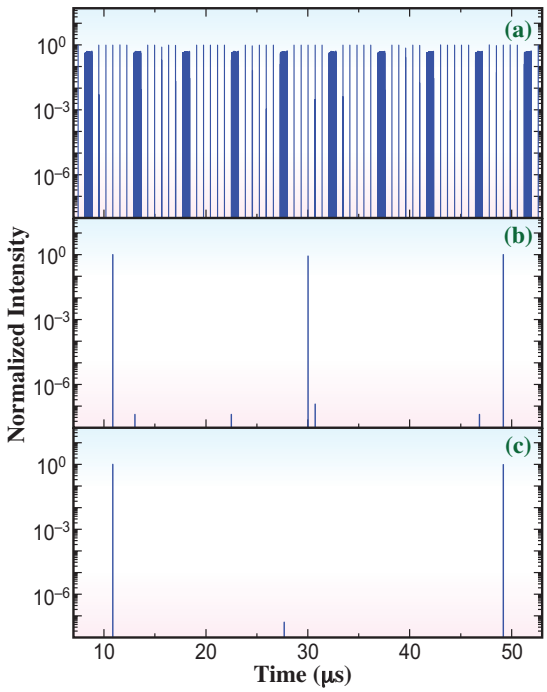

Fig. 3. Time structure of X-ray pulses of **(a)** before chopping, **(b)** chopping with grooves A and B, and **(c)** chopping with groove B.

X-rays transmitted by the chopper hit a copper plate, and scattered X-rays and fluorescence were detected using an avalanche photodiode. A time spectrum was collected by the mulch channel scaler. Figure 3(a) shows the time structure of X-ray pulses without using the chopper. The bunch structure consists of 5 isolated bunches, and a multi-bunch portion, which increases the total stored current to 100 mA. Figure 3(b) shows the results when using the chopper to select one single bunch X-rays every four periods. It is clear that all other pulses are effectively blocked by the chopper. Figure 3(c) shows the results of using only grooves B (Fig. 2(c)), resulting in the transmission of one single bunch X-rays every eight periods. The ratio of the selected pulses to the suppressed pulses is around 1:5,000,000, sufficient for many time-resolved measurement techniques.

In summary, we have developed an X-ray beam chopper suitable for pump-probe studies of electronic devices and using high-frequency pulsed lasers it can select a single pulse every four or eight periods of the SPring-8 bunch structure. Time-resolved measurements with the high repetition rate chopper enable the use of bending-magnet beamlines. As well as the chopper described here, we have also developed an aluminum chopper suitable for X-ray energies less than 20 keV, and also a smaller, lower cost version. We anticipate that their use will facilitate many time-resolved studies.

Hitoshi Osawa*, Togo Kudo and Shigeru Kimura

SPring-8/JASRI

*E-mail: hitoshio@spring8.or.jp

References

[1] Y. Fukuyama *et al.*: Rev. Sci. Instrum. **79** (2008) 045107.
[2] R. Tucoulou *et al.*: J. Synchrotron Rad. **5** (1998) 1357.
[3] M. Gembicky *et al.*: J. Synchrotron Rad. **14** (2007) 133.
[4] M. Gembicky *et al.*: J. Synchrotron Rad. **12** (2005) 665.
[5] M. Cammarata *et al.*: Rev. Sci. Instrum. **80** (2009) 015101.

SACLA Beam Performance

SACLA maintained smooth operations throughout 2013. Annual public user time increased 10% following advances in optimization of the tuning and preparation procedures. Significant improvements in laser performance produced gains both in intensity and repetition rate.

1) Intensity enhancement

Figure 1 shows the progress of laser intensity since the first lasing. The laser pulse energy, which was around 300 μJ at the end of 2012, increased to 400 μJ before the summer shutdown and up to about 500 μJ in autumn 2013 due to diligent tuning efforts. Since then, a highly intense laser with pulse energy around 500 μJ has been routinely available for user experiments as shown in Fig. 2. The measured gain curve shows that this greater intensity comes from the enhanced amplification in the latter half of the undulator beamline. The performance likely results from the following cause. By optimizing the parameters in the multi-stage bunch compressor, a second broader peak is formed in addition to the main sharp peak in the beam current profile. The sharp peak with a high current quickly initiates the lasing and soon reaches the state of power saturation. The broader peak with a low current slowly starts lasing and contributes to increasing amplification in the second half of the undulator beamline.

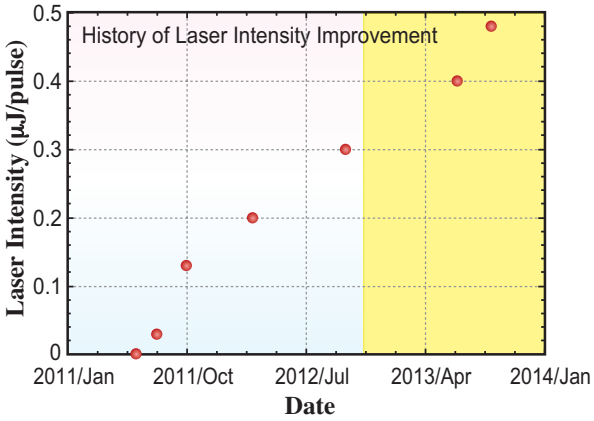

Fig. 1. Progress of SASE XFEL laser intensity from the first lasing in June 2011. The yellow area shows the part of 2013.

2) Beam repetition rate increase

Figure 3 shows the change in repetition rate during 2013. The repetition rate began at 10 pps at the beginning of 2013 and increased to 30 pps by the middle of November. To reduce the RF trip rate, we made two improvements. The first was reducing the rate of electric discharge in the RF structures by RF conditioning. The second was modifying the interlock of the Thyratron (High voltage switch) so as to ignore

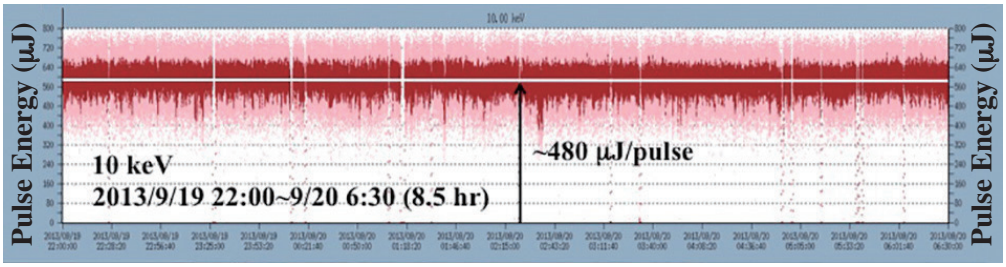

Fig. 2. XFEL intensity variation during the user experiment at a photon energy of 10 keV.

a single misfire in the first minute. This interlock modification was performed by proving the reliability through operation testing. The interlock modification is effective for improving laser availability, however, a misfire of the Thyratron causes a large wavelength shift and produces a single unavailable shot for experiments requiring great precision. We therefore provided users with an error flag indicating the unavailable shot so that these shots could be ignored in later analyses.

3) Successful beam commissioning of XSBT (XFEL to Synchrotron Beam Transport)

Following preparation activities, beam tuning began in the first week of September to transport the electron beam from SACLA to the dump of the booster synchrotron. The tuning was successfully completed by injecting the sharp beam to the dump without significant beam losses. The facility passed inspection in the second week of September. The XSBT line is now available for transporting the beam from SACLA to the storage ring.

4) Accelerator operation upgrade

SACLA has the capacity to install up to five XFELs. Currently, two beamlines, BL1 (broad band) and BL3 (SASE), are in operation and the second SASE beamline, BL2 is under construction and targeting completion in the summer of 2014. In order to effectively utilize the multi-SASE beamlines after introducing a pulse-by-pulse switching system, SACLA must change the laser wavelength for every beamline where different experiments are planned. Since the required wavelength range is much larger than that produced by adjusting the K-values of the undulator, we have developed a special operation scheme named TIME (Time Interleaved MultiEnergy acceleration) [1] that can change beam energy widely and stably using the pulse-by-pulse technique. We have already performed a proof-of-concept experiment at SACLA and proven that the scheme has sufficient stability and a changeable energy range. Figure 4 shows a schematic illustration of the TIME scheme.

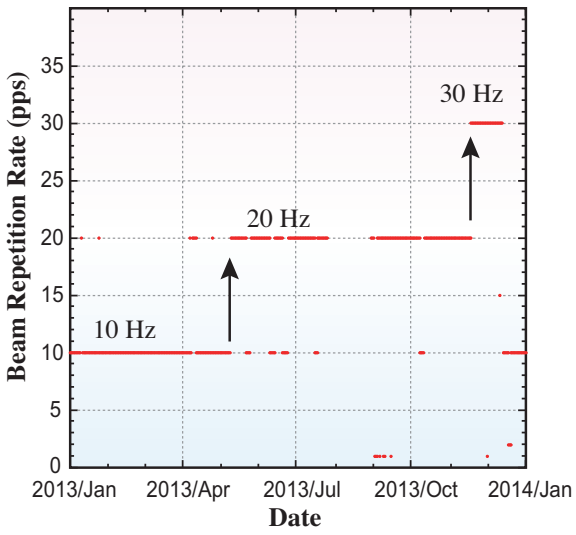

Fig. 3. History of the repetition rate change in 2013.

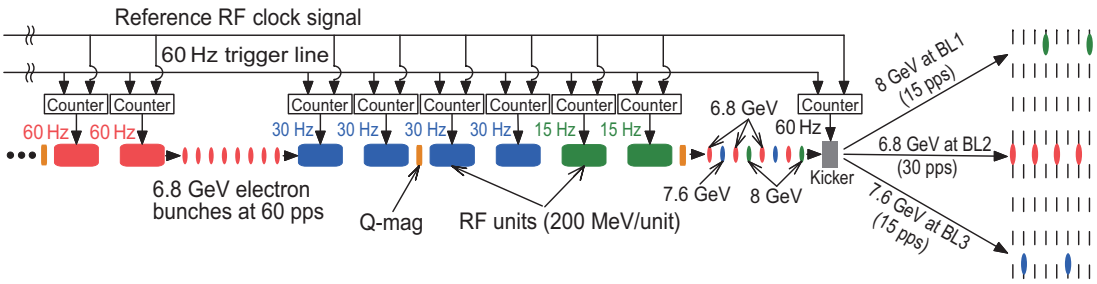

Fig. 4. Schematic illustration of the TIME operation [1].

Hitoshi Tanaka

RIKEN SPring-8 Center

E-mail: tanaka@spring8.or.jp

Reference

[1] T. Hara *et al.*: PRSTAB **16** (2013) 080701.

SACLA
New Apparatus, Upgrades & Methodology

To realize the unique potential of SACLA to lead with innovations in science and industrial applications requires the on-going development of experimental methods and instruments. In 2013, we continued to improve X-ray optics, diagnostics, detectors, and experimental instruments. In this section, we introduce two achievements in X-ray optics and methodology.

1) Generation of an intense 50-nm X-ray spot with a two-stage focusing system

The brilliant, coherent, and femtosecond X-ray pulses from SACLA provide an unprecedented opportunity to generate an extremely intense X-ray beams by applying a proper focusing system. In collaboration with a team led by Prof. Kazuto Yamauchi of Osaka University, we successfully produced state-of-the-art X-ray mirror optics that have a very high efficiency without distorting wavefronts. These technologies were leveraged to construct a 1-μm focusing system at SACLA [1], enabling us to achieve a high intensity level of 10^{18} W/cm^2. This intensity level triggers the generation of X-ray multi-photon processes and nonlinear phenomena. Some of these findings [2,3] are reported in this volume.

If we could increase the intensity by two-orders of magnitude, we would reach a new regime that is governed mainly by nonlinear interactions. To achieve this, we developed a new focusing system at SACLA (Fig. 1). A unique point of the design is to use a pair of focusing systems, both in the Kirkpatrick-Baez geometries, which are placed with a separation of approximately 70 m. The first system is used to expand the beam size at the second system, while the second system enables the generation of an extremely small spot while keeping a large working distance between the last mirror and the sample point. With the two-stage focusing system, we generated a 50-nm focused X-ray beam with an extreme intensity of 10^{20} W/cm^2 [4]. The high intensity was utilized to observe the two-photon absorption phenomenon in the hard X-ray range [5]. This system offers an excellent opportunity to investigate X-ray quantum optics, high-energy density science, and even high-energy physics, such as an evaluation of the QED framework.

2) Dispersive X-ray absorption spectroscopy with grating beam splitter

Intense SASE-XFEL light with a reasonable bandwidth (~50 eV at 10 keV) is suitable for conducting dispersive spectroscopy that enables single-shot detection in a wide spectral region. However, a stochastic spike structure in the frequency (and temporal) domain can complicate analysis, especially when conducting a normalizing

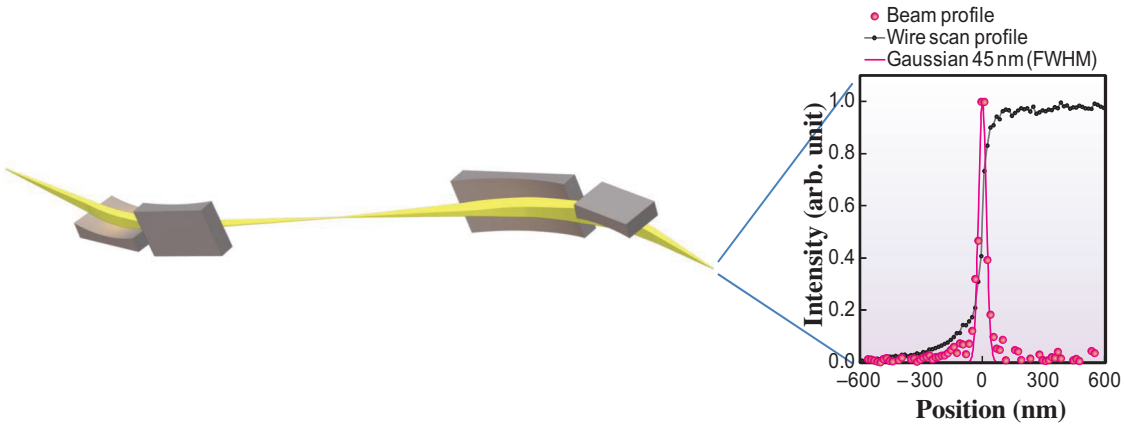

Fig. 1. Schematic view of a two-stage focusing system and a vertical beam profile at a focus measured using the knife-edge scanning method.

procedure. To address this challenge, we developed a new scheme that combines our single-shot dispersive spectrometer [6] with a grating beam splitter, as shown in Fig. 2. With this approach, we could produce a pair of nearly identical replica of spectrographs. By inserting a sample in one of the branches, we could measure a differential dispersive spectrum. Since we could simultaneously measure a wide range of spectrum without scanning a monochromator, this method proved highly useful for advanced research in the field of ultrafast chemistry by performing pump-probe measurements in combination with optical lasers. As a first step, we successfully performed a proof-of-principle experiment with zinc foil [7]. We then applied the method to time-resolve absorption spectroscopy. We measured the differential spectra of the Fe(III)$(C_2O_4)_3^{3-}$ complex around the K-edge of the Fe atom at several pump-probe time delays and observed a rise time of 260 ± 50 fs [8]. Our results open up the possibility of using time-resolved X-ray spectroscopy to observe transient phenomena at the femtosecond time scale. Exciting research in the future will reveal transient dynamics of chemical reactions at an atomic scale with a very short timescale at femto- and atto-second levels.

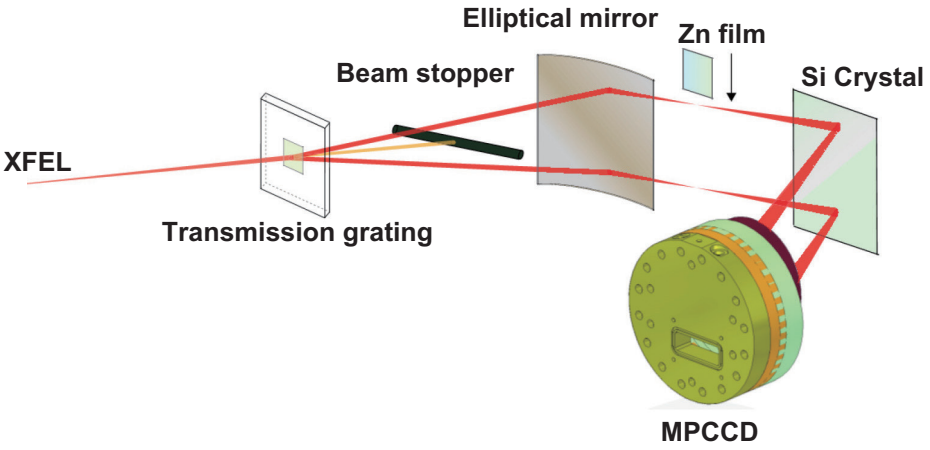

Fig. 2. Schematic setup for dispersive X-ray absorption spectroscopy using a grating beam splitter.

Makina Yabashi

RIKEN SPring-8 Center

E-mail: yabashi@spring8.or.jp

References

[1] K. Yumoto *et al.*: Nature Photon. **7** (2013) 43.
[2] H. Fukuzawa *et al.*: Phys. Rev. Lett. **110** (2013) 173005.
[3] K. Tamasaku *et al.*: Phys. Rev. Lett. **111** (2013) 043001.
[4] H. Mimura *et al.*: Nature Commun. **5** (2014) 3539.
[5] K. Tamasaku *et al.*: Nature Photon. **8** (2014) 313.
[6] Y. Inubushi *et al.*: Phys. Rev. Lett. **109** (2012) 144801.
[7] T. Katayama *et al.*: Appl. Phys. Lett. **103** (2013) 131105.
[8] Y. Obara *et al.*: Opt. Exp. **22** (2014) 1105.

FACILITY STATUS

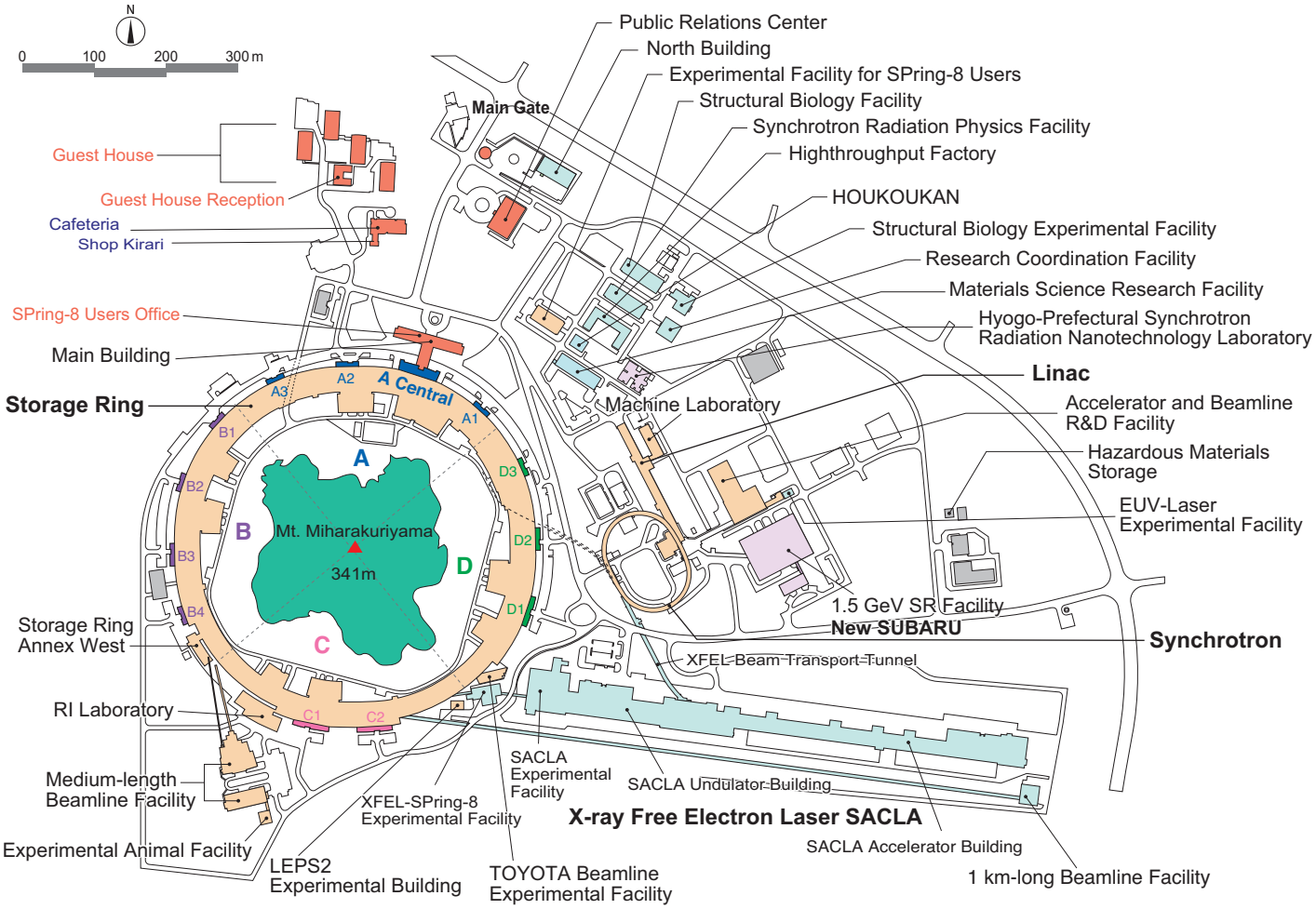

SPring-8

I. Introduction

General

As one of the most advanced COEs of photon science in the world, SPring-8 was fully operational during FY2013. The accelerator complex ran reliably with an extremely short downtime of 20 hours and an annual operation time of 4265 hours as described in the following chapters. Due to this excellent availability, the total number of users visiting SPring-8 in FY 2013 for their experiments was 13,381, bringing the total since the inauguration in 1997 to 168,107. By using the achievements of R&D, the electron storage ring began operating with a lower emittance in May 2013. To improve energy efficiency, the cooling water and air-conditioning systems of the accelerator complex were completely renovated in the beginning of 2014.

Review

At the national level, the Ministry of Education, Culture, Sports, Science and Technology conducted an intensive review of SPring-8 from April–September 2013. According to the official report, the committee identified five priorities for the next five years:

(1) SPring-8 should deepen its cooperation with the user community, promote its infrastructure upgrades and users support, expand the user base, and enhance human resource development in related areas.

(2) By offering opportunities for technology exchanges, SPring-8, as a COE of Japan, should organically link "knowledge" and "challenge" that universities, research institutes and companies possess, thereby promoting innovative research outcomes.

(3) In parallel to strengthening international collaborations, SPring-8 should cooperate with the *Photon Beam Platform* as well as other *Specific Advanced Large Research Facilities* in Japan, and attempt to create novel users and to strengthen user support.

(4) RIKEN and JASRI, as the owner and the Registered Institution of Facilities Use Promotion of SPring-8, respectively, should enhance their self-inspections in a unified manner.

(5) Systematically maintaining its scientific infrastructure further to realize stable operations, SPring-8 should improve its operational efficiency and attempt to elongate its user time.

As the Registered Institution of Facilities Use Promotion of SPring-8, JASRI itself also conducted interim reviews for the following contact beamlines; (i) BL07LSU University-of-Tokyo Synchrotron Radiation Outstation (The University of Tokyo), (ii) BL15XU WEBRAM (National Institute for Materials Science), (iii) BL16XU SUNBEAM ID (SUNBEAM Consortium), (iv) BL16B2 SUNBEAM BM (SUNBEAM Consortium), (v) BL24XU Hyogo ID (Hyogo Prefecture), (vi) BL33XU TOYOTA (TOYOTA Central R&D Lab., Inc.), and (vii) BL44XU Macromolecular Assemblies (Institute for Protein Research, Osaka University). In reference to their excellent organizations and outstanding achievements, JASRI approved the continuations of all the beamlines reviewed.

International Collaborations

When the French President, Monsieur Francois Hollande, visited Japan, there was a signing ceremony held at the French Embassy in Tokyo in June 2013, in order to conclude a Memorandum of Understanding between SOLEIL, RIKEN SPring-8 Center, and JASRI. Also in attendance were Mr. Ichita Yamamoto, Minister of State for Science and Technology Policy, and the French Minister for Higher Education and Research, Mrs. Geneviève Fioraso.

Signing ceremony held at the French Embassy in Tokyo in June 2013 to conclude a Memorandum of Understanding between SOLEIL, RIKEN SPring-8 Center, and JASRI.

To mutually advance research and achievements through regional collaboration, the Asia-Oceania Forum for Synchrotron Radiation Research has played an

Asia-Oceania Forum for Synchrotron Radiation Research 2013 held on September 21-24, 2013 at Himeji.

important role. Started in 2006 at KEK, Japan, the member states have organized an annual forum. The forum returned to Japan when the Japanese Society for Synchrotron Radiation Research and SPring-8 co-hosted it in combination with the Cheiron School, calling the entire event the Cheiron Week. Honored by the presence of Mr. Kisaburo Tokai, the Chairman of the Special Committee on Promotion of Science and Technology, and Innovation, the House of Representatives, the forum was held September 21-24, 2013 at Himeji. For the 160 participants, the forum was highly informative, especially for young scientists and engineers from the region.

II. Machine Operation

The operation statistics for last five fiscal years are shown in Fig. 1. In FY2013, the total operation time of the accelerator complex was 4280.9 h. The operation time of the storage ring was 4265.4 h, 79.9% of which (3408.5 h) was available for SR experiments. The downtime resulting from failure accounted for 0.58% (20 h) of the total user time, and no great loss of user time exceeding several hours occurred. The operation time for FY2013 was about 1000 h less than a typical fiscal year, due to the large-scale renovations of the aging utilities of the cooling water and air-conditioning system. However, with the top-up injection, a high availability (ratio of net user time to the planned user time) was achieved (e.g., 99.3% for FY2013). The total tuning and study time of 852.5 h was used for machine tuning, for the studies of the linac, booster synchrotron and storage ring, and also for the beamline tuning and study.

Operations in two different filling modes were provided for the following user time: 54.6% was several-bunch mode, such as the mode of 29 equally spaced trains of 11 bunches) and 45.4% was hybrid filling mode, such as the mode of 1/14-partially filled multi-bunch with 12-isolated bunches. The multi-bunch mode was not operational in FY2013, and the several bunch mode was the predominant filling mode. The 203-bunch mode and the mode of 29 equally spaced trains of 11 bunches reached 25.8% and 28.8% of the total user time, respectively. The new hybrid-filling mode of 11/29-partially filled multi-bunch with a 5.0-mA isolated bunch. For the hybrid filling mode, 1.6 mA, 3.0 mA, or 5.0 mA is stored in each isolated bunch. An isolated bunch impurity better than 10^{-10} is routinely maintained in the top-up operation. Table I summarizes of the useful beam parameters of the storage ring, while Table II summarizes the beam filling patterns.

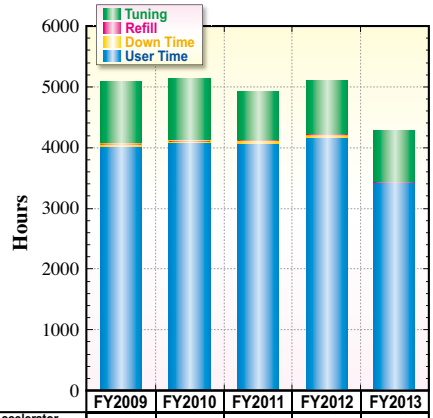

	FY2009	FY2010	FY2011	FY2012	FY2013
Accelerator Operation Time	5168.8	5125.6	4918.6	5078.8	4280.9
Storage Ring Operation Time	5035.4	5096.3	4904.2	5063.1	4265.4
Tuning & Study (Acc. & BL)	1019.1	1026.6	803	884	852.4
Refill	6.3	5.0	4.4	5.2	3.5
Down Time	34.8	27.5	57	39.2	20
Mean Time Between Failures	122.9	178.4	117.7	107.7	214.5
Achieved User Time	4014.9	4071.6	4058.5	4155.6	3408.5
Planning User Time	4056.0	4104.0	4120.0	4200.0	3432.0
Availability (%)	99.0	99.2	98.5	98.9	99.3

Fig. 1. Operation statistics for most recent five fiscal years.

Table I. Beam parameters of SPring-8 storage ring

Energy [GeV]	8
Number of buckets	2436
Tunes (ν_x / ν_y)	40.14 / 19.35
Current [mA]:	
single-bunch	12
multi-bunch	100
Bunch length (σ) [psec]	13
Horizontal emittance [nm·rad]	2.4*
Vertical emittance [pm·rad]	4.8*
Coupling [%]	0.2
RF Voltage [MV]	16
Momentum acceptance [%]	~3
Beam size (σ_x / σ_y)* [μm]	
Long ID section	333 / 7
ID section	316 / 5
BM1 section	94 / 12
BM2 section	100 / 12
Beam divergence (σ_x' / σ_y')* [μrad]	
Long ID section	8 / 0.7
ID section	9 / 1.0
BM1 section	58 / 0.5
BM2 section	68 / 0.5
Operational chromaticities (ξ_x / ξ_y)	+2 / +2**
Lifetime [h]:	
100 mA (multi-bunch)	~200
1 mA (single-bunch)	~20
Horizontal dispersion [m]:	
Long ID section	0.153
ID section	0.146
BM1 section	0.039
BM2 section	0.059
Fast orbit stability (0.1 – 200 Hz) [μm]:	
horizontal (rms)	~4
vertical (rms)	~1

* Assuming 0.2% coupling
** With bunch-by-bunch feedback

Table II. Filling patterns in FY2013

	bunch current (mA)	lifetime (h)
203 bunches	0.5	25 ~ 30
11 bunch-train × 29	0.3	35 ~ 50
11/29 - filling + 1 single bunch	5.0 (single)	40 ~ 50
1/7 - filling + 5 single bunches	3.0 (single)	18 ~ 25
1/14 - filling + 12 single bunches	1.6 (single)	18 ~ 25

III. Beamlines

The SPring-8 storage ring can accommodate up to 62 beamlines: 34 insertion devices, 4 long undulators, and 24 bending magnets. At the time of writing, 56 beamlines are in operation, and cover a wide variety of research fields related to synchrotron radiation science and technology. The beamlines are classified into the following four types.

(1) Public Beamlines
(2) Contract Beamlines
(3) RIKEN Beamlines
(4) Accelerator Diagnostics Beamlines

There are now 26 fully operational public beamlines. Beamlines, that are proposed and constructed by external organizations, such as universities, research institutes, and private companies, are called contract beamlines, and are exclusively used by contractors for their own research purposes. Currently, 19 contract beamlines are in operation. The contract beamlines include NSRRC BM (BL12B2) and NSRRC ID (BL12XU) beamlines, which were constructed by the National Synchrotron Radiation Research Center in Taiwan. The Catalytic Reaction Dynamics for Fuel Cells beamline (BL36XU) constructed by the University of Electro-Communications and the Laser-Electron Photon II beamline (BL31LEP) constructed by Research Center for Nuclear Physics, Osaka University, began operations in January and October 2013, respectively. The beamlines constructed by RIKEN are called RIKEN beamlines, and are used for RIKEN's own research activities. RIKEN currently has 9 operating RIKEN beamlines and is reconstructing one. In addition, two accelerator diagnostics beamlines are in operation.

To display the beamline portfolio of SPring-8, Fig. 2 shows the beamline map and beamline classification, while Table III presents the research field of each beamline.

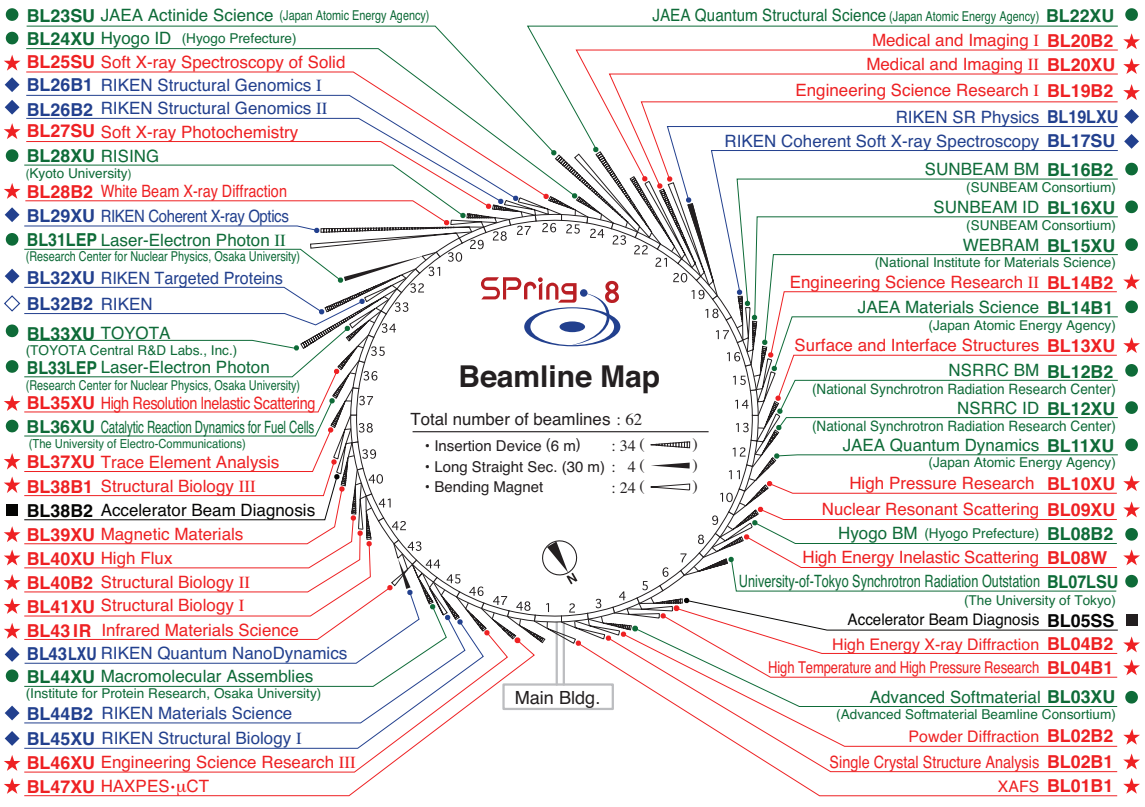

BL: Beamline
B1, B2: Bending Magnets
XU: X-ray Undulator
SU: Soft X-ray Undulator
W: Wiggler

IR: Infrared Radiation
LEP: Laser-Electron Photon
LXU: Long-length X-ray Undulator
LSU: Long-length Soft X-ray Undulator
SS: Straight Section

★ : Public Beamlines
● : Contract Beamlines
◆ : RIKEN Beamlines
■ : Accelerator Diagnostics Beamlines
◇ : Planned or Under Construction

WEBRAM: Wide Energy Range Beamline for Research in Advanced Materials
NSRRC: National Synchrotron Radiation Research Center, Taiwan
RISING: Research & Development Initiative for Scientific Innovation of New Generation Batteries
HAXPES·μCT: Hard X-ray Photoelectron Spectroscopy, Micro-Tomography

Fig. 2. Beamline map.

Table III. List of beamlines

BL #	Beamline Name	(Public Use) or (First Beam)	Areas of Research
★ Public Beamlines			
BL01B1	XAFS	(Oct. 1997)	XAFS in wide energy region (3.8 to 113 keV). XAFS of dilute systems and thin films. Quick XAFS with a time resolution of seconds to as tenth seconds.
BL02B1	Single Crystal Structure Analysis	(Oct. 1997)	Precise crystal structure analysis using high resolution data of single crystal (X-ray energy: 8–115 keV).
BL02B2	Powder Diffraction	(Sept. 1999)	Accurate structure analysis of crystalline materials using powder diffraction data by Rietveld refinements and maximum entropy method (MEM).
BL04B1	High Temperature and High Pressure Research	(Oct. 1997)	High temperature and high pressure research with the multi-anvil press by powder X-ray diffraction, radiography and ultrasonic measurement.
BL04B2	High Energy X-ray Diffraction	(Sept. 1999)	Structural analysis of glass, liquid, and amorphous materials. X-ray diffraction under ultra high-pressure.
BL08W	High Energy Inelastic Scattering	(Oct. 1997)	Magnetic Compton scattering. High-resolution Compton scattering. High-energy Bragg scattering. High-energy fluorescent X-ray analysis.
BL09XU	Nuclear Resonant Scattering	(Oct. 1997)	Lattice dynamics using nuclear inelastic scattering. Mössbauer spectroscopy, especially for the surface/interface study and under the extreme conditions.
BL10XU	High Pressure Research	(Oct. 1997)	Structure analysis and phase transitions under ultra high pressure (DAC experiment). Earth and planetary science.
BL13XU	Surface and Interface Structures	(Sept. 2001)	Atomic-scale structural analysis of surfaces and interfaces of crystalline materials, ultra-thin films, and nanostructures. Surface X-ray diffraction (SXRD). Microbeam diffraction.
BL14B2	Engineering Science Research II	(Sept. 2007)	XAFS in wide energy region (3.8 to 72 keV). XAFS of dilute systems and thin films.
BL19B2	Engineering Science Research I	(Nov. 2001)	Residual stress measurement. Structural analysis of thin film, surface, interface. Powder diffraction. X-ray imaging, X-ray topography. Ultra-small angle X-ray scattering.
BL20XU	Medical and Imaging II	(Sept. 2001)	Microimaging. Hard X-ray microbeam/scanning microscopy, imaging microscopy, microtomography, phase-contrast microtomography with Bonse-Hart interferometer, X-ray holography, coherent X-ray optics, and other experiments on X-ray optics and developments of optical elements. Medical application. Microangiography, refraction-enhanced imaging, radiation therapy, phase-contrast CT using interferometer. Ultra-small angle scattering.
BL20B2	Medical and Imaging I	(Sept. 1999)	Microimaging: microtomography, phase-contrast microtomography with Bonse-Hart interferometer and grating interferometer for biological specimen and other kinds of specimen. Evaluation and development of various kinds of optical elements for novel imaging techniques. Large field X-ray topography.
BL25SU	Soft X-ray Spectroscopy of Solid	(Apr. 1998)	Observation of electronic structures by photoemission spectroscopy (PES). Observation of electronic band structures by angle resolved photoemission spectroscopy (ARPES). Magnetic state study by magnetic circular dichroism (MCD) of soft X-ray absorption. Element-specific magnetization curve measurements by MCD analysis of atomic arrangements by photoelectron diffraction (PED). Observation of magnetic domains by photoelectron emission microscope (PEEM).
BL27SU	Soft X-ray Photochemistry	(May 1998)	Ambient atmospheric pressure Soft X-ray photoabsorption spectroscopy. Chemical state analysis of light elements in dilute samples (NEXAFS). High resolution atomic and molecular electron spectroscopy. Dissociation dynamics of inner-shell excited molecules. (Molecular science) Photoemission and soft-X-ray emission spectroscopy for solids. (Solid state and surface physics)
BL28B2	White Beam X-ray Diffraction	(Sept. 1999)	White X-ray diffraction and topography. Time-resolved energy-dispersive XAFS (DXAFS) for studies of chemical and/or physical reaction process. Biomedical imaging and radiation biology studies.
BL35XU	High Resolution Inelastic Scattering	(Sept. 2001)	Material dynamics on ~meV energy scales using inelastic X-ray scattering (IXS) and, sometimes, nuclear resonant scattering (NRS).
BL37XU	Trace Element Analysis	(Nov. 2002)	X-ray microbeam spectrochemical analysis. Ultra trace element analysis. High energy X-ray fluorescence analysis.
BL38B1	Structural Biology III	(Oct. 2000)	Structural biology. Macromolecular crystallography. Automatic data collection.
BL39XU	Magnetic Materials	(Oct. 1997)	X-ray magnetic circular dichroism (XMCD) spectroscopy and element-specific magnetometry under multiple-extreme conditions. XMCD/XAS using a sub-micron X-ray beam. X-ray emission spectroscopy. Resonant X-ray magnetic scattering.
BL40XU	High Flux	(Apr. 2000)	Time-resolved diffraction and scattering experiments. Microbeam X-ray diffraction and scattering experiments. X-ray photon correlation spectroscopy. Fluorescence analysis. Quick XAFS.
BL40B2	Structural Biology II	(Sept. 1999)	Noncrystalline small and wide angle X-ray scattering.
BL41XU	Structural Biology I	(Oct. 1997)	Structural biology. Macromolecular crystallography. Data collection from small crystals and large unicell crystals. Ultra-high resolution data collection.
BL43IR	Infrared Materials Science	(Apr. 2000)	Infrared microspectroscopy.
BL46XU	Engineering Science Research III	(Nov. 2000)	Structural characterization of thin films by X-ray diffraction and X-ray reflectivity measurement. Residual stress measurement. Time resolved X-ray diffraction measurement. Hard X-ray photoemission spectroscopy.
BL47XU	HAXPES·μCT	(Oct. 1997)	Hard X-ray photoelectron spectroscopy (HAXPES). Depth analysis of angle resolved HAXPES with wide acceptance lens. Projection type microtomography. Imaging type microtomography. Hard X-ray microbeam/scanning microscopy.

BL #	Beamline Name	(Public Use) or (First Beam)	Areas of Research
	● Contract Beamlines		
BL03XU	**Advanced Softmaterial** (Advanced Softmaterial Beamline Consortium)	(Nov. 2009)	Structural characterization of softmaterials using small- and wide-angle X-ray scattering. Grazing-incidence small- and wide-angle X-ray scattering for thin films. X-ray diffraction and reflectivity measurements for softmaterials.
BL07LSU	**University-of-Tokyo Synchrotron Radiation Outstation** (The University of Tokyo)	(Oct. 2009)	Time-resolved soft X-ray spectroscopy, nano-beam photoemission spectroscopy, ultra high-resolution soft X-ray emission spectroscopy, and any methods requiring the highly brilliant soft X-ray beam.
BL08B2	**Hyogo BM** (Hyogo Prefecture)	(Jun. 2005)	XAFS in a wide energy region. Small angle X-ray scattering for structural analyses of polymer and nanocomposite materials. X-ray topography. Imaging. Powder diffraction with a high angular-resolution.
BL11XU	**JAEA Quantum Dynamics**	(Oct. 1998)	Nuclear scattering. Surface and interface structure analysis with MBE. Inelastic X-ray scattering. XAFS.
BL12B2	**NSRRC BM** (National Synchrotron Rad. Res. Center)	(Oct. 2000)	X-ray absorption spectroscopy. Powder X-ray diffraction. High resolution X-ray scattering. Protein crystallography.
BL12XU	**NSRRC ID** (National Synchrotron Rad. Res. Center, Taiwan)	(Dec. 2001)	High resolution non-resonant or resonant inelastic X-ray scattering. High resolution near-edge X-ray Raman scattering. Phase transitions under high-pressure, low and high temperatures. High-resolution X-ray absorption and emission spectroscopy. X-ray physics and optics.
BL14B1	**JAEA Materials Science**	(Dec. 1997)	Materials science under high-temperature and high-pressure. *In situ* study on catalysis using dispersive XAFS. X-ray diffraction for structure physics.
BL15XU	**WEBRAM** (National Institute for Materials Science)	(Jan. 2000)	Hard X-ray photoelectron spectroscopy. High-precision X-ray powder diffraction.
BL16B2	**SUNBEAM BM** (SUNBEAM Consortium)	(Oct. 1998)	Characterization of secondary battery related materials, semiconductors, fuel cells, catalysts, and several industrial materials with using X-ray absorption fine structure measurements, X-ray diffraction (including X-ray reflectivity technique) and X-ray topography.
BL16XU	**SUNBEAM ID** (SUNBEAM Consortium)	(Oct. 1998)	Characterization of semiconductor materials, secondary batteries, fuel cells, catalysts, electrical display related materials, and structural materials with using X-ray diffraction, X-ray microbeam based evaluation technique (including X-ray magnetic circular dichroism), and fluorescence X-ray analysis.
BL22XU	**JAEA Quantum Structural Science**	(May 2002)	Materials science under high-pressure. Resonant X-ray scattering. Speckle scattering. Residual stress/strain distribution analysis.
BL23SU	**JAEA Actinide Science**	(Feb. 1998)	Surface chemistry with supersonic molecular beam. Biophysical spectroscopy. Photoelectron spectroscopy. Magnetic circular dichroism.
BL24XU	**Hyogo ID** (Hyogo Prefecture)	(May. 1998)	Surface/interface analysis for industry by fluorescent X-ray analysis, strain measurements and grazing incidence X-ray diffraction. Microbeam formation studies for materials and life sciences. Micro-SAXS for local long-range structure analysis.
BL28XU	**RISING** (Kyoto University) RISING: Research & Development Initiative for Scientific Innovation of New Generation Batteries	(Apr. 2012)	Analysis of rechargeable batteries. Time-resolved X-ray diffraction and XAFS with microbeam. XAFS of dilute systems and thin films. Dispersive XAFS. Hard X-ray photoelectron spectroscopy.
BL31LEP	**Laser-Electron Photon II** (RCNP, Osaka University)	(Apr. 2013)	Production of high intensity GeV photon beam by laser-backward Compton scattering. Hadron physics via photo-nucleon and photo-nuclear reactions. Test and calibration of detectors with GeV gamma-ray and converted electrons/positrons.
BL33LEP	**Laser-Electron Photon** (RCNP, Osaka University)	(Jun. 1999)	Meson photoproduction from nucleon and nucleus. Photoexcitation of hyperons, nucleon resonances, and other exotic states. Photonuclear reactions. Beam diagnoses. Test and calibration of detectors with GeV photon beam.
BL33XU	**TOYOTA** (TOYOTA Central R&D Labs., Inc.)	(Apr. 2009)	Time-resolved XAFS. Characterization of industrial materials, such as catalysts, secondary batteries, fuel cells.
BL36XU	**Catalytic Reaction Dynamics for Fuel Cells** (The University of Electro-Communications)	(Jan.2013)	Real time analysis of catalytic reaction dynamics for fuel cells: time resolved XAFS, 2D spatial resolved XAFS, depth resolved XAFS, 3D laminography XAFS, ambient pressure hard X-ray photoelectron spectroscopy.
BL44XU	**Macromolecular Assemblies** (IPR, Osaka University)	(May 1999)	Crystal structure analysis of biological macromolecular assemblies (e.g. membrane complexes, protein complexes, protein-nucleic acid complexes, and viruses).
	◆ RIKEN Beamlines		
BL17SU	**RIKEN Coherent Soft X-ray Spectroscopy**	(Sept. 2003)	High resolution photoemission spectroscopy. Soft X-ray emission spectroscopy for liquid and biological samples. Soft X-ray diffraction spectroscopy. Surface science.
BL19LXU	**RIKEN SR Physics**	(Oct. 2000)	SR science with highly brilliant X-ray beam.
BL26B1	**RIKEN Structural Genomics I**	(Apr. 2002)	Structural genomics research based on single crystal X-ray diffraction.
BL26B2	**RIKEN Structural Genomics II**	(Apr. 2002)	Structural genomics research based on single crystal X-ray diffraction.
BL29XU	**RIKEN Coherent X-ray Optics**	(Dec. 1998)	X-ray optics, especially coherent X-ray optics.
BL32XU	**RIKEN Targeted Proteins**	(Oct. 2009)	Protein micro-crystallography.
BL43LXU	**RIKEN Quantum NanoDynamics**	(Oct. 2011)	High resolution inelastic X-ray scattering for investigating atomic and electronic dynamics.
BL44B2	**RIKEN Materials Science**	(Feb. 1998)	Structural materials science research using powder X-ray diffraction.
BL45XU	**RIKEN Structural Biology I**	(Jul. 1997)	Time-resolved and static structures of non-crystalline biological materials using small-angle scattering and diffraction techniques.
	■ Accelerator Diagnostics Beamlines		
BL05SS	**Accelerator Beam Diagnosis**	(Mar. 2004)	Accelerator beam diagnostics. R&D of accelerator components. Nano forensic science.
BL38B2	**Accelerator Beam Diagnosis**	(Sept. 1999)	Accelerator beam diagnostics. R&D of accelerator components.

IV. User Program and Statistics

SPring-8 calls for public use proposals twice a year. The submitted proposals are reviewed by the SPring-8 Proposal Review Committee (SPring-8 PRC). Since 1997, SPring-8 has accepted a variety of proposals. The historical change in the proposal categories is summarized in Fig. 3. For the promotion of Industrial Application at SPring-8, the Industrial Application Division was established in 2005. With consultation support for industrial users given by the division's coordinators, currently, Industrial Application Proposals account for approximately 20% of the total number of proposals conducted at the public beamlines. In addition, the Measurement Service was introduced in 2007B, in which the personnel of the Industrial Application Division carry out XAFS measurements on behalf of users at BL14B2. SPring-8 also launched the Mail-in Protein Crystallography Data Collection Service at BL38B1 and the Powder X-ray Diffraction Measurement Service at BL19B2 in 2009B, and Hard X-ray Photoemission Spectroscopy (HAXPES) Measurement Service, Thin Film Analysis (GIXD/XRR) Measurement Service at BL46XU in 2012B. Proposal statistics from 1997B to 2013B are shown in Table IV.

SPring-8 consistently provides ~4000 hours of user beamtime per year. Since beginning operation in 1997, SPring-8 has provided users with a total beamtime of 62,704 hours. The beamtime available to users, the number of experiments conducted, and the number of user visits at the public and contract beamlines are summarized in Table V and in Fig. 4. Part of the proposals is for proprietary use, in which refereed reports may not be required. Figure 5 shows the number of the proprietary use for each research term. The number is increasing for the public beamlines. Figure 6 shows the number of unique users for each fiscal year; there are approximately 1500 new users annually. The number of submitted and approved proposals by research term, the approved rate, the total shift of the beamtime for the public beamlines are summarized in Fig. 7. The approved rate is about 70% since the inception of SPring-8. The breakdowns of approved proposals sorted by user affiliation at the public and contract beamlines are shown in Fig. 8 and Fig. 9, respectively. The numbers of the approved proposals sorted by research area at the public and contract beamlines are shown in Fig. 10 and Fig. 11, respectively.

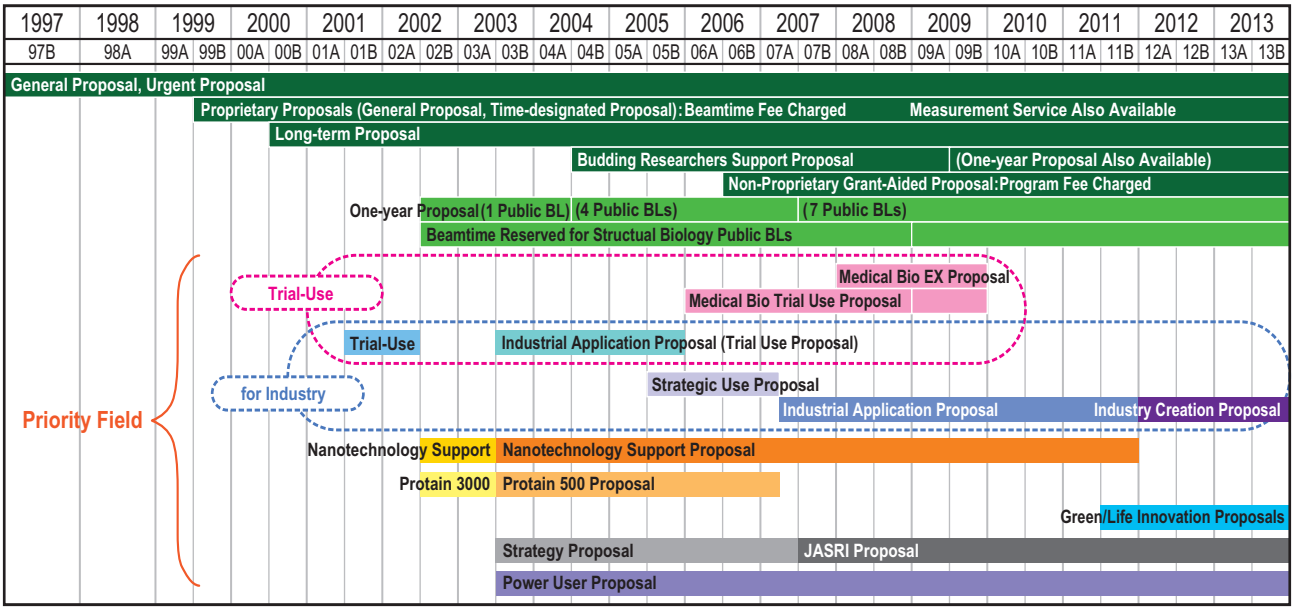

Fig. 3. Categories of proposals for the public beamlines.

Table IV. Numbers of submitted proposals and approved proposals by research term

Research Term	Deadline	Submitted proposals	Approved proposals
1997B: 1997.10 - 1998.03	1997.1.10	198	134
1998A: 1998.04 - 1998.10	1998.1.6	305	229
1999A: 1998.11 - 1999.06	1998.7.12	392	258
1999B: 1999.09 - 1999.12	1999.6.19	431	246
2000A: 2000.02 - 2000.06	1999.10.16	424	326
2000B: 2000.10 - 2001.01	2000.6.17	582	380
2001A: 2001.02 - 2001.06	2000.10.21	502	409
2001B: 2001.09 - 2002.02	2001.5.26	619	457
2002A: 2002.02 - 2002.07	2001.10.27	643	520
2002B: 2002.09 - 2003.02	2002.6.3	751	472
2003A: 2003.02 - 2003.07	2002.10.28	733	563
2003B: 2003.09 - 2004.02	2003.6.16	938	621
2004A: 2004.02 - 2004.07	2003.11.4	772	595
2004B: 2004.09 - 2004.12	2004.6.9	886	562
2005A: 2005.04 - 2005.08	2005.1.5	878	547
2005B: 2005.09 - 2005.12	2005.6.7	973	624
2006A: 2006.03 - 2006.07	2005.11.15	916	699
2006B: 2006.09 - 2006.12	2006.5.25	867	555
2007A: 2007.03 - 2007.07	2006.11.16	1099	761
2007B: 2007.09 - 2008.02	2007.6.7	1007	721
2008A: 2008.04 - 2008.07	2007.12.13	1009	749
2008B: 2008.10 - 2009.03	2008.6.26	1163	659
2009A: 2009.04 - 2009.07	2008.12.11	979	654
2009B: 2009.10 - 2010.02	2009.6.25	1076	709
2010A: 2010.04 - 2010.07	2009.12.17	919	665
2010B: 2010.10 - 2011.02	2010.7.1	1022	728
2011A: 2011.04 - 2011.07	2010.12.9	1024	731
2011B: 2011.10 - 2012.02	2011.6.30	1077	724
2012A: 2012.04 - 2012.07	2011.12.8	816	621
2012B: 2012.10 - 2013.02	2012.6.28	965	757
2013A: 2013.04 - 2012.07	2012.12.13	880	609
2013B: 2013.10 - 2013.12	2013.6.20	905	594

Notes:
1997B-2006B: The number of proposals are indicated as of submission deadline.
After 2007A: The total number of proposals are indicated.
The number of longterm proposals are counted by beamline, that is,
if the project leader uses two beamlines, it is counted as two proposals.

Table V. Numbers of experiments and users at public and contract beamlines by research term

Research Term	User time (hours)	Public BL		Contract BL	
		Experiments	Users	Experiments	Users
1997B: 1997.10 - 1998.03	1,286	94	681	–	–
1998A: 1998.04 - 1998.10	1,702	234	1,252	7	–
1999A: 1998.11 - 1999.06	2,585	274	1,542	33	467
1999B: 1999.09 - 1999.12	1,371	242	1,631	65	427
2000A: 2000.02 - 2000.06	2,051	365	2,486	100	794
2000B: 2000.10 - 2001.01	1,522	383	2,370	88	620
2001A: 2001.02 - 2001.06	2,313	474	2,915	102	766
2001B: 2001.09 - 2002.02	1,867	488	3,277	114	977
2002A: 2002.02 - 2002.07	2,093	545	3,246	110	1,043
2002B: 2002.09 - 2003.02	1,867	540	3,508	142	1,046
2003A: 2003.02 - 2003.07	2,246	634	3,777	164	1,347
2003B: 2003.09 - 2004.02	1,844	549	3,428	154	1,264
2004A: 2004.02 - 2004.07	2,095	569	3,756	161	1,269
2004B: 2004.09 - 2004.12	1,971	555	3,546	146	1,154
2005A: 2005.04 - 2005.08	1,880	560	3,741	146	1,185
2005B: 2005.09 - 2005.12	1,818	620	4,032	187	1,379
2006A: 2006.03 - 2006.07	2,202	724	4,809	226	1,831
2006B: 2006.09 - 2006.12	1,587	550	3,513	199	1,487
2007A: 2007.03 - 2007.07	2,448	781	4,999	260	2,282
2007B: 2007.09 - 2008.02	2,140	739	4,814	226	1,938
2008A: 2008.04 - 2008.07	2,231	769	4,840	232	1,891
2008B: 2008.10 - 2009.03	1,879	672	4,325	217	1,630
2009A: 2009.04 - 2009.07	1,927	669	4,240	238	1,761
2009B: 2009.10 - 2010.02	2,087	722	4,793	275	2,144
2010A: 2010.04 - 2010.07	1,977	685	4,329	293	2,483
2010B: 2010.10 - 2011.02	2,094	744	4,872	325	2,812
2011A: 2011.04 - 2011.07	2,131	740	4,640	309	2,773
2011B: 2011.10 - 2012.02	1,927	730	4,576	319	2,769
2012A: 2012.04 - 2012.07	1,972	637	4,304	285	2,692
2012B: 2012.10 - 2013.02	2,184	771	5,072	314	3,181
2013A: 2013.04 - 2013.07	1,837	633	4,053	275	2,835
2013B: 2013.10 - 2013.12	1,570	610	3,770	286	2,723
	62,704	18,302	117,137	5,997	50,970

Note:
The number of longterm proposals are counted by beamline, that is, if two beamlines were used for one experiment, those are counted as two experiments.

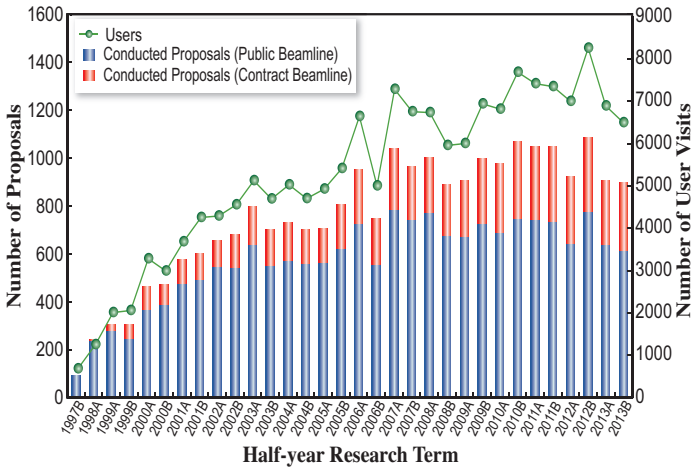

Fig. 4. Numbers of user visits and conducted experiments.

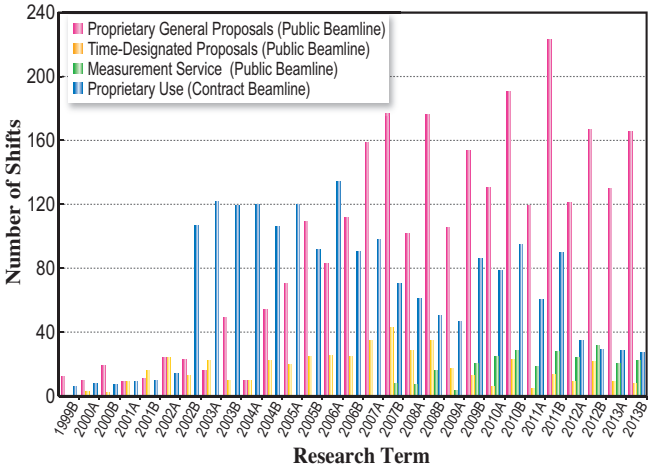

Fig. 5. Number of shifts for proprietary proposals. One shift is 8 hours at SPring-8 beamlines.

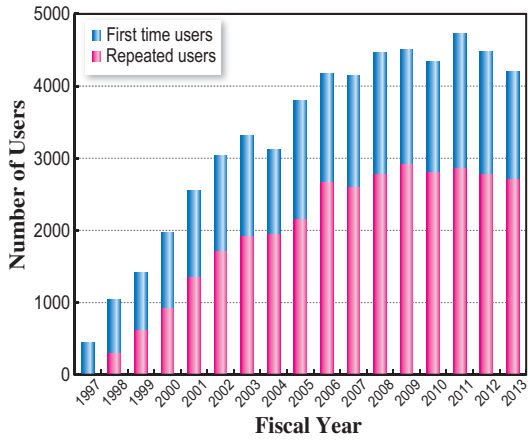

Fig. 6. Numbers of user visits and conducted experiments.

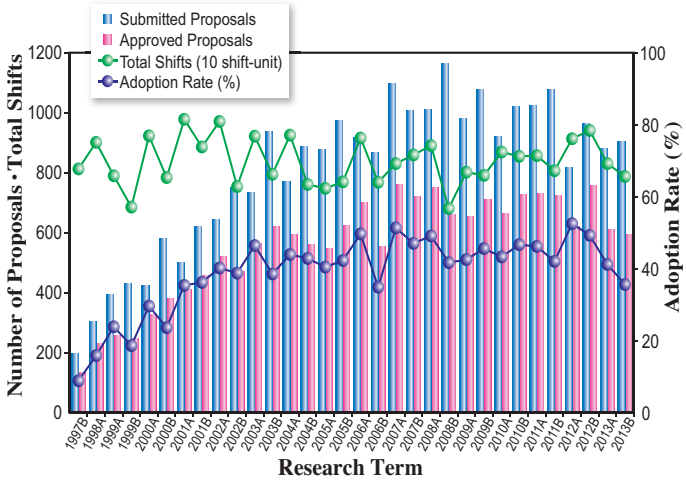

Fig. 7. Numbers of submitted proposals and approved proposals by research term (public beamlines).

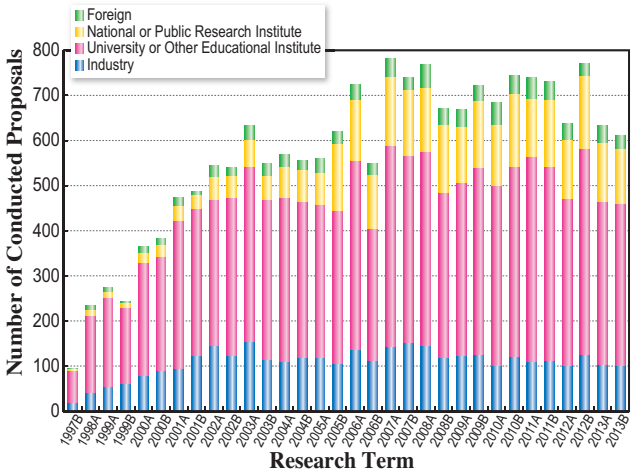

Fig. 8. Number of conducted proposals by project leaders (public beamlines).

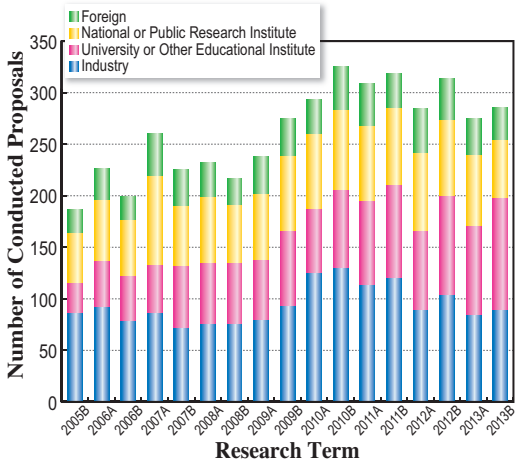

Fig. 9. Number of conducted proposals by affiliation categories (contract beamlines).

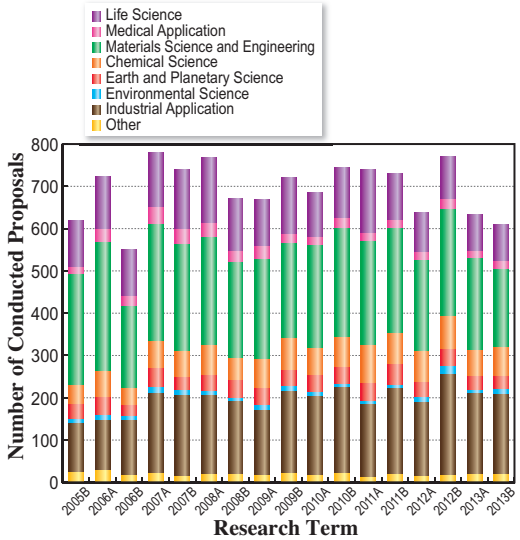

Fig. 10. Number of conducted proposals by research area (public beamlines).

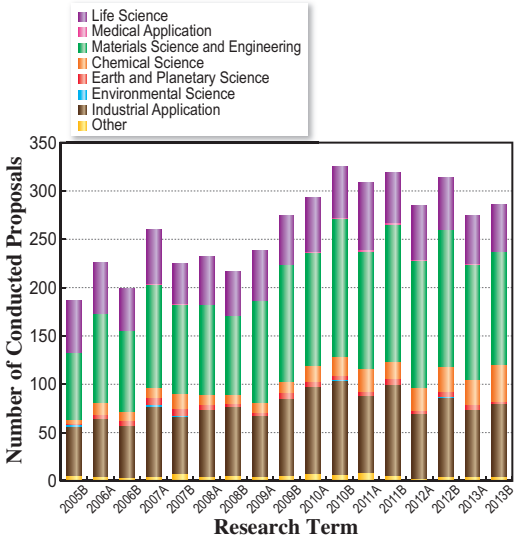

Fig. 11. Number of conducted proposals by research area (contract beamlines).

V. Research Outcome

As of March 2014, the number of registered refereed papers is 9,163, of which 7,503 papers resulted from the use of public beamlines, 1,752 from that of contract beamlines, 1,057 from RIKEN beamlines, and 479 papers from hardware/software R&D. Note that papers that used two or more beamlines are counted separated for each beamline. Figure 12 shows the annual statistics of refereed papers.

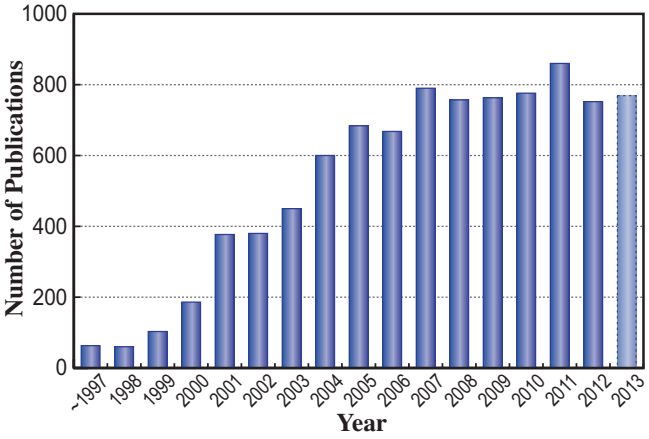

Fig. 12. Number of refereed publications as of March 2014.

VI. Budget and Personnel

When SPring-8 started operation in 1997, it was jointly managed by RIKEN, JAERI (JAEA, as it is known today), and JASRI. However, JAERI withdrew from management of SPring-8 on September 30, 2005. Today SPring-8 is administered by RIKEN and JASRI in a collaborative manner.

Figure 13 shows the annual budget allocated to operations, maintenance, and promotion of SPring-8 from FY1997 to date. The budget for FY2013 was 8.918 billion yen.

As of October 2013, RIKEN and JASRI have a total of 511 staff members (Fig. 14).

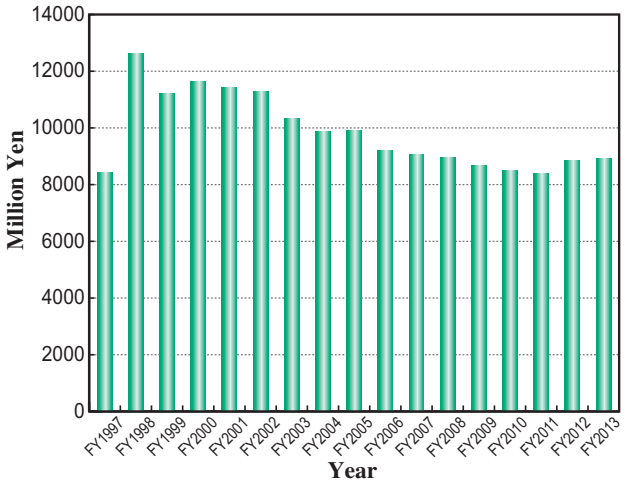

Fig. 13. SPring-8 budget.

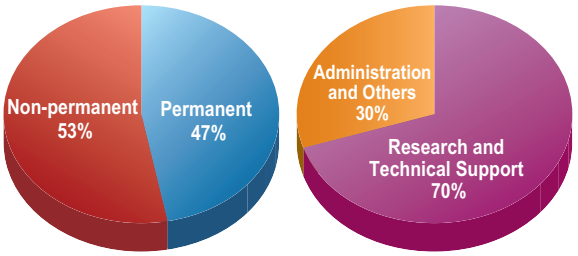

	by Type		by Field		Others
	Permanent	Non-permanent	Research and Technical Support	Administration and Others	Visiting Scientists and Students
RIKEN	48	142	150	40	534
JASRI	191	130	207	114	121

Including double counts.

Fig. 14. Personnel at SPring-8: JASRI and RIKEN.

VII. Research Complex

The facilities of SPring-8, SACLA, and NewSUBARU form a Center of Excellence (COE) at the SPring-8 campus, where JASRI, public beamline users, contractors of contract beamlines, RIKEN, and the University of Hyogo work in close cooperation, forming a research complex where each member plays its own role to deliver high-quality results in the field of synchrotron radiation science and technology. Figure 15 shows the SPring-8 research complex, and the operation and management of each research facility. The organizational charts of RIKEN and JASRI, which are at the center of this research complex, are shown in Fig. 16 and Fig. 17, respectively.

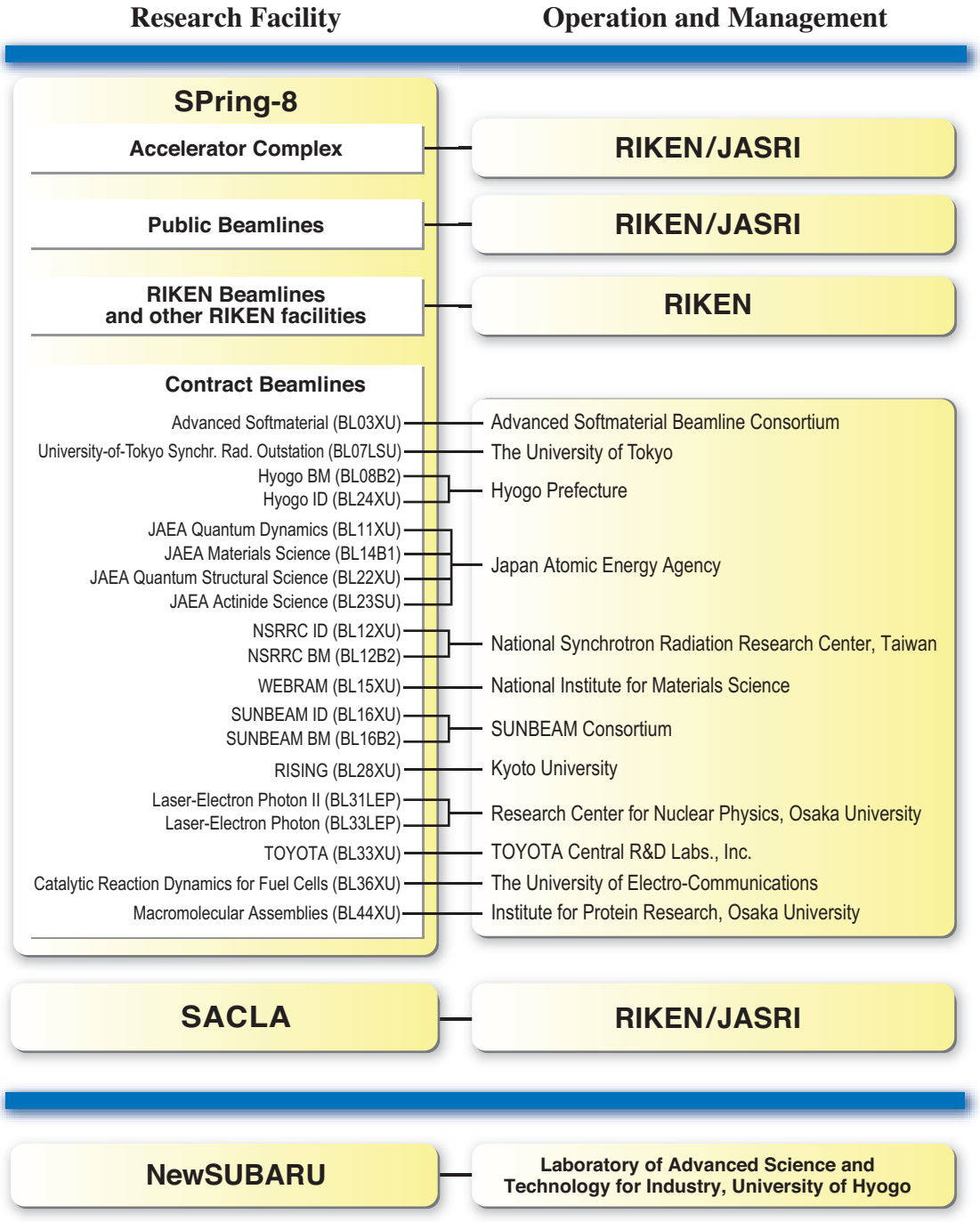

Fig. 15. SPring-8 research complex as of April 2014.

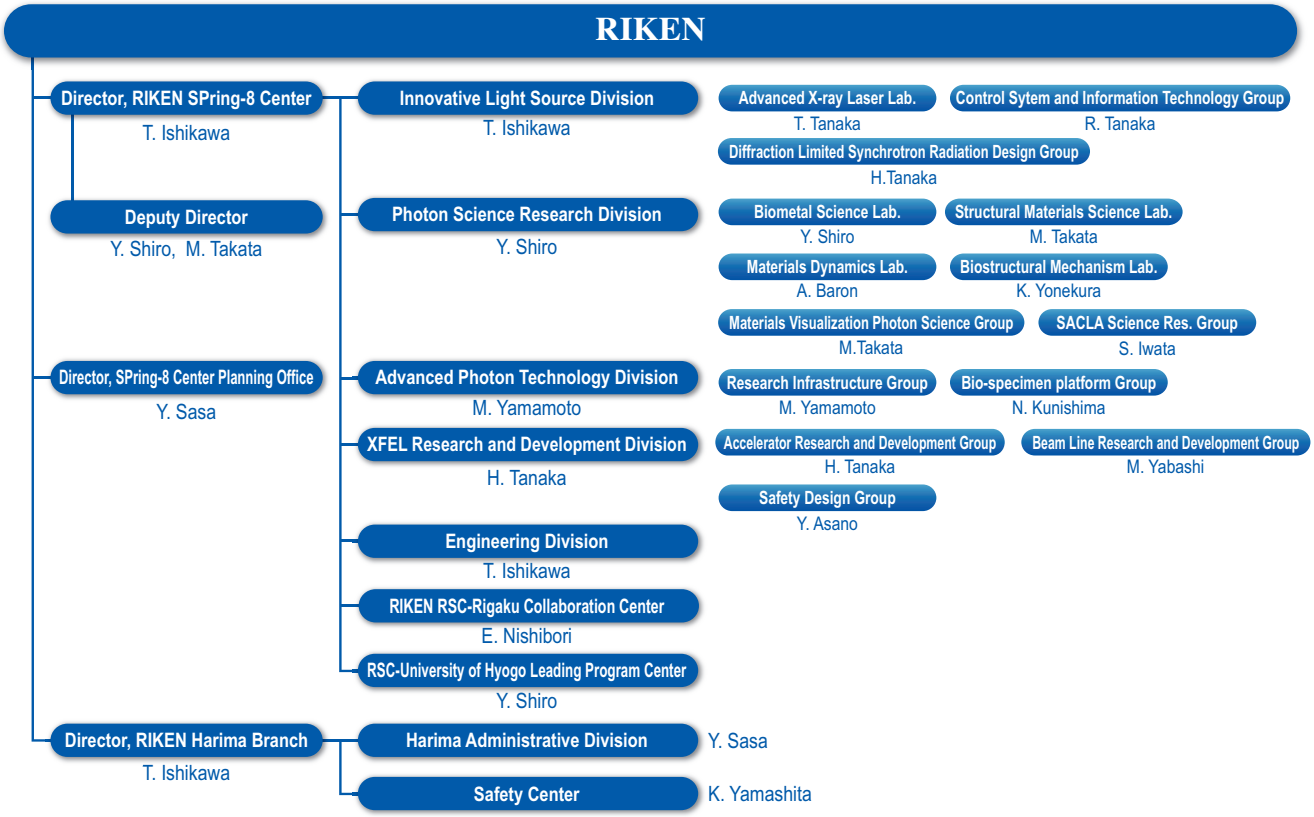

Fig. 16. RIKEN Harima Branch chart as of April 2014.

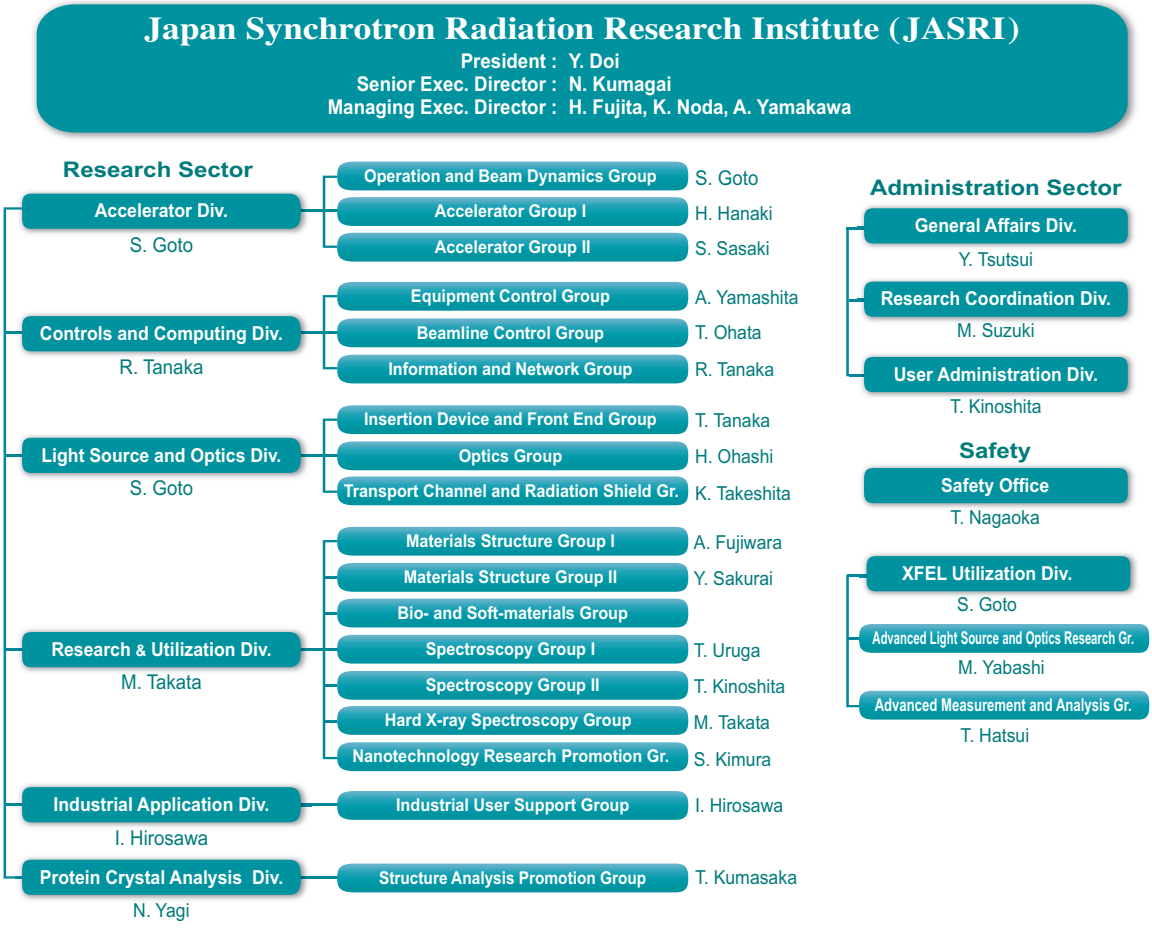

Fig. 17. JASRI chart as of April 2014.

VIII. Users Societies, Conferences, and Other Activities

SPring-8 Users Community (SPRUC)

The **SPring-8 Users Society** was organized in May 1993, before SPring-8 existed, to discuss the construction of and the scientific research studies at SPring-8. During the construction and development phases, the SPring-8 Users Society made enormous contributions in constructing the beamlines and promoting the utilization of SPring-8 through discussions among users and between users and facility staff. The number of members in the SPring-8 Users Society has been constant around 1,200, but the number of SPring-8 users has exceeded 10,000. Consequently, the SPring-8 Users Society had to be reformed to represent all SPring-8 users and to continue to contribute to the promotion, utilization, and upgrades of SPring-8 as it evolves.

In April 2012, a new organization, SPring-8 Users Community (SPRUC), was formed; it includes not only all users but also potential users interested in SPring-8. In terms of its organization, SPRUC has a remarkable feature. About 30 institutes (principal universities and national research institutes), where many users belong, participate in SPRUC to discuss the promotion and utilization of SPring-8 from strategic and perspective viewpoints.

One of the key activities of SPRUC is to host an annual SPring-8 symposium at a site of one of its members in conjunction with RIKEN and JASRI. The SPring-8 symposium 2013 which had a theme of "Innovative Science & Technology for the Next Generation," was held at Kyoto University on 7 and 8 September 2013. In addition, SPRUC provides a Young Scientist Award to recognize pioneering achievements in photon science by individual young scientists using SPring-8. The award ceremony and winning lecture are held at the SPring-8 Symposium. SPRUC2013 Scientist Young Award was conferred to two young scientists (Dr. Alexander Gray, SLAC National Accelerator Laboratory and Mr. Keita Ito, University of Tsukuba). The SPring-8 Symposium 2014 is scheduled for September at The University of Tokyo.

SPRUC established a Project Committee in March of 2013. A working group (WG), which is comprised of subject-matter experts working together to achieve specific goals, is formed under the Project Committee. In March 2013, the "WG on Future vision of SR source" was organized to promote discussions about the grand design of domestic light source projects. In June 2013, the "WG on Reorganization of SPRUC Research Groups" was established to solve the current problems in the organization of SPRUC Research Groups and to improve their activities. In December 2013, the "WG on Graduate Programs" was organized to discuss an effective on-site education for young scientists.

Users Meeting

The meetings for users jointly organized by the SPring-8 Users Society and/or the Industrial User Society of SPring-8, and JASRI and RIKEN are listed below.

• The 10th Report Meeting on SPring-8 Industrial Application
September 5-6, 2013 – Hyogo Prefecture Citizens' Hall, Kobe, Hyogo

• SPring-8 Symposium 2013
September 7-8, 2013 – Kyoto University, Uji, Kyoto

Conferences and Workshops

The conferences and workshops organized, sponsored, or hosted by RIKEN, JASRI, or both in 2013 are listed below.

• The 2nd Workshop Frontier Softmaterial Beamline (BL03XU), SPring-8
January 9, 2013 – Kyushu University, Fukuoka, Fukuoka

• The 26th Annual Meeting of Japanese Society for Synchrotron Radiation Research
January 11-14, 2013 – Nagoya University, Nagoya, Aichi

• 4th International Symposium on Diffraction Structural Biology 2013
May 26-29, 2013 – Nagoya City Hall to promote small to medium enterprises, Nagoya, Aichi

• The 31st Seminar on Interface Science in Kansai, Japan
"Surface and Interface World by Synchrotron Radiation"
August 2-3, 2013 – SPring-8, Sayo, Hyogo

• The 5th Workshop on the Basis of Synchrotron Radiation
August 2-3, 2013 - The University of Tokyo, Komaba, Tokyo

• Light and Particle Beams in Materials Science 2013
August 28-31, 2013 – EPOCHAL TSUKUBA, Tsukuba, Ibaraki

• The 7th Asia Oceania Forum for Synchrotron Radiation Research
September 21-24, 2013 - Egret Himeji, Himeji, Hyogo

• The 6th Workshop on the SPring-8 Budding Researchers Support Program
December 6, 2013 - Campus Innovation Center, Shibaura, Tokyo

• Neutron Industrial Use Seminar
December 13, 2013 – Plaza for Citizens of Chiba Prefecture, Kashiwa, Chiba

Other Activities

• The 21th SPring-8 Open House
April 27, 2013 – SPring-8, Sayo, Hyogo

• The 13th SPring-8 Summer School 2013
June 30 - July 3, 2013 – SPring-8, Sayo, Hyogo

• The 7th AOFSRR School - Cheiron School 2013
September 24 - October 3, 2013 – SPring-8, Sayo, Hyogo


AOFSRR 2013


AOFSRR


37
XU


JASRI SPring-8 コンファレンス2014
SPring-8
～最先端光サイエンスの世界～


の仲間たちと記念撮影!

SACLA

I. Introduction

SACLA is the world's second X-ray free electron laser (XFEL), following the Linac Coherent Light Source (LCLS) in the US. Currently, these are the only two XFELs in operation. SACLA delivers the shortest wavelength XFEL. SACLA achieved its first lasing on June 7, 2011, within three months of electron beam commissioning, and launched user operations from 2012A. The user selection system for SACLA is based on that used by SPring-8. SACLA has an independent proposal review committee, the SACLA Proposal Review Committee (SACLA PRC), which reviews all received proposals.

II. Machine Operation & Beamlines

Our second year of operations proceeded without any significant issues. Operation statistics are summarized in Table VI. The ratio of downtime to user time was kept below 7.3%, a reasonably low rate for linac-based light sources.

Table VI. Operation statistics for FY2013

	Time (h)
Total operation time	7017
User time	3459
Facility tuning time	860
Study time	2698
Downtime	252 (7.3% of user time)

In 2013, two beamlines, BL3 for XFEL and BL1 for broadband spontaneous light, were open for users, while all experiments were conducted with BL3. The key components, the 1-μm focusing system and the synchronized optical laser system, were utilized for many experiments.

III. User Program and Statistics

SACLA calls for public use proposals twice per year. Proposals fall into two categories: General Proposals for general research with no specific research theme, while the Priority Strategy Proposals for strategic themes identified based on national policy. Currently there are two strategic themes: Hierarchical Structure Dynamics of Biomolecules and Pico/Femto Second Dynamic Imaging. Table VII shows the research themes for each group are as follows:

Table VII. Research themes for each group

1. Hierarchical Structure Dynamics of Biomolecules	1-1 Structural Analysis of Drug-targeted Membrane Protein Nanocrystals
	1-2 Imaging of Whole Cell and Its Components in the Living State
	1-3 Single Molecule Structural Analysis of Supramolecular Complex
	1-4 Dynamics Research Combining Single Molecule X-ray Diffraction Experiments and Supercomputer Analysis
	1-5 Dynamic Structural Analysis Using Pump-Probe Techniques
2. Pico/Femto Second Dynamic Imaging	2-1 Gas-Phase/Liquid-Phase/Solid-Phase Reaction Dynamics
	2-2 Ultrafast Interface Reaction Processes
	2-3 Charge Generation/Charge Transfer Dynamics
	2-4 Ultrafast Processes under Extreme Conditions
	2-5 Dynamic X-ray Spectroscopy

Table VIII, Figs. 18 and 19 provide statistics on proposals, users, and beamtime. Among the proposals carried out, the number of general proposals were 13, 8, 9, and 11 during 2012A, 2012B, 2013A, and 2013B, respectively.

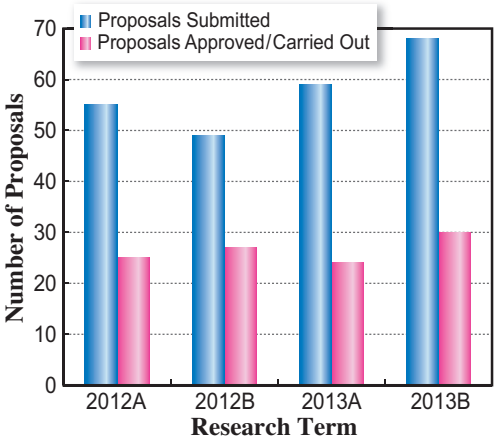

Fig. 18.

Table VIII. Number of proposals submitted, proposals approved/carried out, cumulative users and beamtime available by research term

Half-year Research Term	Proposals Submitted	Proposals Approved/Carried Out	Cumulative Users	Beamtime Carried Out (Shifts)
2012A	55	25	297	126
2012B	49	27	461	154
2013A	59	24	268	117
2013B	68	30	410	139

One shift = 12 hours at SACLA beamlines

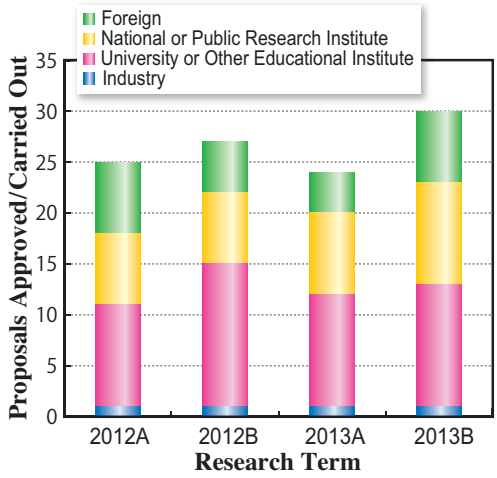

Fig. 19.

IV. Research Outcome

Fifteen original papers were published and registered in the SACLA information database. These include two papers in Physical Review Letters (see Chemical Science in this volume, pages 78 and 80), one in Nano Letters, and one in Nature Photonics.

NewSUBARU

The NewSUBARU synchrotron light facility is operated by the Laboratory of Advanced Science and Technology for Industry (LASTI), University of Hyogo. This facility consists of an electron storage ring and nine beamlines. Electron injection is supplied from a 1 GeV linac of the SPring-8 facility. The conceptual layout of the NewSUBARU facility is illustrated below.

(1) Five beamlines were upgraded for advanced research and industrial application. Upgraded beamlines are marked in yellow in the figure below. For example, there have been improvements in the beamline control system and an upgrade of spectrometer in the industrial analysis beamline BL05. A large EUV mirror reflectivity meter was installed on BL10. One of the LIGA beamlines, BL11, was remodeled for advanced industrial manufacturing.

(2) Laser Compton scattering gamma-ray beamline BL01 was used for precise measurements of electron energy in the storage ring.

All NewSUBARU beamlines are open for industry use. Promotion of both use and technical assistances industrial users is supported by MEXT's "Project for Creation of Research Platforms and Sharing of Advanced Research Infrastructure."

Shuji Miyamoto
Director of LASTI, University of Hyogo

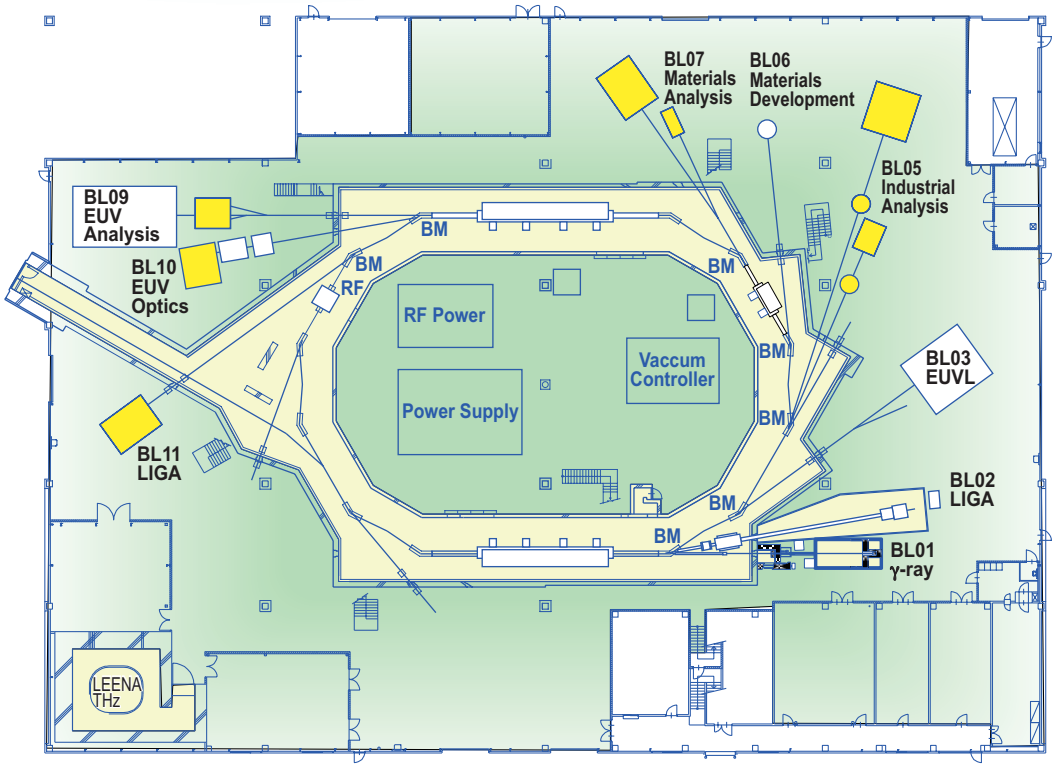

Laser Compton scattering γ-ray beamline at NewSUBARU

Laser Compton scattering γ-ray (LCSγ) beamline BL01 [1-3] at NewSUBARU has been upgraded. A new irradiation hutch for the γ-ray beam has been added in collaboration with Konan University. The user use of γ-ray beams with photon energy of up to 76.3 MeV has begun with maximum γ-ray beam power of 0.33 mW.

The LCSγ's are unique photon source generated by scattering of laser photon by relativistic electron beam. Schematic of LCSγ is shown in Fig. 1. The maximum γ-ray photon energy at head on collision is calculated by kinematics as

$$E_\gamma = 4E_L\gamma^2 / (1+\gamma^2\theta^2 + 4\gamma E_L/mc^2) ,$$

where $\gamma = 1+E_e/mc^2$ is the Lorentz factor, E_e is an electron energy, mc^2 is the rest energy of electrons, E_L is a laser photon energy, θ is the scattering angle of γ-ray relative to the electron beam axis, and $4\gamma E_L/mc^2$ is the recoil effect. When the Nd:YVO_4 laser (wavelength of 1064 nm) is scattered by a 1-GeV electron, the maximum scattered photon energy is E_γ =17.5 MeV. The angular distribution of the γ-ray photon energy is calculated by the above equation, as shown in Fig. 2. A quasi-monochromatic γ-ray beam is obtained by extracting small angle scattering using an axial collimator. Polarization of the laser beam is also conserved at the beam axis. Due to these special features of the LCSγ, this γ-ray source was used for nuclear physics and an astro-nuclear physics research, as well as generation of useful isotopes, non-destructing inspection of bulk material by γ-ray radiography and positron annihilation.

In brief, the experimental setup is as follows: a beam of 974-MeV electrons is injected from the SPring-8 linear accelerator into the NewSUBARU storage ring. The energy of the storage electrons is a relative value with ~1% uncertainty based on the magnetic field strength and the beam optics of the storage ring [4], hereafter referred to as the "nominal" energy in this paper.

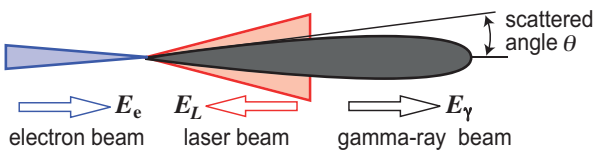

Fig. 1. Schematic of laser Compton scattering γ-ray generation at head-on collision.

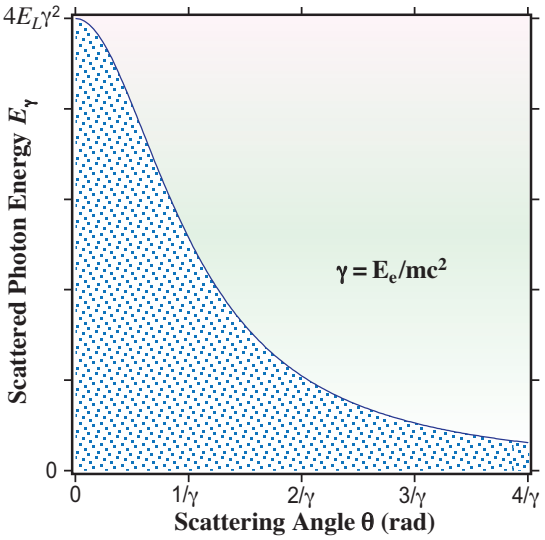

Fig. 2. Dependence of the γ-ray photon energy on the scattering angle θ.

We performed absolute calibration of electron beam energies of the storage ring NewSUBARU in the nominal energy range of 0.55 - 1.0 GeV [5]. The technique of laser Compton backscattering has been developed to accurately determine electron beam energies [6] as an alternative to the technique of resonant spin depolarization [7], which is limited to high energy electrons because of spin depolarization time [8].

We also performed the energy calibration systematically with the following steps, (1) production of low-energy LCSγ beams in collisions of CO_2 laser photons with electrons at ten nominal energies, from 974 MeV to 550 MeV; (2) measurements of LCSγ beams with a high-purity germanium (HPGe) detector; (3) energy calibration of the HPGe detector with standard γ-ray sources.

Figure 3 indicates the experimental setup for the measurement in the γ-ray beamline BL01 of the NewSUBARU synchrotron light facility. A grating-fixed CO_2 laser (INFRARED INSTRUMENTS, IR-10-WS-GF-VP) oscillated at a single line of the strongest master transition P(20). The central wavelength of the P(20) transition is known (=10.5915 μm ± 3 Å) with a bandwidth of 1.3 Å in FWHM. The accuracy of the wavelength of CO_2 laser is 4.1×10^{-5}.

The CO_2 laser photons produced outside the storage ring vault were led through four mirrors and one lens into the vacuum tube of the ring to a collision

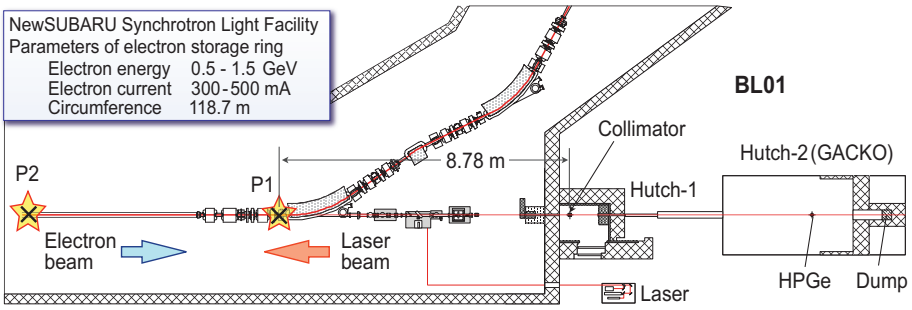

Fig. 3. Two γ-ray irradiation hutches are shown. Layout of laser Compton scattering γ-ray beam source in NewSUBARU BL01. Two collision points and two γ-ray irradiation hutches are shown.

point P1 in the straight section of the storage ring. The collision point P1 for the CO_2 laser is located at the distance of 8.78 m from a collimator set in the experimental Hutch 1. The collision point P2 for the Nd:YVO_4 laser is located at 18.47 m from the collimator. A coaxial HPGe detector (64 mm in diameter × 60 mm in length) was mounted in Hutch 2 and aligned with synchrotron radiation to measure the low-energy LCSγ's. The HPGe detector was calibrated with the standard γ-ray sources, ^{60}Co including the sum peak, ^{133}Ba, ^{137}Cs, and ^{152}Eu and a natural radioactivity ^{40}K. After the injection of electrons into the NewSUBARU storage ring, the electron beam was decelerated to the nominal energy of 950 MeV, and subsequently down to 550 MeV in steps of 50 MeV, followed by a production of the LCSγ beam and measurements with the HPGe detector at every energy.

The difference between the calibrated energy E(measure), and the nominal energy E(nominal), ΔE = E(measure) – E(nominal), is shown in Fig. 4. The 4th-order polynomial fit to the data gives

$$\Delta E = -4.6949 \times 10^{-10}(E^n)^4 + 1.3017 \times 10^{-6}(E^n)^3 - 1.3596 \times 10^{-3}(E^n)^2 + 0.63854(E^n) - 103.94$$

Here ΔE, E(measured) and E^n = E(nominal) are given in MeV. The difference between the nominal and calibrated energies is 10.92 MeV (1.36%) at the nominal energy of 800 MeV. The electron beams in the storage ring NewSUBARU have been systematically calibrated in the nominal energy range of 550 - 974 MeV by using low-energy LCSγ beams produced with a CO_2 laser. For more information about this experiment and analysis, please see Ref. [5].

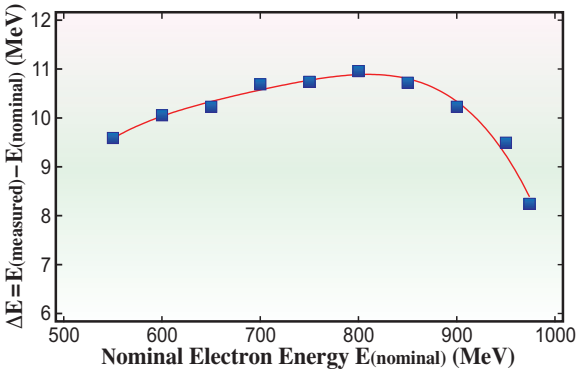

Fig. 4. The difference ΔE of the calibrated energy E(measured) from the nominal energy E(nominal) of the electron beams, ΔE = E(measured) – E(nominal), at the NewSUBARU storage ring.

S. Miyamoto[a,*], H. Utsunomiya[b], T. Shima[c] and S. Amano[a]

[a] NewSUBARU, LASTI, University of Hyogo
[b] Department of Physics, Konan University
[c] Research Center for Nuclear Physics, Osaka University

*E-mail: miyamoto@lasti.u-hyogo.ac.jp

References

[1] S. Miyamoto *et al.*: Radiat. Meas. **41** (2007) S179.
[2] S. Amano *et al.*: Nucl. Instrum. Meth. Phys. Res. A **602** (2009) 337.
[3] K. Horikawa *et al.*: Nucl. Instrum. Meth. Phys. Res. A **618** (2010) 209.
[4] A. Ando *et al.*: J. Synchrotron Rad. **5** (1998) 342.
[5] *H. Utsunomiya, T. Shima, K. Takahisa, D.M. Filipescu, O. Tesileanu, I. Gheorghe, H.-T. Nyhus, T. Renstrom, Y.-W. Lui, Y. Kitagawa, S. Amano, S. Miyamoto: IEEE Trans. Nucl. Sci.* ***61*** *(2014) 1252.*
[6] L.C. Hsu *et al.*: Phys. Rev. E **54** (1996) 5657.
[7] Ya. S. Derbenev *et al.*: Part. Accel. **10** (1980) 177.
[8] R. Klein *et al.*: Nucl. Instrum. Meth. Phys. Res. A **384** (1997) 293.

Editor
Naoto Yagi
SPring-8 / JASRI

Editing, Design & Layout
Marcia M. Obuti-Daté
SPring-8 / JASRI

Printing
ROKKO Publishing & Sale Co.

J A S R I
Information & Support System Section
Users Administration Division

1-1-1 Kouto, Sayo-cho, Sayo-gun
Hyogo 679-5198 • JAPAN
Tel. +81-(0)791 58-2797 Fax. +81-(0)791 58-1869

E-mail: frontiers@spring8.or.jp
http://www.spring8.or.jp/

August 2014

SPring-8 SACLA

http://www.spring8.or.jp

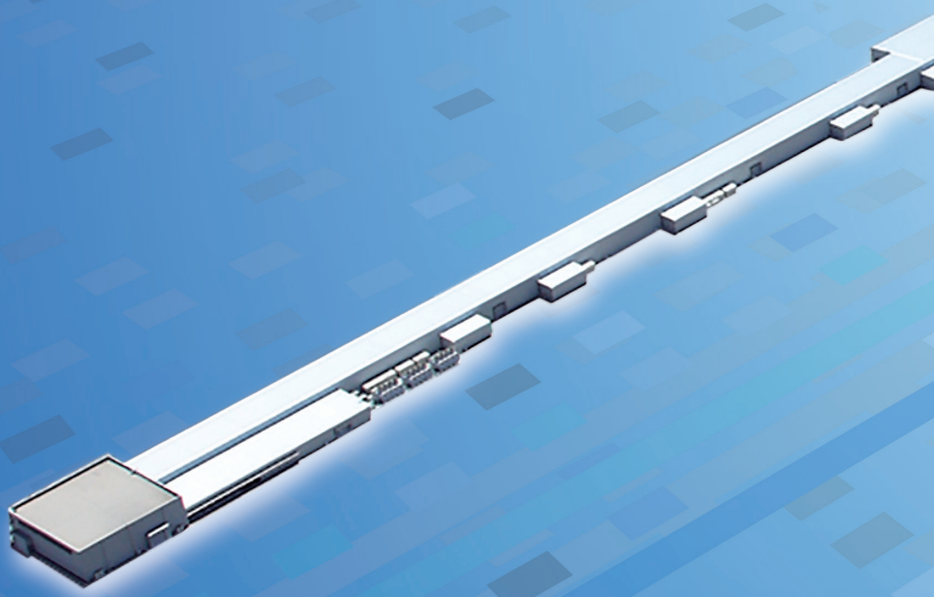

Japan Synchrotron Radiation Research Institute
1-1-1 Kouto, Sayo-cho, Sayo-gun, Hyogo 679-5198, Japan